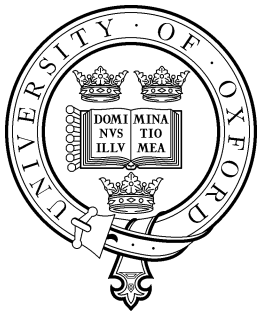
The Role of Grain Boundaries in Plastic Deformation



Diana Avadanii
University College
University of Oxford

A thesis submitted for the degree of
Doctor of Philosophy

Trinity 2022

Declaration

I hereby declare that I wrote and composed this thesis and that none of the work has been submitted for any other degree or professional qualification. I confirm that the work of this thesis is my own except where explicitly stated.

Acknowledgements

Lonely is the road of the self-made individual. Thankfully, I am very far from this notion as I have benefited from incredible mentorship and community during my DPhil journey. I will do my best to succinctly acknowledge everyone who has contributed to my academic and personal trajectory while I pursued my DPhil, while acknowledging that a significantly greater number of people have contributed in small, but impactful ways in the everyday unfolding of life. My degree has been fully funded by the UK National Environmental Research Council, and the Oxford Doctoral Training Partnership (DTP) under the administration of the very helpful Victoria Forth.

First and foremost, I have to acknowledge and thank my supervisors and mentors, from whom I have learnt a huge amount in terms of science and leadership. Lars Hansen has been part of my academic journey since my undergraduate years, as a tutor at University College and later as a DPhil advisor. His scientific guidance, mentorship, and friendship have been so incredibly generous and insightful that a mere Acknowledgements section could not do them justice. I am incredibly fortunate to have been one of his doctoral students and join his academic family. Similarly, Conall Mac Niocaill has been part of my academic trajectory since my undergraduate studies. Conall has kindly adopted me halfway through this degree and has provided support and advice in navigating the institutional aspects of the degree. His office sofa has served as a "therapy" sofa numerous times, for which I am very grateful. I met Angus Wilkinson in the last year of my undergraduate studies, when I undertook interdisciplinary research as part of my degree. Later, he has welcomed me as the "geologist" in his research group. I am incredibly grateful to Angus for all his support of my scientific ambitions, incredible mentorship, and friendship. Throughout the years it has been incredibly insightful and inspirational to witness my advisors lead their scientific groups, fulfill various administrative and

leadership roles in academia, and interact with the broader international scientific community. I consider myself beyond fortunate for having such role models and I will always cherish the lessons I have learnt from them.

Alongside their academic guidance, my supervisors have facilitated a number of successful scientific collaborations, my active participation to international conferences, and stimulating group meetings. I want to thank Katharina Marquardt for the samples studied in two chapters in this thesis, for her patient crystallography explanations, introducing me to TEM, and for facilitating data collection at Imperial College London. David Wallis has facilitated a research trip to the University of Utrecht, where we collected data alongside Markus Ohl. In the Earth Sciences Department at Oxford I am also grateful for the support and collaboration of James King and Jamie Long from the workshop, who have made the last research chapter of this thesis possible.

I am grateful for all the feedback and stimulating conversations that the members of the Rock and Mineral Physics Group have provided, as well as their insightful life advice. I am particularly in debt to Kathryn Kumamoto, for samples, support, and interesting conversations on spherical nanoindetation, Christopher Thomas for his insight on nanoindentation and friendly conversations, and Amanda Dillman, Annia Fayon, and Mark Zimmerman for their hospitality when I visited University of Minnesota. I am fortunate to have an academic brother in this research group, Thomas Breithaupt, who always listened patiently and compassionately when research was frustrating.

I am also incredibly grateful for all the scientific mentorship and insight I have gained within the Oxford Micromechanics Group. I want to thank David Armstrong for his enthusiastic support of my research. Anna Kareer brought order into my journey with spherical nanoindentation alongside laughs and friendship. Phani Karamched was always there with advice and laboratory help when I needed something done quickly or a lab crisis was unfolding. Ed Darnborough has helped me achieve important goals within my research when lab access was limited. The OMG has also introduced me to wonderful colleagues who provided laughs along the journey, such as Robin De Meyere, Chris Magazzeni, and Kay Song.

My life as a graduate student has been enriched by my peers who were also pursuing their doctoral degrees. The Oxford DTP has brought new and wonderful friends in my life, such as Thomas Hornigold, the best lunch companion one could have in the Biochem Cafe, and new colleagues in the Earth Sciences Department, such as Hamish Couper, Will Hartz, Sean Selzer, and Richard Thomas, who alongside older friends such as Grace Manley and Chris Theaker made my time in department considerably more fun. It would be amiss to not thank the Office 30.18 for the years of fun dinners, and work-appropriate banter. Ian Cawood, Amber Madden-Nadeau, Ritwika Sengupta, Luke Jenkins, and Edward Baker have been the best office mates one could ask for. My life in the Earth Sciences department has been enriched by inspirational people such as Gwen Antell, and by my wonderful mentor, friend, and kindred spirit, Adina Pusok.

Outside the scientific life on South Parks Road, my time as a DPhil student has been enriched by friends at the sports clubs at Oxford. I have come across incredibly inspirational women at the Oxford University Kickboxing Club and Linacre Ladies that Lift.

Throughout my time at Oxford, I have always called University College my home. I am grateful for all the friends and memories I made as a MCR member. Being a Junior Dean has been a true highlight of my graduate studies and I want to thank all the JD team, Alizeh Tariq Paracha, Hannah Farley, Karima Chiuri, Melvin Obadha, and Rachel Wheatley, for their steady friendship and warm support. All the staff and senior management at University College have been enormously helpful throughout my studies and residence in college. I am particularly thankful to "three As": Andrew Bell, Angela Unsworth, and Andrew Gregory for the support, patience, and kindness they have extended me throughout the years.

I am very grateful, and for ever in debt to the friends from all walks of life who have helped me in the most difficult times such as James Parker, Adam Foster, Georgiana Dima, Nicholas Temple-McCune, and many, many more. I am thankful to my friends from high school: Anca Amariei, Alex Pavaloi, Miruna Gaina, Corina Ismail, and undergraduate years: Ion Ambrinoc, Serban Ilca, Stefan Cucea, Octavian Movilianu, Jacob Forshaw, Matthew Brady, Catherine Scanlon, Annya Emmos, Alina Harvey, who have put up with their fair share of phone calls and visits when research was moving

slowly or life got difficult. My sibling, Teo, and parents, who eventually stopped asking when I will finish this DPhil, have been breaths of fresh air throughout the years.

Last, but not least, I am grateful for the unconditional love and support of my late partner, almost-Dr Alexander Temple-McCune, which will last me a lifetime.

I will strive to make you all proud.

Abstract

Grain boundaries in polycrystalline materials underpin deformation processes in both low- and high- temperature regimes. The study of grain boundary types relies on the investigation of small volumes of material containing one interface. This thesis presents small-scale mechanical tests on forsterite grain boundaries. Forsterite is the Mg-rich end member of the solid solution of the mineral olivine.

Olivine is a key geological material influencing large-scale, long-term planetary deformation processes on rocky planets. Studies on the deformation of olivine at low temperatures and high stresses have emphasized the importance of a grain-size effect impacting the yield stress. Laboratory observations have demonstrated that aggregates with smaller grains are stronger than aggregates with coarser grains. However, the interactions between intracrystalline defects and grain boundaries leading to this effect remain unresolved in olivine. Moreover, most of our understanding of the role of grain boundaries in the deformation of olivine is inferred from comparison of experiments on single crystals to experiments on polycrystalline samples. In this study, we use high-precision mechanical testing of synthetic forsterite bicrystals with well characterised interfaces and directly observe and quantify the mechanical properties of olivine grain boundaries. We perform room-temperature spherical and Berkovich nanoindentation tests on low- and high- angle grain boundaries. We observe that in the high-angle grain boundary sample, the interface acts as a site of microplasticity and as a barrier to incoming dislocations. The low-angle grain boundary does not interact with other crystalline defects in a measurable manner. Additionally, we conduct *in-situ* micropillar compression tests at high-temperature (700°C) on low- and high-angle grain boundaries. In these *in-situ* experiments, the boundary is contained within the micropillar and oriented at 45° to the loading direction to promote shear along the boundary. We observe differences in deformation

style between the pillars containing the grain boundary and the pillars in the crystal interior. The pillars containing the grain boundary consistently support elastic loading to higher stresses than the pillars without a grain boundary. Moreover, the pillars without the grain boundary sustain larger plastic strain. Post-deformation advanced microstructural characterization confirms that under these experimental conditions, sliding did not occur along the grain boundary. These observations support the hypothesis that at our experimental conditions grain boundaries are relatively stronger compared to the crystal interior, and some grain boundaries can act as potent sources of dislocations in olivine.

Studying grain boundaries and their interaction with crystalline defect relies on small-scale, high-precision mechanical testing and microstructural characterization. One such technique is instrumented nanoindentation with a continuous stiffness measurement, which has gained increased popularity in material sciences. Studies implementing spherical nanoindentation rely on the implementation of different methodologies for instrument calibration and for circumventing tip shape imperfections. In this study, we test, integrate, and re-adapt published strategies for tip and machine stiffness calibration for spherical tips. We propose a routine for independently calibrating the effective tip radius and the machine stiffness using three reference materials (fused silica, sapphire, glassy carbon) and validate our proposed workflow against key benchmarks. We apply the resulting calibrations to data collected in materials with varying ductility (olivine, titanium, tungsten) to extract indentation stress-strain curves. We synthesize these analysis routines in a single workflow for use in future studies aiming to extract and process data from spherical nanoindentation.

Another strategy for investigating grain boundaries and microstructure evolution represents *in-situ* mechanical testing. In order to test materials under simple shear studies implement different strategies to transform a far-field compressive or tensile applied stress into shear stress in both mesocale and microscale specimens. In this study, we describe an apparatus developed to investigate *in-situ* ductile materials by directly applying a simple shear to a thin sheet of material. We propose a novel sample geometry compatible with established techniques for strain characterization and specimens with a wide range of starting microstructures. We demonstrate

the capabilities of our apparatus by deforming solder alloys and aluminium, and use optical digital image correlation and electron microscopy for the *in-situ* characterization of the deforming sample.

Contents

1 Introduction **1**

1.1 Brief overview of defects in olivine 3

1.2 Interactions between grain boundaries and dislocations in plastic deformation 8

1.3 The importance of grain boundaries in the deformation of olivine in geological processes 12

1.4 Experimental strategies for the investigation of mechanical properties of grain boundaries 13

1.5 Aims and Outline 16

2 Calibration and data analysis routines for nanoindentation with spherical tips **19**

2.1 Introduction 22

2.2 Experimental aspects 23

2.3 Results and Analysis 24

2.3.1 Theoretical background 24

2.3.2 Calibrations on materials with known moduli 26

2.3.2.1 Determination of effective radius 26

2.3.2.2 Determination of machine stiffness 28

2.3.2.3 Benchmarks 32

2.3.3 Characterization of materials with unknown Young's moduli . 35

2.3.3.1 Zero-point correction 35

2.3.3.2 Calculation of Young's moduli 37

2.3.3.3 Calculation of stress-strain curves and the yield point 38

2.4 Conclusion 42

3 The role of grain boundaries in low-temperature plasticity of olivine revealed by nanoindentation 43
3.1 Introduction . . . 46
3.2 Materials and Methods . . . 47
3.2.1 Samples . . . 47
3.2.2 Micromechanical testing . . . 48
3.2.3 Data Analysis . . . 50
3.2.3.1 Spherical nanoindentation . . . 50
3.2.3.2 Berkovich nanoindentation . . . 51
3.2.4 Microstructural characterization . . . 52
3.2.4.1 HR-EBSD . . . 52
3.2.4.2 Transmission electron microscopy . . . 53
3.2.5 Analysis of slip transfer . . . 53
3.3 Results . . . 54
3.3.1 Mechanical testing . . . 54
3.3.2 Microstructural characterization . . . 58
3.4 Discussion . . . 68
3.4.1 The role of grain boundaries as a source of dislocations . . . 69
3.4.2 Slip transmission across GBs . . . 70
3.4.3 Impact of grain boundaries on large-scale plasticity of olivine aggregates . . . 72
3.5 Conclusions . . . 74

4 Direct testing of forsterite bicrystals via *in-situ* micropillar experiments at 700°C 75
4.1 Introduction . . . 78
4.2 Experimental methods . . . 80
4.2.1 Sample preparation . . . 80
4.2.2 Mechanical testing . . . 82
4.2.3 Calculations of stress and strain . . . 83
4.2.4 Microstructural investigations . . . 85
4.3 Results . . . 85
4.3.1 Low-angle grain boundary bicrystal . . . 85
4.3.2 High-angle grain boundary sample . . . 92
4.4 Discussion . . . 94
4.4.1 The impact of grain boundaries on micropillar deformation . . . 95

4.4.2 Slip band analysis 99
4.5 Implications 102

5 A novel torsion stage for the *in-situ* investigation of ductile materials under simple shear 103
5.1 Introduction 106
5.2 Brief review of material deformation in simple shear 106
5.3 Annular torsion apparatus 110
5.3.1 Rotary stage and SEM compatibilities 110
5.3.2 Stage controls: input 110
5.3.3 Sample geometry 110
5.3.4 Optical measurements 111
5.3.5 *In-situ* measurements 112
5.4 Demonstration of simple shear deformation of ductile materials . . . 112
5.4.1 Sample materials 113
5.4.2 PbSn 113
5.4.3 Sn 117
5.4.4 Al 117
5.5 Discussion 123
5.5.1 Implications and limitations 123
5.5.2 Comparison with existing strategies for simple shear testing . 124
5.5.3 Future applications and developments 125
5.6 Conclusion 126

6 Conclusion 129
6.1 Summary of Results 130
6.2 Future Directions 131

A Supplementary Materials for Chapter 2 133

B Supplementary Materials for Chapter 3 137

C Supplementary Materials for Chapter 4 145

D Supplementary Materials for Chapter 5 153

Bibliography 155

List of Figures

1.1 Schematic of defects in crystalline materials adapted from Demouchy (2021). 5

1.2 a) Diagram of a sharp indent penetrating a polycrystalline sample. Some examples of dislocations generated under the indent are drawn. The sources of these dislocations could be within the crystal lattice or the grain boundaries under the indent. Pile-ups of dislocations at a grain boundary could result in slip transmission via dislocations generated on the opposite side of the interface. b) Example of slip planes intersecting at a grain boundary. 11

2.1 a) Load-displacement data collected with a spherical tip with a nominal radius of 10 μm in different materials with known moduli. b) Curve subtraction of displacement at the same load. The cut-off load for each set of experiments is marked by the dashed horizontal lines in a). The slope of these curves is proportional to the effective tip radius according to Equation 2.8. 26

2.2 Summary of results for effective radius determined as the slope of a line fit through data calculated as the subtraction of elastic load-displacement curves at the same load in different reference materials following the method of Li et al. (2013) (Equation 2.8). The dashed line represents the 1:1 proportionality. 29

2.3 a) Linear fit for a spherical tip with a nominal radius of 10 μm following Li et al. (2013). Note the curvature in the data obtained by subtracting sapphire displacement from fused silica displacement according to Equation 2.8. b) Effective radius calculated using the first numerical derivative of data in a) against load and an exponential fit. All values for R_{eff} in Figure 2.2 and the values for R_{eff} at a constant load can be found in Supplementary Materials, Table A.1. 29

2.4 a) Load-displacement data for a spherical tip with a nominal radius of 20 μm in different materials with known moduli overlapped with predictions using a constant effective radius (blue) and radius as a function of depth (red) in Equation 2.4. b) Calculations of machine stiffness using sapphire data in Equation 2.3. c) Calculations of machine stiffness using fused silica data in Equation 2.3. 31
2.5 Young's modulus calculated using Equation 2.10 against expected values using) an effective radius as a constant for data collected with a diamond tip with $R_n = 5$ μm and reported values for the harmonic contact stiffness and b) an effective radius as a function of load and stiffness correction of the reported harmonic contact stiffness according to Equation 2.9. Note the differences in vertical scales. The reference values of the effective Young's modulus are plotted with dashed lines, and are calculated using the values in Table 2.1 and Equation 2.5. . . 32
2.6 a) The effective tip shape calculated with data as reported and b) the effective tip shape calculated with corrected displacement and harmonic stiffness data for spherical tips with varying radii. The green curve represents the tip shape for a perfect sphere, with the contact radius calculated using Equation 2.15 with values for R from Figure 2.2. . . 34
2.7 Measurements of Young's modulus for a) tungsten (average $E_{\text{eff}} = 306.7 \pm 14.2$ GPa), b) titanium (average $E_{\text{eff}} = 99.5 \pm 4.7$ GPa), and c) olivine (average $E_{\text{eff}} = 183.8 \pm 8.8$ GPa) using data collected with a tip with a nominal radius of 50 μm. The orange arrow indicates the approximate position of the elastic-plastic transition, which is absent in the fully elastic experiments on olivine. 37
2.8 Summary of stress-strain curves in a) tungsten, b) titanium, and c) olivine collected with spherical tips of varying radii. The dashed lines have the slope equal to the average E_{eff} across all indents. The displayed values of E_{eff} correspond to $E_s = 400 \pm 9$ GPa in tungsten, $E_s = 108 \pm 8$ GPa in titanium, and $E_s = 205 \pm 9$ GPa in olivine. The corresponding load-displacement curves are presented in Supplementary Materials (Figure A.3). 39

2.9 a) Example of S^3/P parameter calculations using Equations 2.24 and 2.25 proposed by Hackett et al. (2019) using both reported (light colours) and corrected (dark colours) values. The corresponding stress-strain curve is presented in the insert. A filled-blue circle marks the yield point on the corrected data in a) and the insert. The data were collected with a tip with $R_n = 20$ μm. A smoothing window with an interval of 5 is applied to S_{slope}. We present calculations for a) olivine and b) titanium. c) Yield stress corresponding to the divergence point in a) for olivine across tips with varying radii. The power law fit with an exponent of -0.09 has been determined by Kumamoto et al. (2017) using spherical nanoidentation on similar samples, but deploying a different strategy for defining the yield stress. 40

3.1 a) Schematic depicting the grain-boundary geometry and lower-hemisphere projection of the LAGB bicrystal. Examples are depicted of a slip system with an incoming slip direction b_{in} towards the grain boundary (GB) and an outgoing slip system with the direction vector b_{out}. b) Schematic depicting the grain-boundary geometry and lower-hemisphere projection of the HAGB bicrystal. The indented surface is perpendicular to Z_0. Note that the indentation direction is consistent between crystals A and B in both samples. 49

3.2 Selected results from spherical indentation using the 4 and 6 μm tips in Table 3.1 in the a) LAGB sample and b) HAGB sample. The diagram on the right depicts the three categories of indents: indents with a residual mark centered on the GB, indents where the GB intersects the residual mark but is offset from its centre, and indents in a single crystal near the grain boundary. The stars mark examples of points identified as the initiation of plasticity and therefore the yield stress. Further details of the location of indents can be found in Figures B.1, B.3. 55

3.3 Summary of results from spherical indentation in the (a) LAGB sample and (b) HAGB sample. The open symbols correspond to the stress at the initiation of plasticity. In indents without a pop-in (red), the initiation of plasticity is equivalent to the yield stress. The variation in the load at pop-in with distance from the grain boundary, and the corresponding shear stresses are presented in Figures B.6 and B.9 in Supplementary Materials. 56
3.4 Summary of results using a Berkovich indenter tip (Table 3.1). The hardness data are coloured according to each crystal in Figure 3.1. The indents that left an imprint with the centre overlapping the trace of the grain boundary are marked in red (for details, see Figures B.2, B.4). 57
3.5 Summary of Berkovich nanoindentation results. The hardness at different indentations depths, h is displayed against distance from the grain boundary. 58
3.6 HR-EBSD results in the LAGB sample. a) Total GND densities around Berkovich indents at various distances from the grain boundary. b) Total GND densities around a spherical indent near the grain boundary. All maps have the same scalebar of 5 μm. The lower hemisphere plot indicates the crystal orientations for each crystal. The black outline marks the indent imprint in the material. 59
3.7 HR-EBSD maps around indents in the HAGB sample. a) Total GND densities around spherical indents at various distances from the grain boundary. b) Total GND densities around Berkovich indents near the grain boundary. All maps have the same scalebar of 5 μm. The lower hemisphere plot indicates the crystal orientations for each crystal. The black outline marks the indent imprint in the material. 60
3.8 Geometrical transfer factor between the possible slip systems active in the bicrystals in this study. The first row represent the m' factor in a) the LAGB bicrystal and b) the HAGB bicrystal, and the second row displays the M factor in the a) LAGB bicrystal and the HAGB bicrystal. The slip systems considered are represented by the slip direction, $\mathbf{b}$, and the normal to the slip plane, $\mathbf{n}$. The normal to the grain boundary is denoted by $\mathbf{N_{GB}}$. In the b) and d) panels the second and last columns and rows correspond to the slip systems with the greatest Schmid factor in Table 3.2. 63

3.9 Bright-field STEM imaging of the spherical indent in Figure 3.7a placed on top of the high-angle grain boundary. The lower hemisphere projection corresponds to the viewing plane. The boxes mark the position of the images at higher magnification. The corresponding stress-strain curve is presented in Figure B.8a. The annotations present interpretations of possible line directions, **l**, and the plane normal, **n**, of the slip plane. 64
3.10 Bright-field STEM imaging of a spherical indent placed near the grain boundary in crystal A in the HAGB sample. The annotations are similar to Figure 3.9. The corresponding stress-strain curve is presented in Figure B.8b. 65
3.11 Bright-field STEM image of a spherical indent in the single crystal B within the HAGB sample. The corresponding stress-strain curve is presented in panel c, and highlights that there is no further flow after the pop-in event. Note that the viewing direction is flipped compared to Figures 3.9 and 3.10. 66
3.12 Bright-field STEM imaging of a Berkovich indent placed near the high-angle grain boundary in crystal B. The corresponding load-displacement curve is presented in Figure B.5. 67

4.1 Sample assembly for the low-angle grain boundary in (a) and the high-angle grain boundary in (b). Panel a) is a colourised image of the low-magnification *in-situ* view of the micropillars. The coloured axes represent the sample surface coordinate convention. Panel b) is a colourised image of the high-angle grain boundary bicrystal assembly imaged with the stage tilt (ST) and tilt correction (TC) with the least distortion along the Z_0 axis (i.e., parallel to the pillar vertical axis). The orientation of the samples is described using lower hemisphere stereographic plots of the crystallographic axes. Both samples are tested at the same stage rotation (SR) and stage tilt (ST). Full details of pillar geometry are in table 4.1. Images of the pillars before deformation can be found in Supplementary Materials (Figure C.1). 81

4.2 Load-displacement data for the micropillars described in Table 4.1. The left column corresponds to pillars in the single crystals, and the right column corresponds to pillars containing an interface. The outlined groups indicate tests conducted at similar maximum load and length of hold, as described in Table 4.2. 87
4.3 Examples of load-displacement curves alongside *in-situ* images. The white numbers on the images correspond to the marked red points in the load-displacement curves. The arrows mark slip bands. 88
4.4 Compilation of stress-strain curves for the Fo014 sample with a low-angle grain boundary. Note the different scales of the vertical axes. The magenta stars mark the yield stress determined from *in-situ* observations. 89
4.5 Compilation of stress-strain curves for the Fo011 sample with a high-angle grain boundary. Note the different scales of the vertical axes. The magenta star markers mark the yield stress determined from *in-situ* observations. 90
4.6 Compilation of images of deformed a) pillar 8 in the LAGB sample and b) pillars 5 and 6 containing the HAGB. The coordinate annotation references the coordinate system in Figure 4.1. All scalebars are 2 μm. Note that the images (and thus the angle) in panel a) have no tilt correction (TC) applied for the stage tilt (ST) of 25°. SEM characterization of all the pillars can be found in Supplementary Materials, Figures C.4 and C.5. 91
4.7 STEM images of a FIB lamella cut parallel to the indentation direction in pillar 6 in the HAGB sample. The lower hemisphere diagram is rotated such that the center of the diagram coincides with the axis perpendicular to the plane of view. a) Dark-field image of pillar 6 after deformation. b) Bright-field image of the upper part of deformed pillar 6. 93
4.8 a) Yield stress from stress-strain curves in Figures 4.4a and 4.5a against Vickers indentation data from Darot et al. (1985) and Evans and Goetze (1979) on forsterite and olivine, respectively. All the included Vickers indents are at a maximum load of 0.5 N. b) Lower hemisphere plots describing the different orientations of the crystallographic axes with respect to the indentation direction. 99

5.1 Summary of experimental strategies to study material deformation under shear. Figures a-e depict *in-situ* techniques. a) Micro double shear testing diagram adapted after Heyer et al. (2014). b) 'S'-shaped micropillar test adapted after Gigax et al. (2019). c) Tensile experiment with a notch adapted after Masuda et al. (2016). d) Uniaxial shear stage schematic adapted after Bae and Ghosh (2003). e) Our proposed sample geometry. f) Compact forced-simple-shear diagram adapted from Gray III et al. (2016), and further modified by Nizolek et al. (2021). g) Shear punch test diagram adapted after Lancaster et al. (2022). h) Equal-channel angular pressing test diagram adapted after Valiev and Langdon (2006). 107
5.2 Overview of the apparatus presented in this study, as assemblied on a FEI QUANTA 650 scanning electron microscope. 109
5.3 Shear stress across the sample calculated for a sample thickness of 3 mm and a channel thickness 2 mm using Equation 5.1. The upper diagram represents a schematic cross section though the sample. The diagram is not drawn to scale. 111
5.4 Full strain DIC results for the Euler-Almanasi strain in the PbSn sample for the a) ε_{xx}, the b) ε_{xy} and the c) ε_{yy} component, presented without subtracting the rigid body rotation of the sample. Due to the DIC set-up (Xiong et al., 2021), the images appear mirrored, and consequently the driver at the bottom appears to be rotating anticlockwise. 114
5.5 The distribution of maximum, in-plane shear strains in the TPbSn sample. The calculation uses the values of strain presented in Figure 5.4. 115
5.6 SEM characterization of the TPbSn4 sample after deformation and paint removal. The surface is presented after deformation, without any further polishing or preparation. The images were captured with the stage tilted at 70° and have an applied corresponding tilt correction via the SmartSEM interface. 116
5.7 *In-situ* imaging of deforming Sn using ARGUS^{TM}. The lower left boxes indicate the imposed rotation angle and the time. 118

5.8 Post-deformation SEM and EBSD characterization of the TSn1 sample. a) Sample overview composed of multiple SEM images. The sample thickness corresponding to the channel area is < 0.5 mm. b) EBSD map of $\beta-$Sn with crystal orientations depicted in the inverse pole figure (IPF) with respect to the direction perpendicular on the viewing plane (Z-axis). 119
5.9 Full strain DIC results for the Euler-Almanasi strain in the high-purity Al sample, for the a) ε_{xx} component, the b) ε_{xy} component, and the ε_{yy} component, presented without subtracting the rigid body rotation of the sample. Due to the DIC set-up (Xiong et al., 2021), the images appear mirrored, and consequently the driving shaft at the bottom appears to be moving anticlockwise. 120
5.10 The distribution of maximum, in-plane shear strains in the high-purity Al sample. The calculation uses the values of strain presented in Figure 5.9. Note the different values of the colour map compared to Figure 5.9. 121
5.11 a, b) SEM characterization of the TAl4 sample after deformation and paint removal. The surface is presented after deformation, without any further polishing or preparation. c,d) ARGUS^{TM}images of the fiducial mark and the area of localised strain. The images were captured with the stage tilted at 70° and have an tilt correction applied via the SmartSEM interface. For the acquisition of these images the EBSD camera was positioned at 35 mm from the sample, and had a tilt of 4°. 122
5.12 a) *In-situ* images captured with ARGUS^{TM}of the TAl2 sample. b) Post-deformation SEM and EBSD characterization of the sample displayed alongside an inverse pole figure (IPF) depicting crystallographic orientations with respect to the direction perpendicular on the viewing plane (Z-axis). 123

A.1 Effective tip shape calculated with corrected data in olivine, tungsten, and titanium, with tips with varying radii. Note the differences in the horizontal axis. For largest tip radii, the indent experiments in olivine are purely elastic, whereas the residual imprint increases with decreasing radius, as displayed by the segment corresponding to the unloading. 134
A.2 Schematic flow-chart diagram summarising Section 2.3.2 in blue and Section 2.3.3 in green. 135

A.3 Load-displacement curves in olivine, titanium, and tungsten collected during displacement-controlled experiments with spherical tips with nominal radii ranging $2 - 50$ μm 136

B.1 Backscatter images depicting the arrays placed in the LAGB sample with a spherical indenter as detailed in Table 3.1. The position of the further microstructural investigations with respect to the other indents and the GB is marked by the magenta square. The numbers hear each indent mark corresponds to the order in which the indents have been places. 138

B.2 Backscatter images depicting the arrays placed in the LAGB sample with a sharp indenter. The position of the further microstructural investigations with respect to the other indents and the GB is marked by the magenta square. The numbers hear each indent mark corresponds to the order in which the indents have been places. 139

B.3 Backscatter images depicting the arrays placed in the HAGB sample with a spherical indenter as detailed in Table 3.1. The position of the further microstructural investigations with respect to the other indents and the GB is marked by the magenta square. The numbers hear each indent mark corresponds to the order in which the indents have been places. 140

B.4 Backscatter images depicting the arrays placed in the HAGB sample with a sharp indenter. The position of the further microstructural investigations with respect to the other indents and the GB is marked by the magenta square. The numbers hear each indent mark corresponds to the order in which the indents have been places. 141

B.5 Examples of load-displacement curves collected with a Berkovich tip, arranges according to distance d from the grain boundary. The indents are part of array11f in Figure B.4. Microstructural TEM investigations corresponding to indent 11 are presented in Figure 3.12 and HR-EBSD investigations are presented in Figure 3.7. 142

B.6 Load at pop-in in spherical indents placed in the a) LAGB sample and b) in the HAGB sample displayed with respect to distance from the grain boundary. The indents without a pop-in are not displayed. . . . 142

B.7 Results of Young's modulus calculations using Berkovich (open triangles) and spherical (open circles) nanoindentation in the a) low-angle GB sample and b) high-angle GB sample. The red line corresponds to the average value across all the data points. The Young's modulus is calculated fitting Equation 3.6 over the elastic loading segment for spherical nanoindentation data and using Equation 3.8 to average the value of Young's modulus over indentation depths greater than 200 nm for the Berkovich data. The insert in a) represents an inverse pole figure displaying the average values in both samples against a background coloured according to the theoretical Young's modulus from Abramson et al. (1997) for San Carlos olivine. 143
B.8 Stress-strain curves corresponding to the indents displayed in a) Figure 3.9 and Figure b) 3.10. 143
B.9 Shear stress calculated using the load at pop-in displayed in Figure B.6 and Equation 3.7. For a general isotropic case, we can approximate the theoretical shear strength of a crystal with a Poisson's ratio of 0.24 as $E/15.57$ (e.g., Fang et al., 2021). Using the mean Young's modulus values in Figure B.7 we can calculate the theoretical shear strength for the a) LAGB sample as 15.86 GPa and for the b) HAGB sample as 12.71 GPa. Note that in the single crystal, the shear stress value for dislocation nucleation is closer to the theoretical limit. 144
B.10 Fraction of total GNDs corresponding to each slip system accounted into the HR-EBSD calculation for olivine (Wallis et al., 2016). 144

C.1 SEM images of the micropillars in this study before deformation. The first row represent the side view imaged at stage stilt (ST) of 54°, with a tilt correction (TC) of 36°. The second row in each subfigure represents the top view of the micropillars. The axis represent the coordinate system in the reference plane of the sample surface and remain consistent within each row. The blue arrows mark the trace of the grain boundary. a) Micropillars containing a low-angle grain boundary. b) Micropillars containing the high-angle grain boundary. All scalebars are 2 μm. 146
C.2 Thermal drift of displacements during tests in the a) low-angle grain boundary sample and b) high-angle grain boundary sample. These drifts have been automatically accounted for by the acquisition software. 147

C.3 Example of experiments used for correcting the impact of the compliance of the machine and the sample assembly. a) The prediction is calculated using Equation 4.2 and compared with experiments in the bulk crystal at 700°C (grey) to calculate the error. b) The reported load divided by the computed error is proportional to the compliance of the system. . 148
C.4 Post-deformation SEM characterization of micropillars in the SB sample Fo014. The colour-coded axis track the rotation of the surface rotation with respect to Figure 4.1 a). Stage rotation (SR) and stage tilt (ST) denote the stage position during image acquisition. The tilt correction is 0 in all images. The scalebars are 2 μm. The fracture in P7 is consistent with cleavage on the (010) plane. 149
C.5 Post-deformation SEM characterization of micropillars in the HAGB sample Fo011. The colour-coded axis track the rotation of the surface rotation with respect to Figure 4.1 b). The top row displays images during the deformation experiments for P1, which has been decoupled from the base and lost during the indenter lift. Vertical fracture in P4, P3, and possibly P1 correspond to fracture along the (010) plane, which is the cleavage plane of forsterite (Durham et al., 1979; Darot et al., 1985). For the remaining pillars, the first column is the side view, and the second column is the top view. Stage tilt (ST) and tilt correction (TC) denote image acquisition settings. The scalebars are 2 μm. . . . 150
C.6 Strain versus time in the creep tests detailed in Table 4.2. 151

D.1 Imposed strain path for the *in-situ* experiment on the sample TSn1. . 154

List of Tables

1.1 Summary of the main slip systems in olivine according to the temperature of deformation in experimental studies. These studies use scanning transmission electron microscopy to infer the activity of slip systems. 6

1.2 Summary of documented types of grain boundaries with higher frequency when compared to a normal distribution for orthorhombic crystal lattices, in undeformed synthetic samples and natural peridotites, as well as laboratory deformed olivine samples. 7

2.1 Summary of experiments. Note that the experiments in the reference materials with known elastic moduli are experiments in the elastic deformation regime only. 24

3.1 Summary of experiments on bicrystal samples with a low-angle grain boundary (LAGB) or high-angle grain boundary (HAGB). Experiments were conducted using either sharp or spherical tips, the latter of which had variable nominal radii, R_{n}. The effective radius at the end of elastic loading is indicated for each tip as R_{eff}. The lower case letter at the end of the array number in the HAGB bicrystal corresponds to different samples. The number of tests is expressed as the number of columns times the number of rows of indents across the grain boundary. 49

3.2 Schmid factor, S, describing the relationships between the mean applied pressure and the resolved shear stresses for different slip systems considered in this study. For the HAGB sample, the indentation direction is parallel to $[0\bar{1}1]$, and for the LAGB sample, the indentation direction is approximately parallel to [100]. Because these bicrystals are symmetric tilt boundaries, the Schmid factor is the same for all slip systems in crystal A and B for both samples. 61

4.1 Details of micropillars tested in this study, manufactured on a low-angle grain boundary (LAGB) bicrystal and a high-angle grain boundary (HAGB) bicrystal. 80
4.2 Details of the mechanical tests on micropillars described in Table 4.1. 86

5.1 Sample details 113

A.1 Summary of results presented in Figure 2.2. For each nominal radius R_n the Table presents R_{eff} calculated similar to Li et al. (2013) using data collected in fused silica (FS), glassy carbon (GC), and sapphire (SPH) and R_{eff} calculated as a function of load as outlined in Section 2.3.2.1. 133

Chapter 1

Introduction

"It is the defects which bring the crystal to life. Without the defects the crystal would be dead just like the universe if it were empty."

Kröner et al. (1981)

Modern understanding of grain boundaries has emerged from the seminal work of Read and Shockley (1950), who provided the first theoretical descriptions of grain boundaries. Nine years later, in a famous talk at the American Physical Society in December 1959, titled "There is Plenty of Room at the Bottom", Richard P. Feynman outlined his scientific vision of atom manipulation as the end goal of the ongoing miniaturisation of the study of materials (Feynman, 1992). His now visionary talk was centered around what scientists *could* achieve within the the bounds of physical laws, regardless of the limits of existing techniques at the time.

Shortly after the 1959 talk, there was increasing progress within an emerging, unrelated field investigating the opposite side of the space spectrum of physical systems: the relative motion of continents. In 1961 R.S Dietz proposed a "largely intuitive" model for sea-floor spreading (Dietz, 1961)—alongside a similar concept by H.H Hess popularised at the same time (Hess et al., 1962)—on the basis of observations of sea-floor bathymetry, volcanism, and earthquakes at the edges of oceanic plates (Chapter 1, Kearey et al., 2009). Further observations of magnetic lineations alongside mid-ocean ridges discussed by F.J. Vine and D. H. Matthews in 1963 have consolidated the evidence for the theory of sea floor spreading (Vine and Matthews, 1963). These observations mark the start of decades of study into modern plate tectonics, and its underlying mechanisms.

In the following decades, the theory of plate tectonics has prompted numerous lines of investigation. One area of ongoing research has been the laboratory deformation of rocks and minerals under Earth-like conditions. These studies were aiming to quantify the flow stress of various minerals and extrapolate it to geological conditions in order to estimate the mechanical properties of the deforming lithosphere. Early examples of rock-deformation apparatuses, widely used to this date, include those of Griggs (1967) and Paterson (1970) (in use starting 1963), which were building upon previous models presented by Griggs (1936). Starting in the 1980s, geoscientists have increasingly adopted techniques used in materials science for probing small volumes of material at room pressure and varying temperatures using sharp diamond tips. Early examples in the study of olivine, a mineral relevant for mechanical properties of Earth's upper mantle, include the experiments of Evans and Goetze (1979) and Darot et al. (1985).

Building upon previous work in materials science and rock and mineral deformation, I am investigating in this thesis the role of grain boundaries in the permanent deformation of materials. This interdisciplinary study investigates grain boundaries in one of the most important mineral in rocky planets, olivine, using state of the art

techniques historically developed for the investigation of crystalline materials in metallurgy. My research into the deformation of materials has also prompted development and improvement of methodologies for investigating the mechanical properties of grain boundaries in deforming materials. Last, but not least, this thesis implements a shift of perspective in the conceptualization of deforming materials, from a polycrystalline material to a network of grain boundaries, *as there is plenty of room in between.*

1.1 Brief overview of defects in olivine

Olivine is the dominant mineral in Earth's upper mantle and occurs as a solid solution between forsterite (Mg_2SiO_4) and fayalite (Fe_2SiO_4) (Chapter 17, Karato, 2008). The crystal symmetry of olivine belongs to the orthorombic system, with three orthogonal axes of various lengths (e.g., in forsterite a = 4.754 Å, b = 10.1971 Å, c = 5.9808 Å, Demouchy (2021)). Studies of the dynamics and properties of the upper mantle (e.g., upper-mantle viscosity) extrapolate laboratory derived flow-laws of olivine (commonly San Carlos olivine samples, $(Mg_{1.7}Fe_{0.2})SiO_4$) to geological conditions in order to predict upper-mantle dynamics, or compare the simulated results of plate dynamics to geophysical observations (e.g., Hunter and Watts, 2016). Thus, the pursuit of understanding upper mantle deformation over geological timescales has brought the mechanisms of deformation of olivine to the centre of investigative efforts in the past decades.

Permanent deformation of materials relies on the movement and interaction of crystal defects. Point defects (e.g., vacancies, interstitial atoms) disturb the crystal lattice at one atomic site, and are classified as 0-dimensional defects. Figure 1.1a exemplifies a vacancy in a crystal lattice. The entropy of a crystal decreases non-linearly with the density of vacancies or self-interstitials, and thus crystals with a finite concentration of vacancies are more energetically favourable (for a detailed overview of point defects in olivine, see Hansen and Kohlstedt, 2015; Demouchy, 2021). The movement of vacancies enables solid-state diffusion and underpins high-temperature deformation and recovery processes in olivine (Hansen and Kohlstedt, 2015).

Dislocations are one-dimensional lattice defects that result in a relative shift between regions in the same crystal lattice, as exemplified in Figure 1.1a. Dislocations are non-equilibrium defects and thus, dislocation-free crystals are generally more energetically favourable (Hansen et al., 2011). Dislocations are described via two vectors corresponding to the direction of the lattice displacement caused by the movement of a dislocation through the crystal lattice (**b**, Burgers vector) and the

direction of the dislocation along its length (**l**, line vector) (Figure 1.1b). Dislocations which displace the crystal parallel to the line direction (**b** $\parallel$ **l**) are termed screw dislocations, and dislocations which displace the crystal lattice perpendicular to their line direction (**b** $\perp$ **l**) are termed edge dislocations (Figure 1.1b). Dislocations move through the crystal lattice by glide and climb. For glide of dislocations to occur, the applied shear force must overcome the local resistance of the crystal lattice (Chapter 2, Frost and Ashby, 1982). Edge dislocations glide on a plane defined by **b** $\times$ **l**, while screw dislocations glide on the plane of least resistance. The climb of a dislocation perpendicular to its glide plane is a non-conservative motion and relies on the diffusion of vacancies. Thus, slip systems in a crystal are defined by **b** and the vector normal to the slip plane, **n** and noted as [uvw](hkl) or [uvw]{hkl}, where slip occurs on planes belonging to the same family (Hansen and Kohlstedt, 2015; Demouchy, 2021). In olivine, the activity of slip systems is controlled by temperature, stress, pressure, and oxygen fugacity (Hansen et al., 2021; Hansen and Kohlstedt, 2015). Table 1.1 summarises the main slip systems in olivine documented in samples deformed in the laboratory. Experimental investigations indicate that at temperatures lower than 1000°C, slip with the [001] direction dominates, while at temperatures higher than 1000°C, slip with the [100] direction is activated and contributes significantly to accommodating strain (e.g., Phakey et al., 1972; Demouchy et al., 2012, 2014; Thieme et al., 2018).

Two dimensional defects include planar features such as twin, grain, and interphase boundaries. A grain boundary represents an interface in a single-phase crystalline material across which there is a change in the misorientation of the crystal lattice (A.P.Sutton and R.W.Balluffi, 1995), as exemplified in Figure 1.1c. The crystallographic description of grain boundaries requires five independent parameters: three rotations describing the misorientation between the adjacent crystal lattices and two rotations describing the tilt and trace of the grain-boundary plane (Read and Shockley, 1950; Marquardt and Faul, 2018). The structure and energy of grain boundaries are related to the misorientation angle across the interface. For example, for small misorientations ($< 20°$) the interface can be constructed from periodic arrays of dislocations with either a screw character (resulting in a twist low-angle grain boundary) or an edge character (resulting in a tilt low-angle grain boundary, Figure 1.1c) (Hansen and Kohlstedt, 2015; Demouchy, 2021; A.P.Sutton and R.W.Balluffi, 1995; Marquardt et al., 2015). With increasing misorientation between the adjacent crystal lattices, the grain-boundary structure becomes more disorganised and can not be described by periodic dislocations. High-angle grain boundaries can have a general, or a "special"

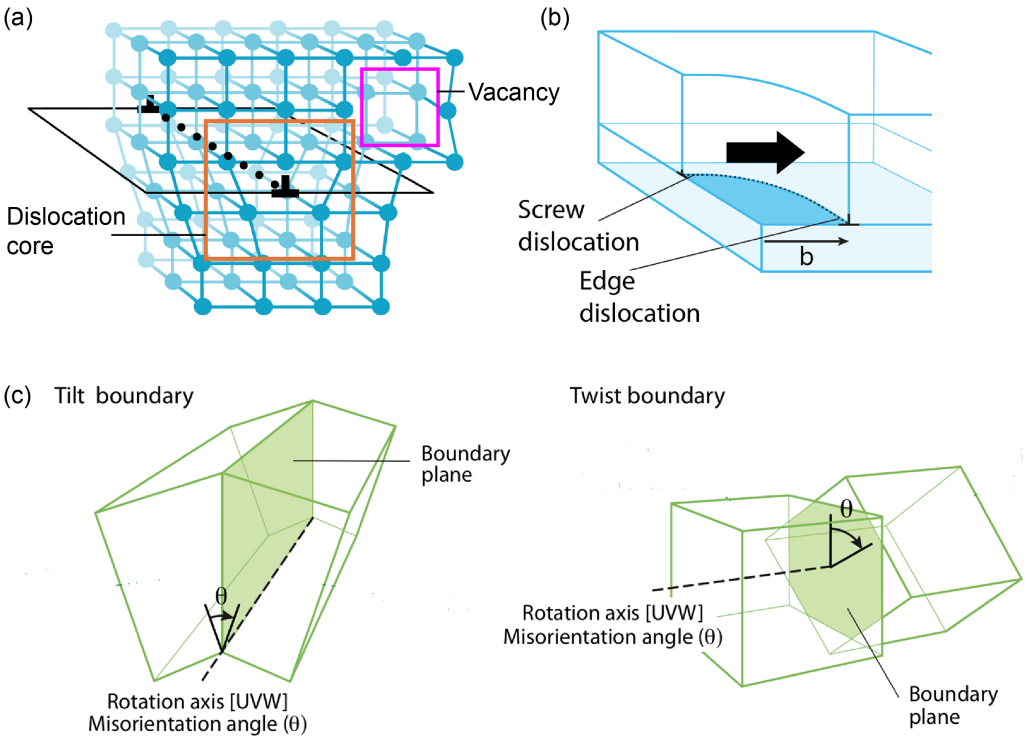


Figure 1.1: Schematic of defects in crystalline materials adapted from Demouchy (2021).

Temperature °C	Slip systems	Reference
< 800	[001](100), [001]{110}	Raleigh (1968)
	[001](010)	Druiventak et al. (2011)
		Idrissi et al. (2016)
		Wallis et al. (2020)
800–1000	[100](010), [001](100)	Phakey et al. (1972)
	[001]{120}, [001]{130}	Mussi et al. (2015b, 2014)
	[001]{110}, [100]{041}	Demouchy et al. (2013)
	[100](010), [100]{011}	Demouchy et al. (2014)
		Gasc et al. (2019)
1000	[100]{0kl}, [001]{110}	Raleigh (1968); Phakey et al. (1972)
		Demouchy et al. (2013)
		Thieme et al. (2018)
> 1150	[100](001), [001](100)	Durham et al. (1979)
	[001](010), [100](010)	Bai and Kohlstedt (1992)
	[001]{hk0}	Darot and Gueguen (1981)
	[100]{0kl}	Demouchy et al. (2012)
		Thieme et al. (2018)
		Hansen et al. (2012b)

Table 1.1: Summary of the main slip systems in olivine according to the temperature of deformation in experimental studies. These studies use scanning transmission electron microscopy to infer the activity of slip systems.

character, which is defined by the overlap of certain lattice sites of the two crystal lattices (e.g., Marquardt et al., 2015). For example, in forsterite with a b/c ratio of 1/2, a 60° rotation about the [100] axis on (011) planes generates a symmetrical, low-energy, high-angle grain boundary noted as 60°[100]/(011) (Marquardt et al., 2015; Marquardt and Faul, 2018; Hartmann et al., 2010; Heinemann et al., 2001; Adjaoud et al., 2012). Marquardt et al. (2015) conclude that the most frequent grain boundaries in olivine rocks are 90° tilt GBs around the [001] axis, with the (010), (100), or (001) planes in contact on each side of the interface. Imposed high-temperature deformation at laboratory conditions leads to a change in the distribution of grain-boundary types with increasing strain, as documented by Ferreira et al. (2021). Table 1.2 summarises the most frequent types of grain boundaries in natural- and laboratory-made olivine samples.

	Laboratory sample	Natural peridotite	Reference
Undeformed	low-angle ($0 - 25°$) about [100] or [010], 60°/[100], 90°(100)||(010), 90°(001)||(001)		Marquardt et al. (2015)
	60°/[100] with {0kl} planes		Marquardt and Faul (2018)
		low-angle ($0 - 25°$) about [100] or [010], 60°/[100], tilt 90°/[001]	Scott et al. (2014), characterised by Marquardt et al. (2015)
Deformed	low-angle tilt GB||(100)		Demouchy et al. (2014)
	low-angle GB||(010), GB||($hk0$)		Hansen et al. (2012b), characterised by Ferreira et al. (2021)

Table 1.2: Summary of documented types of grain boundaries with higher frequency when compared to a normal distribution for orthorhombic crystal lattices, in undeformed synthetic samples and natural peridotites, as well as laboratory deformed olivine samples.

1.2 Interactions between grain boundaries and dislocations in plastic deformation

Grain boundaries influence the physical properties of polycrystalline materials and play a key role in their deformation. The mechanics of the interaction of grain boundaries with other defects relies on the temperature of deformation (e.g., Hirth, 1972). Studies using experiments, theory, and numerical simulations all indicate that there are three main types of interactions: i) absorption of lattice dislocations at the grain boundary, ii) emission of lattice dislocations from the grain boundary, and iii) slip transmission across grain boundaries (Hirth, 1972; Javaid et al., 2021; Bayerschen et al., 2016; A.P.Sutton and R.W.Balluffi, 1995, Chapter 12). The activation and relative dominance of these processes depends on both temperature, which controls the mobility of defects, and the character of the grain boundary (Hirth, 1972). The interactions of grain boundaries and dislocations have been studied at length in metals (for review, see Kacher et al., 2014) and in ceramics (e.g., Mitchell, 1979). These studies proposed criteria for predicting the response of the grain boundary to an incoming dislocation gliding in the direction of $\mathbf{b}_{\text{in}}$ on the slip plane with the normal $\mathbf{n}_{\text{in}}$ (Lee et al., 1989, 1990; Bayerschen et al., 2016; Kacher et al., 2014) (Figure 1.2). These criteria include:

- Minimal slip misalignment across the grain boundary, quantified by the geometrical m' factor

$$m' = (\mathbf{n}_{\text{in}} \cdot \mathbf{n}_{\text{out}})(\mathbf{b}_{\text{in}} \cdot \mathbf{b}_{\text{out}}), \tag{1.1}$$

  where $\mathbf{b}_{\text{out}}$ and $\mathbf{n}_{\text{out}}$ correspond to the outgoing slip direction and normal to the slip plane, respectively (Figure 1.2). The misalignment for different slip systems across a grain boundary can also be quantified by the geometrical M factor accounting for the tilt of the grain boundary

$$M = (\mathbf{l}_{\text{in}} \cdot \mathbf{l}_{\text{out}})(\mathbf{b}_{\text{in}} \cdot \mathbf{b}_{\text{out}}), \tag{1.2}$$

$$\mathbf{l} = \mathbf{n} \times \mathbf{N}_{\text{GB}}, \tag{1.3}$$

  where $\mathbf{l}$ represents the intersection between the slip plane and the grain boundary plane, and $\mathbf{N}_{\text{GB}}$ is the normal to the grain boundary plane. These factors have a value of 1 for a perfectly aligned system and a transparent grain boundary and a value of 0 if the boundary acts as a perfect obstacle (Luster and Morris, 1995; Shen et al., 1986).

- Maximised resolved shear stresses on the outgoing slip plane. For example, this shear stress could be generated by dislocations piling up on the opposite side of the interface (e.g., Li, 1963; Hall, 1951) (Figure 1.2).

- Minimal residual Burgers vector in the grain-boundary plane after transmission should, i.e., minimal increase in the strain energy of the grain boundary (Lee et al., 1989, 1990; Dewald and Curtin, 2007).

- Small resolved shear stresses and normal compressive stresses on the grain boundary (Dewald and Curtin, 2007, 2011).

- Accounting for different types of grain boundaries, as grain boundaries with lower static interfacial energy are stronger barriers to slip transmission and dislocation nucleation (Sangid et al., 2011).

Grain boundaries can also act as effective sources of lattice dislocations (Chapter 12, A.P.Sutton and R.W.Balluffi, 1995). Generating dislocations from grain boundaries relies on the activation of grain-boundary sources either by the resolved shear stresses from the imposed macroscale stress or by the local shear stresses generated by other defects (e.g., dislocation pile-ups) (Figure 1.2a). Investigations in metals have proposed a number of mechanisms in which grain boundaries can act as dislocation sources (for details, see Chapter 12, A.P.Sutton and R.W.Balluffi, 1995). These studies have identified two distinct scenarios: 1) the source lies directly in the interface and half-loops extend from the interface into the neighboring crystal lattices, and 2) the source lies in the crystal lattice in the immediate vicinity of the interface, and it is activated by stress concentrations or incompatibility stresses with half loops extending in both lattices (Chapter 12, A.P.Sutton and R.W.Balluffi, 1995). Li (1963) and Murr (1975) proposed a model of dislocation emission from grain boundaries involving grain-boundary ledges (grain-boundary dislocations accommodating GB curvature) that can either act as stress concentrators mediating the nucleation of dislocation loops in the immediate vicinity of the grain-boundary plane (Varin et al., 1987; Hirth, 1972), or can be sheared in the GB plane and generate partial slip in the crystal lattice (Li, 1963; Price and Hirth, 1972; Hirth, 1972). Alternatively, stress concentration in the crystal lattice could be generated by line defects in the grain-boundary plane (extrinsic GB dislocations) (Varin et al., 1987; Murr, 1981; Gleiter, 1977; Sangal et al., 1991) or by the elastic anisotropy introduced by the juxtaposed crystals (Hirth, 1972; Hook and Hirth, 1967).

The impact of the density of interfaces on the deformation of a polycrystalline material (i.e., grain size) is dependent on the temperature of deformation. In the **low-temperature plasticity** regime, permanent deformation is accommodated by the glide of lattice dislocations through the crystal, which is the rate-limiting process in this deformation regime. Due to the low temperatures, recovery mechanisms relying on diffusion are suppressed (Chapter 2, Frost and Ashby, 1982). In the initial stage of straining polycrystalline materials, incompatibility "microplastic" stresses in the grain-boundary regions can be relieved by emission of dislocations (A.P.Sutton and R.W.Balluffi, 1995; Maaß and Derlet, 2018). This process generates local heterogeneities in the distribution of dislocations around the grain-boundary network, which in turn impacts further deformation at larger plastic strains by generating grain-boundary sections more resistant to penetration by incoming lattice dislocations (A.P.Sutton and R.W.Balluffi, 1995; Hook and Hirth, 1967; Hirth, 1972). Microscopically, these interactions contribute towards a size effect, in which samples with smaller grain sizes are stronger than samples with coarser grains. These observations are attributed to the empirical Hall-Petch effect (Hall, 1951; Petch, 1953), which has been widely documented in metals (for review, see Cordero et al., 2016). *Thus, at low temperatures of deformation polycrystalline materials become stronger with the increase of density of grain boundaries*, until the volume of grain boundaries exceeds that of the crystalline lattice and an inverse Hall-Petch effect is observed.

With increasing temperatures (i.e., temperature $>$ 0.4·melting temperature), the contribution of faster diffusional transport enables further types of plastic deformation involving grain boundaries. One such mechanism is **grain-boundary sliding** (GBS) involving the shear displacement of two crystal lattices parallel to their shared interface and localised in the interface region (Chapter 12, A.P.Sutton and R.W.Balluffi, 1995). This deformation style is accommodated by a range of possible plastic and elastic mechanisms controlled by temperature, local stress field, and grain-boundary character (A.P.Sutton and R.W.Balluffi, 1995). Sliding at grain boundaries can be accommodated by the motion of lattice dislocations in the vicinity of the interface by both glide and climb (e.g., Ashby, 1972; Crossman and Ashby, 1975; Ishida and Brown, 1967), by elastic processes (e.g., Cosandey et al., 1991; Mosher and Raj, 1974), or by diffusion within the interface (e.g., Raj and Ashby, 1972). It is expected that the activation energy for moving vacancies within the grain-boundary plane is lower compared to the one for lattice diffusion (e.g., Si diffusion in olivine, Fei et al., 2016). *Thus, at elevated temperatures of deformation, polycrystalline materials become weaker with increasing density of grain boundaries.*

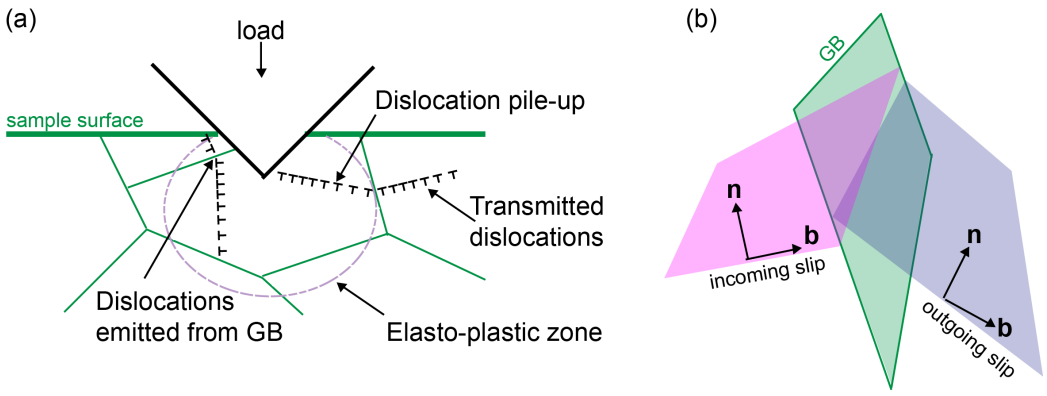


Figure 1.2: a) Diagram of a sharp indent penetrating a polycrystalline sample. Some examples of dislocations generated under the indent are drawn. The sources of these dislocations could be within the crystal lattice or the grain boundaries under the indent. Pile-ups of dislocations at a grain boundary could result in slip transmission via dislocations generated on the opposite side of the interface. b) Example of slip planes intersecting at a grain boundary.

In olivine, the impact of the density of the grain-boundary network (or grain size) on deformation with increasing temperatures is demonstrated by the experiments of Hansen et al. (2019). The authors investigated grain-size effects by deforming assemblies of samples with a fine grain-size component, and a coarse grain-size component within the same experimental conditions (Hansen et al., 2019). The experiments reveal that the yield stress of polycrystalline olivine depends on grain size, and decreases with increasing temperature. The experiments also reveal that strain hardening after yielding is grain-size independent (Hansen et al., 2019). Moreover, when deforming the same sample assembly over a range of temperatures, the mechanical data indicate that samples with finer grain sizes become progressively weaker with an increase in temperature (Hansen et al., 2019). Microstructural investigations of samples deformed in the grain-boundary sliding regime by Hansen et al. (2011, 2012b) reveal that the distribution of grain-boundary types changes with deformation, and that dislocations are transmitted through low-angle grain boundaries, but not across the high-angle grain boundaries (Ferreira et al., 2021). The authors hypothesise that dislocations are absorbed at grain boundaries via diffusion-enabled climb (Ferreira et al., 2021).

1.3 The importance of grain boundaries in the deformation of olivine in geological processes

The upper-mantle dynamics underpinning plate formation, subduction, and collision on Earth represents an intensive area of ongoing research. The upper mantle has olivine-rich rocks with grain sizes ranging from < 10 μm in shear zones to a few mm in the parts of the upper mantle under smaller deviatoric stresses (Chapter 17, Karato, 2008). These estimations rely on measurements of grain sizes in naturally deformed peridotites (e.g., Warren and Hirth, 2006) and rapidly exhumed mantle xenoliths (e.g., Lallemant et al., 1980; Scott et al., 2014). Microstructural investigations on exhumed sheared peridotites indicate that the distribution and heterogeneity of grain sizes across the upper mantle controls the grain-size dependant mechanisms required for strain localisation over geological time scales (e.g., Drury et al., 1991; Johanesen and Platt, 2015; Newman and Drury, 2010). Thus, the distribution of grain boundaries and their associated properties in upper mantle rocks could underpin the mechanisms leading to strain localisation during tectonic processes.

The strength of the lithosphere is predominantly controlled by the low-temperature plasticity of olivine (Mei et al., 2010; Hansen et al., 2019; Hunter and Watts, 2016; Watts and Zhong, 2000; Hansen et al., 2020). In this deformation regime, experimental studies predict a grain-size dependence of the yield stress (Hansen et al., 2019; Koizumi et al., 2020). Hansen et al. (2019) predicted that the strength of the lithosphere displays a strong grain-size dependence over the first 2% of strain, which impacts the response of the lithosphere to an applied load in different tectonic settings (e.g., Hunter and Watts, 2016). These extrapolations reconciled studies using geophysical measurements indicating that the flexural response of the lithosphere around the Hawaiian islands (Zhong and Watts, 2013) requires a weaker lithosphere compared to the apparently stronger oceanic lithosphere at Pacific subduction trenches (Hunter and Watts, 2016). Moreover, with increasing deformation over geological timescales, the relative mechanical properties of grain boundaries within the grain boundary network (e.g., GB segments oriented favourably for slip transmission vs. unfavourably oriented GBs) generate additional plastic anisotropy in the deforming polycrystalline olivine.

Low-temperature plasticity of olivine also impacts strength in the brittle-ductile regime. Field studies document a scale dependent roughness of fault surfaces, which implies microscopic yielding at the contact of asperities on fault zones (Brodsky et al., 2016; Thom et al., 2017). In the seismogenic oceanic lithosphere, the shear strength and yield stress of asperities on fault surfaces are controlled by low-temperature

plasticity in the olivine-rich material (Thom et al., 2022). Thus, the distribution and density of grain boundaries also impact processes in the brittle-ductile regime.

Increasing temperatures with depth lead to activation of diffusion processes in the deformation of olivine rocks. At these conditions, several mechanisms have been proposed to operate grain boundary sliding such as diffusion-controlled GBS (Ashby, 1972; Maruyama and Hiraga, 2017; Sundberg and Cooper, 2008), dislocation-accommodated GBS (Ashby, 1972; Ohuchi et al., 2015; Hansen et al., 2011, 2012b; Hirth and Kohlstedt, 2003), and elastically-accommodated GBS (Jackson et al., 2014). These grain-size sensitive mechanisms dominate upper mantle deformation, contributing to the development of a crystal preferred orientation and seismic anisotropy over long timescales (Hansen et al., 2012b; Ohuchi et al., 2015; Maruyama and Hiraga, 2017), and to the dissipation of seismic waves over short timescales (1–1000 s, Jackson et al. (2014)). Microstructural studies on naturally deformed peridotites indicate that deformation accommodated by GBS plays a key role in grain-size reduction and subsequent strain localization in the oceanic lithosphere (Warren and Hirth, 2006; Drury et al., 1991; Johanesen and Platt, 2015; Newman and Drury, 2010).

1.4 Experimental strategies for the investigation of mechanical properties of grain boundaries

The mechanics of grain boundaries and their interaction with other types of defects have been studied with the use of theoretical, experimental, and numerical techniques (A.P.Sutton and R.W.Balluffi, 1995). In this section, I am focusing on experimental studies, with an emphasis on small-scale, direct testing of grain boundaries. Experimental investigations of the mechanics of grain boundaries deploy one or both of the main strategies of investigation: 1) using bicrystals, and/or 2) testing small volumes of material containing a general grain boundary. A bicrystal is a composite object of two crystals brought in contact by a shared interface (Chapter 1, A.P.Sutton and R.W.Balluffi, 1995). Pond and Vlachavas (1983) introduced the crystallographic framework for describing and classifying a planar interface between crystals, with both theoretical and practical applications. In practice, manufacturing bicrystals allows the targeted investigations of specific GBs and has been successfully implemented in studies of metals with high ductility (e.g, Ta, Weaver et al. (2018); Cu, Imrich et al. (2014); Al, Ng and Ngan (2009); Kunz et al. (2011); Sn, Gong and Wilkinson (2016); Ni, Kheradmand et al. (2016)) and intermetallics, which are more brittle under macroscale testing (e.g., NiAl, Vehoff et al., 1997). The key advantage of synthesizing

bicrystals with the scope of studying grain boundaries is that the interface can have the orientation and symmetry of choice, with little curvature, impurities, or deformation around it. Grain-boundary diffusion and structure in geological materials, such as forsterite and garnet, have been studied using bicrystals with specific high-symmetry, low-energy grain boundaries (Polednia et al., 2020; Marquardt and Faul, 2018; Hartmann et al., 2010; Heinemann et al., 2005; Marquardt et al., 2011). However, while studies on deformation of bicrystals have provided useful insight into the dynamics of small-scale deformation in metals (e.g., Dehm et al., 2018), deformation studies of bicrystals in geological materials are lacking.

Nanomechanical testing using diamond indenters enabled probing small volumes of material under different strain (Figure 1.2a). Berkovich nanoindenter tips are three sided, self-similar pyramids, which result in material deformation at an effective indentation strain of 8%, independent of the indentation depth (Chapter 3, Fischer-Cripps and Nicholson, 2004). Spherical indenter tips probe material deformation at different strain with indentation depth (Chapter 3 Fischer-Cripps and Nicholson, 2004). In polycrystalline materials, nanoindentation can be implemented to isolate the mechanics of a grain boundary under an applied load (e.g., Figure 1.2a). Previous work in metals investigated processes such as dislocation transmission through grain boundaries by collecting load-displacement data at various distances from the same grain boundary using both Berkovich (e.g., Britton et al., 2009; Wang and Ngan, 2004; Ohmura and Tsuzaki, 2007; Voyiadjis and Zhang, 2015; Aifantis et al., 2006) and spherical indenter tips (e.g., Kalidindi and Vachhani, 2014; Vachhani et al., 2016b). For example, spherical nanoindentation in Al reveals that the yield stress can increase with increasing proximity to a grain boundary (e.g., Vachhani et al., 2016b). Similar effects have been observed in an Al bicrystal tested with Berkovich indentation (Aifantis et al., 2006). Moreover, recent improvements in high-throughput nanoindentation mapping (e.g., Wheeler, 2021; Besharatloo and Wheeler, 2021; Hintsala et al., 2018) significantly improve the time-scales of data collection and spatial coverage of mechanical data in samples with complex microstructures. Thus, one key advantage of nanomechanical testing is the potential of coupling microstructural information and mechanical properties of interfaces over sample surfaces of statistical significance. However, as indicated in Figure 1.2, the lack of knowledge of grain boundary inclination under the surface, and consequently under the indent, represents a key caveat for the meaningful interpretation of nanoindentation data of general grain boundaries in anisotropic materials.

Studying mechanical properties of grain boundaries has been enabled by increased capabilities of miniaturising mesoscale experiments and deforming small volumes of material *in-situ* (for review, see Dehm et al., 2018). Further expansion of the temperature of *in-situ* deformation capabilities to up to 1000°C (Wheeler et al., 2015; Kacher et al., 2019) enabled the study of a wider variety of deformation mechanisms (e.g., Korte-Kerzel, 2017). Microcompression over wide ranges of temperatures facilitates the study of slip bands and their transmission across interfaces, and the probing of the shear strength of interfaces (Dehm et al., 2018; Korte-Kerzel, 2017). *In-situ* shear testing requires manufacturing complex sample geometries that enable the transformation of an applied far field compression or tension stress into shear stress. For example, a cylindrical micropillar used for compression testing can be modified with two side notches into a "S"-shaped micropillar to generate shear stresses parallel to the loading direction (e.g., Gigax et al., 2019; Mayer et al., 2015). The key application of this testing technique has been in the investigation of Cu-Si interfaces (Gigax et al., 2019) and nanolaminate materials (Mayer et al., 2015) as it represents a powerful tool for investigating the individual shear properties of planar features (e.g., grain boundaries). However, the majority of *in-situ* testing techniques require complex, time-consuming sample preparation using focused ion beam (FIB) milling.

In olivine, the impact of grain boundaries on deformation has been investigated by comparing the mechanical properties of single crystals with polycrystalline samples of varying grain sizes. Laboratory investigations of low-temperature plasticity involved either single-crystal (e.g., Demouchy et al., 2013; Gaboriaud et al., 1981; Goetze and Evans, 1979; Idrissi et al., 2016; Hansen et al., 2019; Kumamoto et al., 2017; Koizumi et al., 2020) or polycrystalline samples (e.g., Druiventak et al., 2011; Hansen et al., 2019; Katayama and Karato, 2008; Mei et al., 2010; Raterron et al., 2004; Kumamoto et al., 2017; Koizumi et al., 2020). In these experiments it is challenging to separate the microphysics associated with interactions between dislocations and grain boundaries. For example, while nanoindentation tests (Kumamoto et al., 2017) and transmission electron microscopy investigations of deformed olivine (Thieme et al., 2018; Wallis et al., 2020) indicate that grain boundaries might act as dislocation sources, direct evidence of this phenomenon is lacking. The measurements presented by Kumamoto et al. (2017) could be explained by dislocation generated either from grain boundaries or from the high initial dislocation density. Furthermore, the mechanisms of slip transfer between grains in olivine remain unresolved in both low-temperature plasticity and deformation at higher temperatures (e.g., Ferreira et al., 2021; Bollinger et al., 2019).

1.5 Aims and Outline

In this thesis I am investigating the interactions between dislocations and grain boundaries in forsterite, and contributing towards the development of techniques for the study of grain boundaries and microtexture evolution in materials more broadly.

Chapter 2 investigates in detail the impact of calibration and data analysis routines on data collected with spherical nanoindentation tips. I analysed data collected on three materials with different known elastic moduli, in order to independently calibrate the effective tip radius and machine stiffness. The calibration has been applied to data collected on materials with varying ductility in order to extract stress-strain curves. The methods developed in this chapter integrate and build on published literature and provide a guide for extracting and processing data from spherical nanoindentation.

Chapter 3 aims to clarify the role of grain boundaries in the low-temperature plasticity of forsterite and provides evidence of the microphysics underlying the grain-size effect documented by Hansen et al. (2019). To this end, I conducted nanoindentation experiments and high-resolution microscopy characterization on forsterite bicrystals with a low- and high-angle grain boundary. These experiments reveal the impact of different grain boundaries on generating dislocations and acting as a barrier to dislocation motion.

Chapter 4 aims to investigate the shear strength of forsterite grain boundaries at 700°C. This study provides direct observations documenting the interactions between grain boundaries and dislocations by deploying small-scale, uniaxial, *in-situ* mechanical testing of two pure forsterite bicrystals. The experiments are performed at a temperature of 700°C with a sample orientation designed to maximise the resolved shear stress on the grain-boundary plane and promote grain-boundary sliding.

Chapter 5 describes an apparatus and sample geometry developed for the *in-situ* testing of materials in simple shear. I present the novel apparatus in the context of existing strategies for material testing in simple shear, and demonstrate its capabilities by testing PbSn, Sn, and Al samples. Moreover, this apparatus can also be implemented in the study of Earth materials. Studying olivine rheology via an analogous organic material, borneol $C_{10}H_{18}O$, has been a successful line of investigation in previous studies (e.g., Sasaki et al., 2019), due to the low melting temperature of this analogous material (200°C).

This chapter also aims to identify outstanding materials science issues to which the proposed sample design could meaningfully contribute.

Finally, Chapter 6 summarises the results presented in this thesis and identifies areas of future research. In this section, I focus on identifying outstanding questions related to fosterite deformation and application of the results presented in this thesis to the bulk deformation of materials.

Chapter 2

Calibration and data analysis routines for nanoindentation with spherical tips

"Maybe because indentation experiments are so simple and convenient we are misled into believing that their unsophisticated interpretation will provide precise information concerning the elastic and plastic properties of the specimen."

D. Tabor, 1996

A similar version of this chapter has been prepared for publication in the *Journal of Materials Research*, with the following author list:

Diana Avadanii[1], Anna Kareer[2], Lars Hansen[3], Angus Wilkinson[2]

[1] Department of Earth Sciences, University of Oxford
[2] Department of Materials, University of Oxford
[3] Department of Earth and Environmental Sciences, University of Minnesota

For this study, I have assembled the samples to be tested, collected some of the data, analysed and interpreted the data, wrote the code for data analysis, and wrote the first draft of the manuscript.

Abstract

Instrumented spherical nanoindentation with a continuous stiffness measurement has gained increased popularity in material science studies in brittle and ductile materials alike. These investigations span hypotheses related to a a wide range of microphysics involving grain boundaries, twins, dislocation densities, ion-induced damage and more. These studies rely on the implementation of different methodologies for instrument calibration and for circumventing tip shape imperfections. In this study, we test, integrate, and re-adapt published strategies for tip and machine stiffness calibration for spherical tips. We propose a routine for independently calibrating the effective tip radius and the machine stiffness using three reference materials (fused silica, sapphire, glassy carbon), which requires the parametrization of the effective radius as a function of load. We validate our proposed workflow against key benchmarks, such as variation of Young's modulus with depth. We apply the resulting calibrations to data collected in materials with varying ductility (olivine, titanium, tungsten) to extract indentation stress-strain curves. We also test the impact of the machine stiffness on recently proposed methods for identification of yield stress, and compare the influence of different conventions on assessing the indentation size effect. Finally, we synthesize these analysis routines in a single workflow for use in future studies aiming to extract and process data from spherical nanoindentation.

2.1 Introduction

Instrumented nanoindentation has become a widely-used technique for material characterization. The array of available tip geometries allows material analysis over a wide range of stress states. Indentation with a rigid, spherical tip has recently gained popularity due to key advantages of this geometry compared to sharp tip geometries (e.g., Berkovich). Indentation with a sphere induces a stress field under the indenter that is not self similar, and therefore the indentation strain progressively increases with indentation depth (see Chapter 3 in Fischer-Cripps, 2011; Pharr et al., 2010). Thus, load-displacement data can be transformed into indentation stress-strain curves, which facilitate the investigation of the full elasto-plastic response of materials. Moreover, nanoindentation with indenters of varying radii provides insight into size effects associated with deformation and enables correlation of small-scale material testing with macroscopic tests (e.g., Pathak and Kalidindi, 2015b). For example, in certain materials, indentation using tips with large radii results in stress-strain curves with a hardening coefficient similar to that of uniaxial tests, while data obtained using indenters with smaller radii display an indentation size effect (e.g., Spary et al., 2006; Weaver and Kalidindi, 2016). In spherical nanoindentation, the indentation size effect is underpinned by both material hardening with increasing indentation strain, as well an increase in hardness with decreasing spherical radii (Swadener et al., 2002; Pharr et al., 2010; Hou et al., 2008; Herbert et al., 2001). Finally, bursts of displacement in the stress-strain curves (called "pop-ins") provide valuable insight into initiation of plasticity at small scales and display an additional size effect in spherical nanoindentation, in which the stress at pop-in increases with decreasing tip radius (Zhu et al., 2008; Morris et al., 2011a; Shim et al., 2008; Patel and Lee, 2020).

The potential to produce a large number of measurements and generate indentation stress-strain curves from a small volume of material makes spherical nanoindentation a desirable technique with a wide range of applications. For example, spherical nanoindentation has been deployed to investigate yield stress and size effects in brittle engineering ceramics and natural minerals (e.g., Hackett et al., 2019; Zhu et al., 2008; Kumamoto et al., 2017; Hansen et al., 2020; Stich et al., 2022; Fang et al., 2021), the mechanical properties of twin and grain boundaries in metals (e.g., Vachhani et al., 2016a; Weaver et al., 2018; Li et al., 2021b), the effects of ion-induced damage in metals and alloys (e.g., Bushby et al., 2012; Armstrong et al., 2015; Pathak et al., 2017), the relationship between structure and mechanical properties in biomaterials (bone (e.g., Pathak et al., 2012), human enamel (e.g., He et al., 2006)), elasto-plastic transitions in

bulk metallic glasses (e.g, Choi et al., 2012; Bei et al., 2004), and fracture in thin films (e.g., Zhang et al., 2017; Mercier et al., 2017). This versatility of mechanical testing using spherical indentation has motivated studies on the reliability of measurements and prompted efforts to improve data analysis. Investigations into the methodology of spherical indentation highlight the importance of accurate knowledge of tip radius (Leitner et al., 2018; Li et al., 2013; Bushby and Jennett, 2000), machine stiffness, (Li et al., 2013; Kang et al., 2012; Cabibbo et al., 2012), differences among nanoindenter apparatus (Cabibbo et al., 2012), and the impact of different data-analysis routines on the extracted material properties (Pathak and Kalidindi, 2015b; Kalidindi and Pathak, 2008a).

In this contribution, we test, integrate, and adapt several published strategies for calibration of spherical tip shape and machine stiffness, and implement a routine to calibrate the effective radius and machine stiffness using purely elastic indentation data collected on materials with varying elastic moduli. This synthesis results in an improved workflow to accurately extract stress-strain curves. We also develop a procedure for characterization of tip shape and machine stiffness for tips that are not perfectly spherical, relying on the obtained indentation data from reference materials. We emphasize that the cumulative impact of imperfections in spherical tips, inconsistencies in sample mounting, and variations among instruments reduce the repeatability and overall meaningful interpretation of data collected across multiple studies. To this end, we outline a calibration routine using fused silica, sapphire, and glassy carbon as reference materials. We then implement the resulting calibration to extract indentation stress-strain curves from tungsten, olivine, and titanium. Details of the experiment set-up are outlined in Section 2.2. We suggest that future studies using spherical nanoindentation, would benefit from detailed reports of how the tip and machine stiffness calibration satisfy different benchmarks for meaningful comparison among different published results. Ultimately, we intend for this contribution to serve as a detailed guide to deliver the full potential of spherical nanoindentation as a materials characterisation technique with application to a broad range of materials with varying ductility.

2.2 Experimental aspects

Nanoindentation tests with spherical tips and continuous stiffness measurements were performed on a displacement-controlled indenter (Nanoindenter G200, Agilent Technologies) with the frequency target set at 45 Hz, the harmonic displacement

target set at 2 nm, and the loading rate divided by load as $\frac{\dot{P}}{P} = 0.05s^{-1}$. We used diamond spherical tips ($E_\mathrm{i} = 1141$ GPa, $v_\mathrm{i} = 0.07$) with a 2–50 μm range of nominal tip radii (Table 2.1). The data collection was undertaken with a default machine stiffness, $S_\mathrm{default} = 3.67 * 10^6$ N/m.

In order to assess tip calibration and data analysis routines, we have mounted reference materials with known moduli (fused silica, sapphire, and glassy carbon) on the same stub as materials with unknown elastic moduli (olivine, W, Ti) using the smallest amount of epoxy necessary. This set-up mediates differences in assembly stiffness due to the mounting substrate. The olivine single crystal sample used in this study is the undeformed sample also used by Kumamoto et al. (sample MN1, 2017); Wallis et al. (sample MN1, 2020). Both the titanium and tungsten samples are undeformed, commercially-available pure samples, with grain sizes in the ranges of 10–50 μm and 10–100 μm, respectively.

We performed 270 nanoindentation tests in total, with at least 9 tests for each tip reported in Table 2.1. Nanoindentation experiments in materials with known Youngs modulus were performed at small loads, resulting in elastic load-displacement curves (Table 2.1). We have measured the harmonic contact stiffness throughout the loading and unloading paths in all experiments.

Table 2.1: Summary of experiments. Note that the experiments in the reference materials with known elastic moduli are experiments in the elastic deformation regime only.

	Nominal tip radius, R_n							
	2 μm	5 μm	10 μm	20 μm	50 μm			
Material	Maximum load (N)					Young's Modulus, E_s, (GPa)	Poisson ratio, v_s	Grain size (μm)
fused silica	$2.5 * 10^{-3}$	$8 * 10^{-2}$	$1 * 10^{-1}$	$2 * 10^{-1}$	$3 * 10^{-1}$	72	0.17	single crystal
sapphire	$2.5 * 10^{-3}$	$8 * 10^{-2}$	$1 * 10^{-1}$	$2 * 10^{-1}$	$3 * 10^{-1}$	420	0.28	single crystal
glassy carbon	$1.5 * 10^{-3}$	$1 * 10^{-2}$	$3 * 10^{-2}$	$5 * 10^{-2}$	$1 * 10^{-1}$	34	0.27	-
olivine	$8 * 10^{-2}$	$2.5 * 10^{-1}$	$3.8 * 10^{-1}$	$6.5 * 10^{-1}$	$6.5 * 10^{-1}$	-	0.24	single crystal
Ti	$2.5 * 10^{-2}$	$8 * 10^{-2}$	$1.5 * 10^{-1}$	$3 * 10^{-1}$	$4 * 10^{-1}$	-	0.35	35
W	$5.5 * 10^{-2}$	$2 * 10^{-1}$	$3.2 * 10^{-1}$	$6 * 10^{-1}$	$6 * 10^{-1}$	-	0.29	> 50

2.3 Results and Analysis

2.3.1 Theoretical background

Instrumented nanoindentation measures the displacement of the indenter tip in response to an applied load, P. The total measured displacement, h_total, is a combination of the displacement due to surface deformation of the sample, h_sample, and the deflection due to the machine stiffness, h_mach. This interaction can be expressed as

two deforming elements connected in series, for which the displacements are (Li and Bhushan, 2002; Oliver and Pharr, 1992b; Swadener and Pharr, 1999)

$$h_{\text{total}} = h_{\text{sample}} + h_{\text{mach}}. \tag{2.1}$$

The value of h_{mach} can be estimated from the machine stiffness, S_{mach}, according to $h_{\text{mach}} = P/S_{\text{mach}}$, where the machine stiffness accounts for the combined stiffness from the indenter tip and the loading frame. The common procedure is to determine S_{mach} for an instrument by performing a series of experiments with a Berkovich tip in a material with known elastic modulus. This method allows both the area function of the tip and the stiffness of the loading frame to be determined simultaneously (Oliver and Pharr, 1992b). The obtained value of the machine stiffness is used as the default stiffness, S_{default}, which is generally applied by the instrument software when collecting and reporting new data. However, previous studies using spherical indenters have indicated that the stiffness during experiments is a function of the applied load, rather than a single value (Li and Bhushan, 2002; Cabibbo et al., 2012). Consequently, this procedure for calibration of the area function and machine stiffness can lead to systematic errors in subsequent experiments if the applied loads are significantly different than those used in the calibration (Li et al., 2013).

It is possible to explicitly implement a calibration routine for spherical indentation tips in order to identify S_{mach} for each machine-tip pair, as well as to determine the effective radius of the tip. Following Li and Bhushan (2002), we express the reported displacement as

$$h_{\text{rep}} = h_{\text{total}} - \frac{P}{S_{\text{default}}} + h_0, \tag{2.2}$$

where h_0 accounts for errors arising from the initial contact between the sample surface and the indenter tip.

Because the stiffness of a particular indenter tip combined with the stiffness of the other components of the instrument are unknown, we can describe h_{rep} as

$$h_{\text{rep}} = h_{\text{sample}} + \frac{P}{S_{\text{mach}}} - \frac{P}{S_{\text{default}}} + h_0. \tag{2.3}$$

For cases in which the response of the material is purely elastic, h_{sample} can be modelled according to Hertzian mechanics as the elastic displacement, h_{e} (Johnson, 1970),

$$h_{\text{e}} = P^{2/3} \left(\frac{4}{3} \sqrt{R_{\text{eff}}} E_{\text{eff}} \right)^{-2/3}, \tag{2.4}$$

for which

$$\frac{1}{E_{\text{eff}}} = \frac{1 - \upsilon_{\text{s}}}{E_{\text{s}}} + \frac{1 - \upsilon_{\text{i}}}{E_{\text{i}}} \tag{2.5}$$

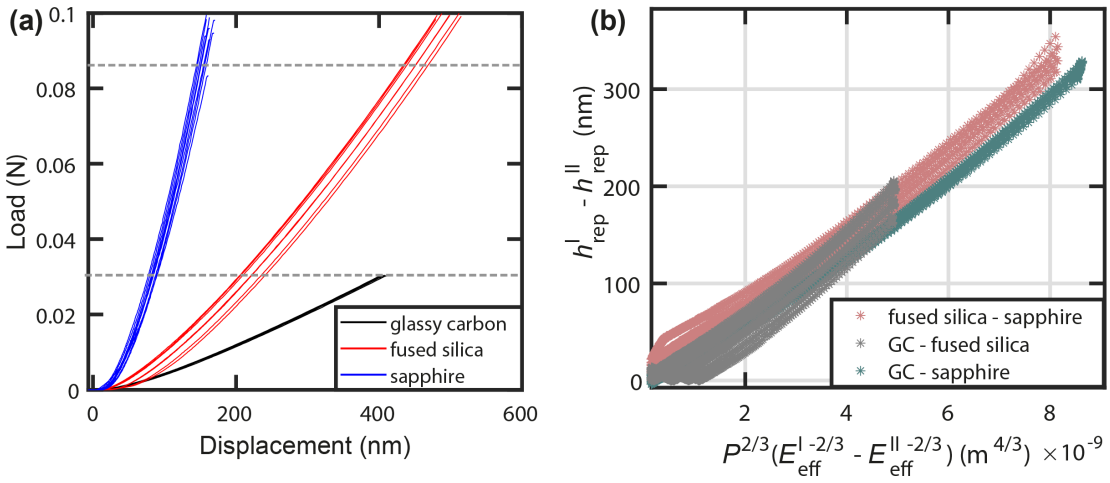


Figure 2.1: a) Load-displacement data collected with a spherical tip with a nominal radius of 10 μm in different materials with known moduli. b) Curve subtraction of displacement at the same load. The cut-off load for each set of experiments is marked by the dashed horizontal lines in a). The slope of these curves is proportional to the effective tip radius according to Equation 2.8.

and

$$\frac{1}{R_{\text{eff}}} = \frac{1}{R_{\text{s}}} + \frac{1}{R_{\text{i}}}. \tag{2.6}$$

E_{eff} and R_{eff} are the reduced elastic modulus and tip radius, and are expressed as a function of the elastic moduli and Poisson's ratios of the sample (E_{s} and υ_{s}) and indenter tip (E_{i} and υ_{i}) and of the radius of the sample surface (R_{s}) and indenter tip (R_{i}). For a purely elastic contact and a flat sample surface, the curvature of the surface is infinity so that $R_{\text{eff}} = R_{\text{i}}$.

2.3.2 Calibrations on materials with known moduli

2.3.2.1 Determination of effective radius

Studies employing spherical nanoindentation implement various strategies for calculating the effective radius, R_{eff} (Pathak and Kalidindi, 2015b; Li and Bhushan, 2002; Leitner et al., 2018; Bushby and Jennett, 2000). The value of R_{eff} can be calculated by using equation 2.6 and the nominal tip radius provided by the manufacturer (Hackett et al., 2019). More commonly, R_{eff} is calculated by fitting Equation 2.4 to data collected using fused silica (Swadener and Pharr, 1999; Pathak and Kalidindi, 2015b; Patel and Lee, 2020). Alternatively, R_{eff} can be displayed as a function of depth using data from fully elastic experiments in multiple reference materials and adjusting the fit for other variables (e.g., machine stiffness) to achieve converging values of R_{eff} as a

function of depth, in materials with a wide range of elastic moduli (Field and Swain, 1993; Bushby and Jennett, 2000; Zhu et al., 2008). Complications in implementing these methods arise due to the impact of machine stiffness on reported displacement values and of tip shape imperfections, which are difficult effects to deconvolve. These errors can lead to unrealistic differences in the values of R_{eff} obtained with different reference materials (e.g., fused silica and sapphire) (Li and Bhushan, 2002; Bushby and Jennett, 2000; Zhu et al., 2008). Moreover, errors in the calibration of R_{eff} can lead to inconsistencies in stress-strain measurements on the same material with different indenter tips. These potential discrepancies motivate the need for a calibration routine in which the machine stiffness and effective radius are both determined in a self-consistent manner (Li and Bhushan, 2002).

To circumvent these issues, we implement the method proposed by Li et al. (2013) to find the machine stiffness and effective radius for each machine-tip pair in Table 2.1. Although Li et al. (2013) applied their calibration routine to two reference materials, we extend this analysis to three reference materials. This approach relies on the difference in reported displacements at the same load in elastic experiments on different materials with known elastic moduli. Following Li et al. (2013), we rearrange Equation 2.3 to define the error in displacement, h_{err}, as

$$h_{\text{err}} = h_{\text{rep}} - h_{\text{e}} - h_0 = \frac{(S_{\text{default}} - S_{\text{mach}})P}{S_{\text{default}} S_{\text{mach}}}. \tag{2.7}$$

The main assumption with this approach is that, at a given load, h_{err} is the same for different reference materials. For two reference materials (noted as I and II), using Equation 2.3 and data collected at the same load, we can subtract the reported elastic displacement in material II, $h_{\text{rep}}^{\text{II}}$, from the reported elastic displacement in material I, $h_{\text{rep}}^{\text{I}}$. The $\frac{P}{S_{\text{mach}}}$ and $\frac{P}{S_{\text{default}}}$ terms in Equation 2.3 corresponding to each material cancels out for the same load P such that (Li et al., 2013)

$$h_{\text{rep}}^{\text{I}} - h_{\text{rep}}^{\text{II}} = P^{2/3} \left(\frac{4}{3} \sqrt{R_{\text{eff}}} \right)^{-2/3} \left({E_{\text{eff}}^{\text{I}}}^{-2/3} - {E_{\text{eff}}^{\text{II}}}^{-2/3} \right) + h_0^{\text{I}} - h_0^{\text{II}}. \tag{2.8}$$

We apply Equation 2.8 to data collected from fused silica, glassy carbon, and sapphire as outlined in Section 2.2. In Figure 2.1, we display the reported elastic load-displacement curves in the reference materials collected with a tip with nominal radius $R_{\text{n}} = 10$ μm, and mark the the load and displacement used in Equation 2.8 with a dashed horizontal line. Figure 2.1b reports the differences calculated using Equation 2.8 between reported displacement in fused silica and sapphire, glassy carbon and fused silica, and glassy carbon and sapphire as a function of a term proportional

to $P^{2/3}$. Thus, according to Equation 2.8 the slope of the graph in Figure 2.1b is proportional to R_{eff}, and the intersection with the vertical axis is the difference in the displacement error due to surface contact in the two materials ($h_0^{\text{I}} - h_0^{\text{II}}$).

One key observation in Figure 2.1b is that the average slope of the curves systematically varies among the three pairs of reference materials. This observation is ubiquitous among our experiments, as can be seen in Figure 2.2, which demonstrates that the best-fit R_{eff} varies by up to 40% depending on the pair of reference materials. This result is contrary to expectations arising from the analysis of Li et al. (2013), which suggests that R_{eff} should not depend on the reference materials used in calibration.

Part of this discrepancy results from the curves in Figure 2.1b departing from linearity, which implies that R_{eff} is not a constant for any given calibration. This issue is accentuated in 2.3a, which presents data comparing fused silica to sapphire and a linear fit assuming constant R_{eff}. There is clearly curvature in the data not captured by the linear fit. Since the subtraction method proposed by Li et al. (2013) accounts for the effects of machine stiffness when calculating R_{eff}, we interpret the curvature of the data in Figure 2.3a to instead result from departure of the tip shape from a perfect sphere. Imperfections in tip shape could be accounted for by the parametrization of R_{eff} as a function of displacement. However, measured displacements are also affected by the machine stiffness, which is unknown at this point in the analysis. Therefore, we instead choose to express the effective radius as a function of load. Figure 2.3b presents R_{eff} as a function of load as calculated from the first derivative of the curve in Figure 2.3a. We fit an offset power law function (i.e., $f(x) = \mathrm{a}x^{\mathrm{b}} + \mathrm{c}$) to these data to allow R_{eff} to be easily estimated for any given load. We only fit this function to data comparing fused silica and sapphire because the data involving glassy carbon corresponds to smaller loads (Figure 2.1a), for which the data are considerably noisier. The data trend in Figure 2.3b matches the expectation of convergence to a single value for R_{eff} at larger loads. Comparing Figure 2.2 with Figure 2.3b, we note that at higher loads, the calculations following Li et al. (2013) overestimate the values for R_{eff}, which could lead to underestimations of stress (e.g., Bei et al., 2016; Gao and Bei, 2016)(see Table A.1).

2.3.2.2 Determination of machine stiffness

For a robust interpretation of stress-strain curves obtained using spherical indentation, the impact of machine stiffness has to be determined for each combination of instrument and tip and can be reported as a function of load (Li et al., 2013; Kang et al., 2012; Cabibbo et al., 2012). To assess the magnitude of the machine stiffness, Figure 2.4a

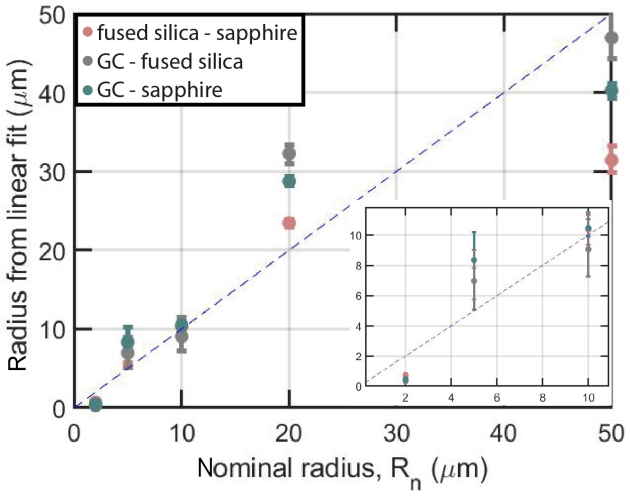


Figure 2.2: Summary of results for effective radius determined as the slope of a line fit through data calculated as the subtraction of elastic load-displacement curves at the same load in different reference materials following the method of Li et al. (2013) (Equation 2.8). The dashed line represents the 1:1 proportionality.

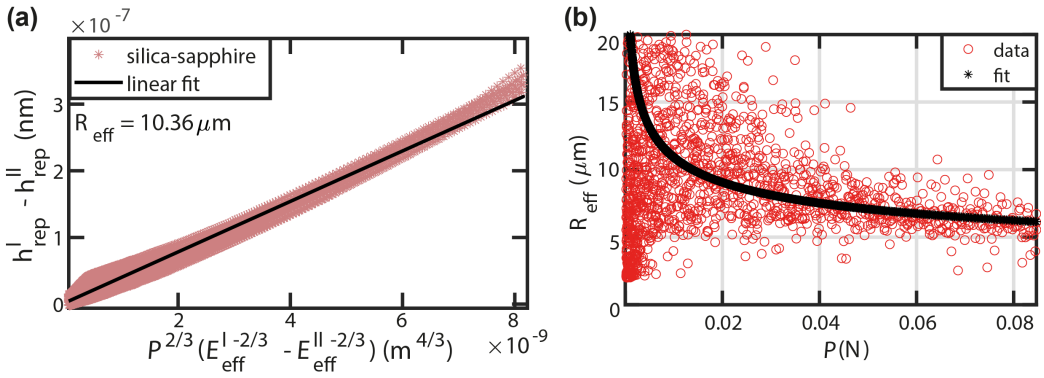


Figure 2.3: a) Linear fit for a spherical tip with a nominal radius of 10 μm following Li et al. (2013). Note the curvature in the data obtained by subtracting sapphire displacement from fused silica displacement according to Equation 2.8. b) Effective radius calculated using the first numerical derivative of data in a) against load and an exponential fit. All values for R_{eff} in Figure 2.2 and the values for R_{eff} at a constant load can be found in Supplementary Materials, Table A.1.

compares the reported loads and displacements to the predicted displacement using Equation 2.4. We implement R_{eff} either as a constant (blue curve, similar to Figure 2.3a) or as a function of load (red curve, similar to Figure 2.3b). Although the load-dependent R_{eff} is in better agreement with the reported data, there is still some mismatch in the displacements, which corresponds to h_{err} and which we attribute to the apparent stiffness of the system. We use R_{eff} as a function of load in conjunction with h_{err} and the known value of S_{default}, stated in Section 2.2, to calculate S_{mach} according to Equation 2.7. We plot this machine stiffness, S_{mach}, as a function of load for sapphire and fused silica in Figures 2.4b and c. For comparison, we also plot S_{mach} assuming R_{eff} is constant. In Figures 2.4b and c, we plot the result of calculations of S_{mach} amongst tests in sapphire and fused silica, as there is no particular reason for using one data set over another when substituting in Equation 2.7. We emphasize that the data from both reference materials converge to similar values of S_{mach}, which are $\sim 0.7 * 10^7$ N/m for tip with a nominal radius of 20 μm presented in Figure 2.4. Note that the variability in S_{mach} resulting from tests on sapphire (Figure 2.4c) and fused silica (Figure 2.4b) is directly related to how well the Hertzian prediction in Figure 2.4a fits the reported data. As demonstrated in Figure 2.4a, the elastic prediction overestimates the reported displacement, which means $h_{\text{rep}} - h_{\text{e}}$ is negative and, therefore, the resulting effective machine stiffness $(P/(h_{\text{rep}} - h_{\text{e}}))$ is negative. This negative effective machine stiffness does not imply that the machine actually has negative stiffness. Instead, the negative effective stiffness results from the default stiffness used by the software, S_{default}, being smaller than the actual S_{mach}.

The stiffness of the machine-tip pair needs to be accounted for when evaluating the reported harmonic contact stiffness. We model the machine-tip pair and the sample response as a series of elastic elements (Li and Bhushan, 2002) and propose a correction for the reported harmonic contact stiffness using

$$\frac{1}{S_{\text{corr}}} = \frac{1}{S_{\text{rep}}} + \frac{1}{S_{\text{default}}} - \frac{1}{S_{\text{mach}}}, \tag{2.9}$$

where S_{corr} is the corrected contact stiffness and S_{rep} is the reported contact stiffness during the experiment, collected with S_{default}. Equation 2.9 can be implemented by linearly fitting S_{mach} as a function of load in Figure 2.4b. In this step, choices of data cut-off will impact the slope of the fitted line. This is the key step in which we recommend an iteration between the fitting procedure and the outcome of the data correction verified in key benchmarks.

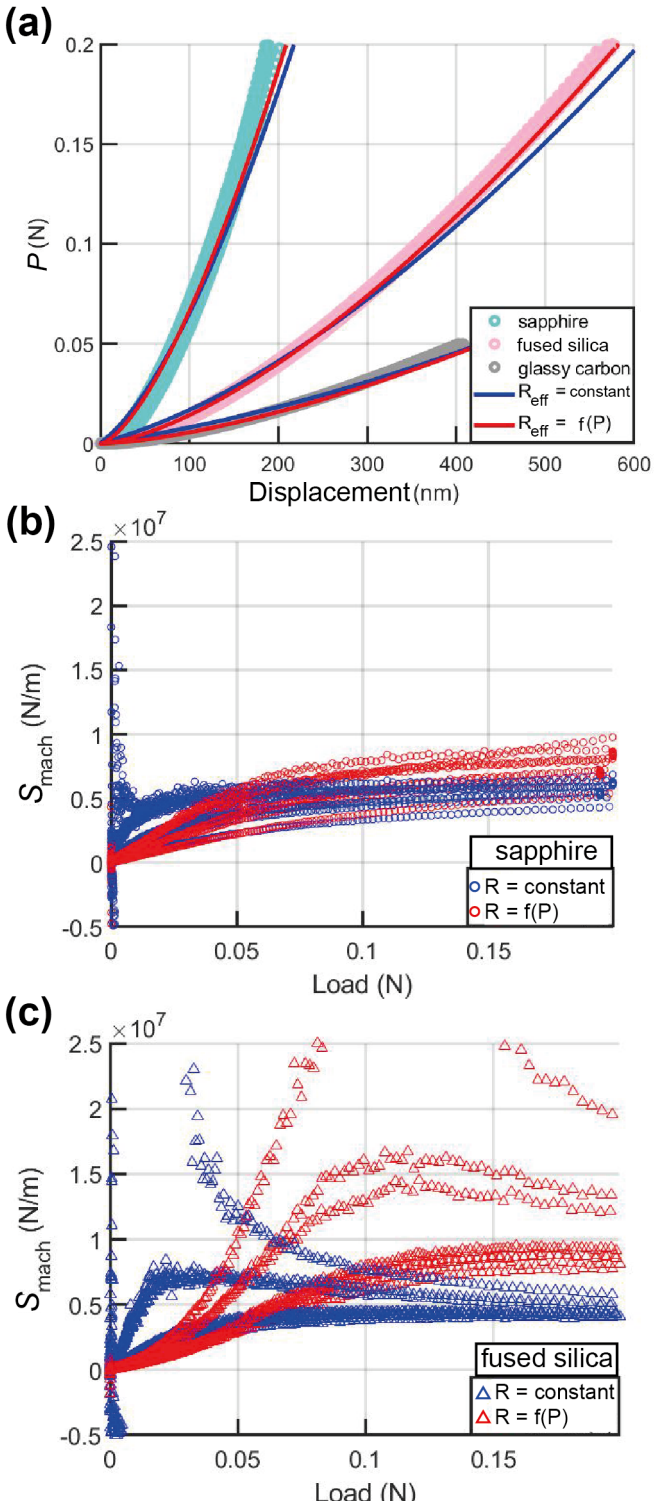


Figure 2.4: a) Load-displacement data for a spherical tip with a nominal radius of 20 μm in different materials with known moduli overlapped with predictions using a constant effective radius (blue) and radius as a function of depth (red) in Equation 2.4. b) Calculations of machine stiffness using sapphire data in Equation 2.3. c) Calculations of machine stiffness using fused silica data in Equation 2.3.

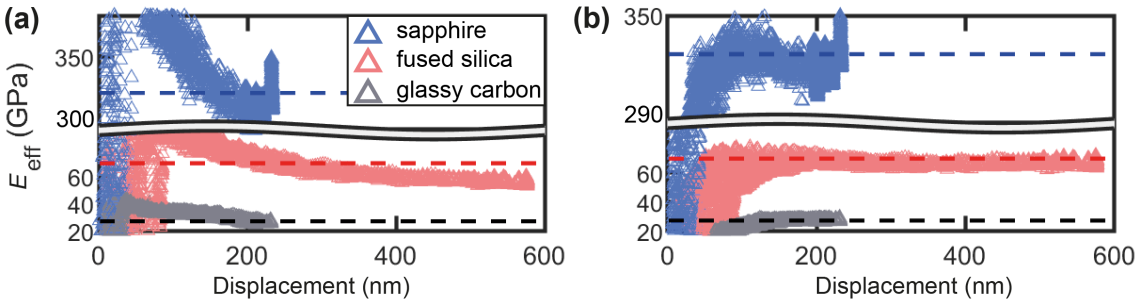


Figure 2.5: Young's modulus calculated using Equation 2.10 against expected values using) an effective radius as a constant for data collected with a diamond tip with $R_n = 5$ μm and reported values for the harmonic contact stiffness and b) an effective radius as a function of load and stiffness correction of the reported harmonic contact stiffness according to Equation 2.9. Note the differences in vertical scales. The reference values of the effective Young's modulus are plotted with dashed lines, and are calculated using the values in Table 2.1 and Equation 2.5.

2.3.2.3 Benchmarks

Calibrations of spherical tips can be assessed with a variety of key benchmarks. The most common benchmark in nanoindentation is observation of a constant Young's modulus with depth (e.g., Leitner et al., 2018). Following the derivation from Hackett et al. (2019) and using Equations 2.4 and 2.9, we can express the effective Young's modulus as

$$E^*_{\text{eff}} = \sqrt{\frac{S^3_{\text{corr}}}{6PR_{\text{eff}}}}. \tag{2.10}$$

Using Equation 2.10, we assess the impact of different formulations for R_{eff} on the Young's modulus calculated with the harmonic stiffness measurement. In Figure 2.5, we present the impact of the proposed corrections on the Young's modulus calculated using Equation 2.10 for a tip with a nominal radius of 5 μm. Using the continuous stiffness measurement to estimate the Young's modulus, results in a calculation with enhanced noise and should only be used as a reference. We observe in Figure 2.5 that defining R_{eff} as a function of load (e.g., Figure 2.3b) results in the convergence of E_{eff} towards expected values at smaller depths than defining R_{eff} as a constant value (e.g., Figure 2.3a).

Another important benchmark is a consistent effective tip shape measured in multiple reference materials over the elastic depth. Conceptual models of spherical indentation indicate that a plot of the contact depth, h_c, versus the contact radius, a, determined from the harmonic stiffness should be representative of the effective indenter shape (Merle et al., 2012; Pathak and Kalidindi, 2015b). In the case of

elastic spherical indentation, the effective tip shape is expected to be the same during loading and unloading for a given tip regardless of which reference material is used. We calculate the contact depth, h_c, using (Sneddon, 1965a; Oliver and Pharr, 1992b)

$$h_c = h_{rep} - \xi \frac{P}{S}, \tag{2.11}$$

where ξ is a geometric factor equal to 0.75 for spherical indents (Fischer-Cripps, 2011; Oliver and Pharr, 1992b). Implementing corrections due to the impact of the system stiffness, we calculate the corrected contact depth, h_c^*, as

$$h_c^* = h_{rep} - h_{err} - \xi \frac{P}{S_{corr}}. \tag{2.12}$$

We calculate the contact radius using both reported and corrected values, (Oliver and Pharr, 1992b)

$$a = \frac{S_{rep}}{2E_{eff}} \tag{2.13}$$

and

$$a_{corr} = \frac{S_{corr}}{2E_{eff}}. \tag{2.14}$$

We compare the effective tip shape with the shape predicted for a perfect sphere, a_{pred}, according to the geometrical relationship

$$a_{pred} = \sqrt{2R_{eff}h_c - h_c^2}. \tag{2.15}$$

Note that for perfectly elastic indents $h_c = h_e/2$ (Basu et al., 2006).

Figure 2.6 summarises the impact of the proposed calibration routines and data corrections on the effective tip shape. We observe in Figure 2.6a that the uncorrected data display significant discrepancies between the apparent tip shape and the ideal predicted tip shape calculated using the constant radii summarised in Figure 2.2. We also observe that, the apparent tip shape varies depending on the reference material, with the sapphire data set exhibiting the most significant discrepancies. Figure 2.6b indicates that our proposed strategies for data correction result in good agreement between the apparent tip shape and the tip shape calculated with the best-fit, constant radius. These corrections also result in a consistent apparent tip shape among different reference materials.

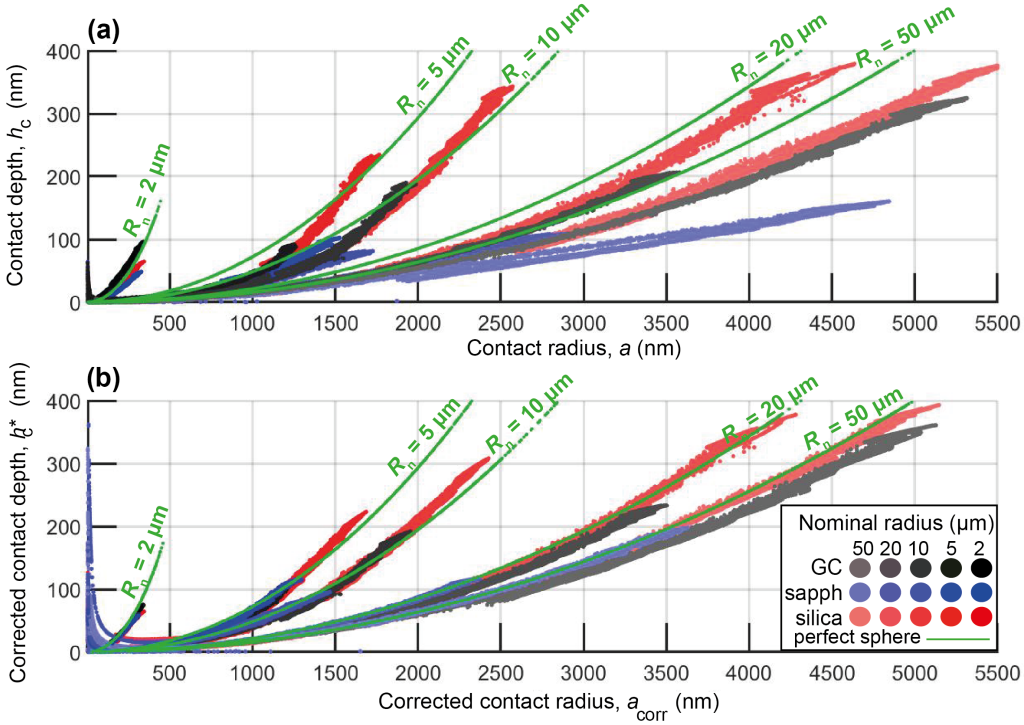


Figure 2.6: a) The effective tip shape calculated with data as reported and b) the effective tip shape calculated with corrected displacement and harmonic stiffness data for spherical tips with varying radii. The green curve represents the tip shape for a perfect sphere, with the contact radius calculated using Equation 2.15 with values for R from Figure 2.2.

2.3.3 Characterization of materials with unknown Young's moduli

In section 2.3.2 we determined that two key parameters (the effective radius and machine stiffness) are needed for each combination of machine and indenter tip (Figure 2.6) to calculate the Young's modulus and stress-strain curves using load-displacement data (Figure A.3, Supplementary Materials). We implement these calibrations to extract stress-strain curves in samples of W, Ti, and olivine described in Section 2.2 (see Table 2.1).

2.3.3.1 Zero-point correction

A key step in analysing reported load-displacement data is the identification of the point of zero-displacement and zero-load, i.e., the zero-point correction. The impact of the zero-point correction on the estimations of R_{eff} and stress-strain curves has been a focus in previous analysies of spherical nanoindentation data (Kalidindi and Pathak, 2008a; Pathak and Kalidindi, 2015b; Moseson et al., 2008). In our approach for calibrating spherical tips using reference materials of known elastic moduli, the last term in Equation 2.8 already accounts for errors in the point of initial contact. However, the methods discussed above do not provide a means for finding the effective point of zero contact in data acquired in materials with unknown elastic moduli.

Kalidindi and Pathak (2008a) proposed a method for determining the effective point of contact by using the relationship between the load, displacement, and harmonic stiffness measurements for the elastic portion of an indentation test,

$$S_{\text{rep}} = \frac{3P}{2h_{\text{e}}} = \frac{3(\widetilde{P} - P^*)}{2(\widetilde{h_{\text{e}}} - h^*)}, \tag{2.16}$$

where $\widetilde{h_{\text{e}}}$ and $\widetilde{P}$ represent the measured values of elastic displacement and load, respectively, and h^* and P^* represent the values of displacement and load at the actual point of contact, respectively. These values can be found by re-arranging Equation 2.16 to yield a linear relationship between $\widetilde{P} - \frac{2}{3}S\widetilde{h_{\text{e}}}$ and S, with the slope equal to $-\frac{2}{3}h^*$ and the vertical intercept equal to P^*. Thus, the corrected load-displacement data are the reported data minus the values for P^* and h^*. One major advantage of this approach is that no *a priori* knowledge of E_{eff} or R_{eff} is necessary. This approach is also suitable for anisotropic materials (Kalidindi and Pathak, 2008a; Pathak and Kalidindi, 2015b). However, this method also relies on accurate identification of the elastic loading segment for fitting by linear regression, which is often a subjective procedure since, in practice, the transition between elastic and plastic deformation is

not sharply defined (e.g., Figure 4 in Kalidindi and Pathak, 2008a). This difficulty in identifying the most appropriate segment of data for a linear fit introduces significant variations in the calculated stress and strain (Weaver et al., 2016).

In this section, we present an alternative formulation proposed by Breithaupt et al. (2017), which is adapted from Kalidindi and Pathak (2008a) for the zero-point correction of load-displacement data. We calculate the values for P^* and h^* by minimising the residual, r^*, between the data and predictions of perfect elasticity in the stress-strain curve. Thus, we define the residual, r, as (Breithaupt et al., 2017)

$$r = \sigma - E_{\text{eff}}\varepsilon, \tag{2.17}$$

where the indentation stress, σ, and strain, ε, are defined according to Kalidindi and Pathak (2008a) and Pathak and Kalidindi (2015b) as

$$\sigma = E_{\text{eff}}\varepsilon, \tag{2.18}$$

$$\sigma = \frac{P}{\pi a^2}, \tag{2.19}$$

$$\varepsilon = \frac{4h_{\text{e}}}{3\pi a}. \tag{2.20}$$

We can substitute these definitions for stress, strain, and contact radius in Equation 2.17 and rearrange to yield

$$r = \frac{4E_{\text{eff}}^2}{3\pi}\Big(\frac{3P - 2Sh_{\text{e}}}{S^2}\Big). \tag{2.21}$$

Recasting Equation 2.21 in terms of reported and corrected values for load and displacement (similar to Equation 2.16), and summing the absolute error yields the proportionality (Breithaupt et al., 2017)

$$r_{\text{total}} \propto \sum \left|\left| \frac{3(\widetilde{P} - P^*) - 2S(\widetilde{h_{\text{e}}} - h^*)}{S^2} \right|\right|. \tag{2.22}$$

The residual in Equation 2.22 describes the departure from elasticity. In practice, we find the values for h^* and P^* by minimising r_{total}. We subtract the values for h^* and P^* from the uncorrected reported values to yield the corrected data for the point of zero contact. The advantage of this approach is that a significantly larger portion of the data set is used than in the linear regression by Kalidindi and Pathak (2008a), and therefore the correction is less sensitive to accurate identification of the elastic segment.

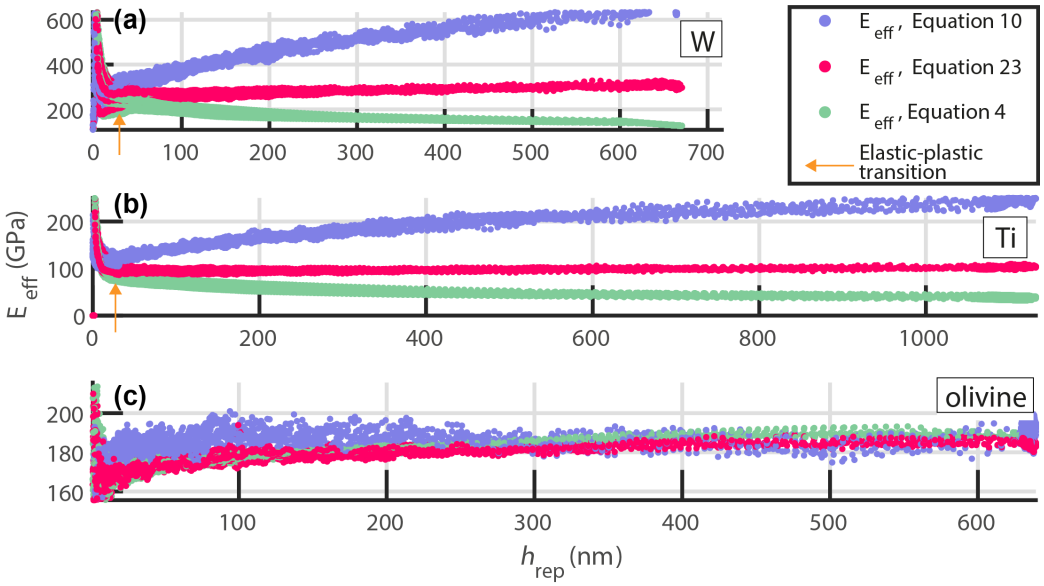


Figure 2.7: Measurements of Young's modulus for a) tungsten (average $E_{\text{eff}} = 306.7 \pm 14.2$ GPa), b) titanium (average $E_{\text{eff}} = 99.5 \pm 4.7$ GPa), and c) olivine (average $E_{\text{eff}} = 183.8 \pm 8.8$ GPa) using data collected with a tip with a nominal radius of 50 μm. The orange arrow indicates the approximate position of the elastic-plastic transition, which is absent in the fully elastic experiments on olivine.

2.3.3.2 Calculation of Young's moduli

After the reported load-displacement data ($\widetilde{P}$ and $\widetilde{h}$) are corrected for the effective point of contact by subtracting P^* and h^*, respectively, we can calculate the effective elastic modulus. In stiffer materials (e.g., olivine), with a clearly identifiable segment of elastic load-displacement, E_{eff} can be determined from Equation 2.4, which requires the elastic displacement and effective radius to be known. However, any error in R_{eff} or in determining the elastic segment will significantly impact estimations of the effective Young's modulus. Importantly, if plastic yield occurs, then the elastic displacement is not explicitly known and the sample curvature, R_{i}, becomes finite and modifies R_{eff} according to Equation 2.6. This influence of plastic yielding is not easily accounted for and leads to an erroneous depth dependence of E_{eff}.

We can also use Equation 2.10 to evaluate the Young's modulus over the elastic segment, as previously done for reference materials in Figure 2.5. However, this figure also demonstrates that the moduli estimated with this method are less reliable at shallow depths. Moreover, Equation 2.10 also relies on R_{eff} and is therefore subject to the same effects as the previous method if plastic yielding occurs.

Finally, we can calculate E_{eff} using data collected with a tip describing a perfect

sphere by combining Equations 2.14 and 2.15,

$$E_{\text{eff}} = \frac{\sqrt{\pi}}{2} \frac{S_{\text{corr}}}{\sqrt{2\pi R_{\text{eff}} h_{\text{c}} - \pi h_{\text{c}}^2}}. \tag{2.23}$$

We implement Equation 2.23 with corrected values for the harmonic stiffness measurement and the contact depth. As previously illustrated in Figure 2.6, these corrections result in load-displacement data that can be described with a constant R_{eff}. This approach is complementary to the one presented by Leitner et al. (2018), who modify the parameters in Equation 2.15 describing the geometry of the perfect tip for a given material (Leitner et al., 2018). The advantage of our approach is that it considers more closely the contact mechanics of the machine-tip-sample system. Furthermore, Equation 2.23 is applicable even after plastic yielding, and therefore the Young's modulus can be estimated for the entirety of the experiment, which is particularly advantageous for materials with a short or noisy elastic segment. Moreover, any issues related to tip calibrations or machine stiffness corrections will result in moduli that are not constant with indentation depth.

Figure 2.7 displays these three approaches to calculate Young's modulus for tungsten, titanium, and olivine using data collected with a tip with a nominal radius of $R_{\text{n}} = 50$ µm. As expected, the calculated moduli are comparable for elastic indentation (Figure 2.7 c), but diverge after plasticity initiates, at which point Equations 2.4 and 2.10 are no longer applicable. Moreover, Equation 2.23 implemented with corrected values for h_{c} and R_{eff} and parameters for a perfect sphere yields constant values for Young's modulus with depth that are in agreement with previously published values for the tested materials (e.g, Kumamoto et al., 2017; Pathak and Kalidindi, 2015b).

2.3.3.3 Calculation of stress-strain curves and the yield point

Figure 2.8 presents stress-strain curves calculated for tungsten, titanium, and olivine using the spherical tips in Table 2.1 and Equations 2.19 and 2.20 for stress and strain, respectively, as defined by Pathak and Kalidindi (2015b) and Kalidindi and Pathak (2008a). All materials display an indentation size effect, in which the yield stress increases with decreasing effective contact radius. Note that the polycrystalline materials display a wider spread of stress values than the olivine single crystal, due to plastic anisotropy (e.g., Britton et al., 2010; Weaver et al., 2016). Figures 2.8a and b display E_{eff} values corresponding to averages of $E_{\text{s}} = 400 \pm 9$ GPa in W, and $E_{\text{s}} = 108 \pm 8$ GPa in Ti, which is in line with published values for W and on the lower end of the spectrum for Ti (Pathak and Kalidindi, 2015b; Britton et al., 2010; Weaver

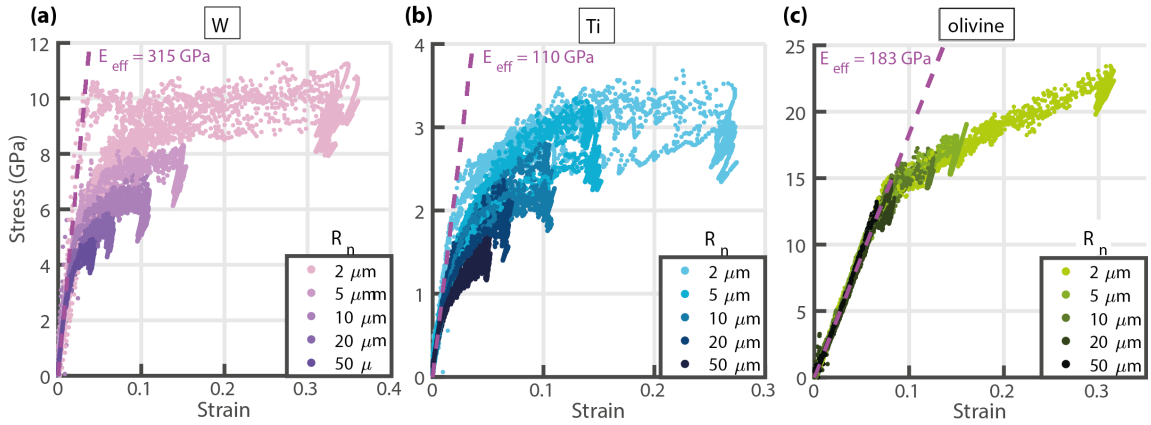


Figure 2.8: Summary of stress-strain curves in a) tungsten, b) titanium, and c) olivine collected with spherical tips of varying radii. The dashed lines have the slope equal to the average E_{eff} across all indents. The displayed values of E_{eff} correspond to $E_{\text{s}} = 400 \pm 9$ GPa in tungsten, $E_{\text{s}} = 108 \pm 8$ GPa in titanium, and $E_{\text{s}} = 205 \pm 9$ GPa in olivine. The corresponding load-displacement curves are presented in Supplementary Materials (Figure A.3).

et al., 2016). We calculate an indentation flow stress ranging between 4 and 10 GPa for W. In comparison, studies of indentation size-effects using sharp tips document a hardness of 4 GPa in W at the greatest contact depths (e.g., Javaid et al., 2018; Maier et al., 2015). We calculate an indentation flow stress ranging between 1 and 3.5 GPa for Ti, in agreement with published spherical nanoindentation results in single crystals (Weaver et al., 2016). We note the absence of pop-ins in the stress-strain curves, which have been previously documented using spherical nanoindentation in both W (Patel and Lee, 2020) and Ti single crystals (Weaver et al., 2016).

Furthermore, Figure 2.7 highlights the divergence of the different formulations for calculating the effective modulus marks the yield point of the material. This result has a similar basis to the method proposed by Hackett et al. (2019). This method has the significant advantage of determining the onset of yielding by exploiting the instantaneous differences in two independent computations of the elastic parameter S^3/P. This method does not require *a priori* knowledge of R_{eff} or E_{eff}. One computation exploits the definition of the stiffness obtained by differentiation (Rowland) of the load-displacement curve, such that (Hackett et al., 2019)

$$S_{\text{slope}} = \left(\frac{dP}{dh}\right)^3 P^{-1}. \tag{2.24}$$

The second computation uses the measured harmonic contact stiffness (Hackett et al., 2019)

$$S_{\text{CSM}} = \frac{S^3}{P}. \tag{2.25}$$

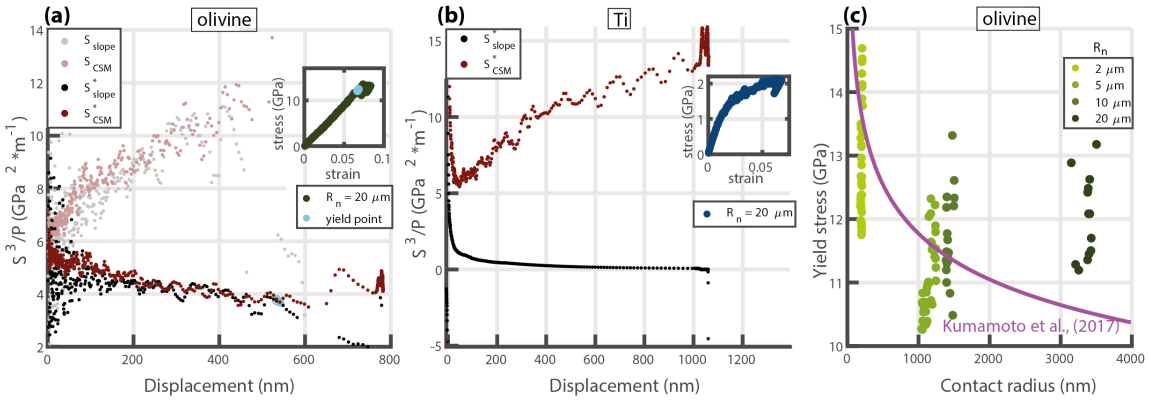


Figure 2.9: a) Example of S^3/P parameter calculations using Equations 2.24 and 2.25 proposed by Hackett et al. (2019) using both reported (light colours) and corrected (dark colours) values. The corresponding stress-strain curve is presented in the insert. A filled-blue circle marks the yield point on the corrected data in a) and the insert. The data were collected with a tip with $R_n = 20$ µm. A smoothing window with an interval of 5 is applied to S_{slope}. We present calculations for a) olivine and b) titanium. c) Yield stress corresponding to the divergence point in a) for olivine across tips with varying radii. The power law fit with an exponent of -0.09 has been determined by Kumamoto et al. (2017) using spherical nanoidentation on similar samples, but deploying a different strategy for defining the yield stress.

In Figure 2.9a, we compute the elastic parameter S^3/P for an indent in olivine collected using a tip with a nominal radius of 20 µm, using both reported values for S and h as well as corrected values according to Equations 2.7 and 2.9. The light coloured data represents reported values, which are significantly different to the corrected data displayed in darker colours. The blue filled symbols mark the divergence point in the two independent calculations of the S^3/P parameter and the corresponding position of the this point on the stress-strain curve for the same indent (insert in Figure 2.9a). Note that in Figure 2.9a the point of divergence is shifted by about 150 nm after applying a machine stiffness correction. Figure 2.9a highlights a key caveat of this method, which is high sensitivity to the machine stiffness corrections and the zero-point correction. Thus, while Hackett et al. (2019) propose a convenient method for determining the yield point in ceramics and glasses, the sensitivity of the S^3/P parameter to the stiffness of the machine-tip-sample assembly could introduce significant errors and inconsistencies.

We are unable to distinguish an elastic segment implementing the method proposed by Hackett et al. (2019) in titanium and tungsten, as intuitively displayed by the diverging calculations for E_{eff} at small depths in Figure 2.7. For example, Figure 2.9b displays the S^3/P parameter computed for Ti using data collected with a tip with

a nominal radius of 20 μm, and corrected S and h values. The two calculations of the S^3/P parameter diverge at very small indentation depths (< 50 nm) consistent with the onset of plasticity at small displacements. Thus, this method is suitable only for materials displaying an elastic segment of minimum ~ 100 nm (Hackett et al., 2019). Figure 2.9 emphasizes that in ductile materials the zero-point correction and determination of the Young's modulus following the methods proposed by Kalidindi and Pathak (2008a) and Pathak and Kalidindi (2015b) rely on data collected at small depths, which is heavily impacted by the noise of the contact mechanics.

To date, previous studies have deployed different conventions for determining the yield stress in spherical nanoindentation stress-strain curves (e.g., Herbert et al., 2001). In this study, we picked the diverge point exemplified in Figure 2.9a for all indents in olivine, and summarised the corresponding yield values in Figure 2.9c as a function of their contact radii. Kumamoto et al. (2017) used spherical nanoindentation and quantified a size effect in olivine in which the yield stress is proportional to the contact radius according to a power law with an exponent of -0.09. Figure 2.9c displays a size effect with some deviations from this this power law. The discrepancy is due to the difference in the definition for the yield point, and possibly due to material anisotropy. Kumamoto et al. (2017) present stress-strain curves in annealed single crystals with a strain excursion (pop-in) associated with dislocation nucleation and glide after a longer segment of elastic loading compared to deformed samples. This phenomena documented in materials with scarce dislocation sources is attributed to the requirement of a larger deformation volume for activating dislocation sources (e.g., Shim et al., 2008; Morris et al., 2011a; Bei et al., 2016). The method outlined by Hackett et al. (2019) deploys a definition of the yield stress as the end of the elastic loading segment. However, in the indents displaying a pop-in, the point of divergence in Figure 2.9a corresponds to the increased stresses required for initiation of plasticity. Kumamoto et al. (2017) define yield stress as the intersection of the projected slope of the stress hardening after pop-in on the elastic loading, in line with other studies using spherical nanoindentation (e.g., Pathak and Kalidindi, 2015b). Therefore, the discrepancy at larger contact radii in Figure 2.9c is consistent with the differences in the two conventions for the yield point. Other studies implement a definition of the yield stress as the stress at a strain chosen by convention for a meaningful comparison with data obtained in uniaxial macroscale tests (e.g., 0.2% in Patel and Kalidindi, 2016; Iskakov and Kalidindi, 2022; Courtright et al., 2021; Khosravani et al., 2018; Weaver et al., 2016). The calculated yield stress is a key outcome of spherical indentation and

the choice of convention can influence the quantification of size effects in materials (e.g., Herbert et al., 2001).

2.4 Conclusion

We investigated in detail and further improved published methodologies for independently determining two key instrument parameters in spherical nanoindentation: system stiffness and effective radius of the indenter tip. To this end, we collect elastic data in reference materials with known moduli and highlight complexities in determining the effective radius using published protocols (e.g., Li et al., 2013). We suggest a routine underpinned by the formulation of the effective radius as a function of load to overcome experimental errors. We benchmark our methodology against key markers in spherical nanoindentation. We implement the tip calibrations on data collected on materials with unknown Young's modulus and varying ductility to calculate stress-strain curves. A summary diagram of this routine can be found in Supplementary Materials (Figure A.2). These curves reveal a spherical indentation size effect in which the stress increases with indentation depth and with decreasing contact radius. We also test the influence of instrument parameters on published methodologies for determining the yield stress in materials with a significant elastic loading segment (e.g., Hackett et al., 2019) and highlight the importance of consistency when establishing a convention for determining the yield stress.

Chapter 3

The role of grain boundaries in low-temperature plasticity of olivine revealed by nanoindentation

"Put simply, the boundary regions are in a more advanced state of hardening."

A.P.Sutton and R.W.Balluffi (1995)

A similar version of this chapter has been prepared for publication in the AGU *Journal of Geophysical Research: Solid Earth*, with the following author list:

Diana Avadanii[1], Lars Hansen[2], Katharina Marquardt[3], Markus Ohl[4], David Wallis[5], and Angus Wilkinson[6]

[1] Department of Earth Sciences, University of Oxford
[2] Department of Earth and Environmental Sciences, University of Minnesota
[3] Department of Materials, Imperial College London
[4] Department of Earth Sciences, Utrecht University
[5] Department of Earth Sciences, University of Cambridge
[6] Department of Materials, University of Oxford

For this study, I collected all the nanoindentation data, analysed and interpreted the nanoindentation data, wrote the code for the nanoindentation data analysis, collected, analysed, and interpreted all the EBSD data, assisted in person during foil preparation and data collection via electron microscopy imagining, and wrote the first draft of the manuscript.

Abstract

Olivine is a key geological material influencing large-scale, long-term planetary deformation processes on rocky planets. Studies on the deformation of olivine at low temperatures and high stresses have emphasized the importance of a grain-size effect impacting olivine yield stress. Laboratory studies indicate that aggregates with smaller grains are stronger than aggregates with coarser grains. However, the interactions between intracrystalline defects and grain boundaries leading to this effect remain unresolved in olivine. In this study, to directly observe and quantify the mechanical properties of olivine grain boundaries, we conduct nanoindentation tests on well characterized bicrystals. We perform room-temperature spherical and Berkovich nanoindentation tests on low- and high- angle grain boundaries. We observe that in the high-angle grain boundary sample, the interface acts as a site of microplasticity and as a barrier to incoming dislocations. The low-angle grain boundary does not interact with other crystalline defects in a measurable manner. We suggest that the distribution of grain boundary types in olivine-rich rocks plays a key role in generating local differences during deformation.

3.1 Introduction

The strength of Earths lithosphere controls a variety of geodynamic phenomena. Examples include the dip of subducting slabs (Billen and Hirth, 2007), the flexural response of oceanic lithosphere to tectonic forces (Watts and Zhong, 2000; Hunter and Watts, 2016), and the geodetically measurable surface strain rates in continental collision zones (England and Molnar, 2015). Olivine is the main constituent of Earth's upper mantle, and consequently, the deformation mechanisms operating in olivine at different geological stress and temperature conditions dominate the strength of the oceanic lithospheric (Watts and Zhong, 2000; Hunter and Watts, 2016; Pleus et al., 2020; Korenaga, 2020). In the portions of oceanic lithosphere supporting the most stress, the key deformation mechanism controlling long-term behaviour is low-temperature plasticity (Hansen and Kohlstedt, 2015; Mei et al., 2010). In this depth range, diffusion and recovery are relatively slow, and the rate of deformation is limited by the glide of dislocations through the crystal lattice (Hansen and Kohlstedt, 2015; Frost and Ashby, 1982, Chapter 2).

Laboratory investigations of the rheology of olivine have generated several different calibrations of flow laws for low-temperature plasticity, which further disagree with geophysical measurements when extrapolated to geological conditions (e.g., Mei et al., 2010; Hunter and Watts, 2016; Watts and Zhong, 2000). Some of the disagreements among laboratory studies have been reconciled by a size effect (Kumamoto et al., 2017; Hansen et al., 2019; Koizumi et al., 2020). Kumamoto et al. (2017) predicts that samples with grain sizes typical of the upper mantle (0.1–1 cm) are weaker than the finer grained (1–10 μm) samples tested in laboratory studies. The mechanical data of Hansen et al. (2019) highlight that the yield strength of olivine decreases with increasing grain size during initial loading, but the steady state flow stress is grain-size independent after strain hardening. The grain-size sensitivity of the yield stress in the olivine aggregates on the first cycle of deformation demonstrates that the macroscopic yield stress is fundamentally controlled by the density of the grain boundaries in the material (Hansen et al., 2019). Further studies documenting the deformation structures in the samples of Hansen et al. (2019), confirm that long-range interactions of dislocations represent the underlying cause for the observations of strain hardening (Wallis et al., 2020) but the specific cause of the size effect on yield strength remains poorly constrained Hansen et al. (2019).

The decrease in yield strength with an increase in grain size is a well documented phenomena generally referred to as the Hall-Petch effect. Models of this effect rely on

the mechanisms of slip transfer between grains and dislocation generation at grain boundaries (for review, see Cordero et al., 2016). In olivine, previous laboratory investigations of low-temperature plasticity involved experiments with either single-crystal (e.g., Demouchy et al., 2013; Gaboriaud et al., 1981; Goetze and Evans, 1979; Idrissi et al., 2016; Hansen et al., 2019) or polycrystalline samples (e.g., Druiventak et al., 2011; Hansen et al., 2019; Katayama and Karato, 2008; Mei et al., 2010; Raterron et al., 2004) at thermo-mechanical conditions similar to the upper mantle (e.g., Raterron et al., 2004; Mei et al., 2010). In these well established experiments it is challenging to unpick the microphysics associated with interactions between dislocations and grain boundaries. While previous nanoindentation tests (Kumamoto et al., 2017) and transmission electron microscopy investigations of deformed olivine (Thieme et al., 2018; Wallis et al., 2020) indicate that grain boundaries might act as dislocation sources, we lack direct probing of this phenomena. For example, Kumamoto et al. (2017) highlights differences in mechanical data representative of small volumes of annealed single crystals and predeformed polycrystalline samples. The observations presented by Kumamoto et al. (2017) could be interpreted as either grain boundaries or the high initial dislocation density promoting further dislocation generation. Furthermore, the impact of different grain boundaries on the mechanisms of slip transfer in olivine remains unresolved in both low-temperature plasticity and deformation at high temperatures (e.g., Ferreira et al., 2021; Bollinger et al., 2019).

This study aims to clarify the role of grain boundaries in low-temperature plasticity of olivine, and contributes towards explaining the grain-size effect and hardening observed by Hansen et al. (2019). In this study, we conduct nanoindentation experiments and high-resolution microscopy on high-purity forsterite (Mg_2SiO_4) bicrystals as an analog to iron-bearing olivine. Our experiments and microstructural analyses aim to quantify the role of low- and high-angle grain boundaries in slip transmission and dislocation generation. The only free variable in our experimental set-up is the vertical grain boundary between two annealed crystals, which are symmetric across the interface.

3.2 Materials and Methods

3.2.1 Samples

We use pure forsterite bicrystal samples to investigate a low-angle grain boundary (LAGB, 13°, [100]/(016)) (e.g., Gardés et al., 2021; Adjaoud et al., 2012) and a high-angle grain boundary (HAGB, 60°, [100]/(011)) (e.g., Fig 7 of Adjaoud et al.,

2012). The bicrystals were prepared using the wafer-bonding technique (Heinemann et al., 2001, 2005; Hartmann et al., 2010). This technique generates synthetic grain boundaries free of induced deformation and chemical contamination. The grain-boundary misorientation angle is precisely controlled to generate symmetric, low-energy, and near-coincidence grain boundaries (Hartmann et al., 2010; Heinemann et al., 2001, 2005; Marquardt et al., 2015; Adjaoud et al., 2012). Samples similar to the HAGB sample used in this study have previously been characterized in detail, revealing that the grain-boundary width is less than 1 nm and the plane is faceted on the nanometre-scale (see Fig 9, Marquardt and Faul, 2018). Further structural descriptions can be found in Adjaoud et al. (2012). Schematic illustrations of the sample geometries are presented in Figure 3.1. We use one bicrystal sample for the investigation of the low-angle grain boundary (LAGB) and three similar samples for the investigation of the high-angle grain boundary (HAGB) due to the limited grain-boundary length suitable for testing.

3.2.2 Micromechanical testing

We used nanoindentation to examine the mechanical properties of our samples at high spatial resolution (e.g., Vachhani et al., 2016b). We placed arrays of equally spaced indents into the bicrystals so that the indents lie at varying distances from the grain boundary (Table 3.1). We categorize indents into three main groups: 1) indents within the single crystals, 2) indents near the grain boundary, such that the grain boundary intersects the residual impression of the indent, and 3) indents directly on top of the boundary such that the residual impression is centered on the boundary. Nanoindentation tests were conducted on a Nano Indenter® G200, using continuous stiffness measurement on the loading segment of the experiment (Oliver and Pharr, 1992a). We employed both Berkovich and spherical indenter tips and conducted tests to a variety of maximum indentation depths. Table 3.1 provides details of each experiment. The experiments were performed at a target of indentation strain rate (loading rate divided by the load) of 0.05 s^{-1}. Further details regarding placement of indents with respect to the grain boundary can be found in Supplementary Materials (Figures B.4, B.3, B.2, B.1).

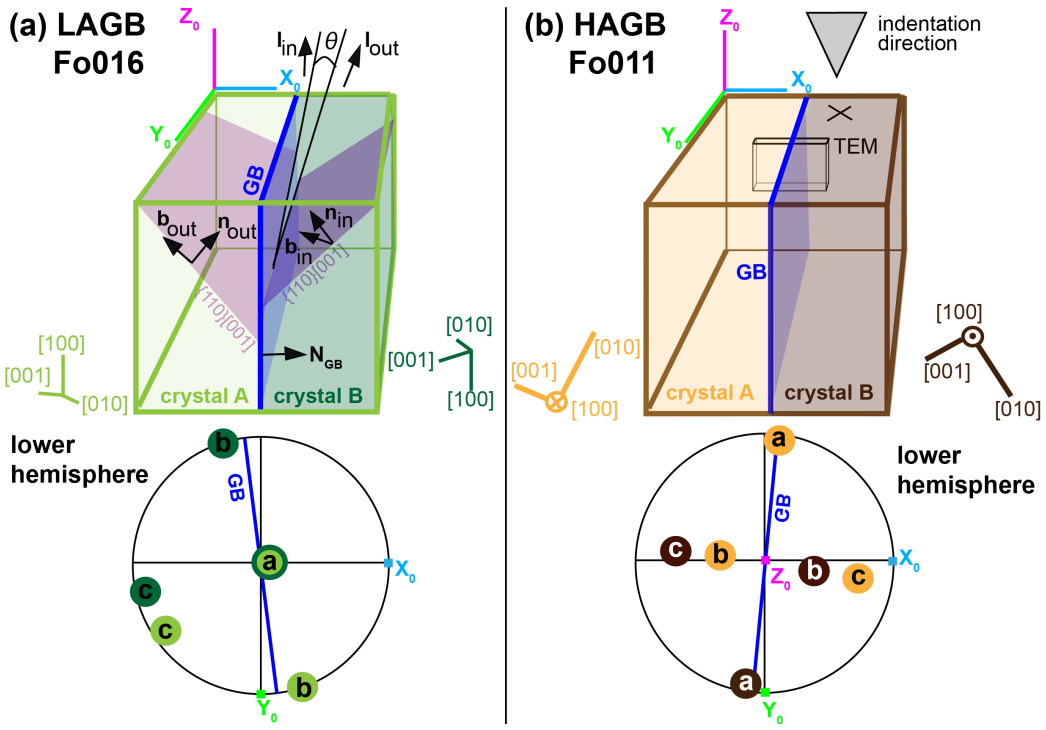


Figure 3.1: a) Schematic depicting the grain-boundary geometry and lower-hemisphere projection of the LAGB bicrystal. Examples are depicted of a slip system with an incoming slip direction b_{in} towards the grain boundary (GB) and an outgoing slip system with the direction vector b_{out}. b) Schematic depicting the grain-boundary geometry and lower-hemisphere projection of the HAGB bicrystal. The indented surface is perpendicular to Z_0. Note that the indentation direction is consistent between crystals A and B in both samples.

Table 3.1: Summary of experiments on bicrystal samples with a low-angle grain boundary (LAGB) or high-angle grain boundary (HAGB). Experiments were conducted using either sharp or spherical tips, the latter of which had variable nominal radii, R_{n}. The effective radius at the end of elastic loading is indicated for each tip as R_{eff}. The lower case letter at the end of the array number in the HAGB bicrystal corresponds to different samples. The number of tests is expressed as the number of columns times the number of rows of indents across the grain boundary.

Tip	LAGB Fo016					HAGB Fo011					
	Array	Tests	Spacing (μm)	Max depth (nm)	Microscopy HREBSD	Array	Tests	Spacing (μm)	Max depth (nm)	Microscopy HREBSD	TEM
Berkovich	array1	6x4	40	1000		array4a	3x8	10	500		
	array2	1x4	40	1000		array11f	3x10	12	700	Ind11,12	Ind11
	array3	10x6	15	700	Ind25	array12f	3x10	13	700	Ind1, 2, 5, 6	
	array8	4x7	8	350	Ind6, 11, 14						
$R_{\text{eff}} \sim 7$μm	array1	6x6	30	600							
$R_{\text{n}} = 5$μm	array4	3x8	15	600	Ind11,14	array2a	3x10	15	700	Ind11, 14	
$R_{\text{eff}} \sim 6$μm						array3a	3x5	15	500	Ind1	
$R_{\text{n}} = 5$μm	array10	3x8	13	600	Ind16	array12e	3x8	13	600	Ind11, 16, 17, 20, 21	Ind11
$R_{\text{eff}} \sim 4$μm	array11	3x8	13	600		array13e	3x8	13	600		Ind14
						array14e	3x8	13	600		Ind4

3.2.3 Data Analysis

3.2.3.1 Spherical nanoindentation

In this study, we used three different spherical tips with nominal radii, R_{n}, of 5 and 10 μm. We analyze data from spherical indents using a calibration routine adapted after Li et al. (2013) using three reference materials with different Young's moduli (fused silica, glassy carbon, sapphire) and outlined in detail in Chapter 2. This routine generates a calibrated function for the effective radius, R_{eff}, and the machine stiffness, S_{mach}, as a function of load for each tip (Table 3.1).

We transform the load and displacement into stress and strain following the method proposed by Pathak and Kalidindi (2015a); Kalidindi and Pathak (2008b). We calculate the indentation stress, σ, and strain, ϵ, as

$$\sigma = \frac{P}{\pi a^2}, \tag{3.1}$$

$$\epsilon = \frac{4h^*}{3\pi a}, \tag{3.2}$$

where P is the reported load corrected for the point of zero load, a is the contact radius, and h^* is the reported displacement corrected for machine stiffness and the point of zero displacement. We calculate the contact radius as $a = \frac{S^*}{2E_{\mathrm{eff}}}$, where S^* is the corrected contact stiffness, and E_{eff} is the effective Young's modulus. We correct the reported displacement, h_{rep}, according to

$$h^* = h_{\mathrm{rep}} - \frac{P}{S_{\mathrm{mach}}} + \frac{P}{S_{\mathrm{default}}} - h_0, \tag{3.3}$$

where S_{default} is the default machine stiffness during data collection ($S_{\mathrm{default}} = 3.7 \times 10^7$ N/m) and S_{mach} is the stiffness for each indenter-tip pair determined in a manner similar to Li et al. (2013), following Section 2.3.2. The term h_0 represents the error in the default determination of the point of zero displacement and zero load. Adapting the formulation proposed by Kalidindi and Pathak (2008b), we determine h_0 by minimizing the residual function (Breithaupt et al., 2017)

$$r = \sum \left|\left| \frac{3(P_{\mathrm{rep}} - P_0) - 2S(h_{\mathrm{rep}} - h_0)}{S^2} \right|\right|. \tag{3.4}$$

We calculate E_{eff} for each indent by using the calibrated effective radius, R_{eff}, and

fitting the elastic loading segment with the Hertzian relationship

$$h_{\mathrm{e}} = P^{2/3}\left(\frac{4}{3}\sqrt{R_{\mathrm{eff}}}E_{\mathrm{eff}}\right)^{-2/3}, \tag{3.5}$$

$$\frac{1}{E_{\mathrm{eff}}} = \frac{1-\upsilon_{\mathrm{s}}}{E_{\mathrm{s}}} + \frac{1-\upsilon_{\mathrm{i}}}{E_{\mathrm{i}}}, \tag{3.6}$$

where E_{eff} is the effective Young's modulus, $\upsilon_{\mathrm{s}} = 0.24$ is the Poisson's ratio of the sample, $\upsilon_{\mathrm{i}} = 0.07$ is the Poisson's ratio of the diamond tip, E_{s} is the unknown Young's modulus of the sample, and $E_{\mathrm{i}} = 1141$ GPa is the Young's modulus of the diamond tip.

In most of our experiments, the transition between elastic and plastic deformation is marked by a burst of displacement in the load-displacement data and of strain in the stress-strain curves, termed a pop-in. Using Hertzian mechanics described in Equation 3.6, the load at pop-in, $P_{\text{pop-in}}$, and the corresponding effective tip radius at the pop-in, $R_{\text{eff-pop-in}}$, we calculate the maximum shear stress immediately beneath the surface, assuming an elastically isotropic solid, (Morris et al., 2011b; Johnson, 1970)

$$\tau_{\max} = 0.31\left(\frac{6P_{\text{pop-in}}E_{\mathrm{eff}}^2}{\pi^3 R_{\text{eff-pop-in}}^2}\right)^{1/3}. \tag{3.7}$$

In spherical nanoindentation, the stress field under the indent is nonuniform. The stress at any one point also resolves differently on the available slip systems. We approximate our tests as an uniaxial test to calculate the Schmid factor, s, describing the ratio of the *uniform* applied stress and the resolved shear stress on a plane (Schmid and Boas, 1950).

3.2.3.2 Berkovich nanoindentation

Berkovich nanoindenter tips are three-sided pyramids that are self similar, which results in constant effective indentation strain of 8% regardless of the indentation depth (Chapter 3, Fischer-Cripps and Nicholson, 2004). For these tests, the effective Young's modulus is calculated as (Oliver and Pharr, 1992a)

$$E_{\mathrm{eff}} = \frac{\sqrt{\pi}}{2}\frac{S}{\sqrt{A}}, \tag{3.8}$$

where S is the measured contact stiffness and A is the contact area. For a Berkovich indenter, the contact area is defined by

$$A(h_{\mathrm{c}}) = 24.5h_{\mathrm{c}}^2 + C_1 h_{\mathrm{c}}^1 + C_2 h_{\mathrm{c}}^{1/2} + ... + C_8 h_{\mathrm{c}}^{1/28}, \tag{3.9}$$

where the contact depth, h_c, is defined as

$$h_c = 0.72\frac{P}{S}. \tag{3.10}$$

The constants C_1 through C_8 are determined by calibration with an isotropic material of known elastic moduli, in our case fused silica (Oliver and Pharr, 1992a). Finally, the hardness, H is given by

$$H = \frac{P}{A}. \tag{3.11}$$

3.2.4 Microstructural characterization

3.2.4.1 HR-EBSD

We investigated the residual impressions of the nanoindentation tests using high-angular resolution electron backscatter diffraction (HR-EBSD). For this purpose, we collected EBSD patterns on an Oxford Instruments NordlysNano EBSD detector and stored them for subsequent cross-correlation analysis. We mapped regions including indents placed in the vicinity of the grain boundary using step sizes of 0.05–0.15 μm. We calculated small distortions of diffraction patterns by cross correlating regions of interest (ROIs) within a diffraction pattern with the same ROIs in a reference diffraction pattern (Britton and Wilkinson, 2011, 2012; Wilkinson, 2006; Wilkinson et al., 2006; Wallis et al., 2016). Similar to Wallis et al. (2016), we used 100 overlapping ROIs of 256x256 pixels within each diffraction pattern of 1344 x 1024 pixels. We selected one reference point in each crystal, at a distance of at least 5 μm from the margin of the imprint left by the indents. Small shifts between the ROIs in the patterns are used to quantify the lattice distortion, which is comprised of the elastic strain and the lattice curvature due to geometrically necessary dislocations (GNDs). In plane stress tensor components are calculated assuming linear elasticity from measured strains. These stresses are calculated relative to the stress state at the selected reference point in the undeformed crystal (for details, see Wallis et al., 2019). We assume the stresses acting normal to the specimen surface are fully relaxed. GNDs densities are calculated for olivine via the procedure established by Wallis et al. (2016, 2019) implementing Nye-Kröner analysis Nye (1953); Kröner et al. (1981). The basis for the analysis of the GND content relies on the assumption that the displacement field (and hence, sample surface) is continuous, such that the integration of the displacement around a closed loop is zero Wilkinson and Randman (2010). Equivalently, the curl of the displacement gradient across the surface is assumed to be zero Wilkinson and Randman (2010). In practice, any interruption of the continuity of the sample surface (i.e., cracks) violates this assumption.

3.2.4.2 Transmission electron microscopy

To investigate the interaction between the dislocations and the grain boundary beneath spherical and Berkovich indents, we imaged thin foils using transmission electron microscopy (TEM). We prepared the TEM foils perpendicular to the high-angle grain boundary as depicted in Figure 3.1b, using a FEI Helios® Nanolab G3 Dualbeam system at the Utrecht University microscopy center (e.g., Figure 3, Liu et al., 2016). We coated the samples with a 9 nm of Pt/Pd and then used a standardized procedure to mill and lift out the TEM foil (e.g., Ohl et al., 2020). We imaged two samples in the HAGB bicrystal (spherical indents 11 in array12e and 14 in array13e, Table 3.1) using an FEI Talos® F200X with an acquisition acceleration voltage of 200 kV and a beam current of 5–10 nA, also at the Utrecht University microscopy center (e.g., Ohl et al., 2020). We additionally imaged two samples in the HAGB bicrystal (Berkovich indent 11, array11f, and spherical indent 4, array14e, Table 3.1) using a JEOL® 2100F microscope at Imperial College London. The microscope was operated with an acquisition voltage of 200kV, and an emission current of 120 μA.

3.2.5 Analysis of slip transfer

For indents in the vicinity of the GB, we can estimate the geometric constraint on transmission of slip from one grain to another. We use average crystal orientations from the EBSD data and knowledge about the grain-boundary geometry to calculate the geometrical relationships among different systems on each side of the grain boundary (for a review, see Bayerschen et al., 2016; Javaid et al., 2021), as depicted in Figure 3.1a. We use the formulation proposed by Luster and Morris (1995) to calculate a geometrical factor, m',

$$m' = (\mathbf{n}_{\text{in}} \cdot \mathbf{n}_{\text{out}})(\mathbf{b}_{\text{in}} \cdot \mathbf{b}_{\text{out}}), \tag{3.12}$$

where $\mathbf{n}_{\text{x}}$ are unit vectors normal to the slip plane, $\mathbf{b}_{\text{x}}$ are unit vectors along the slip direction, and the subscripts denote incoming and outgoing slip systems similar to Figure 3.1a. We note that, although slip systems in either crystal are denoted as incoming or outgoing, the actual direction of dislocation motion is irrelevant in these calculations. This factor ranges from 0 for the GB acting as a complete barrier, to 1 for the GB being transparent to dislocation motion (Javaid et al., 2021). However, this formulation only depends on the misorientation between crystals and does not depend on the orientation of the grain-boundary plane. In our experiments, we know the trace and the inclination of the grain boundary in each bicrystal, which allows

us to calculate a geometrical GB transmissibility factor, M, proposed by Shen et al. (1986) to account for the GB inclination

$$M = (\mathbf{l}_{\text{in}} \cdot \mathbf{l}_{\text{out}})(\mathbf{b}_{\text{in}} \cdot \mathbf{b}_{\text{out}}), \tag{3.13}$$

$$\mathbf{l} = \mathbf{n} \times \mathbf{N}_{\text{GB}}, \tag{3.14}$$

where $\mathbf{l}$ is a unit vector along the intersection between the slip plane and the grain boundary plane, and $\mathbf{N}_{\text{GB}}$ is the normal to the grain boundary plane. In the samples described in Figure 3.1, $\mathbf{N}_{\text{GB}}$ is [016] for the LAGB sample, and [011] for the HAGB sample. Due to the high symmetry of the grain-boundary configuration, $\mathbf{N}_{\text{GB}}$ is the same for both crystals in each bicrystal (Hartmann et al., 2010; Marquardt and Faul, 2018; Adjaoud et al., 2012). In Equation 3.14, slip transfer is favoured for the combination of slip systems that minimize the angle between $\mathbf{l}_{\text{in}}$ and $\mathbf{l}_{\text{out}}$, and the angle between $\mathbf{b}_{\text{in}}$ and $\mathbf{b}_{\text{out}}$ in Figure 3.1 (Bayerschen et al., 2016; Javaid et al., 2021). These factors quantify the geometrical misalignment of the incoming and outgoing slip systems, and additional criteria (e.g., minimised residual Burgers vector in the GB plane) have to be satisfied in order to predict slip transmission across a grain boundary Bayerschen et al. (2016).

3.3 Results

3.3.1 Mechanical testing

We tested the mechanical properties of the forsterite bicrystals using spherical indenters. Figure 3.2 presents examples of stress-strain curves derived from tests on the LAGB and HAGB samples with varying position relative to the grain boundary. A key feature of these curves is the prevalence of pop-ins, which are evident as departures from the elastic modulus by strains of a few percent at near-constant stress followed by decreases in stress and strain along gradients similar to the elastic modulus before the onset of further plastic flow. In the LAGB sample (Figure 3.2a), almost all stress-strain curves exhibit pop-ins. However, indents placed on top of the boundary (i.e., those where the residual indent overlaps the trace of the grain boundary) display pop-ins at lower stresses compared to those that do not intersect the grain boundary. In the HAGB sample (Figure 3.2b), the indents placed on top of the grain boundary (Figure B.3) have the pop-in suppressed or occurring at significantly lower stresses compared to indents further away from the GB, for which almost all indents have pop-ins.

Another key feature of the stress-strain curves is the magnitude of stress reached prior to plastic deformation. Figure 3.2b highlights the conventions that we use in

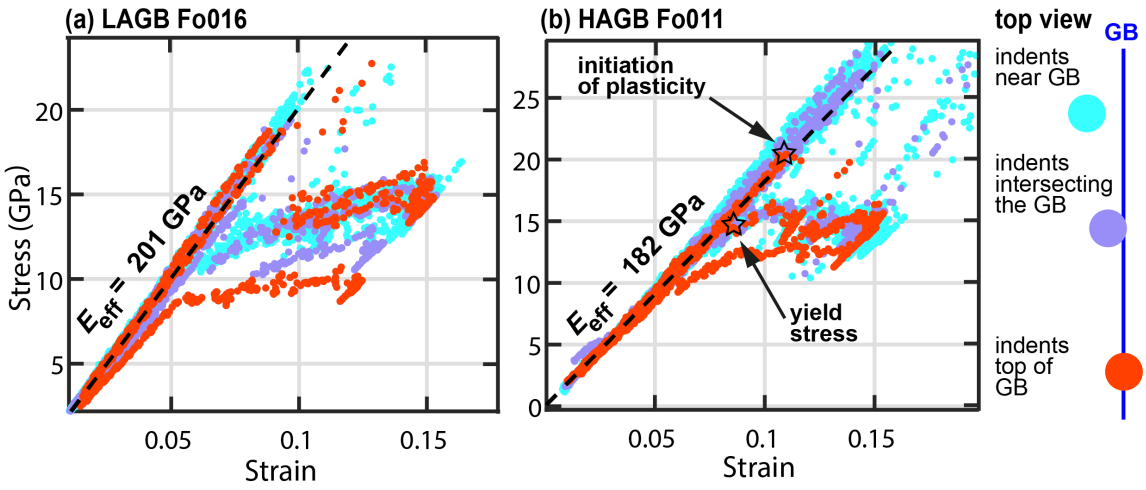


Figure 3.2: Selected results from spherical indentation using the 4 and 6 μm tips in Table 3.1 in the a) LAGB sample and b) HAGB sample. The diagram on the right depicts the three categories of indents: indents with a residual mark centered on the GB, indents where the GB intersects the residual mark but is offset from its centre, and indents in a single crystal near the grain boundary. The stars mark examples of points identified as the initiation of plasticity and therefore the yield stress. Further details of the location of indents can be found in Figures B.1, B.3.

describing the initiation of plasticity and the yield stress. We refer to the initiation of plasticity as the stress at the end of the elastic-loading segment. If a pop-in is not present, then the initiation of plasticity can also be referred to as the yield stress. Figure 3.3 displays the variations in stress at the initiation of plasticity with distance from the grain boundary in both samples. The indents lacking a pop-in are marked with red symbols. Figure 3.3 distinguishes among data collected with different indenter tips, due to a documented size-effect in spherical nanoindentation in which stress increases with decreasing tip radii (e.g., Pathak and Kalidindi, 2015a). Figure 3.3a presents data in the LAGB sample and highlights that the stress at the initiation of plasticity does not significantly vary with distance from the grain boundary, even for indents close to or on top of the boundary. Figure 3.3b presents stress at the initiation of plasticity in the HAGB sample. Unlike in the LAGB sample, the initiation of plasticity occurs at stresses approximately 5–15 GPa lower for indents placed on top of the grain boundary relative to typical values of those either side. These trends in the stress data in Figure 3.3 are consistent with the trends displayed by the load at pop-in (see Figure B.6), and the corresponding shear stress (see Figure B.9).

Measurements using sharp indenters test the strength of the material at an effective strain of 8%. Figure 3.4 displays hardness versus indentation depth for both samples.

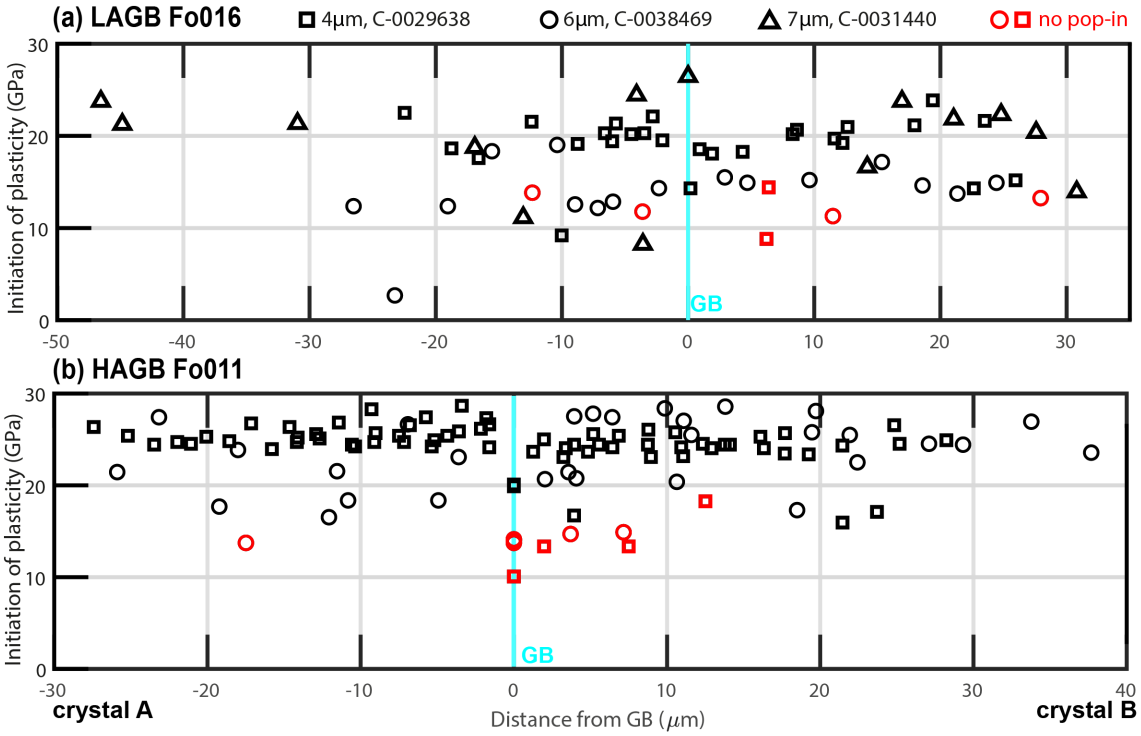


Figure 3.3: Summary of results from spherical indentation in the (a) LAGB sample and (b) HAGB sample. The open symbols correspond to the stress at the initiation of plasticity. In indents without a pop-in (red), the initiation of plasticity is equivalent to the yield stress. The variation in the load at pop-in with distance from the grain boundary, and the corresponding shear stresses are presented in Figures B.6 and B.9 in Supplementary Materials.

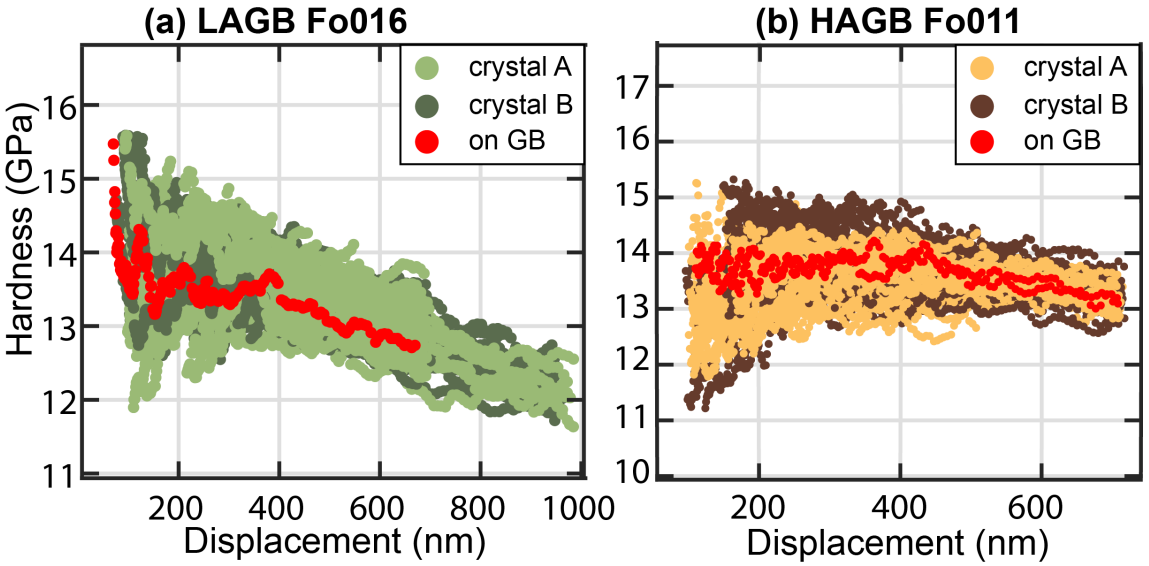


Figure 3.4: Summary of results using a Berkovich indenter tip (Table 3.1). The hardness data are coloured according to each crystal in Figure 3.1. The indents that left an imprint with the centre overlapping the trace of the grain boundary are marked in red (for details, see Figures B.2, B.4).

Each crystal has a corresponding colour, whereas the indents placed on top of the grain boundary are displayed in red (see Figures B.2, B.4). Figure 3.4 exhibits a nanoindentation size effect, in which hardness decreases with increasing displacement. The indents placed on the grain boundary are similar to the indents placed in either crystal in both the LAGB and the HAGB samples. The load-displacement data collected using a Berkovich indenter tip does not present significant (i.e., $>$ 2–3 nm) bursts in displacement (pop-ins) (see Figure B.5).

Figure 3.5 displays the hardness at constant depth, as a function of the distance from the grain boundary. As illustrated in Figure 3.5a, the hardness measured in the LAGB sample is independent of distance to the boundary. The data also presents a subtle hardness contrast among the two crystals due to plastic anisotropy, with the hardnesses of crystal B being approximately 0.5 GPa lower than those of crystal A. The average hardness at 500 nm depth is 13.5 ± 0.036 GPa in crystal A and 12.8 ± 0.1 GPa in crystal B. Figure 3.5b demonstrates that hardnesses far from the boundary are comparable between crystals in the HAGB sample, with an average hardness at 500 nm of 13.6 ± 0.4 GPa in crystal A and 13.8 ± 0.4 GPa in crystal B. However, in contrast to the LAGB sample, the HAGB sample exhibits a systematic change in hardness with decreasing distance to the boundary, and the indentation size effect raises the profile to higher hardnesses at shallower indentation depths. Hardness

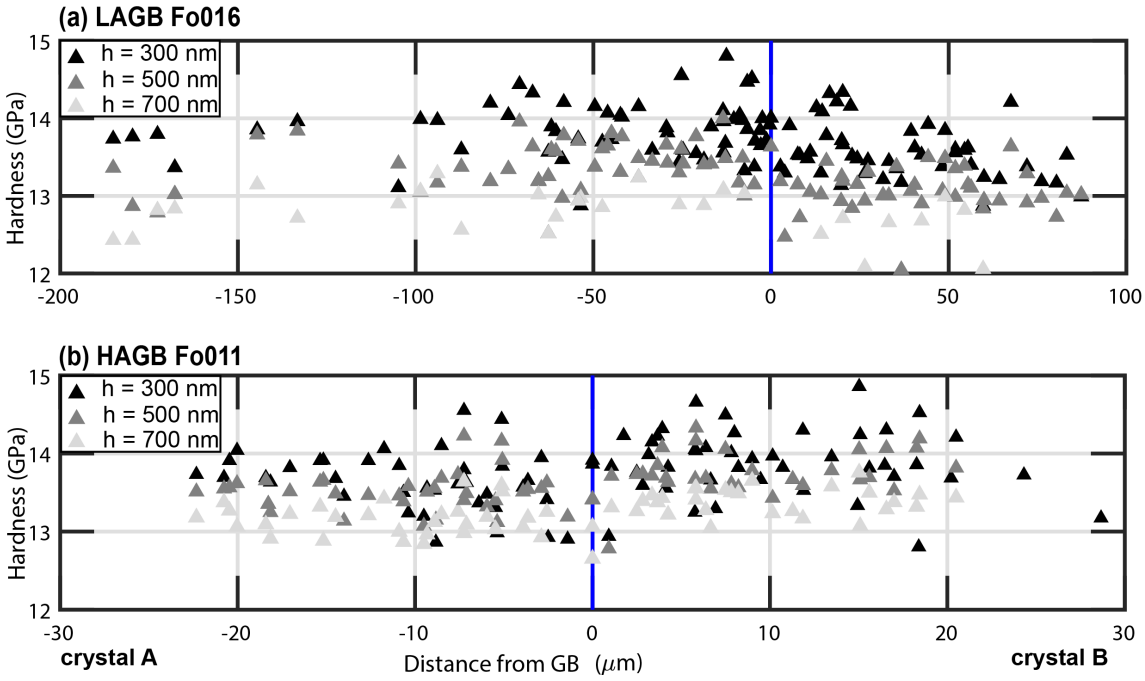


Figure 3.5: Summary of Berkovich nanoindentation results. The hardness at different indentations depths, h is displayed against distance from the grain boundary.

increases by a few hundred megapascals and peaks at a distance of 5 μm from the boundary, but indents placed on top of the grain boundary display hardnesses that are a few hundred megapascals lower than those far from the boundary.

3.3.2 Microstructural characterization

Microstructural characterization with HR-EBSD reveals significant accumulations of geometrically necessary dislocations (GNDs) around indents. Figure 3.6 presents maps in the LAGB sample around sharp and spherical indents. This particular crystal orientation, with [100] perpendicular to the mapping area, is subject to elevated levels of background noise in the GND density calculation for typical olivine slip systems (see Figure 8 in Wallis et al., 2019). The indents are surrounded by zones of elevated GND density, with values $> 10^{15}$ m^{-2}. Figure 3.6a displays GND densities around Berkovich indents positioned at varying distances from the grain boundary. The middle indent is centered in crystal B and intersects the grain boundary. Consequently, elevated GND densities are also present in crystal A around the same indent. However, the indent in crystal A with a center at $\sim$ 1.5 μm from the grain boundary does not exhibit detectable dislocations in crystal B. In Figure 3.6, the middle panel presents a Berkovich indent centered over the grain boundary. This indent does not exhibit

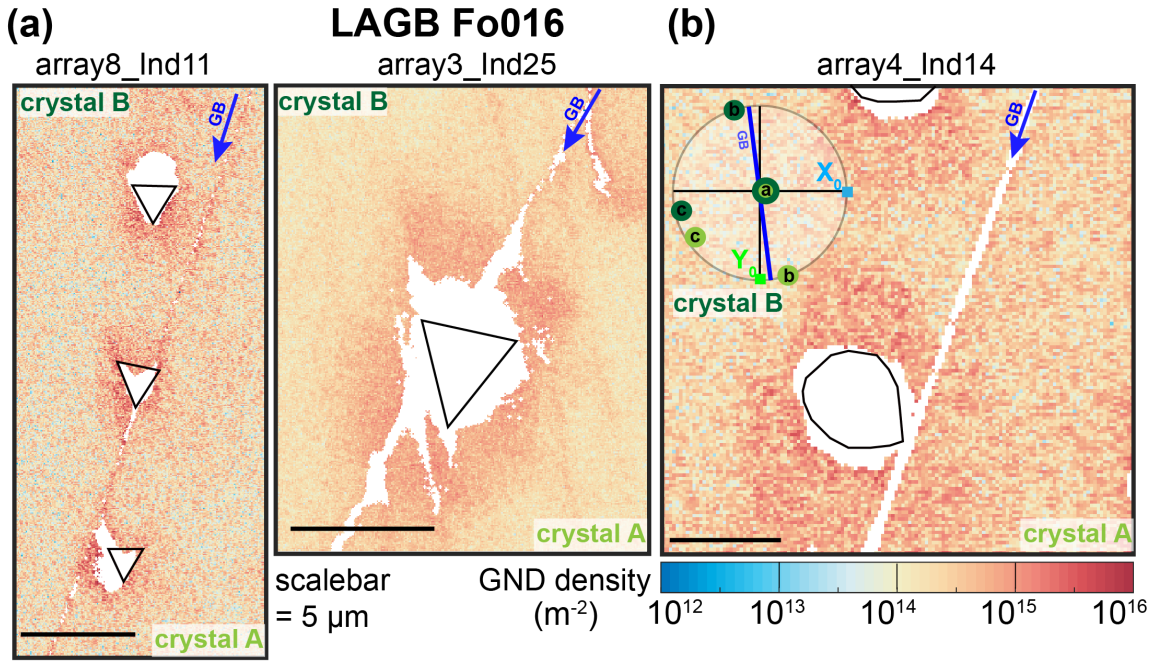


Figure 3.6: HR-EBSD results in the LAGB sample. a) Total GND densities around Berkovich indents at various distances from the grain boundary. b) Total GND densities around a spherical indent near the grain boundary. All maps have the same scalebar of 5 μm. The lower hemisphere plot indicates the crystal orientations for each crystal. The black outline marks the indent imprint in the material.

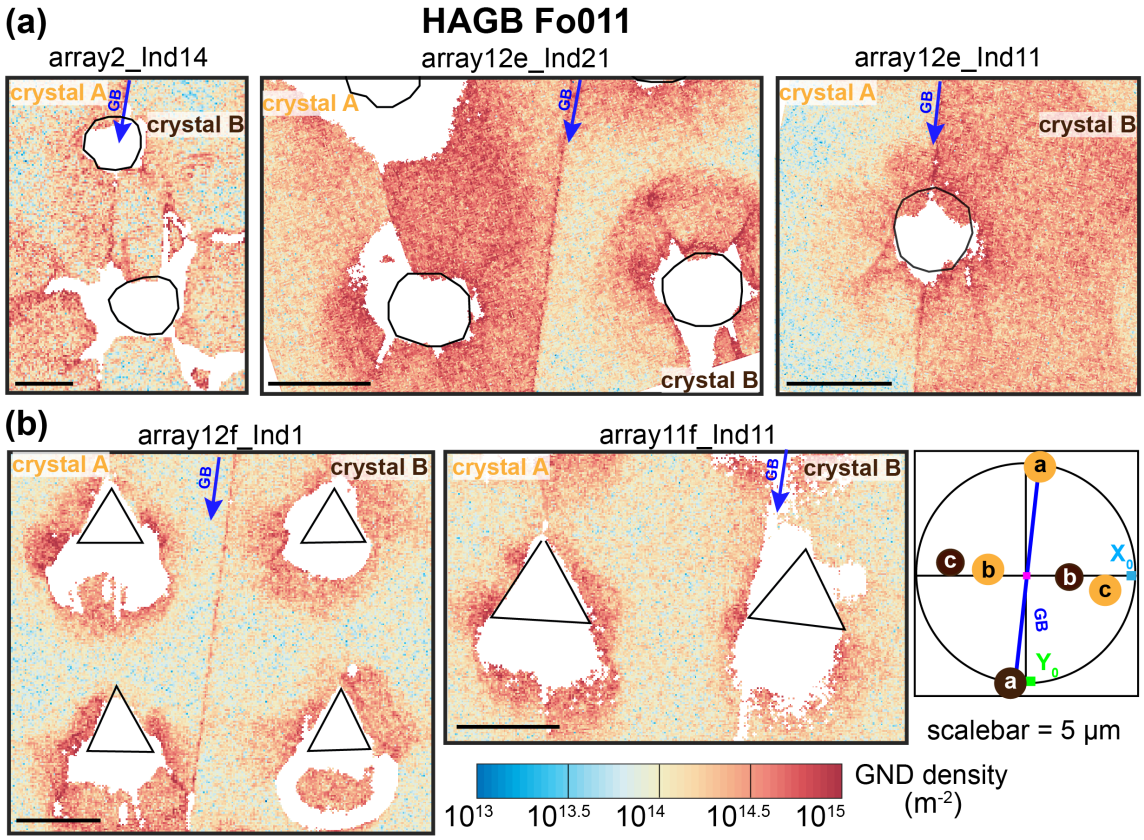


Figure 3.7: HR-EBSD maps around indents in the HAGB sample. a) Total GND densities around spherical indents at various distances from the grain boundary. b) Total GND densities around Berkovich indents near the grain boundary. All maps have the same scalebar of 5 μm. The lower hemisphere plot indicates the crystal orientations for each crystal. The black outline marks the indent imprint in the material.

GNDs with a symmetric distribution in both crystals. The corresponding hardness for this indent is lower than the indents in the bulk crystal (Figure 3.5b). Figure 3.6b presents elevated GND densities around a spherical indent with the center ~ 2.3 μm from the grain boundary. This indent exhibits elevated GND densities in crystal B, but essentially no detectable GNDs in crystal A.

Figure 3.7 presents GND densities in the HAGB sample. The GND density is asymmetrically distributed around indents and reaches values $> 10^{15}$ m^{-2}. The grain boundary abruptly interrupts the distributions of GND density surrounding both spherical and Berkovich indents placed nearby the grain boundary. This interaction between the GND density distribution and the grain boundary is most evident for indents within ~ 7 μm of the boundary. Indents placed on top of the grain boundary do exhibit elevated GND densities in both crystals. Elevated GNDs are also present along cracks around spherical indents in Figure 3.7a. The proportions of the total

Table 3.2: Schmid factor, S, describing the relationships between the mean applied pressure and the resolved shear stresses for different slip systems considered in this study. For the HAGB sample, the indentation direction is parallel to $[0\bar{1}1]$, and for the LAGB sample, the indentation direction is approximately parallel to [100]. Because these bicrystals are symmetric tilt boundaries, the Schmid factor is the same for all slip systems in crystal A and B for both samples.

Slip system	LAGB Fo016	HAGB Fo011
[100](010)	0	0
[001](010)	0	0.43
[001](100)	0.087	0
[100](011)	0.087	0
[100](001)	0.087	0
[001](110)	0.062	0.35
[001](130)	0.029	0.43

GND density made up of dislocations of different slip systems are presented in Figure B.10.

We calculate the uniaxial Schmid factor in the single crystals for common slip systems in olivine (e.g., Tommasi et al., 2000; Mussi et al., 2014; Wallis et al., 2020) and display it in Table 3.2. Due to the symmetric nature of each bicrystal, the estimated Schmid factors are approximately the same in both crystals of each bicrystal. Notably, crystals in the LAGB sample are unfavourably oriented for all the slip systems considered ($S < 0.1$ in all cases), with [001] and [100] within 3° of the sample surface and normal to the sample surface, respectively. In contrast, crystals in the HAGB sample are well aligned ($S > 0.3$) for slip on the [001]{hk0} and [001](010) slip systems.

We calculate several geometrical factors to assess the transparency of the grain boundary to slip transfer and present them in Figure 3.8. The m' factor is calculated using Equation 3.12 and quantifies the slip transmission between an incoming and outgoing slip system across a grain boundary (Figure 3.1a), with values of 1 for a perfectly transparent grain boundary and 0 for a grain boundary acting as a perfect barrier. The values of m' for the LAGB sample suggest near perfect transmission for the same incoming and outgoing slip system due to the small misorientation between the two crystals (13°). Slip transfer between different slip systems is also potentially easy for a significant number of the cases considered (e.g., from [001](130) to [001](010), Figure 3.8a). Values of m' also indicate that, by comparison, slip transfer is unfavourable in the HAGB sample for most slip systems considered (Figure 3.8b). The only favourably oriented systems are slip transfer from [100](001) to [100](011) and from [100](011) to [100](010). The M factor is also a geometrical factor quantifying

slip transmission, but additionally accounts for the tilt of the grain boundary according to Equation 3.14. In our samples, the grain boundary is subvertical, with a tilt of $\sim 2^{\circ}$, which we approximate as vertical in this analysis. In both samples, the values of the M factor predict that the grain boundary is transparent for an increased number of slip systems compared to values of m' (Figure 3.8c and d).

Further detailed characterization using scanning TEM (STEM) presents evidence for the activity of different slip systems, and reveals dislocation structures present and their interaction with the grain boundary in the HAGB sample. Figure 3.9 characterizes spherical indent 11 (see location in Figure 3.7a), which is approximately centered on the grain boundary. The lower hemisphere diagram in Figure 3.9 corresponds to the viewing plane. Complex dislocation structures are present in both crystals. Dislocation loops are present in both crystals, which we interpret as dislocations on the [001](100) slip system. Both crystals present pile-ups of dislocations with increasing spacing further away from the grain boundary, which we interpret as dislocation activity on the [100](010) slip system. Dislocations appearing as lines are present in both crystals and suggest the activity of [001](010) slip system. Some of the dislocation structures present in both crystals, along lines perpendicular to the loading direction, could correspond to slip system activity within the [100]{0kl} family. In addition, panel 1 in Figure 3.9 reveals that slip bands intersect and displace the grain boundary plane, creating roughness with wavelengths and amplitudes of tens of nm. Sets of dislocations on different slip systems commonly intersect one another and, in some instances, loop segments of one dislocation type (e.g., on (100)) are pinned against dislocations of a different type (e.g., on (010)). Occasional microcracks have traces approximately parallel to those of the dislocation sets and the grain boundary, but are mostly at low angles to the specimen surface, consistent with the expectation that they form during unloading.

Figure 3.10 presents STEM characterization of a spherical indent in crystal A in the proximity of the grain boundary. The imprint of the spherical indent ends at the grain boundary and exhibits an asymmetric cross-section. The majority of the dislocation structures are present in crystal A including dislocation loops, pile-ups, and intersections of different slip systems (panel 1). The zone of high dislocation density present in crystal A terminates abruptly at the grain boundary (panel 2) with only scarce dislocations present in crystal B (panels 2 and 3). The dislocations in crystal B are loops on the (100) plane and the [001](010) slip system (e.g., panel 2). Unloading cracks are present parallel to slip bands and along the grain-boundary plane.

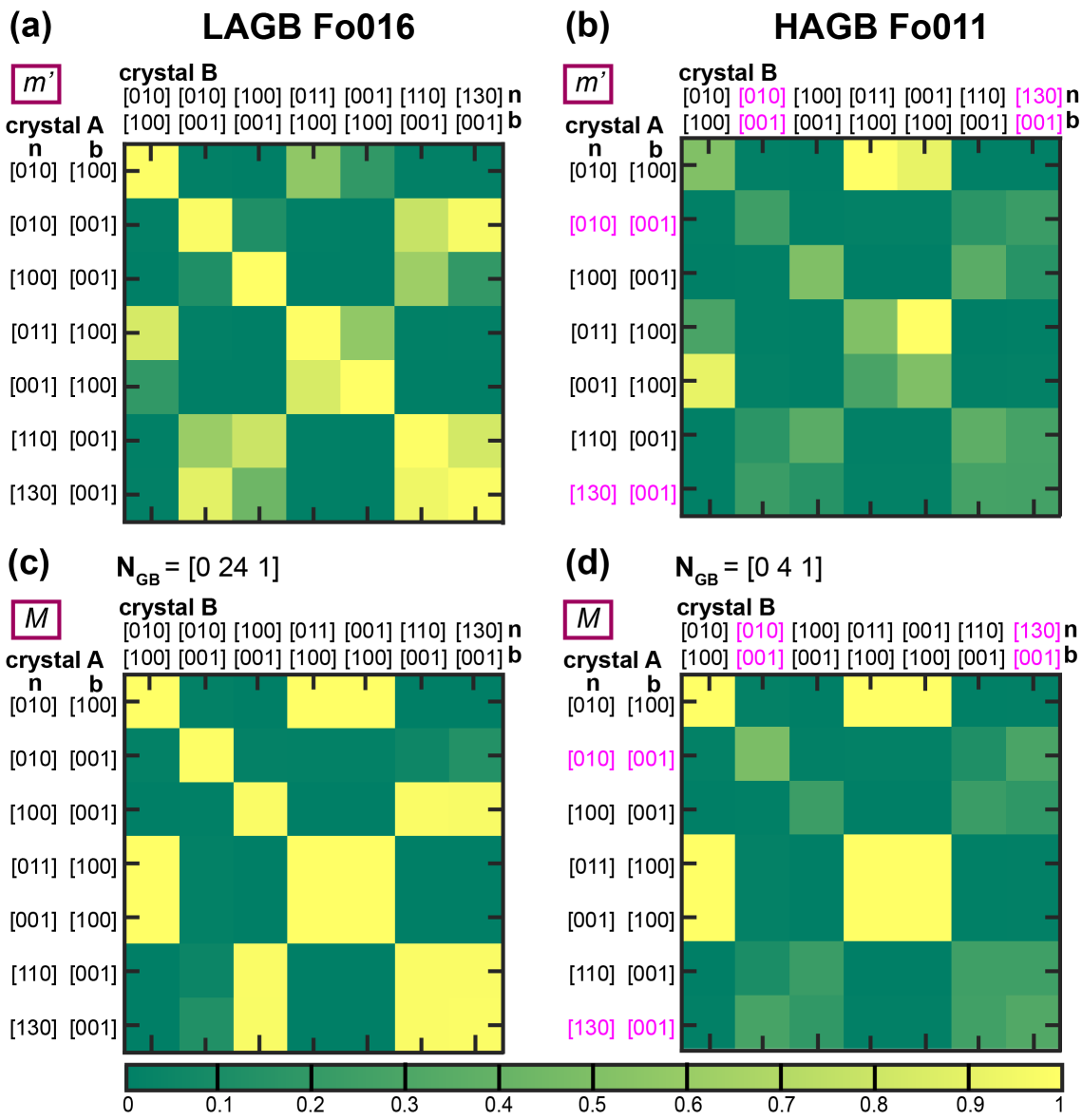


Figure 3.8: Geometrical transfer factor between the possible slip systems active in the bicrystals in this study. The first row represent the m' factor in a) the LAGB bicrystal and b) the HAGB bicrystal, and the second row displays the M factor in the a) LAGB bicrystal and the HAGB bicrystal. The slip systems considered are represented by the slip direction, $\mathbf{b}$, and the normal to the slip plane, $\mathbf{n}$. The normal to the grain boundary is denoted by $\mathbf{N_{GB}}$. In the b) and d) panels the second and last columns and rows correspond to the slip systems with the greatest Schmid factor in Table 3.2.

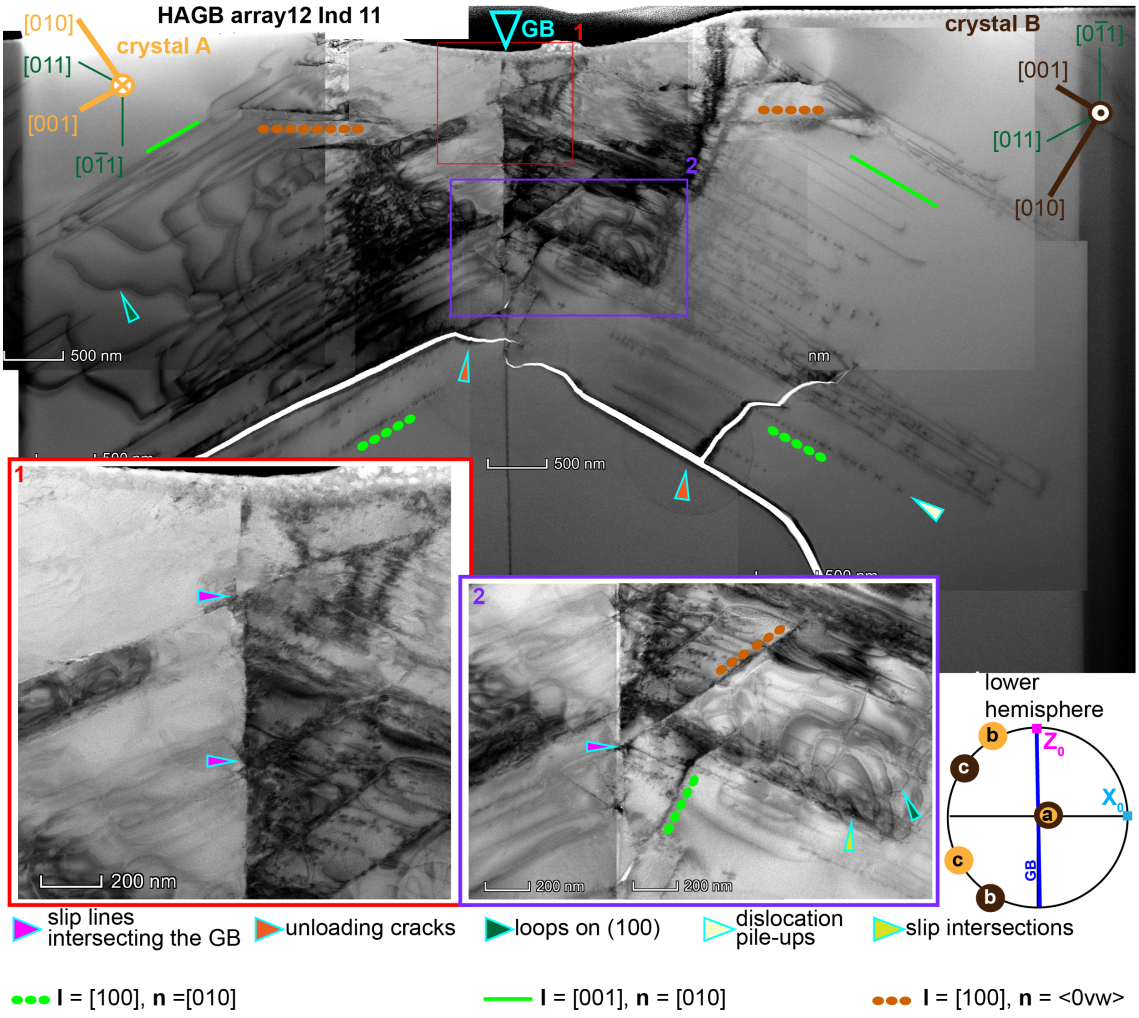


Figure 3.9: Bright-field STEM imaging of the spherical indent in Figure 3.7a placed on top of the high-angle grain boundary. The lower hemisphere projection corresponds to the viewing plane. The boxes mark the position of the images at higher magnification. The corresponding stress-strain curve is presented in Figure B.8a. The annotations present interpretations of possible line directions, **l**, and the plane normal, **n**, of the slip plane.

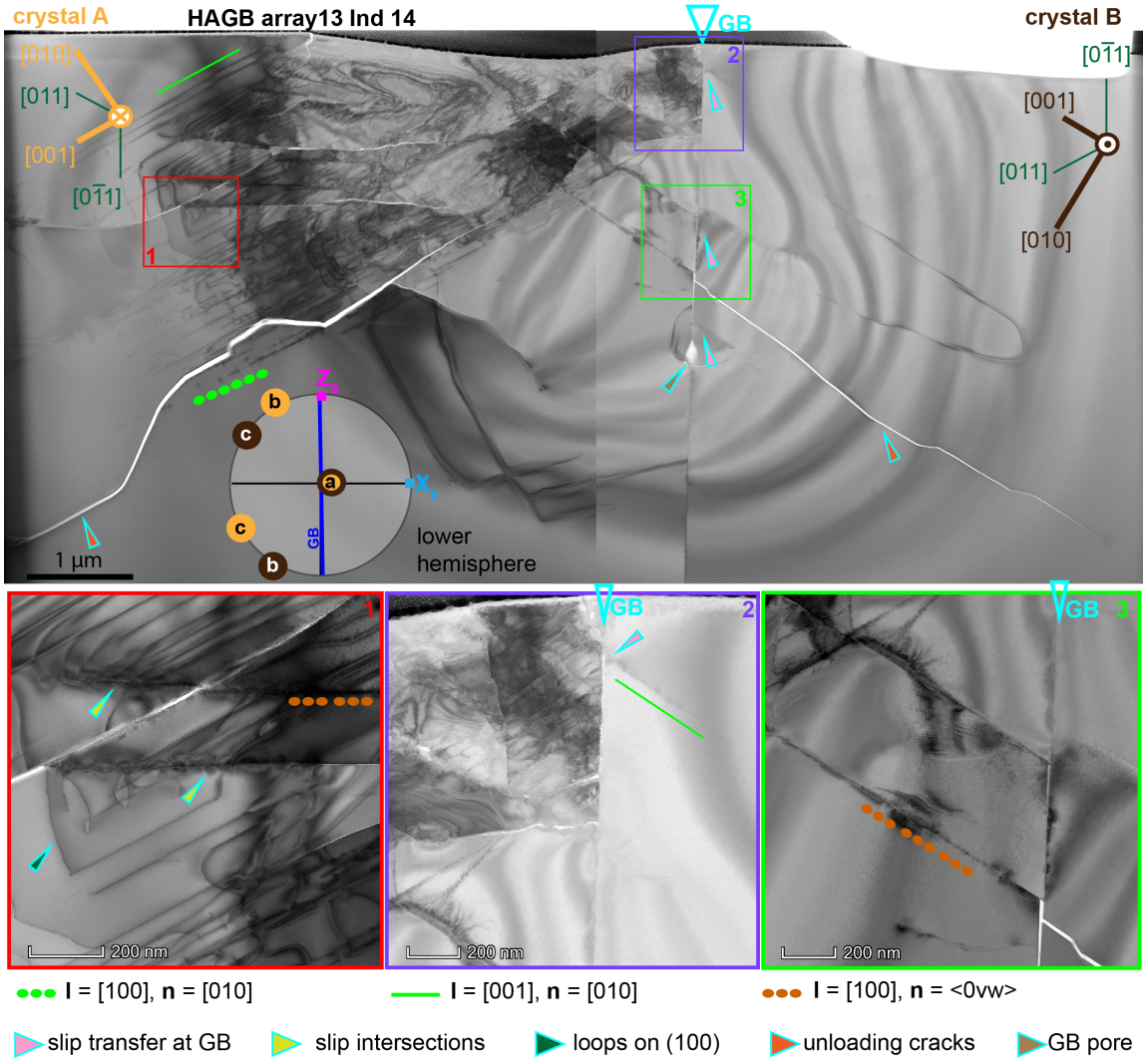


Figure 3.10: Bright-field STEM imaging of a spherical indent placed near the grain boundary in crystal A in the HAGB sample. The annotations are similar to Figure 3.9. The corresponding stress-strain curve is presented in Figure B.8b.

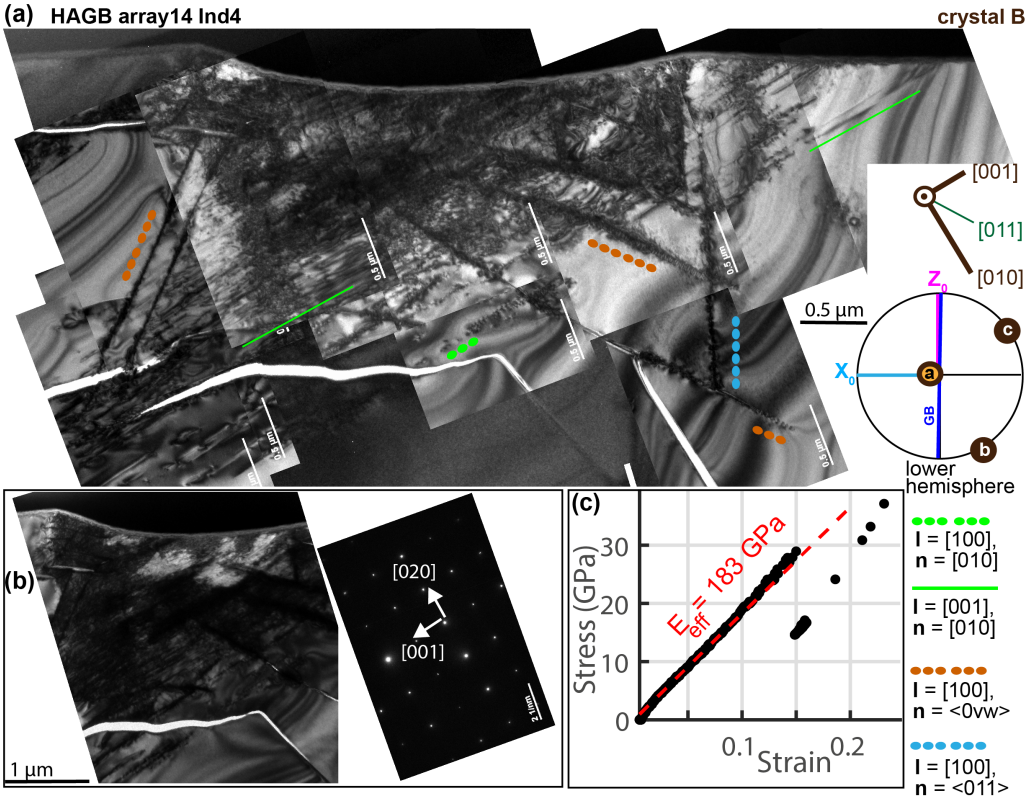


Figure 3.11: Bright-field STEM image of a spherical indent in the single crystal B within the HAGB sample. The corresponding stress-strain curve is presented in panel c, and highlights that there is no further flow after the pop-in event. Note that the viewing direction is flipped compared to Figures 3.9 and 3.10.

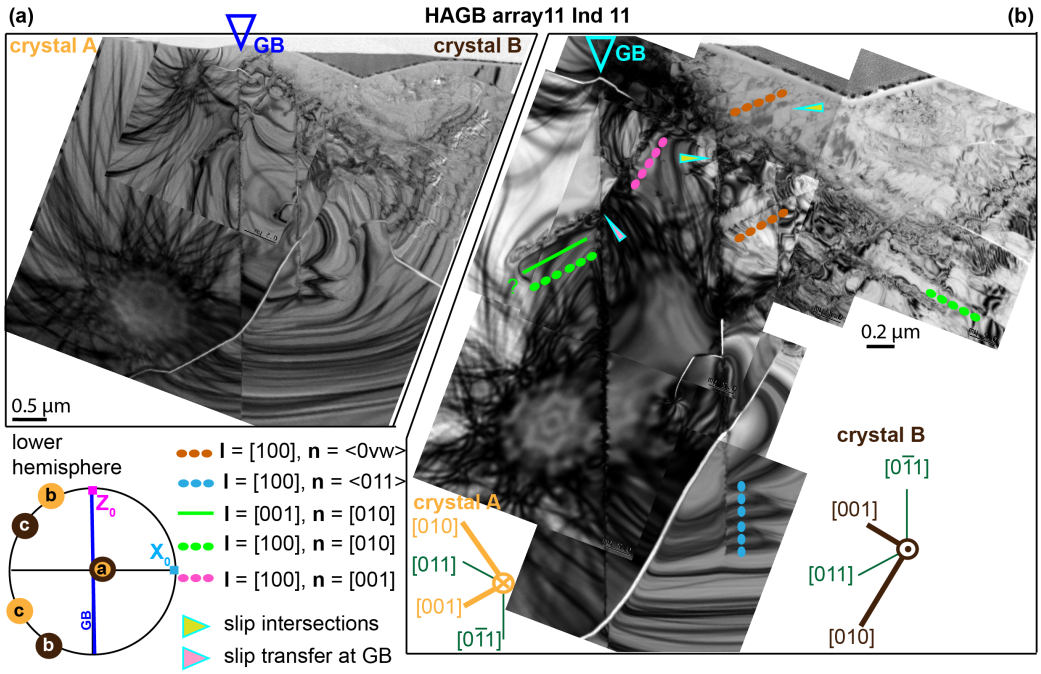


Figure 3.12: Bright-field STEM imaging of a Berkovich indent placed near the high-angle grain boundary in crystal B. The corresponding load-displacement curve is presented in Figure B.5.

Figure 3.11 presents the dislocation structures in crystal B in the HAGB sample under a spherical indent that was stopped shortly after the initiation of plasticity. These microstructures reflect the dislocations generated during a pop-in after a longer segment of elastic loading compared to indents on the grain boundary or within its immediate vicinity. The dislocation structures are complex, with the intersection of dislocations active on the [001](010), [100](010) (green), and different [100]{0kl} slip systems (orange and blue). Figure 3.11b presents a dark-field image collected with optimal conditions for [001] and [020].

Figure 3.12 displays the microstructures beneath an indent made with a sharp Berkovich tip and placed in crystal B in the vicinity of the grain boundary. The dislocation structures present activity and intersections of the [100]{0kl} (orange and blue) and [100](010) (green) slip systems. 3.12b presents dislocations consistent with the activity of [100](001) (pink) generated under the indent and piling up at the grain boundary. An array of dislocations consistent with the activity of the [100](010) or [001](010) slip systems (green) appears on the other side of the interface. This interaction indicates slip transfer at the grain boundary from crystal B to crystal A in Figure 3.12b.

3.4 Discussion

The interaction between grain boundaries and lattice dislocations underpins a series of key phenomena in the deformation of crystalline materials, including strain hardening and the influence of grain size on yield strength (Hirth, 1972; Han et al., 2018). Experiment, theory, and numerical simulation all indicate that there are three main types of interactions: i) emission of lattice dislocations from the GB, ii) absorption of lattice dislocations at the grain boundary, and iii) slip transmission across GBs (Hirth, 1972; Javaid et al., 2021; Bayerschen et al., 2016; A.P.Sutton and R.W.Balluffi, 1995, Chapter 12).

In this study, we describe nanoindentation with sharp and spherical indenters on two forsterite bicrystals with high-symmetry and low-energy grain-boundary configurations (Figure 3.1) to isolate these different types of interactions. The indents were placed at varying distances from the vertical grain boundary (see Figures B.4, B.3, B.2, B.1). The symmetry of the crystals on each side of the grain boundary results in nanoindentation loading along a consistent crystal direction across the bicrystals. For the LAGB sample, the indentation direction is parallel to [100], while for the HAGB sample the indentation direction is parallel to $[0\bar{1}1]$. Although the stress field in indentation is spatially heterogeneous and impacted by crystal anisotropy, the consistent indentation direction means that distance to the grain boundary is the only free variable in our experiments. Our key interpretation is that the HAGB used in this study facilitates dislocation nucleation, while also acting as a barrier to slip transmission. In contrast, the LAGB exhibits no detectable impact on the initiation of plasticity or slip transmission. Several recent investigations have focused on the impact of grain size on deformation of olivine by low-temperature plasticity regime (Kumamoto et al., 2017; Hansen et al., 2019; Koizumi et al., 2020). When materials deform by this mechanism, yield strength typically exhibits a negative correlation with grain sizes, traditionally described by the empirical Hall-Petch effect (Hall, 1951; Petch, 1953). In fact, Hansen et al. (2019) use this effect to explain the observed negative dependence of yield stress on grain size in San Carlos olivine. Although a wide variety of microphysical models predict this relationship (for a review, see Cordero et al., 2016), Hansen et al. (2019) identify several subsets of models that are consistent with their observations. The key microphysical processes in these models include 1) dislocation pile-up at grain boundaries that harden the material until the boundaries act as dislocation sources (Hall, 1951; Petch, 1953; Cottrell and Bilby, 1949), 2) the difficulty of emission of dislocations from grain boundaries during plastic deformation

(Bata and Pereloma, 2004), 3) emission of dislocations from grain boundary ledges that subsequently lead to strain hardening (Li, 1963; Li et al., 2016), and 4) the emission of dislocations from grain boundaries due to elastic incompatibilities that subsequently lead to strain hardening (Meyersm and Ashworth, 1982). In the following sections, we discuss observations from our experiments that help evaluate the role of these processes in the deformation of olivine.

3.4.1 The role of grain boundaries as a source of dislocations

Several of the aforementioned models rely on grain boundaries acting as dislocation sources. As illustrated in Figures 3.3 and 3.5, mechanical data from our experiments display decreased hardnesses at the HAGB compared to the crystal interior, while there is no detectable change at the LAGB. Specifically, the reduction in the hardness at the initiation of plasticity in spherical indents provides direct evidence that the HAGB assists the generation of dislocations. This trend is consistent for deformation at strains $< 15\%$ across the two nanoindentation techniques. In the case of the HAGB sample the stress required for generating and gliding dislocations drops from ~ 25 GPa to < 20 GPa from the crystal interior to the grain boundary region (Figure 3.3b). Similarly, the maximum shear stresses reached for the initiation of plasticity on the grain boundary (< 10 GPa) are smaller when compared to the shear stresses required in the single crystal (> 10 GPa). The shear stresses at pop-in in the single crystal approach the theoretical limit (12.7 GPa in the HAGB sample and 15.8 GPa in the LAGB sample), indicating that stress at the initiation of plasticity is controlled by the distribution of dislocation sources in the deforming volume (Figure B.9) (e.g., Fang et al., 2021). In metals, similar observations using spherical nanoindentation on twin boundaries have been attributed to generation of dislocations at the twin boundary (Li et al., 2021a). In addition, our experiments reveal that a low-energy LAGB, comprised of arrays of periodic c-dislocations (Heinemann et al., 2005) is not a potent source of dislocations (Figure 3.3a and B.9).

Detailed investigations of spherical indents placed on top of the HAGB reveal complex dislocation structures. In Figure 3.9 slip bands extend from the grain boundary into the crystal interior, suggesting their origin at the boundary. These dislocations could be generated from a source in the grain-boundary plane or within its immediate vicinity (A.P.Sutton and R.W.Balluffi, 1995, Ch 12). Drawing inspiration from investigations of metals, we suggest a number of hypotheses for the specific mechanism of dislocation nucleation. Li (1963) and Murr (1975) proposed a model of

dislocation emission from grain boundaries involving grain-boundary ledges (grain-boundary dislocations accommodating GB curvature) that can either act as stress concentrators mediating the nucleation of dislocation loops in the immediate vicinity of the grain-boundary plane (Varin et al., 1987; Hirth, 1972), or can be sheared in the GB plane and generate partial slip in the crystal lattice (Li, 1963; Price and Hirth, 1972; Hirth, 1972). Alternatively, stress concentration in the crystal lattice could be generated by line defects in the grain-boundary plane (extrinsic GB dislocations) (Varin et al., 1987; Murr, 1981; Gleiter, 1977; Sangal et al., 1991) or by the elastic anisotropy introduced by the juxtaposed crystals (Hirth, 1972; Hook and Hirth, 1967). These models rely on the grain-boundary structure. Similar samples to the HAGB imaged in Figure 3.9 have been investigated using high-resolution TEM by Marquardt and Faul (2018, Fig 9) and simulated via molecular dynamics by Adjaoud et al. (2012, Fig 7). Marquardt and Faul (2018) present evidence of inclined facets as part of the grain-boundary structure, while Adjaoud et al. (2012) suggest that a lower-symmetry arrangement is more energetically favourable than a higher-symmetry one. Given the importance of GB structure in nucleation of dislocations, we suggest that in our experiments the high-angle GB promotes stress concentrations and activation of dislocation sources in the crystal lattice.

3.4.2 Slip transmission across GBs

The difficulty of slip transmission at grain boundaries significantly contributes to hardening and size effects (Hirth, 1972). The interactions of grain boundaries and dislocations have been studied at length in metals (for review, see Kacher et al., 2014), and in ceramics (e.g., Mitchell, 1979), resulting in a series of proposed criteria for predicting the response of the grain boundary to slip transmission (Lee et al., 1989, 1990; Bayerschen et al., 2016) (Figure 3.1a). These criteria include: 1) minimal slip misalignment across the GB, which translates into M and m' factors of 1 for a perfectly aligned system (Luster and Morris, 1995; Shen et al., 1986), 2) maximised resolved shear stresses on the outgoing slip plane, and 3) minimal magnitude of the residual Burgers vector in the grain-boundary plane after transmission (Kacher et al., 2014; Bayerschen et al., 2016).

Nanoindentation tests positioned in the vicinity of the grain boundary directly test the ability of the boundary to transmit or resist strain. Previous work in metals has investigated dislocation transmission through grain boundaries by collecting load-displacement data using both spherical (e.g., Kalidindi and Vachhani, 2014; Vachhani et al., 2016b) and sharp (e.g., Britton et al., 2009; Wang and Ngan, 2004; Ohmura

and Tsuzaki, 2007; Voyiadjis and Zhang, 2015; Aifantis et al., 2006) indenter tips. As an illustrative example, spherical nanoindentation in Al reveals that the yield stress can increase with increasing proximity to a grain boundary (e.g., Vachhani et al., 2016b). Similar effects have been observed in an Al bicrystal tested with Berkovich indentation (Aifantis et al., 2006). For our samples, spherical indentation does not reveal an increase in stress at the initiation of plasticity near either grain boundary (Figure 3.3b). However, as discussed above, the initiation of plasticity in most of our spherical indents is defined by a pop-in and therefore primarily relates to the processes of dislocation nucleation, rather than the ease of dislocation motion. In contrast, hardnesses measured with Berkovich indentation relate primarily to the ease of dislocation motion. We note that the hardness in the HAGB sample increases with increasing proximity to the grain boundary, and exhibits maximum values at a distance of ~ 5 μm (Figure 3.5b). In addition, Figure 3.5b also indicates that the dependence of hardness on position may be slightly different in crystal A than in crystal B. Although we assume that the tilt boundaries are perfectly parallel to the indentation direction, the plane of the HAGB is actually 2–3° from normal to the sample surface. It is possible that this small deviation underpins the differences in the hardness trends in proximity to the grain boundary. Another possible explanation is the relative orientation of the indenter tip with respect to the grain boundary in each crystal (see Figure B.4), with the side of the pyramid parallel or subparallel to the GB trace in crystal B and the corner or the pyramid perpendicular to the GB in crystal A. This azimuthal rotation of the Berkovich tip influences the magnitude of the resolved shear stresses on each available slip system and the grain boundary beneath the indent (e.g., Chen et al., 2018; Aifantis et al., 2006; Javaid et al., 2021).

These observations of mechanical properties are supported by the theoretical predictions of slip transmission, given by m' and the M factors, and by microstructural observations of dislocation structures under the indents. When accounting for the loading direction in our experiments, the Schmid factor indicates that a limited number of slip systems are oriented such that the resolved shear stresses will promote dislocation in the single crystal beneath the indent, followed by pile-up at the grain boundary (Table 3.2). In the mechanical data, there is no observable hardening with proximity to the GB in the LAGB sample at either the initiation of plasticity (Figure 3.3a) or at 8% strain (Figure 3.5a), suggesting that the grain boundary exerts little to no resistance to slip transfer, in line with the geometrical predictions. The hardening in the proximity of the GB in the HAGB sample (Figure 3.5b) alongside the asymmetrical residual mark of the indent (Figure 3.10) indicate that the grain

boundary acts as a barrier to incoming dislocations generated beneath the indenter, as expected from the geometrical predictions in Figure 3.8b and d. In Figure 3.10 the incoming slip generated in crystal A likely represents activity of [001](010) with an uniaxial Schmid factor of 0.43 (Table 3.2). Crystal A also presents evidence of activity of [100]{0kl} and [100](010), and although the uniaxial Schmid factor is 0, the non-uniform stresses under the spherical indenter (e.g., Li et al., 2011) could promote these slip systems. Evidence of outgoing slip systems in crystal B is present in the activity of [001](010), and the loop in the [001]{hk0} family. According to the geometrical factors m' (Figure 3.8b) and M (Figure 3.8d) slip transfer from [001](010) to [001](010) has values of ~ 0.4 and ~ 0.6, respectively. Slip transfer from [001](010) to [001]{hk0} has predicted values of 0.3–0.4 for M. Figure 3.12 presents STEM imaging of a Berkovich indent in crystal B in the HAGB sample. The figure presents evidence of slip transfer from crystal B to crystal A, albeit with slip systems that are more difficult to interpret. One interpretation could be that of slip transfer from [100](001) to [001](010), with corresponding m' and M values < 0.1. Another interpretation could be that of slip transfer from [100](001) to [100](010), with corresponding $m' = 0.8$ and $M > 0.9$. Accounting for the significant discrepancy in the geometrical factors within the aforementioned systems, we interpret that Figure 3.12 most likely displays slip transmission from [100](001) to [100](010). The slip transmission documented in Figure 3.12b is not associated with a pop-in, unlike in studies using Berkovich indentation nearby grain boundaries in metals (e.g., Aifantis et al., 2006; Wang and Ngan, 2004; Britton et al., 2009). Figures 3.10 and 3.12 present the grain boundary as largely intact and vertical after slip-transfer, with one example of a vertical crack along the grain boundary at the end of a dislocation pile-up (panel 3, Figure 3.10).

3.4.3 Impact of grain boundaries on large-scale plasticity of olivine aggregates

In this study, we present experiments conducted on synthetic bicrystals and document the connections among mechanical properties, grain-boundary character, nucleation of dislocations, and slip transfer across grain boundaries. These observations from forsterite bicrystals shed light on the microphysics of grain-size dependent deformation mechanisms in olivine aggregates. We suggest that a given type of grain boundary can contribute towards multiple mechanisms of hardening. During macroscale deformation, grain boundaries can act as barriers to lattice dislocations either due to 1) the pre-existing dislocations at the grain boundary due to local yield or 2) the grain

boundary character being unfavourable to slip transmission (Sangid et al., 2011; Hirth, 1972). Grain boundaries acting as sources of dislocations generate complex dislocation structures in their immediate vicinity, leading to an area that is harder to penetrate by incoming lattice dislocations due to forest hardening (e.g., Wallis et al., 2020). These phenomena have been isolated in small-scale experiments in metals (e.g., Dehm et al., 2018; Maaß and Derlet, 2018) and underpin the temperature-dependent grain-size effect of the yield stress in bulk deformation of olivine documented by Hansen et al. (2019). Therefore, our experiments support a model of pre-yield hardening due to local yield at the grain boundaries before macroscopic yielding (i.e., microplasticity, Maaß and Derlet (2018), A.P.Sutton and R.W.Balluffi (1995, Chapter 12)) in the experiments of Hansen et al. (2019). Moreover, Hansen et al. (2019) present data indicating that the magnitude of macroscale strain hardening by intracrystalline back stresses is independent of grain-size of the sample. This observation suggests that interactions amongst dislocations generated in the crystal interior control the post-yield hardening, and there is no detectable interaction with the grain boundaries in the experiments of Hansen et al. (2019). However, according to our experiments, geometrically unfavourable grain boundaries for slip transmission lead to dislocation pile-ups of defects generated within 5 μm of a high-angle grain boundary.

In metals, the interactions between lattice dislocations generated by macroscopic yielding and forest dislocations at grain boundaries lead to strain hardening (Hirth, 1972). Intracrystalline dislocations interacting with grain-boundary areas with an enhanced density of dislocations due to microplasticity could increase the intracrystalline back stresses in small-grained aggregates (e.g., Guo et al., 2020, 2014; Andani et al., 2020). Published TEM investigations of olivine deformed in low-temperature regime and the data in Figure 3.11 reveal tangled dislocations and intersecting slip planes, which are inferred to contribute to strain hardening in single crystal deformation (Phakey et al., 1972; Gaboriaud et al., 1981; Druiventak et al., 2011; Wallis et al., 2020; Mussi et al., 2015a,b). In deformation of a polycrystalline aggregate, dislocations generated during macroscopic yielding interact with the pre-existing dislocations distributed heterogeneously along the grain-boundary network, where the local resolved shear stresses induced microplasticity. During low-temperature plasticity of olivine, this interaction results in an increase in yield strength with a decrease in grain size, followed by hardening dominated by intracrystalline interactions, which has been experimentally documented in olivine (Hansen et al., 2019).

In the context of low-temperature plasticity of olivine-rich materials under geological conditions (e.g., lithosphere bending) the distribution of grain boundaries

with different abilities to transmit strain could impact local strain hardening and localization, before bulk hardening of the material (e.g., Marquardt et al., 2015; Sangid et al., 2011; Andani et al., 2020). In our experiments, the LAGB is transparent to slip transfer, and does not generate plasticity at stresses lower than in the bulk crystal. However, we provide evidence that during macroscale deformation a HAGB can act as a site of microplasticity. The resulting strengthening effect of grain boundaries is particularly emphasized at small strains (A.P.Sutton and R.W.Balluffi, 1995). Moreover, our results could inform future numerical models of microstructural evolution of polycrystalline olivine (e.g., Gardner et al., 2017; Piazolo et al., 2019), and how the relative abundance and distribution of grain boundaries influences the local strain hardening in the deforming lithosphere.

3.5 Conclusions

Nanoindentation and microstructural investigations on pure forsterite synthetic bicrystals with a low-angle grain boundary (13°, [100]/(016)) and a high-angle grain boundary (60°, [100]/(011)) reveal that the HAGB sample acts as a source for dislocations and can prevent slip transmission leading to pile-up of dislocations. In contrast, the LAGB sample does not have a detectable impact on these processes. This initiation of plasticity at high-angle grain boundaries requires lower stresses compared to the crystal interior suggesting that some grain boundaries might act as sites of microplasticity just prior to macroscopic yield. Our results also provide evidence of interactions between dislocations and grain boundaries and support an increase in yield strength with grain size underpinned by dislocations pile-up at the grain boundary. We suggest that the distribution and character of grain boundaries in olivine-rich rocks plays a key role in generating differences in deformation prior to yielding and heterogeneity in the yield stress across the lithosphere.

Chapter 4

Direct testing of forsterite bicrystals via *in-situ* micropillar experiments at 700°C

"Although size-dependant strength scaling in metals usually arises from the presence of kinematic barriers to flow, these samples have no known internal barriers. One may speculate that this remarkable behaviour is associated with changes in the self-exhaustion or annihilation of dislocations, specifically those of screw character."

Uchic et al. (2004)

A similar version of this chapter has been prepared for publication in the journal *American Mineralogist*, with the following author list:

Diana Avadanii[1], Lars Hansen[2], Ed Darnbrough[3], Katharina Marquardt[4], David Armstrong[3], and Angus Wilkinson[3]

[1] Department of Earth Sciences, University of Oxford
[2] Department of Earth and Environmental Sciences, University of Minnesota
[3] Department of Materials, University of Oxford
[4] Department of Materials, Imperial College London

For this study, I prepared the sample surface and manufactured the micropillars, outlined the mechanical testing protocol, assisted virtually during mechanical testing, analysed and interpreted the mechanical data, wrote the code for the data analysis, and wrote the first draft of the manuscript.

Abstract

The mechanics of olivine deformation play a key role in long-term planetary processes, such as the response of the lithosphere to tectonic loading or the response of the solid Earth to tidal forces, and in short-term processes, such as postseismic creep within the upper mantle. Previous studies have emphasized the importance of grain-size effects in the deformation of olivine. However, most of our understanding of the role of grain boundaries in the deformation of olivine is inferred from comparison of experiments on single crystals to experiments on polycrystalline samples. To directly observe and quantify the mechanical properties of olivine grain boundaries, we use high-precision mechanical testing of synthetic forsterite bicrystals with well characterised interfaces. We conduct *in-situ* micropillar compression tests at high-temperature (700°C) on low-angle (4° tilt about [100] on (014)) and high-angle (60° tilt about [100] on (011)) grain boundaries. In these experiments, the boundary is contained within the micropillar and oriented at 45° to the loading direction to promote shear along the boundary. In these *in-situ* tests, we observe differences in deformation style between the pillars containing the grain boundary and the pillars in the crystal interior. *In-situ* observations and analysis of the mechanical data indicate that pillars containing the grain boundary consistently support elastic loading to higher stresses than the pillars without a grain boundary. Moreover, the pillars without the grain boundary sustain larger plastic strain. Post-deformation advanced microstructural characterization confirms that under the conditions of these deformation experiments, sliding did not occur along the grain boundary. These observations support the hypothesis that grain boundaries are stronger relative to the crystal interior at these conditions.

4.1 Introduction

Over the past decades, the rheological behaviour of olivine at the thermo-mechanical conditions of Earth's upper mantle has been the focus of a number of studies, often yielding inconsistent results between subdisciplines (for a review, see Karato, 2010). Laboratory experiments provide insight into olivine deformation under a wide range of conditions and form the basis for calibrating flow laws for extrapolation to geological conditions (e.g., Hirth and Kohlstedt, 2003). However, predictions of the mechanical properties of the lithosphere based on laboratory results are inconsistent and also disagree with estimates based on geophysical observations (e.g., Hunter and Watts, 2016; Zhong and Watts, 2013; Hansen et al., 2019).

One challenge associated with laboratory studies at elevated temperatures and pressures relevant to the upper mantle is separating and quantifying the role of different variables that simultaneously impact deformation (e.g., Thieme et al., 2018; Bollinger et al., 2019; Faul et al., 2011; Hansen and Kohlstedt, 2015). Microstructural analysis is generally only performed after quenching and decompression and after additional sample preparation for the desired characterization technique. This *post-mortem* assessment has constrained previous studies to inference of the microphysical mechanisms of deformation rather than direct observation (e.g., Thieme et al., 2018; Hansen et al., 2012a; Tielke et al., 2016b). However, this obstacle can be overcome by miniaturized mechanical testing at the micron scale, which facilitates the *in-situ* observation of material deformation, and the targeted investigation of key structural features such as grain boundaries (for review, see Kacher et al., 2019).

Planar defects, such as grain boundaries and their density (i.e., grain size), play a key role in ductile deformation of olivine under a wide range of conditions. At low temperatures and high stresses, permanent deformation is accommodated by dislocation generation and the glide of dislocations through the crystal lattice, as diffusion is inhibited (Chapter 2, Frost and Ashby, 1982). In olivine, this regime has been investigated in laboratory studies on single crystals (e.g., Kranjc et al., 2016; Demouchy et al., 2013; Evans and Goetze, 1979; Idrissi et al., 2016) and polycrystalline samples (e.g., Druiventak et al., 2011; Mei et al., 2010; Raterron et al., 2004; Faul et al., 2011) with little agreement among results. However, these past discrepancies have been reconciled by studies documenting a size effect during low-temperature plasticity of olivine (Kumamoto et al., 2017; Hansen et al., 2019; Koizumi et al., 2020). Kumamoto et al. (2017); Koizumi et al. (2020) used mechanical testing at a range of length scales in single crystals, while Hansen et al. (2019) used measurements on

polycrystalline samples with different grain sizes to document a size effect in which permanent deformation at smaller length scales (or smaller grain sizes) requires higher stresses. Observations of stronger samples with decreasing grain size are attributed to the empirical Hall-Petch effect (Hall, 1951; Petch, 1953), a phenomenon widely documented in metals (for review, see Cordero et al., 2016). The microphysics of this effect rely on the interactions between mobile lattice dislocations and grain boundaries (Cordero et al., 2016). In olivine, inferences of these phenomena are based on *post-mortem* microscopy studies of deformed samples (e.g., Wallis et al., 2020).

At increased temperatures, diffusion enables the mobility of defects within the grain boundary plane (Ashby, 1972). Under an applied differential stress, grain boundaries start to slide, which can be accommodated by diffusion of vacancies, mobility of dislocations within the grain boundary plane, or elastic processes (Ashby, 1972). Grain-boundary sliding generates incompatibilities in the crystal lattice, while relaxing the shear stresses within the grain-boundary plane, thus promoting diffusion creep in the crystal lattice (Raj and Ashby, 1971, 1972; Ashby, 1972). In olivine, laboratory-based studies have inferred that grain-boundary sliding (GBS) becomes a dominant deformation mechanism in polycrystalline olivine with certain grain sizes (e.g., Hirth and Kohlstedt, 1995; Hansen et al., 2011; Tielke et al., 2016a; Hansen and Kohlstedt, 2015). This deformation mechanisms is of particular importance to the rheology of the upper mantle as extrapolations of flow laws to geological conditions indicate that GBS is a dominant deformation mechanism in much of the upper mantle, where it contributes towards seismic anisotropy and strain accommodation in diffusion creep (Hansen et al., 2011, 2012b; Ohuchi et al., 2015; Tielke et al., 2016a; Hansen and Kohlstedt, 2015). Moreover, defect motion along grain boundaries could also impact rock properties deforming over short, transient periods (Jackson et al., 2014; Faul and Jackson, 2015). For example, Faul and Jackson (2015) highlight the importance of grain boundaries in seismic attenuation, and indicate that dislocation-related attenuation could also be of importance. Consequently, studies investigating strain accommodation in olivine have placed processes involving grain boundaries under increased significance (e.g., Samae et al., 2021; Bollinger et al., 2019; Sun et al., 2016; Jackson et al., 2014; Cordier et al., 2014; Gasc et al., 2019; Ferreira et al., 2021; Thieme et al., 2018).

Although significant advances have been made towards understanding the structure, composition, and chemistry of grain boundaries in olivine (for review, see Marquardt and Faul, 2018; Demouchy, 2021), we lack direct observations documenting the interactions between grain boundaries and crystal defects. In this study, we contribute towards filling this gap by deploying small-scale, uniaxial, *in-situ* mechanical testing on

Table 4.1: Details of micropillars tested in this study, manufactured on a low-angle grain boundary (LAGB) bicrystal and a high-angle grain boundary (HAGB) bicrystal.

Sample	Pillar	Material	Height (μm)	Top diameter (μm)	Bottom diameter (μm)	Taper angle (°)
Fo014 SB	P5	bicrystal AB	7.2	2.12	3.41	3.9
	P6	crystal A	6.5	2.55	3.58	5.6
	P7	bicrystal AB	7.6	2.38	3.61	3.4
	P8	crystal B	7.2	2.49	3.40	2.9
Fo011 HAGB	P1	crystal A	7.2	2.89	3.60	2.6
	P2	crystal A	7.6	2.79	3.52	2.6
	P3	bicrystal BA	8.4	2.42	3.06	1.9
	P4	crystal B	9.0	2.55	3.67	3.2
	P5	bicrystal BA	8.0	2.42	3.08	2.0
	P6	bicrystal BA	8.0	2.42	3.05	1.8

two pure forsterite (Fo) bicrystals. The experiments are performed at a temperature of 700°C with a sample orientation designed to maximise the resolved shear stress on the grain-boundary plane and promote grain-boundary sliding. Testing a pure Fo synthetic bicrystal allows us to remove the impact of prexisting defects and investigate a specific boundary of known character. This strategy of using bicrystals to probe interface properties has successfully been applied in a number of engineering materials (for review, see Dehm et al., 2018). Furthermore, increased capabilities for testing at high-temperatures have enabled an increasing number of experiments into deformation of ceramic materials (for review, see Korte-Kerzel, 2017). To date, micropillar experiments investigating geological materials have been scarce (Kranjc et al., 2020; Keller et al., 2017; Sly et al., 2020; Montagne et al., 2014; Korte and Clegg, 2009), and none have been conducted on isolated grain boundaries in geological materials. In this contribution, we bring these strategies together to test the relative shear strength of grain boundaries compared to crystal interiors at 700°C.

4.2 Experimental methods

4.2.1 Sample preparation

We investigate two pure forsterite (Fo) bicrystal samples containing a low-angle grain boundary (LAGB, 4°, [100]/(014)) and a high-angle grain boundary (HAGB, 60°, [100]/(011)), respectively. The low-angle grain boundary is parallel to the (014) plane and the two crystals are misoriented around [100]. The high-angle grain boundary is parallel to the (011) plane and the two crystals are misoriented around [100] (Marquardt and Faul, 2018). The samples have been prepared using the wafer-bonding technique (Heinemann et al., 2001; Hartmann et al., 2010). This technique generates synthetic

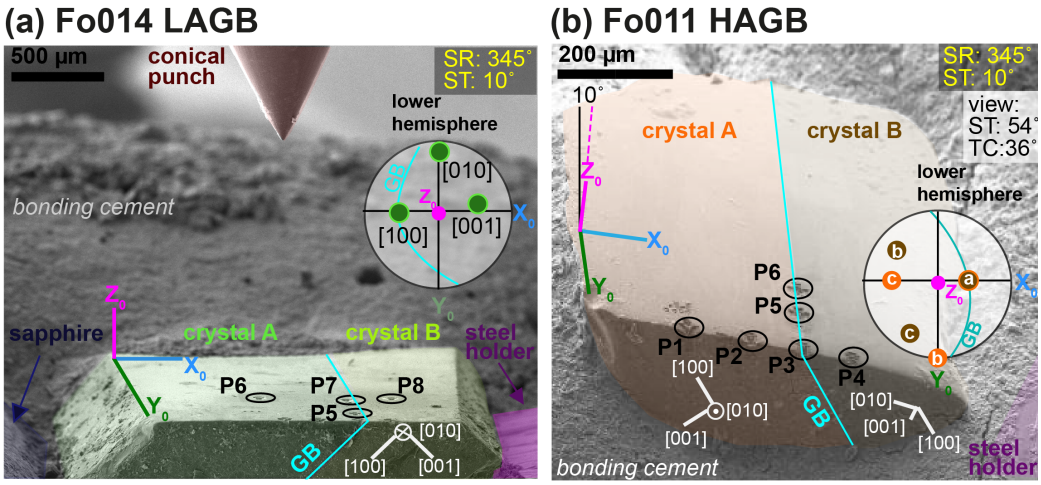


Figure 4.1: Sample assembly for the low-angle grain boundary in (a) and the high-angle grain boundary in (b). Panel a) is a colourised image of the low-magnification *in-situ* view of the micropillars. The coloured axes represent the sample surface coordinate convention. Panel b) is a colourised image of the high-angle grain boundary bicrystal assembly imaged with the stage tilt (ST) and tilt correction (TC) with the least distortion along the Z_0 axis (i.e., parallel to the pillar vertical axis). The orientation of the samples is described using lower hemisphere stereographic plots of the crystallographic axes. Both samples are tested at the same stage rotation (SR) and stage tilt (ST). Full details of pillar geometry are in table 4.1. Images of the pillars before deformation can be found in Supplementary Materials (Figure C.1).

grain boundaries free of any induced plastic deformation and chemical contamination (Heinemann et al., 2001). The grain-boundary misorientation angle is controlled in order to generate symmetric, low-energy, and near-coincidence grain boundaries (Heinemann et al., 2001; Hartmann et al., 2010; Marquardt and Faul, 2018). Similar samples as the HAGB bicrystal used in this study have been characterized in detail by Marquardt and Faul (2018), revealing that the high-angle grain-boundary width is less than 1 nm and the plane is faceted on the nm-scale (Figure 9, Marquardt and Faul, 2018). The same HAGB bicrystal has also been investigated via room-temperature nanoindentation in Chapter 3.

Figure 4.1 displays the bicrystal sample assembly for *in-situ* testing. To maximize shear-stresses on the grain boundary plane, we tilted the bicrystals in a steel mount and polished a new surface at 45° to the grain-boundary plane. Bicrystals were mounted with high-temperature Omegabond-600 cement. The surfaces were polished flat using diamond polycrystalline suspensions with grit sizes ranging from 9 μm down to 0.05 μm. The surfaces were finally polished with colloidal silica. The orientation of the bicrystals relative to the polished surface was determined using electron backscatter diffraction (EBSD).

We tested micropillars containing the grain boundary as well as micropillars manufactured in the crystal interior (Figure 4.1, Table 4.1). Micropillars with nominal diameters of 2–2.5 μm and a height-to-diameter ratio of ∼1:3 were manufactured with a Zeiss-AURIGA Ga+ focused ion beam (FIB) using decreasingly smaller currents from 2 nA to 50 pA. The initial diameter, height, and tapering of the pillars have been measured using scanning electron microscope (SEM) images and are reported in Table 4.1. Some micropillars were manufactured in the margin of the sample for optimal imagining conditions, as the TESCAN Mira3 SEM stage is tiled by 10° with respect to the SEM imagining angle (Figure 4.1). The SEM images of the micropillars before deformation are presented in Supplementary Materials (Figure C.1).

4.2.2 Mechanical testing

The tested micropillars using a flar-end diamond tip with the shape of a 60° cone with a flat end with a nominal diameter of 10 μm. We deformed the micropillars *in-situ* with a Hysitron PI88 SEM Picoindenter. The *in-situ* images were captured with a custom TESCAN Mira3 SEM. The mechanical tests were load-controlled with a trapezoid loading function and maximum a hold segment of 120 s at a temperature of 700°C (e.g., Figure C.6 in Supplementary Materials). Table 4.2 reports the time corresponding to constant load in each experiment. The loading rates for the LAGB

and HAGB bicrystals were 2 mN/s and 0.8 mN/s, respectively. The micropillars within the bicrystal interior have trenches of 20 μm diameter milled around them to aid imaging. Thus, the top 20 % was imaged during *in-situ* testing for the pillars inside the bicrystal interior.

4.2.3 Calculations of stress and strain

Several corrections were applied to the reported load-displacement data. The acquisition software automatically corrects for drift in measured displacement due to the thermal effects, for which the total drift is on the order of 10s on nm (Supplementary Materials, Figure C.2). In addition, we correct load and displacement data for the point of surface contact and machine-assembly compliance.

The experimental set-up in Figure 4.1 is influenced by the compliance of the instrument, the indenter tip, the steel and cement bond used in the sample assembly, and each pillar acting as a cylinder indenting into the substrate. Thus, we can describe the reported displacement, h_{rep}, as

$$h_{\text{rep}} = h_{\text{ms}} + h_{\text{base}} + h_0 + h_{\text{p}}, \tag{4.1}$$

where h_{ms} is the displacement due to the combined impact of the machine stiffness and the stiffness of the mounting assembly, h_{base} is the displacement due to the pillar base indenting into the bulk sample, h_0 is the difference between the reported point of first surface contact and the actual point of surface contact, and h_{p} is the displacement within the pillar of interest in response to an applied load. We account for h_0 by finding the point of surface contact at which displacement and load should be 0 after inspecting the reported load-displacement curves at small loads and noting a sharp increase in reported values.

The combined compliance of the machine and sample assembly is determined by using data collected from elastic experiments in the bulk sample. These experiments are indents at small loads placed in the crystal interior at 700°C, with no residual indent in the sample surface. Since there is no plastic penetration in the bulk sample surface, the contact area remains constant and the conical tip acts as a cylindrical punch. We compare these data to the calculated displacement, h, for an applied load, P, using Sneddon's solution for indenting with a flat-ended cylindrical punch into an elastic half space (Sneddon, 1965b; Fischer-Cripps, 2011, Chapter 3)

$$P = 2aE_{\text{eff}}h, \tag{4.2}$$

where E_{eff} is the reduced modulus and a is the contact radius. We computed the reduced Young's modulus as ${E_{\text{eff}}}^{-1} = \frac{1-vs^2}{Es} + \frac{1-vi^2}{Ei}$ using estimated values for the forsterite Poisson's ratio ($vs = 0.2465$) and Young's modulus ($Es = 180$ GPa) at 700°C (Kumazawa and Anderson, 1969, Table 8) and $Ei = 1150$ GPa, $vi = 0.07$ for the conical indenter. The contact radius a has been estimated by measuring the imprint of the indenter into the sample surface in experiments conducted at higher loads, in which a small amount of plastic displacement (< 100 nm) leads to an observable imprint. The measured diameter of the punch impression on SEM images is 5.6 μm.

We can calculate the error, h_{err}, due to the compliance of the system as the difference between the reported values, h_{rep}, and predicted values, h_{pred} using Equation 4.2. For each pillar, h_{ms} is calculated using the linear fit between h_{err} and P determined for each sample assembly (see Figure C.3 in Supplementary Materials).

The impact of the pillar indenting into the substrate, h_{base}, is computed by using Equation 4.2 and the measured values of the diameter at the bottom of the pillar displayed Table 4.1. This correction is an approximation based on Sneddon's solution (Sneddon, 1965b), and does not account for tapering or aspect ratio of the micropillar acting as a cylindrical punch (Fei et al., 2012).

In order to calculate the stress-strain values using h_{p} determined from Equation 4.1 and reported values of the applied load, P, we make some assumptions regarding the deformation style. First, we assume that the applied load is purely uniaxial and centrosymmetric, the contact area between the flat punch and the deforming pillar stays nominally constant, and it is equal to the area, A_0, at the top of the pillar such that the engineering stress, σ_{A}, is defined as

$$\sigma_{\text{A}} = \frac{P}{A_0}, \tag{4.3}$$

and the engineering strain ε_{A}, is defined as

$$\varepsilon_{\text{A}} = \frac{h_{\text{p}}}{H_i}, \tag{4.4}$$

where H_i is the height of the pillar at the beginning of each test. Note that at the start of the first test the height of the pillars is the height H_0, reported in Table 4.1. The height at the beginning of subsequent tests is H_0 minus the residual displacement, h_{r}, after unloading in the previous test such that $H_i = H_0 - h_{\text{r}_{i-1}}$, where the subscript i denotes each test, and n is the number of total tests of each pillar. The area A_0 at the top of the pillar is calculated using the diameter values reported in Table 4.1. Violating assumptions of constant area of contact through pillar tapering could result

in a stress gradient with the highest stresses at the top of the pillar (Dehm et al., 2018).

Secondly, we calculate the stress-strain values for deformation at constant volume. This calculation assumes plastic deformation only, without any crack formation. We calculate the stress, σ_{V}, at constant volume as

$$\sigma_{\mathrm{V}} = \frac{P}{A_i} = \frac{PL_i}{V_0}, \tag{4.5}$$

where L_i is the length of the pillar during testing and it is equal to the height H_i of the pillar at the start of each test minus the displacement h_{p} into the pillar, and V_0 is the initial volume. We calculate V_0 using the volume formula of a conical frustum

$$V_0 = \frac{\pi H_0}{3}\big[(r_{\mathrm{top}} + H_0 \tan(\beta))^2 + 2r_{\mathrm{top}}^2 + r_{\mathrm{top}} H_0 \tan(\beta)\big], \tag{4.6}$$

where β is the tapering angle measured using SEM images and reported in Table 4.1 and r_{top} is the radius at the top of the pillar. For samples with height to width ratios of 1:3 and taper angles of 2–3° the resulting maximum errors in stress are 10–15% (Dehm et al., 2018). We calculate the strain at constant volume ε_{V} using

$$\varepsilon_{\mathrm{V}} = \ln \frac{L_i}{H_{\mathrm{i}}}. \tag{4.7}$$

4.2.4 Microstructural investigations

We further characterized pillar 6 in the HAGB sample using scanning transmission electron microscopy (STEM) at Imperial College London. For these investigations we coated the sample with a Pt layer and proceeded to prepare a TEM foil parallel to the indentation direction. We used a standardised procedure to mill and lift the TEM foil using a Ga^+ ion beam. We imaged the foil using a dual-beam Helios microscope operated at a voltage of 30 kV and emission current of 86 pA.

4.3 Results

4.3.1 Low-angle grain boundary bicrystal

The bicrystal containing the low-angle grain boundary (LAGB, Fo014) has been mounted such that the grain-boundary plane is at approximately 45° to the loading direction. The [100] axis is shared amongst the two crystals, while the [010] axis is perpendicular to the loading direction (see Figure 4.1a). The two crystals are misoriented around [100] by 4°. The loading direction of pillars in the crystals in the

Table 4.2: Details of the mechanical tests on micropillars described in Table 4.1.

Sample	Pillar	Test	Max load (mN)	load hold (s)	*In-situ* observation
Fo014 SB	P5	1	1	10	system error
		2	8	60	permanent
	P6	1	1	10	system error
		2	8	60	permanent
	P7	1	1	10	system error
		2	2	10	elastic
		3	3	60	permanent
		4	4	60	permanent
	P8	1	1	60	elastic
		2	2	60	permanent
		3	3	60	permanent
		4	4	60	permanent
		5	4	60	permanent
		6	4	120	permanent
		7	5	60	permanent
Fo011 HAGB	P1	1	1	5	elastic
		2	8	5	permanent
		3	8	5	system error
		4	8	5	permanent
	P2	1	1	5	elastic
		2	6	10	permanent
		3	6	10	permanent
		4	6	60	permanent
		5	6	60	permanent
	P3	1	1	5	permanent
		2	8	5	permanent
	P4	1	1	5	elastic
		2	3	5	permanent
		3	3	5	permanent
	P5	1	1	5	permanent
		2	6	60	system error
		3	6	60	permanent
		4	6	60	permanent
	P6	1	1	5	permanent
		2	6	60	system error
		3	6	60	permanent

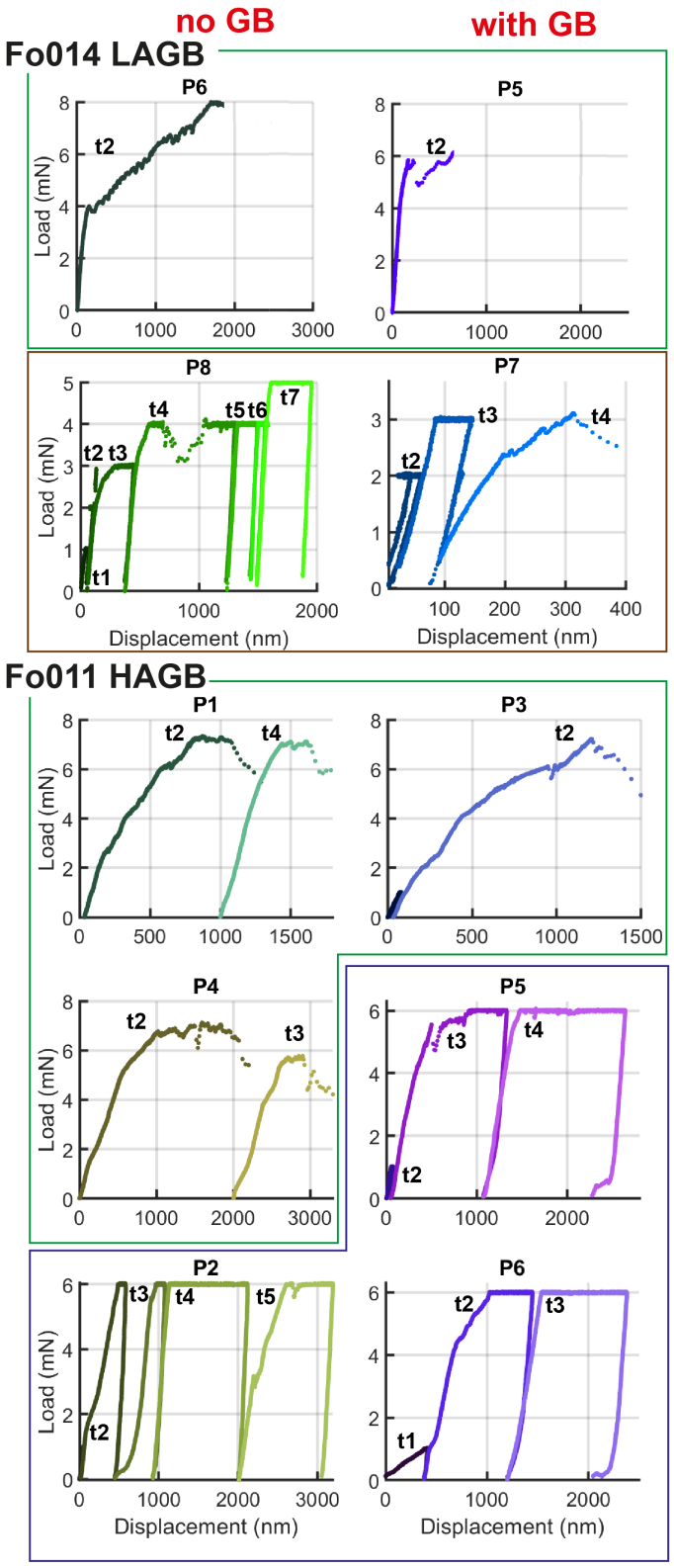


Figure 4.2: Load-displacement data for the micropillars described in Table 4.1. The left column corresponds to pillars in the single crystals, and the right column corresponds to pillars containing an interface. The outlined groups indicate tests conducted at similar maximum load and length of hold, as described in Table 4.2.

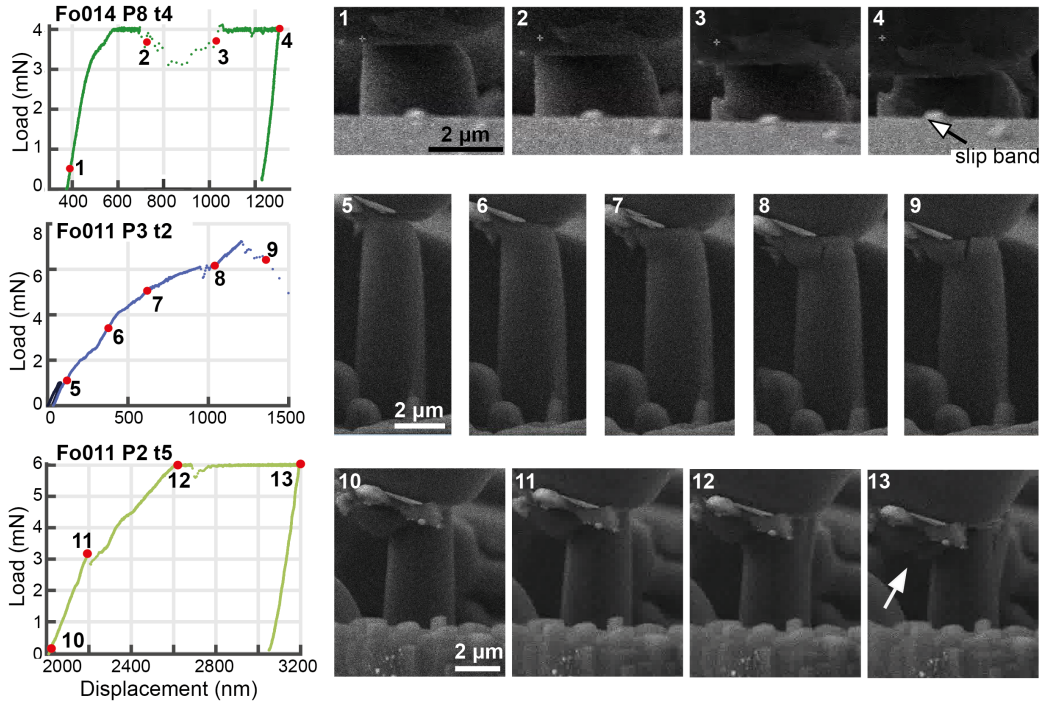


Figure 4.3: Examples of load-displacement curves alongside *in-situ* images. The white numbers on the images correspond to the marked red points in the load-displacement curves. The arrows mark slip bands.

LAGB sample is close to the $[101]_c$ orientation in the convention of a cubic lattice (Durham and Goetze, 1977).

Figure 4.2 presents the reported load-displacement data for Fo014 grouped by the type of test. Pillars 5 and 6 (green outline) were tested with a target load of 8 mN, and pillars 7 and 8 (brown outline) were tested with target loads of 4 and 5 mN, respectively, resulting in repeated creep tests (Table 4.2). In Figure 4.2, the pillar containing the grain boundary (P5) supports higher elastic loads than the pillar without the grain boundary. During the creep tests, pillar 7 containing the grain boundary displays brittle failure after 500 nm of displacement, whereas pillar 8 accommodates 2000 nm of displacement. Figure 4.3 displays further details of the correlation between the mechanical data and the *in-situ* observations. In pillar 8, the significant drop in load during test 4 corresponds to slip band formation at $\sim$ 45° to the loading direction observed *in-situ*. Subsequent slip bands do not have a corresponding load drop in the mechanical data.

Figures 4.4a and c display the stress and strain assuming a constant contact area for the low-angle grain boundary, and Figures 4.4b and d display the same stress and strain but assuming a constant volume. During the tests with a short load hold

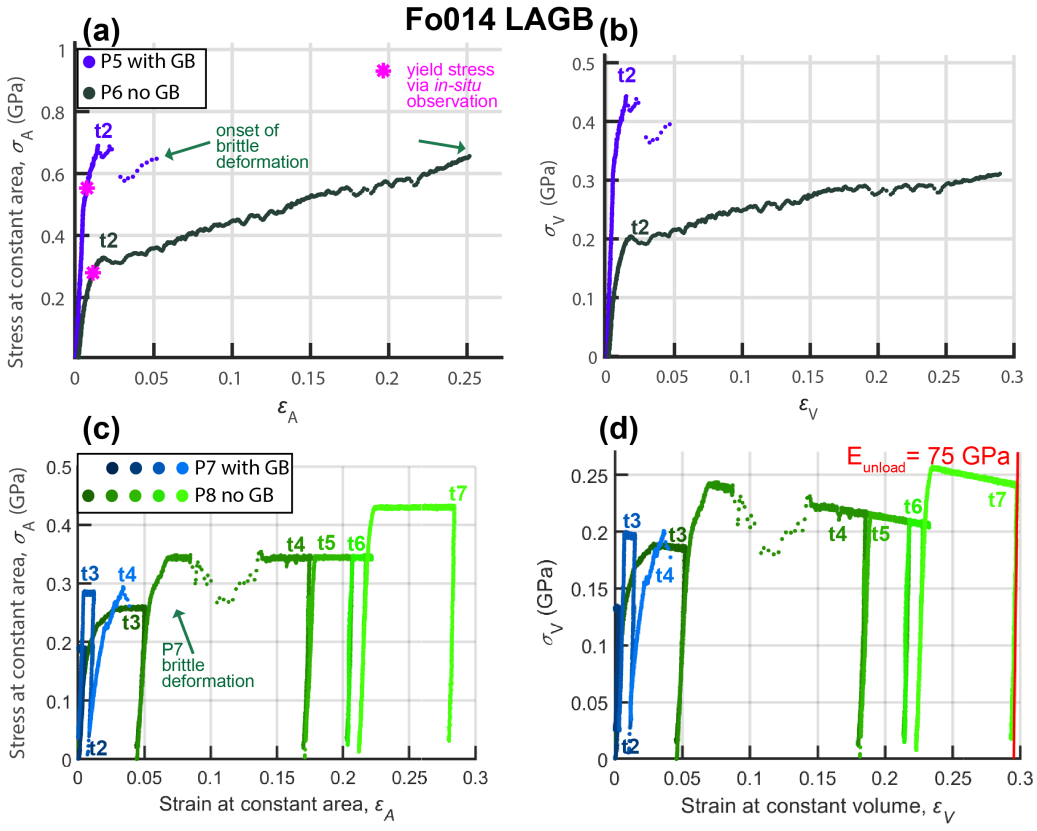


Figure 4.4: Compilation of stress-strain curves for the Fo014 sample with a low-angle grain boundary. Note the different scales of the vertical axes. The magenta stars mark the yield stress determined from *in-situ* observations.

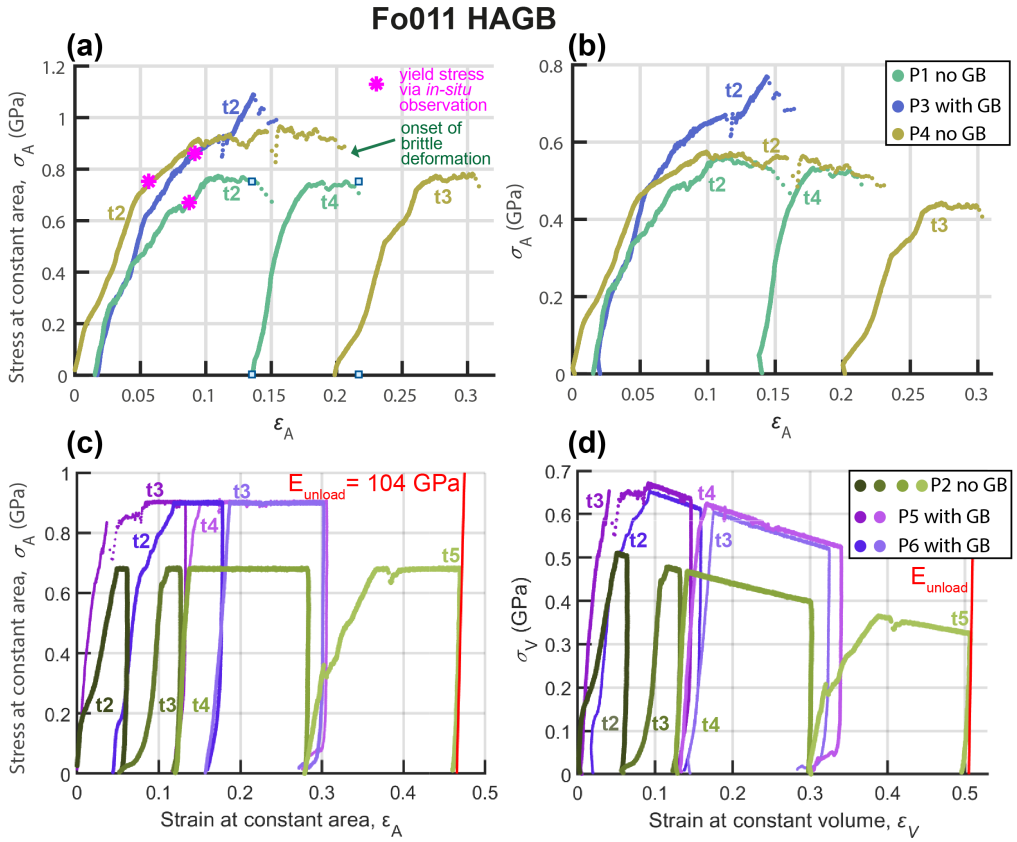


Figure 4.5: Compilation of stress-strain curves for the Fo011 sample with a high-angle grain boundary. Note the different scales of the vertical axes. The magenta star markers mark the yield stress determined from *in-situ* observations.

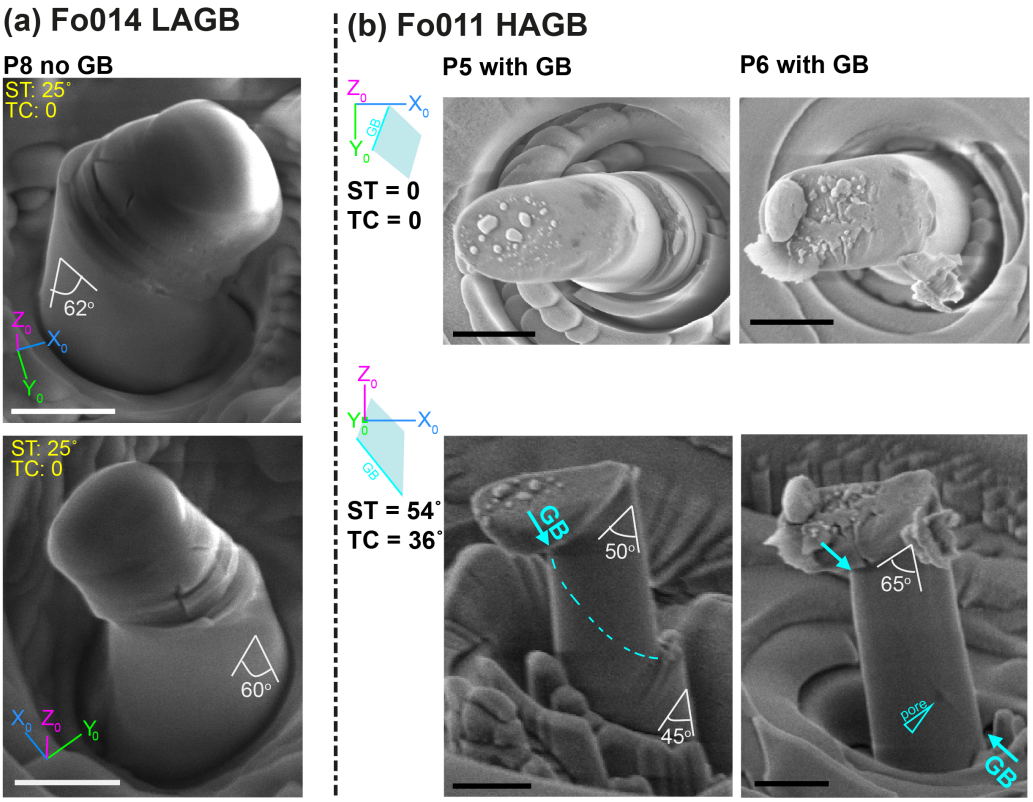


Figure 4.6: Compilation of images of deformed a) pillar 8 in the LAGB sample and b) pillars 5 and 6 containing the HAGB. The coordinate annotation references the coordinate system in Figure 4.1. All scalebars are 2 μm. Note that the images (and thus the angle) in panel a) have no tilt correction (TC) applied for the stage tilt (ST) of 25°. SEM characterization of all the pillars can be found in Supplementary Materials, Figures C.4 and C.5.

segment, the pillar with the grain boundary (P5) yields at a stress of 0.6 GPa, while the pillar without the grain boundary (P6) yields at a stress of 0.3 GPa. During the creep tests in Figure 4.4c, the pillar without the grain boundary (P8) exhibits plasticity at higher stresses and for a significantly increased time (see also Figure C.6a) compared to the pillar with the grain boundary (P7). Consequently, the computed stresses in Figure 4.4b and d have smaller values than the stresses calculated assuming a constant area of contact. Figure 4.6a documents in further detail the slip bands formed during test 4 in pillar 8 and during subsequent tests. We can observe that the deformation in the pillar is localised in the slip band and the base of the pillar is relatively undeformed. The features observed in the stress-strain curves in Figure 4.4c are also detectable in strain- and stress-rate data in Figure C.6, which highlights that P8 accommodates significantly more plastic strain than P7. Except pillar 8, all the pillars in the low-angle grain boundary bicrystal have been deformed to failure. Detailed SEM characterization can be found in Supplementary Materials (Figure C.4).

4.3.2 High-angle grain boundary sample

The bicrystal containing the high-angle grain boundary (HAGB, Fo011) has been mounted such that the grain boundary plane is tilted 30° with respect to the loading direction. The [100] axis is shared amongst the two crystals, which is in the plane of the grain boundary. The two crystals are misoriented around [100] by 60 °. In crystal A_{HAGB} the [010] axis is perpendicular to the loading direction, and the crystal orientation is close to $[101]_c$ in the convention of a cubic lattice (Durham and Goetze, 1977). In crystal B_{HAGB}, the [001] axis is close to being perpendicular to the loading direction (Figure 4.1b).

Figure 4.2 presents the reported load-displacement data grouped by the type of test. Pillars 1, 3, 4 (in the green outline) were tested under a load of up to 8 mN with no hold segment (Table 4.2). The pillar containing the grain boundary (P3) reaches catastrophic failure after one test, whereas the pillars without the grain boundary (P1 and P4) sustain two cyclic tests at 8 mN before catastrophic failure. Pillars 2, 5, 6 (purple outline) were tested with a load function with a hold segment of 60s at the maximum load of 6 mN, which is the approximate load of yielding for pillars 1, 3, 4.

Figure 4.3 presents the *in-situ* deformation of two pillars from the HAGB sample. Pillar 3 (P3) with the GB reaches catastrophic deformation at 6 mN. At this load, a crack initiates subparallel to the loading axis, before complete destruction at 7 mN. Pillar 2 (P2), without the GB, sustains multiple cycles of loading at 6 mN (Figure 4.2). After test 4 the top part of the pillar 2 is deforming by slip bands developed

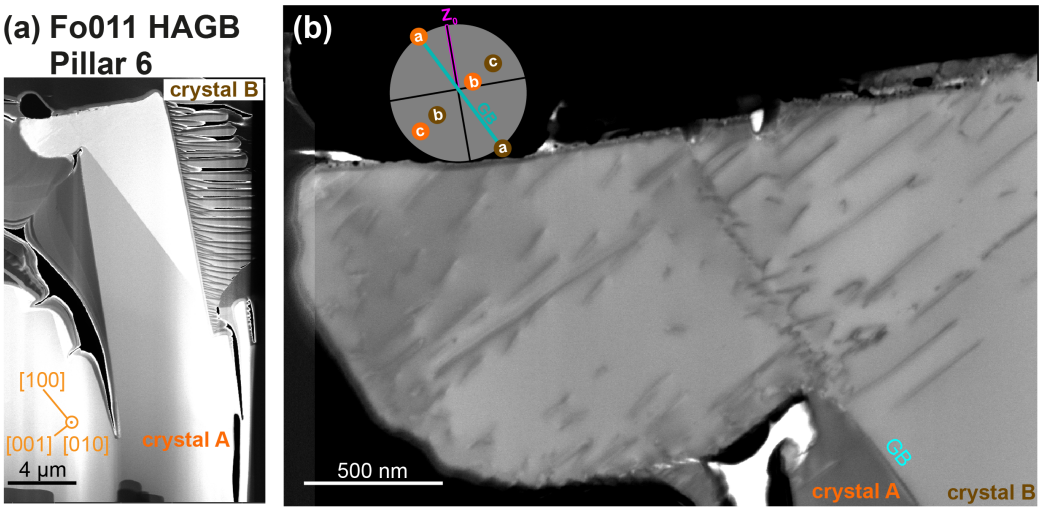


Figure 4.7: STEM images of a FIB lamella cut parallel to the indentation direction in pillar 6 in the HAGB sample. The lower hemisphere diagram is rotated such that the center of the diagram coincides with the axis perpendicular to the plane of view. a) Dark-field image of pillar 6 after deformation. b) Bright-field image of the upper part of deformed pillar 6.

at approximately 45° to the loading direction. Figure 4.3 displays further slip band formation at the top of the pillar during test 5, as well as crack formation at the side of the pillar, parallel to the loading axis. No buckling or deformation is observed at the bottom of pillar 2 (see Supplementary Materials, Figure C.5).

Figures 4.5a and c display the stress-strain curves assuming a constant contact area for the high-angle grain boundary, and Figures 4.5b and d display the same stress and strain but assuming a constant volume. Pillars 1 (P1) and 4 (P4) without the grain boundary (Figure 4.5a) yield at a stress at constant area of 0.7 GPa and 0.75 GPa, respectively. The pillar containing the grain boundary, P3, yields at a stress of approximately 0.9 GPa. Figure 4.5a highlights that the pillars without the grain boundary accommodate more plastic strain prior to failure. Similar to the LAGB sample, assuming deformation at constant volume and using Equations 4.5 and 4.7 results in decreased stress values and moderately increased strain values (Figure 4.5b, d). Stress-strain curves for the creep tests are displayed in Figure 4.5c and d. The pillars with the grain boundary, P5 and P6, deform at an imposed stress of approximately 0.9 GPa, while the pillar without the GB, P2, deforms at an imposed stress of 0.7 GPa. All the HAGB pillars in the creep tests accommodate a similar amount of plastic strain (Figure C.4b). This observation is also highlighted in strain-rate data in Figure 4.6, Supplementary Materials. Figure 4.6b displays post-deformation characterization of P5 and P6. Pillar 5 displays slip bands in both the A_{HAGB} and B_{HAGB} crystals,

while pillar 6 only has slip bands formed in the B_{HAGB} crystal. The slip bands in the micropillars containing the bicrystal BA_{HAGB} have a similar orientation to the ones in P2 in the single crystal A_{HAGB} (Figure 4.3, Supplementary Materials Figure C.5). Notably, the slip bands observable in pillars 5 and 6 are perpendicular to the GB plane, but do not intersect the GB. The interface is intact and does not display any sliding after deformation (Figure 4.6b). In Figure 4.6b we can observe a pore opening along the GB plane that was not present pre-deformation (Supplementary Materials Figure C.1). The pillars tested in this study accommodate plastic deformation mostly at the top of the pillar. This observation indicates that the stress calculations using the top diameter to estimate the contact area are reasonably representative of the stresses associated with deformation of the pillar (Figures 4.4a, c and 4.5a, c).

STEM characterization of P6 presented in Figure 4.7 reveals dislocation structures in the top crystal B_{HAGB}, with dislocation lines appearing perpendicular to the GB plane. Figure 4.7a confirms that dislocation structures are present dominantly in crystal B_{HAGB}, without any crystal lattice distortion in the vicinity of the grain boundary. At higher magnifications in Figure 4.7b, multiple slip systems are observable. We attribute the dislocations with elongated dislocation lines as corresponding to the activity of [001] screw dislocations on the [001](100) slip system. Aditionally, Figure 4.7b displays a dislocation array colinear with the grain boundary, which is consistent with the activity of edge dislocations on the [100](001) slip system. In Figure 4.7, the grain boundary appears offset along the plane with maximum resolved stresses perpendicular to the GB.

4.4 Discussion

In this study, we investigate the role of grain boundaries during deformation of forsterite at 700°C via *in-situ* micropillar compression, and we further characterize a deformed pillar using scanning transmission electron microscopy (STEM). Our key observations are that 1) the pillars with the grain boundary display a slightly higher yield stress, 2) the pillars without the grain boundary display higher plastic strain, and 3) the grain boundary does not accommodate any of the plastic strain. We interpret our results under the assumption that the presence or absence of a grain boundary is the key variable among pillars, aside from any geometrical differences (see Table 4.1). We calculate the resolved shear stresses in pillars displaying slip band formation in order to assess the relative differences in strength between the single-crystal and bicrystalline pillars.

We use the stress values at constant area of contact to estimate the maximum applied shear stress on the grain boundary and the resolved shear stresses, τ, on the available slip systems using the Schmid law (Schmid and Boas, 1950)

$$\tau = \sigma_{\mathrm{A}} \cos(\phi) \cos(\lambda), \tag{4.8}$$

where ϕ is the angle between the normal to the plane and the applied force, and λ is the angle between the slip direction and the applied force. The Schmid factor, $cos(\phi)cos(\lambda)$, ranges from 0 for the least favourably oriented slip plane to 0.5 for the most favourably oriented slip plane. In this paper, we use forsterite to refer to Mg_2SiO_4 and olivine to refer exclusively to compositions including iron, which have been used in previous studies (e.g., San Carlos).

4.4.1 The impact of grain boundaries on micropillar deformation

In Figure 4.8, we compare the yield stress marked in Figures 4.4a and 4.5a against the yield stress calculated from hardness measurements at similar temperatures reported by Darot et al. (1985) in forsterite and Evans and Goetze (1979) in olivine single crystals. In Vickers indentation the maximum depth of contact is proportional to the diagonal of the imprint on the surface by a factor of 7 (Fischer-Cripps, 2011, Chapter 2). This proportionality is a direct result of the Vickers indenter geometry and allows us to transform reported diagonal lengths by Evans and Goetze (1979) and Darot et al. (1985) into indentation contact depth. We plot the reported yield stress by Evans and Goetze (1979) and use a similar constraint factor approach to transform the reported hardness by Darot et al. (1985) into yield stress (Evans and Goetze, 1979).

Figure 4.8a highlights that the micropillars yield at smaller values than olivine at similar temperatures (Evans and Goetze, 1979) and that both data in this and previous studies display a significant size effect in the yield stress of olivine, which follows a power law exponent close to 1. This exponent value is significantly larger than published estimates at room temperature (Hansen et al., 2019; Koizumi et al., 2020) and could be attributed to temperature impact on size effects. For example, in LiF, the dependence of stress on pillar diameter increases with increasing temperature (Soler et al., 2014). However, the discrepancy in yield stress of pillars in the LAGB sample is too significant to be justified solely by size effects. We suggest that in the LAGB the size effect is overprinted by statistics of dislocation nucleation. The yield stress in small volumes of annealed crystals is controlled by the distribution of dislocation sources. In micropillar experiments, these sources can be associated with

the uneven contact between the tip and the top of the pillar, ion implantation due to FIB milling, or pre-existing crystal defects in the micropillar (Dehm et al., 2018). If the grain boundaries in our pillars are potent sources of dislocations, we would expect that the pillars with the grain boundary would yield at smaller stresses than the ones in the bulk crystals. However, Figures 4.8a demonstrates the opposite effect. Thus, we suggest that the higher yield stress of pillars containing the grain boundary in the LAGB sample is underpinned by the combined impact of the size effect and the stochasticity of dislocation nucleation in a volume with scarce sources. In the HAGB sample, the discrepancy in yield stress can be attributed to a size effect.

The discrepancy in yield stress between previous studies at similar temperatures and our study highlighted in Figure 4.8 could be due to experimental errors in approximating stress, sample orientation, or the confining pressure associated with each type of test. Figure 4.8b displays the orientation of the indented surface in different studies and highlights that the data from Darot et al. (1985) in forsterite was collected by indenting on a sample with a similar orientation to LAGB sample. We suggest that stress discrepancies with previous studies presented in Figure 4.8a are due to the difference in confining pressure in each type of test. The lack of a confining media at such small length-scales implies that the dislocations can escape the pillar, and therefore there are no long-range elastic interactions to generate hardening (e.g., Hansen et al., 2019). This phenomena could be further sped up by stress gradients in the pillar generated by tapering, or FIB-induced defects (Montagne et al., 2014). Moreover, TEM investigations under spherical indents in olivine indicate that the radius of the volume of dislocations is on the order or 3–4 μm (sample OP4-2 in Wallis et al., 2020) which is larger than the diameter of all our pillars. Figure 4.7 confirms the presence of dislocations at the edges of the pillar. Studies comparing spherical nanoindentation and micropillar tests within the same grain in steel materials document a good agreement amongst the trends of the stress-strain curves, although the magnitude of the stresses is considerably decreased in the pillar tests (e.g., Figure 25 in Pathak and Kalidindi, 2015a). Studies in calcite also report smaller yield stresses measured using micropillar experiments compared to nanoindentation for the same orientation and temperature (Sly et al., 2020). Studies documenting lower than expected stresses required for dislocation activity in micropillar compression of sapphire frame their observations in a model of heterogeneous dislocation nucleation of partial dislocation loops requiring lower stresses (Montagne et al., 2014). These phenomena could also be leading to the decreased stresses we observe in our experiments. However, other studies on more ductile ceramics compare the stress in micropillar compression

at 5% with the yield stress derived from sharp tip data with good agreement (Zenk et al., 2019). Micropillar compression on spinel at elevated temperatures also generates measurements in broad agreement with experiments at confining pressures, albeit with a possible size effect (Korte and Clegg, 2009).

Our data provide a minimum bound for grain-boundary strength under our experimental conditions. Using the maximum values of the imposed stress before sudden stress drop in Figure 4.4c, the maximum imposed shear stresses on the LAGB are $\tau_{\mathrm{max,LAGB}} = 0.15$ GPa in P7. The maximum imposed shear stresses on the HAGB tilted at 30° from the loading axis are $\tau_{\mathrm{max,HAGB}} = 0.4$ GPa in P5 and P6 (Figures 4.5c). Differences in the imposed creep stress in Figures 4.4c and 4.5c arise due to the small differences in the top diameter of the pillars (see Figure C.4, Table 4.1). We can approximate the high-angle grain boundary viscosity, η, following the formulation of Ashby (1972) as $\eta = \frac{kT}{8bD}$, where k is Boltzman's constant, $D = 10^{-28}m^2/s$ is the grain-boundary diffusion coefficient for $T = 700°C$ and 1 atm (Fei et al., 2012), and $b = 10.19 * 10^{-10}m$ is the greatest cell unit in forsterite. Using Ashby (1972) and constants for forsterite, we compute $\eta = 16.5 * 10^{15}Pa * s$, which translates to a grain-boundary velocity of $4 * 10^{-20}m/s$ for an applied shear force of 0.4 N (e.g., P5 in the HAGB bicrystal), on a grain boundary with 1 nm thickness (Marquardt and Faul, 2018). This calculation indicates that any grain-boundary sliding in these experimental conditions ($T = 700°C$ and 1 atm) would be below the displacement measurement resolution of the apparatus. Alternatively, a displacement of 1 μm would be accommodated in approximately 3 million years. Based on predictions by Ashby (1972) we expect the low tilt GB in the LAGB bicrystal to have an increased viscosity. However, less symmetrical grain-boundaries than the ones in this study are predicted to have a decreased viscosity compared to high-symmetry grain boundaries (Ashby, 1972). Thus, the maximum imposed shear stresses on the GBs ($\tau_{\mathrm{max,LAGB}} = 0.35$ and $\tau_{\mathrm{max,HAGB}} = 0.4$), which have been insufficient to promote deformation along the grain boundary, can be considered a minimum GB shear strength estimate in these temperature and pressure conditions, for contact lengths of 3–3.5 μm.

One consistent, yet qualitative, observation is that the pillars with the GB display a more brittle deformation style in both samples. This suggests that the tests are sampling the elastic impact of the grain-boundary, which acts as a site for maximising differential stresses within the pillar and leads to faster brittle failure in the pillars containing it. Thus, we can hypothesize that in the presence of the bulk crystal acting as a confining medium around the deformation volume containing the GB, the shear

stress concentrations around the GB region could promote the local generation of dislocations.

In these experiments, the GB does not accommodate any of the observable plastic deformation despite having similar or greater Schmid factors than the activate slip systems in the single crystals. In the LAGB sample, the Schmid factor equals 0.5 for both the most favourable slip systems ([001](100) and [100](001)) and the GB plane. In the HAGB sample, the Schmid factors are different for crystal A_{HAGB} (m=0.35 for [001](100)), and similar for the GB plane (m=0.43) and the top crystal B_{HAGB} (m = 0.43 for [001](100)). These Schmid factors indicate that the resolved shear stresses are the same or greater on the grain boundaries when compared to the most favourable slip systems in the crystal interior as other possible slip systems (e.g.,[001]{hk0}) have smaller Schmid factor values. However, the grain boundaries respond only elastically. Therefore, we can conclude that these grain boundaries are stronger than the crystals at 700°C and the geometry of deformation in Figure 4.1.

Figure 4.7 documents the resulting dislocation structures in the deformed crystal B_{HAGB} in P6 and confirms that the HAGB does not accommodate plastic strain. The two main groups of dislocations are consistent with the activity of [001]{hk0} and [100]{0kl} slip systems, which have been previously documented in samples deformed in the low-temperature plasticity regime (e.g., Mussi et al., 2014; Wallis et al., 2020). Figure 4.7b suggests that the shearing of crystal B_{HAGB} over crystal A_{HAGB} generates a complex stress state in which the bottom crystal A_{HAGB} acts as an indenter in the top crystal promoting dislocations parallel to the GB trace. There is some limited evidence of dislocations pilling up at the grain boundary.

Dislocation structures presented in Figure 4.7 are consistent with structures documented in olivine micropillar experiments at room temperature in a single crystal with a $[110]_c$ orientation under a constant stress of $\sim$ 4 GPa (Kranjc et al., 2020). However, the authors interpret the microstructures documented in the pillars after deformation as amorphous slip bands parallel to (100) (Kranjc et al., 2020), formed under a resolved shear stress of 2.2 GPa and a strain rate of $< 10^{-}6s^{-}1$. Evidence of olivine amorphization has been documented at stresses higher than 30 GPa from shock experiments (Jeanloz et al., 1977) and anvil cell experiments (Lacam et al., 1980; Williams et al., 1990; Andrault et al., 1995). Thus, we are reinterpreting the data presented by Kranjc et al. (2020) and provide an alternative explanation to their observations. Data in the Kranjc et al. (2020) experiments agrees well with the low-temperature plasticity flow law calibrated using sharp indentation by Kranjc et al.

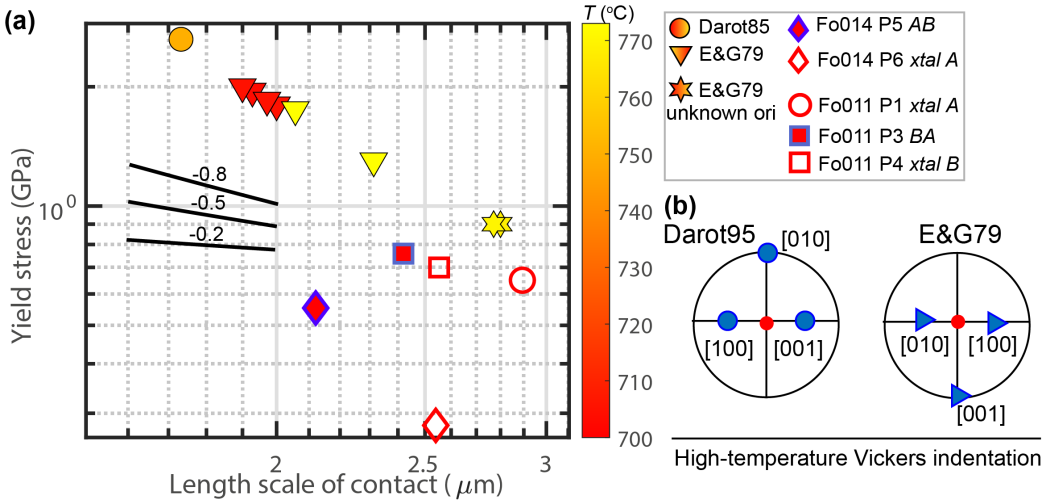


Figure 4.8: a) Yield stress from stress-strain curves in Figures 4.4a and 4.5a against Vickers indentation data from Darot et al. (1985) and Evans and Goetze (1979) on forsterite and olivine, respectively. All the included Vickers indents are at a maximum load of 0.5 N. b) Lower hemisphere plots describing the different orientations of the crystallographic axes with respect to the indentation direction.

(2016). This is further confirmed by Baral et al. (2021) who also additionally demonstrate that at strain rates of $< 10^{-}6s^{-}1$ amorphous olivine is weaker than crystalline olivine by a factor of 2. Therefore, one would expect that the presence of a much weaker, stress-induced phase actively accommodating plastic strain would generate a signal in the stress-strain curves of deformation. The stress-strain curves from Kranjc et al. (2020, see their Supplementary Materials) present no change in the constant stresses of deformation with increasing strain in the pillars that developed shearing (e.g., pillar 6 Kranjc et al., 2020). Their TEM observations of multiple slip bands and dislocations can be reconciled by the presence of slip systems with [001] on (100), (110) or (130) planes, observed dominantly in low-temperature deformation (Mussi et al., 2014). Moreover, TEM data under sharp indents in olivine, do not document any amorphization despite reaching higher stresses and having the deformation volume confined by the bulk crystal (e.g., Wallis et al., 2020; Gaboriaud et al., 1981).

4.4.2 Slip band analysis

In the LAGB (4°, [100]/(014)) sample, pillar 8 in crystal B_{LAGB} displays sustained slip band formation at an angle of 45

°

from the loading axis, towards the positive X_0 direction in the reference frame of the sample surface. This geometry coupled with the crystallographic orientation displayed in Figure 4.1a is consistent with slip in the [001] direction on the (100) plane. For P8, the theoretical Schmid factor has the same value of 0.5 for both [100](001) and [001](100). Therefore, in an uniaxial test the resolved shear stresses are the same on both systems. However, we only observe slip consistent with [001](100). One explanation is that the slight asymmetry in tapering at the top of P8 (Figures 4.3 and C.1) results in different resolved shear stresses on the two possible slip planes, and [001](100) is preferred. Another explanation is related to the energy barriers associated with displacement on these two slip systems. Ab initio calculations of shear on different slip planes of forsterite at zero temperatures indicate that [100](001) displays higher peaks in energy barrier than [001](100) (Durinck et al., 2005). If this relative difference extrapolates linearly at 700°C then in the undeformed crystal in P8 the [001](100) slip system would be energetically more favourable. Our direct observation is consistent with previous experiments on olivine single crystals (Demouchy et al., 2013; Tielke et al., 2016b) and numerical models simulating [100] and [001] glide (Durinck et al., 2007) indicating that at low temperatures (< 1000°C) and high stresses, the [001](100) system dominates deformation.

Using the stress applied at the top of P8 before the significant stress drop associated with slip band formation (Figure 4.3, frames 2–3) we can estimate the critical resolved shear stress for the [001](100) slip system as $\tau_{\mathrm{CRSS}}^{[001](100)} = 0.17$ GPa. This stress is the critical resolved stress required to activate the [001](100) slip system at 700°C in an annealed crystal. Thus, it is intrinsically linked to the stress required to activate dislocation sources and overcome the lattice friction to generate glide of dislocations. However, estimations of the critical resolved shear stress from micropillar experiments are both temperature and size sensitive (e.g., Kamimura et al., 2013; Soler et al., 2014). Notably, only the first slip band generation in P8 is associated with a burst of displacement of ~ 380 nm (Figure 4.3, frames 2–3, Figure C.4) as the stress-strain curves do not display further stress drops despite consistent slip band formation as characterised in Figure 4.6. We attribute this observation to the scarcity of dislocation sources prior to yielding. In load-controlled micropillar tests the displacement bursts are similar to the nanoindentation 'pop-ins', which supports the correlation of the displacement burst in test 4 with a sudden activation of dislocations in a crystal with little initial dislocation sources (Dehm et al., 2018; Kumamoto et al., 2017). Therefore, we can interpret plasticity during test 4 to be governed by dislocation nucleation, while in subsequent tests, plasticity is governed by dislocation motion. Similar stress

drops in micropillar experiments have also been reported in sapphire (Montagne et al., 2014).

In the HAGB sample (60°, [100]/(011)), slip band formation is present in P2 in crystal A_{HAGB}, in P5 in both crystals, and in P6 in the top crystal B_{HAGB} (Figures 4.1, 4.6, Table 4.1). We can observe slip bands at the end of test 4 in P2 in crystal A_{HAGB} (Figure 4.3, frame 10). Post-deformation characterization (Supplementary Materials, Figure C.5) and the orientation of crystal A_{HAGB} (Figure 4.1b) suggest that the deformation is consistent with slip in the [001] direction on the (100) plane at a tilt of 60° from the loading axis. Unlike the stress-strain curve corresponding to P8 in the crystal B_{LAGB}, no significant stress-drop is associated with slip-band formation in P2 in crystal A_{HAGB}, despite the relatively similar orientation of crystal A_{HAGB} and the crystals in the LAGB sample. The orientation of crystal A_{HAGB} with respect to the loading axis requires higher resolved shear stresses of $\tau_{P2} = 0.29$ GPa for the activity of [001](100), due to smaller Schmid factor in crystal A_{HAGB} compared to the crystals in the LAGB sample.

Figures 4.6 and 4.7 indicate that the top crystal B_{HAGB} in pillars 5 and 6 has been sheared with a net displacement towards the $-X_0$ in the sample reference frame, corresponding to the [011] crystallographic axis. Since there is no slip system with the [010] direction in forsterite (Demouchy, 2021), we suggest that this net deformation is generated by one or multiple slip systems in the [001] direction on {hk0} planes (Figure 4.7b). The [001]{hk0} slip systems have also been documented in other studies of olivine deformation at low temperatures and high stresses Demouchy et al. (2013); Mussi et al. (2014); Raterron et al. (2004). Gaboriaud et al. (1981) use high-temperature Vickers indentation on olivine single crystals to suggest that [001]{110} is activated at temperatures greater than 600°C, which is consistent with our experimental conditions. Wallis et al. (2020) present TEM data under a spherical indent in olivine single crystal in a similar orientation with respect to the loading axis as crystal B_{HAGB} (sample OP4-2 in Kumamoto et al., 2017; Wallis et al., 2020). The authors interpret the imaged dislocation structures as the activity of the [001](100) slip system split across multiple partial dislocations (Wallis et al., 2020). Using the angle between the slip trace and the edge of pillars in Figures 4.6 and 4.7, and assuming a slip direction of [001] the resolved shear stresses on the slip bands in the top crystal B_{HAGB} are $\tau_{P5,B} = 0.12$ GPa in P5, and $\tau_{P6,B} = 0.128$ in P6. In P5 both the top and the bottom crystal sustain plasticity. The orientation of the slip bands in the bottom crystal A_{HAGB} in P5 suggest a slip system with the [001] direction on a {hk0}

plane. Accounting for orientation differences we calculate the resolved shear stress $\tau_{\mathrm{P5,A}} = 0.32$ GPa on the [001]{kh0} slip planes in P5 on the bottom crystal $\mathrm{A_{HAGB}}$.

4.5 Implications

In-situ micropillar experiments on pure forsterite grain boundaries at 700°C reveal that pillars containing the grain boundary consistently support higher elastic loads compared to the pillars in the single crystal. Additionally, the pillars in the single crystal sustain higher plastic strain compared to the bicrystalline pillars. The grain boundary has been oriented at approximately 45° to the loading direction. Under these experimental conditions no sliding associated with the grain boundary has been recorded.

Observations presented in this study support the hypothesis that grain interiors are relatively weaker compared to grain boundaries. This hypotheses underpins observations of grain-size effects of the bulk yield stress in olivine low-temperature plasticity (Hansen et al., 2019). However, as grain-boundary diffusion rates increase with temperature (Fei et al., 2016) we expect a decrease in grain-boundary viscosity (Ashby, 1972) and an increase in grain-boundary mediated deformation (e.g., GBS, Hansen et al. (2011)). In a deforming polycrystalline material, the relative strength of the GBs at the same temperature varies with grain boundary character and orientation according to predictions by Ashby (1972). Therefore, with increasing deformation, the distribution of GBs might influence the bulk patterns of plastic anisotropy, and consequently strain localization.

We have also demonstrated that miniaturised mechanical testing facilitates measurements of isolated microstructural features in olivine. Experimental studies on olivine single crystals using a confining pressure document a transition between the dominance of [001](100) slip system (Demouchy et al., 2013; Tielke et al., 2016b) at temperatures smaller than 1000°C, after which [100](001) is also activated (Durinck et al., 2007; Demouchy et al., 2013; Tielke et al., 2016b). Experiments also document a change in relative strengths of [100](010) and [001](010) slip systems with confining pressure (Raterron et al., 2007). Therefore, future micropillar experiments at the higher-end of technical capabilities might provide a detailed, quantifiable, and *in-situ* understanding of the relative strengths of slip systems in olivine alongside increased miniaturisation (e.g., Idrissi et al., 2016).

Chapter 5

A novel torsion stage for the *in-situ* investigation of ductile materials under simple shear

"The first scientific observation of superplasticity dates back to 1912. [...] (78 years of observations) illustrate the fact that superplasticity is potentially an operational deformation mechanism over 20 orders of magnitude of strain rate and encompasses a wide range of polycrystalline materials."

Sherby and Wadsworth (1990)

A similar version of this chapter has been prepared for publication in the journal *Review of Scientific Instruments*, with the following author list:

Diana Avadanii[1], Lars Hansen[2], Katharina Marquardt[3], Phani Karamched[4], Oriol Galvada Diaz[5], and Angus Wilkinson[4]

[1] Department of Earth Sciences, University of Oxford
[2] Department of Earth and Environmental Sciences, University of Minnesota
[3] Department of Materials, Imperial College London
[4] Department of Materials, University of Oxford
[5] Department of Materials, Imperial College London

For this study, I investigated and selected options for the hardware components, liaised with the Earth Sciences technical workshop team for manufacturing of different components, liaised with a specialist company for purchasing a custom-made feedthrough, performed all experiments, prepared samples from solder alloys, prepared all samples for microscopy investigations, imaged the samples after deformation, performed digital image correlation experiments and subsequent data analysis, and wrote the first draft of the manuscript.

Abstract

Experimental deformation of materials under simple shear has been implemented in the investigation of superplasticity, shear-driven failure, and microstructure evolution. To this end, studies implement different strategies to transform a far-field compressive or tensile applied stress into shear stress in both mesocale and microscale specimens. In this study, we describe an apparatus developed to investigate *in-situ* ductile materials by directly applying a simple shear to a thin sheet of material. We propose a novel sample geometry compatible with established techniques for strain characterization and specimens with a wide range of starting microstructures. We demonstrate the capabilities of our apparatus by deforming solder alloys and aluminium, and use optical digital image correlation and electron microscopy for the *in-situ* characterization of the deforming sample.

5.1 Introduction

Material testing under simple shear has been widely implemented in deformation studies with applications ranging from imposing shear on specific slip systems (e.g., Heyer et al., 2014; Borkowski et al., 2018; Wieczorek et al., 2016) and studying mechanisms associated with superplasticity (e.g., Masuda et al., 2016; Rust and Todd, 2011; Bednarczyk et al., 2018; Langdon, 2009) to testing the strength of adhesive joints (e.g., Watson et al., 2019) and material interfaces (e.g., Mayer et al., 2015; Gigax et al., 2019; Chandra and Ghonem, 2001). Currently, the investigation of the interactions between different defects in ductile materials or the shear strength of interfaces relies on strategies to transform a far-field stress applied stress into shear stress. Recently, some of these strategies have been miniaturised in order to facilitate *in-situ* observations and the coupling between crystallography and strain localization during deformation (e.g., Masuda et al., 2016). Although *in-situ* deformation techniques expand the capabilities of investigating fundamental mechanisms, there are still outstanding caveats in each of the different proposed techniques.

In this study, we describe an apparatus and sample geometry developed in order to circumvent some of the current challenges in different techniques and investigate the *in-situ* deformation of ductile materials under simple shear. We start by providing a brief summary of the experimental strategies to investigate materials under simple shear in Section 5.2, and summarize their advantages, caveats, and applications. We present our novel apparatus and proposed sample geometry in Section 5.3, alongside the compatibility with established techniques for microstructure and strain characterization, such as electron backscatter diffraction (EBSD) and digital image correlation (DIC). We probe our design using three different ductile materials and report the results in Section 5.4. In Section 5.5 we discuss our measurements and identify outstanding materials science questions to which our proposed design could make meaningful contributions.

5.2 Brief review of material deformation in simple shear

To date, mechanical testing of materials in simple shear has relied on the transformation of tensile or compressive applied stresses into localised shear stress by implementing different strategies (e.g., Nizolek et al., 2021, and references therein). Technological

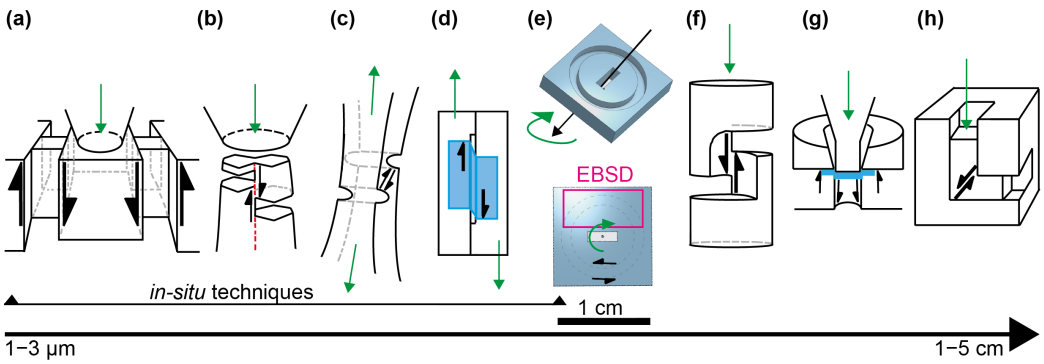


Figure 5.1: Summary of experimental strategies to study material deformation under shear. Figures a-e depict *in-situ* techniques. a) Micro double shear testing diagram adapted after Heyer et al. (2014). b) 'S'-shaped micropillar test adapted after Gigax et al. (2019). c) Tensile experiment with a notch adapted after Masuda et al. (2016). d) Uniaxial shear stage schematic adapted after Bae and Ghosh (2003). e) Our proposed sample geometry. f) Compact forced-simple-shear diagram adapted from Gray III et al. (2016), and further modified by Nizolek et al. (2021). g) Shear punch test diagram adapted after Lancaster et al. (2022). h) Equal-channel angular pressing test diagram adapted after Valiev and Langdon (2006).

advancements of *in-situ* techniques led to the adaptation of macroscale geometries to small-scale testing.

We summarize in Figure 5.1 the key experimental settings utilised for material testing under simple shear across multiple spacial scales. Figure 5.1a presents the geometry of ***in-situ* micro-double shear (MDS)** tests adapted after Heyer et al. (2014). In this testing geometry, a beam with a width of 3–10 μm is supported by thinned regions on each side. A force is imposed on the center of the beam, leading to shearing in the thinned regions, which are fixed to the bulk sample. The key advantage or this experimental design is the possibility of imposing large plastic strains with specific slip systems (Heyer et al., 2014), and it has been implemented in single-crystal studies of Au (Heyer et al., 2014), Cu (Pfetzing-Micklich et al., 2011; Wieczorek et al., 2016), Ni-based superalloys (Laplanche et al., 2018), and Al alloys (Borkowski et al., 2018). In these tests, complications might arise due to relative strength differences of the two shear zones, misalignment of the beam loading, and the impact of the superimposed bending stress on the two shear zones (Heyer et al., 2014; Mayer et al., 2015). Figure 5.1b presents a **"S"-shaped micropillar** compression geometry adapted after Gigax et al. (2019), which generates shear strain due to asymmetric side notches in a micropillar. This testing geometry circumvents mixed stress states, and facilitates material testing under simple shear parallel to the loading direction (Mayer et al., 2015; Gigax et al., 2019). However, the length of the sheared

area is limited by the distances achievable between the two notches on the pillar. The key application of this testing technique has been into the investigation of Cu-Si interfaces (Gigax et al., 2019) and nanolaminate materials (Mayer et al., 2015) as it represents a powerful tool for investigating the individual shear properties of planar features (e.g., grain boundaries). Both techniques require complex sample preparation using focused ion beam (FIB) milling.

Small-scale tensile testing can also be implemented to generate shear stresses (e.g., Nizolek et al., 2021, and references therein). For example, Figure 5.1c presents a schematic adapted after Masuda et al. (2016) of a **modified *in-situ* tensile specimen** with two "U"-shaped channels. These channels induce simple shear on the side of the specimen, which is imaged during deformation. In Figure 5.1c and d, the increased deformation volume facilitates observations on polycrystalline samples. Unlike shear induced in tensile experiments, a notched tensile specimen generates a singular shear direction in the observation plane, with a controlled position with respect to the starting microstructure (Masuda et al., 2016). The testing geometry has been applied for *in-situ* investigations of polycrystalline steel samples (Masuda et al., 2016). **Uniaxial shear stages**, such as the one in Figure 5.1d secure the specimen on two plates pulled in opposite directions (e.g., Bae and Ghosh, 2003; Bouvier et al., 2006). Successful testing of materials on a similar stage has been documented in Al (Bae and Ghosh, 2003; Rust and Todd, 2011; Lopes et al., 2003), and Al-Mg alloys (Alabort et al., 2016). Caveats of testing strategies similar to the ones presented in Figure 5.1c and d include complex stress state, sample rotation, heterogenities induced by specimen clamping, bulging, and different deformation mechanisms operating within the subsurface (Bae and Ghosh, 2003; Rust and Todd, 2011; Bouvier et al., 2006).

Mesoscale testing strategies rely on transforming compressive applied stresses into shear stress (Nizolek et al., 2021). Different sample geometries have been proposed to achieve this stress transfer such as a hat-shaped specimen (Meyer and Manwaring, 1985; Bronkhorst et al., 2006; Nemat-Nasser et al., 1998) and a **compact forced-simple-shear (CFSS)** specimen geometry (Gray III et al., 2016) presented in Figure 5.1f. Furthermore, Gray III et al. (2016) present an additional modification to the specimen such that tensile and complex loading paths are facilitated. The key advantage of the CFSS approach lies in the reproducibility of machined samples, localised plasticity in the shear plane, and the possibility to investigate isolated microstructural features and plastic anisotropy (Gray III et al., 2016). One significant drawback of CFSS tests represents the inability to measure strain on a planar surface, which has been recently

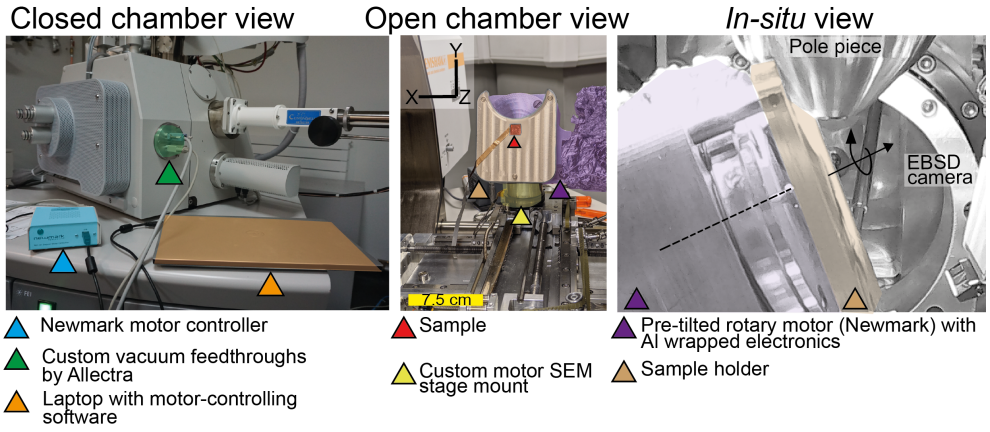


Figure 5.2: Overview of the apparatus presented in this study, as assemblied on a FEI QUANTA 650 scanning electron microscope.

overcome due to a redesign by Nizolek et al. (2021). CFSS studies investigate Al alloys (Gray III et al., 2016; Zhu et al., 2016), Ti (Zhu et al., 2017), and Ta (Nizolek et al., 2021).

The most well established techniques for shear testing use different sample geometries in enclosed deformation assemblies. Unlike other approaches using uniaxial compression such as CFSS specimens, or tensile stages, the geometries presented in Figure 5.1g and h do not permit the imaging of the deforming shear zone during the experiment. **The shear punch test** diagram in Figure 5.1g depicts testing of a disk with a diameter of 8 mm and thickness of 0.5 mm, which is fixed at both ends. A flat-punch indenter applies a compressive force on the middle of the disk, which generates shear stresses at the edges of the disk (for a review, see Lancaster et al., 2022). Previous studies have implemented shear punch tests to investigate Cu, Al, steel, and Ti-6Al-4V (Lancaster et al., 2022). One of the most established techniques for studying shearing patterns is the **equal-channel angular pressing** (ECAP) test depicted in Figure 5.1h (for a review, see Valiev and Langdon, 2006). In these tests, polycrystalline or single crystal samples are pressed through a channel with a corner with a 90° angle, similar to Figure 5.1h, or a curved outer wall of varying degrees (Valiev and Langdon, 2006). ECAP experiments facilitate multiple passes and complex channel geometries such that high strains (e.g., $> 1000\%$) can be achieved (Langdon, 2009; Valiev and Langdon, 2006). These tests have been implemented using a wide range of alloys, with a particular focus on studying superplasticity (Furukawa et al., 2001; Langdon, 2009; Karami and Mahmudi, 2013; Valiev and Langdon, 2006; Sabirov et al., 2008; Bednarczyk et al., 2018; Lin et al., 2005).

5.3 Annular torsion apparatus

5.3.1 Rotary stage and SEM compatibilities

We present an *in-situ* apparatus with both commercially-available and custom-made parts. We use a single-axis, stepper RM-3-111V stage and the corresponding controller from Newmark®. Figure 5.2 presents the apparatus set-up in a FEI Quanta 650 scanning electron microscope (SEM). The rotary stage is vacuum compatible down to 10^{-5} Pa and measures 88 mm in width, 150 mm in length, and 54 mm in height, with a total weight of 1.4 kg. The stage is equipped with a NEMA 17 stepper motor with a 90:1 gear ratio and a 30°/s maximum speed (New). This stage has the capacity to apply a torque up to 4.5 N·m. The commercial components are equipped with custom-made parts such that they can be attached to the SEM stage both horizontally and at a 70° pre-tilt, as exemplified in Figure 5.2. The apparatus is accompanied by custom-made, vacuum-compatible feedthroughs.

5.3.2 Stage controls: input

The stage receives external input encoded by a NSC-A1-E stepper motor controller from Newmark® established via USB. The angular resolution of the encoder is 4000 counts per revolution, which translates to 0.09° per count. The encoder is powered via a +24 VDC power adapter. The motor receives input from stand-alone Newmark® software, in which the user can control the trajectory profile, acceleration, velocity, and deceleration. The software permits input of user-programmed complex motion paths, with multiple segments of velocity changes, or trajectory changes.

5.3.3 Sample geometry

The torque is applied by a driving shaft attached to the motor and inserted through the interior of a sample. The exterior of the sample is held fixed by the sample holder (Figure 5.2). Figure 5.1e presents the sample geometry used in this study from two different viewing angles. The current sample design requires a 1x1 cm square sample with a height of maximum 0.5 cm. The underside of the sample has a recessed channel with a width of 2–2.5 mm. The middle of the sample has a rectangular cut-out through which the screwdriver applies a torque. Our design facilitates torque transmission through the sample such that the thin sheet of material corresponding to the channel deforms in simple shear, the middle of the sample undergoes a rigid body rotation, and the outer part of the sample is fixed. In Figure 5.3, the resolved shear stress, τ

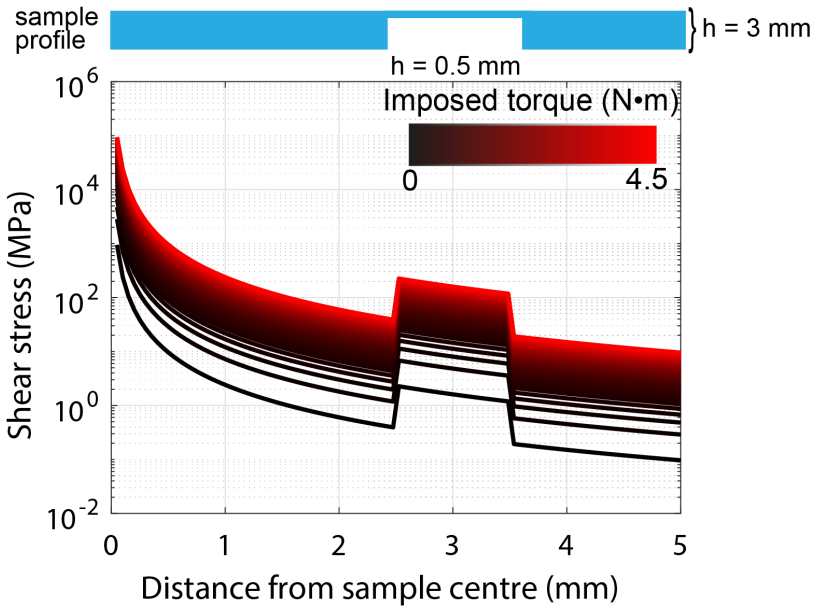


Figure 5.3: Shear stress across the sample calculated for a sample thickness of 3 mm and a channel thickness 2 mm using Equation 5.1. The upper diagram represents a schematic cross section though the sample. The diagram is not drawn to scale.

across the sample depends on the position from the centre of the sample, described by the radius r, and on the imposed torque, M,

$$\tau = \frac{M}{2\pi h r^2}, \tag{5.1}$$

where h is the thickness of the sample parallel to the torque vector and equal to 0.5 mm in the channel and to 3 mm outside of the channel. Figure 5.3 indicates that the shear stress in the channel can be up to 100 MPa according to the position of the channel from the sample centre. Moreover, a smaller channel width ensures less stress variation across it. Most importantly, Figure 5.3 indicates that the geometry of the sample controls the magnitude of the applied shear stress on the deforming material.

5.3.4 Optical measurements

Our apparatus can be also be used for measurements outside the SEM, accompanied by digital image correlation (DIC) analysis. To demonstrate this capability, we have implemented an optical DIC approach while the material was subject to an applied torque similar to the diagram in Figure 5.1e to measure strains on the sample surface.

Our proposed apparatus is compatible with most of the existing experimental set-ups for the application of DIC techniques on deforming materials. We used a pre-existing DIC set-up at the University of Oxford, described by Xiong et al. (2021).

The images were captured with a high-speed camera (Hamamatsu Photonics Ldt -ORCA-Flash 4.0), with a working distance of ~ 0.2 m, an exposure time of 10 ms, and a capture rate of 1 frame per second. The captured images have a 2048x2048 pixel resolution and a field of view of 3.1 mm. We analyse the images using the MATLAB open-source software Ncorr v1.2 (Blaber et al., 2015), which displays good agreement with commercially-available software (Harilal et al., 2014; Lunt et al., 2020). However, computation via Ncorr is significantly more time consuming (Lunt et al., 2020) and consequently, we subsample one data set such that we use one frame every 4 seconds (TPbSn4). We used a total of 1007 frames for the one sample (TPbSn4), and a total of 450 frames for the second sample (TAl4). We use the first image as the reference image and select a region of interest overlapping the main deformation area. In the Ncorr software we chose a subset radius of 30, a subset spacing of 5 pixels, and enable the option for high-strain analysis (Blaber et al., 2015). The software uses an iterative solver for which the exit conditions have been set to the cutoff values of 10^{-4} for the norm of the difference vector and 30 for the iteration number (Blaber et al., 2015).

5.3.5 *In-situ* measurements

Our proposed apparatus is compatible with FEI Quanta 650 scanning electron microscopes. We used this SEM to perform *in-situ* experiments at Imperial College London. The SEM is equipped with a Bruker eFlashHR EBSD camera and eSprit 2.0 software for electron backscatter analysis. While EBSD analysis can be performed after each increment of imposed torque, we have opted to record crystallographic orientations at the start and end of the deformation, and use the ARGUS^{TM} signal to qualitatively assess the crystallographic orientations (e.g., Nolze et al., 2017). We acquired ARGUS^{TM} images with the EBSD detector inserted at a distance of 177.53 mm and at a tilt of 10° from the sample surface tilted at 65°. The key advantage of using the ARGUS^{TM} capabilities for this application is the fast acquisition time of the image compared to EBSD maps. The SEM images were acquired at a working distance of ~ 20 mm, with a voltage of 20 kV, and a 5.5 μm spot size.

5.4 Demonstration of simple shear deformation of ductile materials

We demonstrate the capabilities of our apparatus using three different materials. We implement optical DIC analysis on a PbSn and a high-purity Al sample to characterize the imposed strain field. We demonstrate the *in-situ* compatibility of our apparatus

Table 5.1: Sample details

Sample	Material	Width (mm)	Length (mm)	Height (mm)	Channel width (mm)	Mass (g)
TSn1	pure β-Sn	9.34	9.49	2.28	1.95	1.06
TPbSn4	75%Pb 25%Sn	9.53	9.65	2.70	2.46	1.65
TAl2	pure Al	10.00	9.98	2.86	2.00	0.60
TAl4	pure Al	10.00	9.93	2.92	1.88	0.60

by using a coarse-grained, high-purity β-Sn sample and a finer grained, high-purity Al sample.

5.4.1 Sample materials

We use three different materials to probe the applicability of the proposed apparatus to studying material deformation in simple shear. Table 5.1 details the sample geometry and composition. We used two samples manufactured by casting in a custom Cu cast (TSn1 and TPbSn4) and two machined samples (TAl2, TAl4). All samples have been polished with a diamond suspension followed by colloidal silica and finished with Ar-ion polishing using a Gatan PECS II. The samples used for DIC measurements (TPbSn4, TAl4) were spray painted with a polyurethane paint applied with an airbrush in order to achieve a black background with white speckles, similar to Xiong et al. (2021).

5.4.2 PbSn

We apply DIC analysis on a PbSn sample, prepared with a dark background and white speckles (Table 5.1). Figure 5.4 displays the strain calculation using Ncorr (Blaber et al., 2015) for a sample tested under an imposed twist of 40° with a speed of 0.01°/s. Figure 5.4 documents rigid body rotation in the first 10° of imposed rotation and subsequent strain localization corresponding to the channel width on the other side of the sample, as well as. In the vicinity of the screw driver, strain patterns arise due to the impingement of the driving shaft into the sample, albeit with smaller magnitudes than the strains localized within the channel. We document principal strain and shear strain magnitudes of $\sim 20\%$. With increased rotation, out of plane motion decreases the quality of the image resulting in missing areas in the correlation computation. Figure 5.5 presents maximum in-plane shear strains with values up to $\sim 25\%$.

We characterize sample TPbSn4 using SEM imaging after removing the dye. Figure 5.6 displays the initial intergrowth microstructure of the Pb-Sn sample and superimposed strain localization over a width of 400 μm on the sample surface. The ring of strain localization also displays a grain-size gradient, in which the smallest

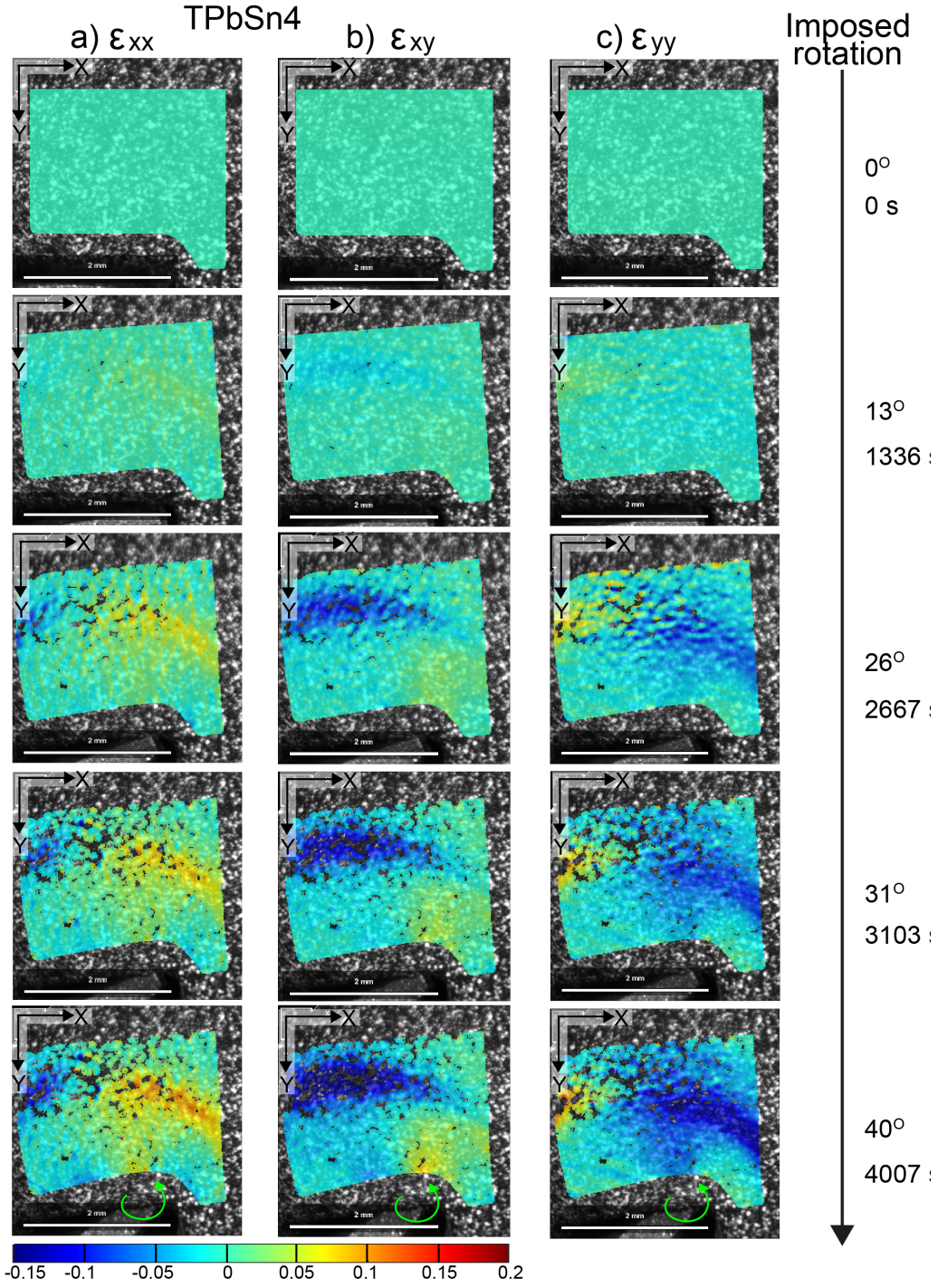


Figure 5.4: Full strain DIC results for the Euler-Almanasi strain in the PbSn sample for the a) ε_{xx}, the b) ε_{xy} and the c) ε_{yy} component, presented without subtracting the rigid body rotation of the sample. Due to the DIC set-up (Xiong et al., 2021), the images appear mirrored, and consequently the driver at the bottom appears to be rotating anticlockwise.

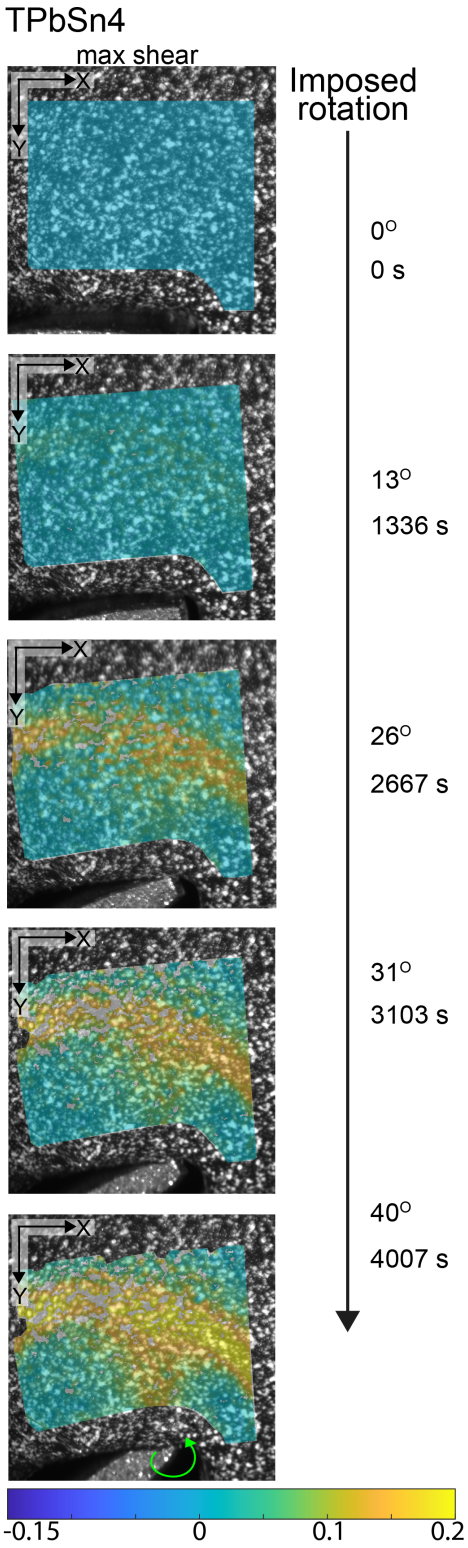


Figure 5.5: The distribution of maximum, in-plane shear strains in the TPbSn sample. The calculation uses the values of strain presented in Figure 5.4.

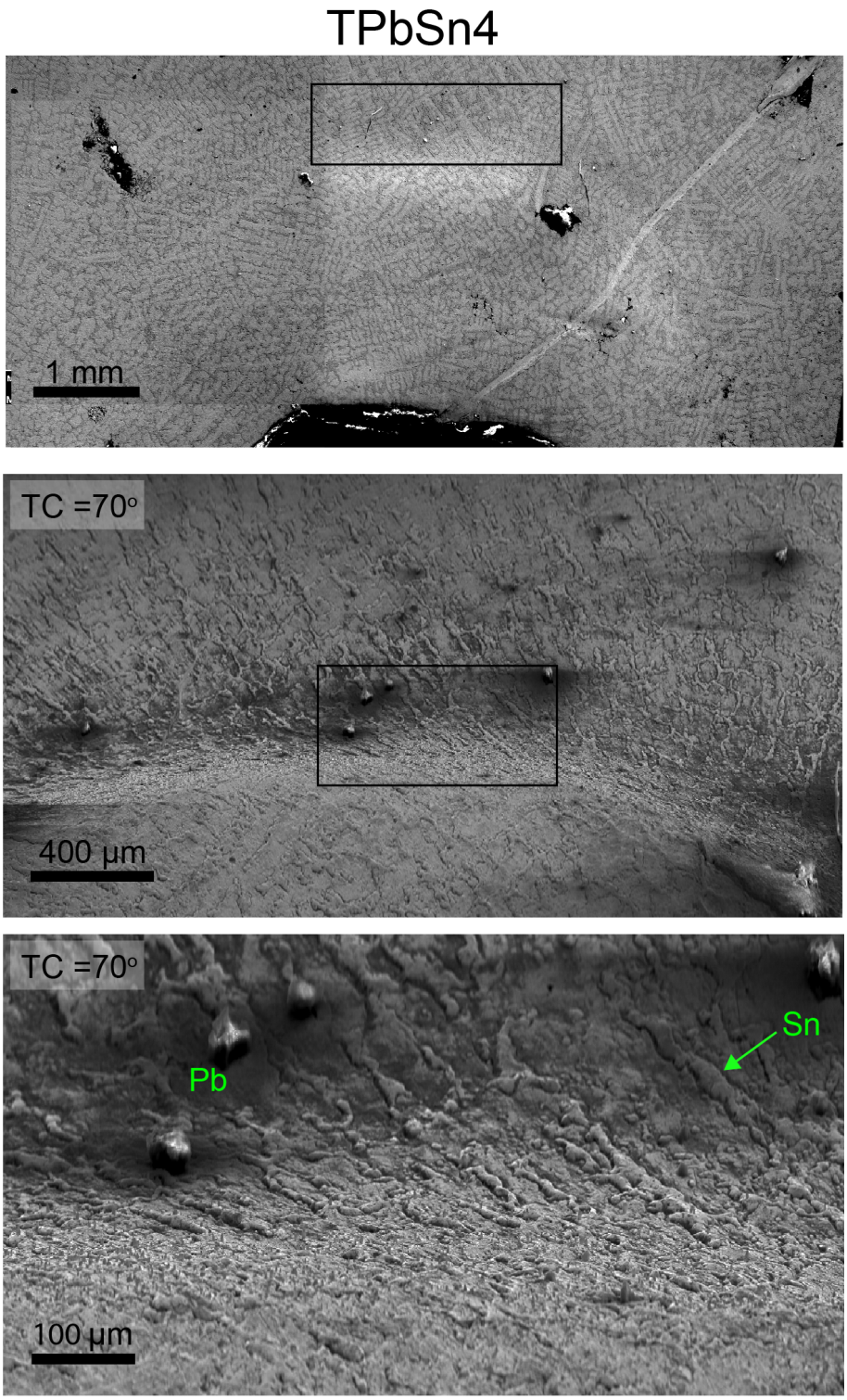


Figure 5.6: SEM characterization of the TPbSn4 sample after deformation and paint removal. The surface is presented after deformation, without any further polishing or preparation. The images were captured with the stage tilted at 70° and have an applied corresponding tilt correction via the SmartSEM interface.

grains are closer to the middle of the sample. This microstructural gradient corresponds to the location of high stresses towards the central side of the channel, as predicted in Figure 5.3.

5.4.3 Sn

We use a β-Sn sample in order to demonstrate the *in-situ* capabilities of our apparatus. Figure 5.7a depicts the ARGUS^{TM}images with increasing imposed deformation and the crystal orientations before deformation. The sample has been deformed according to the rotation path described in Figure D.1 in Supplementary Materials. The figure presents slip band formation in crystal B, and increased buckling and out-of-plane deformation as the imposed rotation angle increases. Figure 5.12b presents several frames capturing the formation of slip bands in crystal B as well as a grain boundary acting as a barrier to slip transmission.

Figure 5.8 displays images of the TSn1 sample after deformation. Figure 5.8a highlights that while some of the strain has localised in the channel cut-out, the driving shaft indented into the sample and significant deformation has been accommodated in the sample centre. Slip bands are present consistently around the deforming area, and the increased levels of deformation have led to crack formation along grain boundaries at the outer edge of the channel.

5.4.4 Al

Optical measurements

We implement the DIC analysis on a high-purity Al sample, prepared with a dark background and with speckles. Figure 5.9 displays the resulting strain calculations using the Ncorr software (Blaber et al., 2015), for a high-purity Al sample tested under an imposed twist of 45° with a speed of 0.1°/s. After sample rotation within the holder, strain localises according to expectations set by sample geometry. Importantly, in high-purity Al, the impingement of the driving shaft into the middle of the sample does not generate strain of measurable magnitudes. Out of plane buckling, and fracture of the sample decreases image quality at the end of the experiment.

We characterize the deformation in sample TAl4 using SEM and ARGUS^{TM}imaging after removing the paint. Figure 5.11a presents the overview of the sample, with the fiducial marks annotated with magenta lines. Post-deformation imaging indicates that the sample has reached failure and that the imposed stress has been accommodated within the channel. Detailed imaging of the area of deformation in Figure 5.11b and

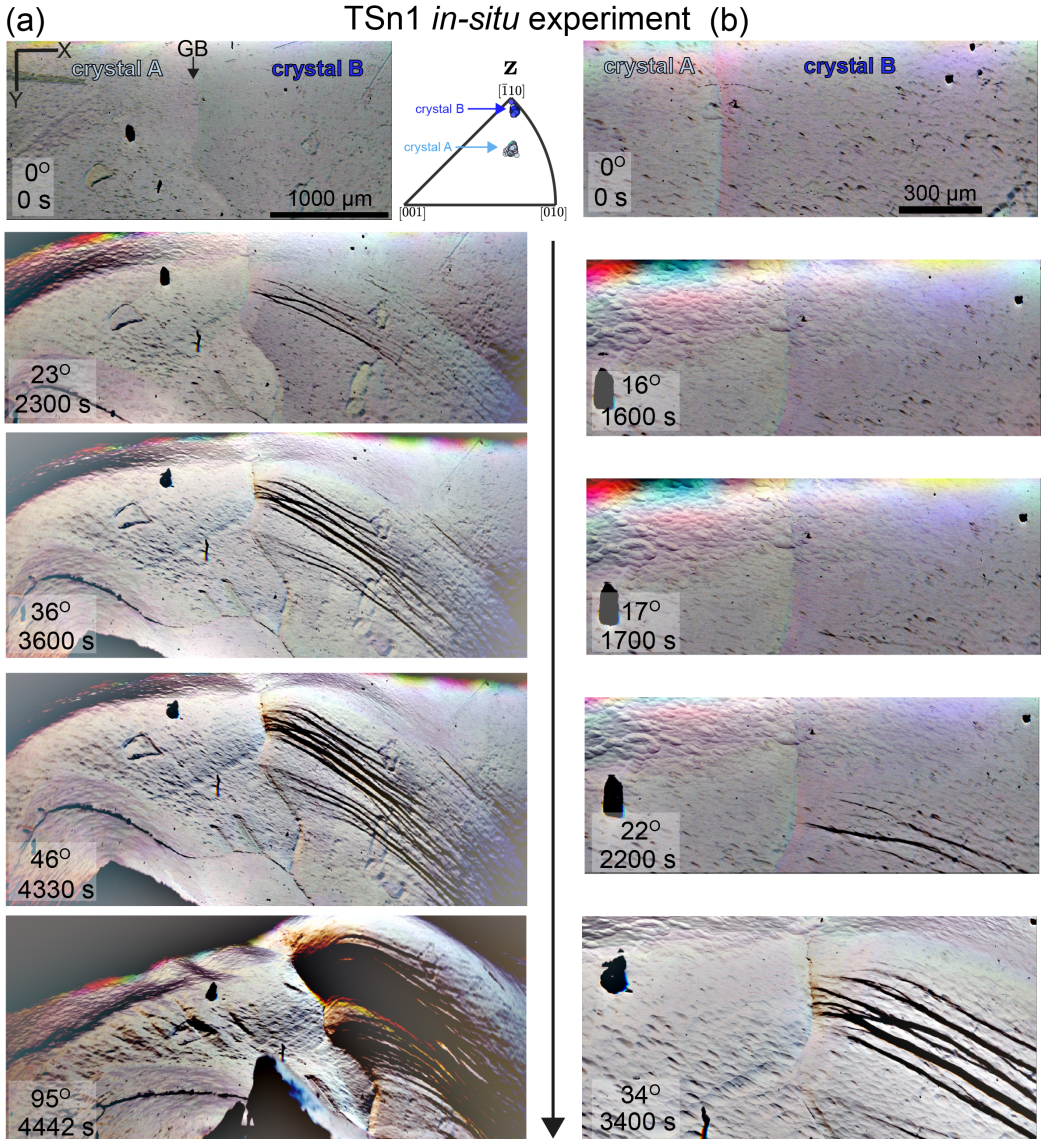


Figure 5.7: *In-situ* imaging of deforming Sn using ARGUS^{TM}. The lower left boxes indicate the imposed rotation angle and the time.

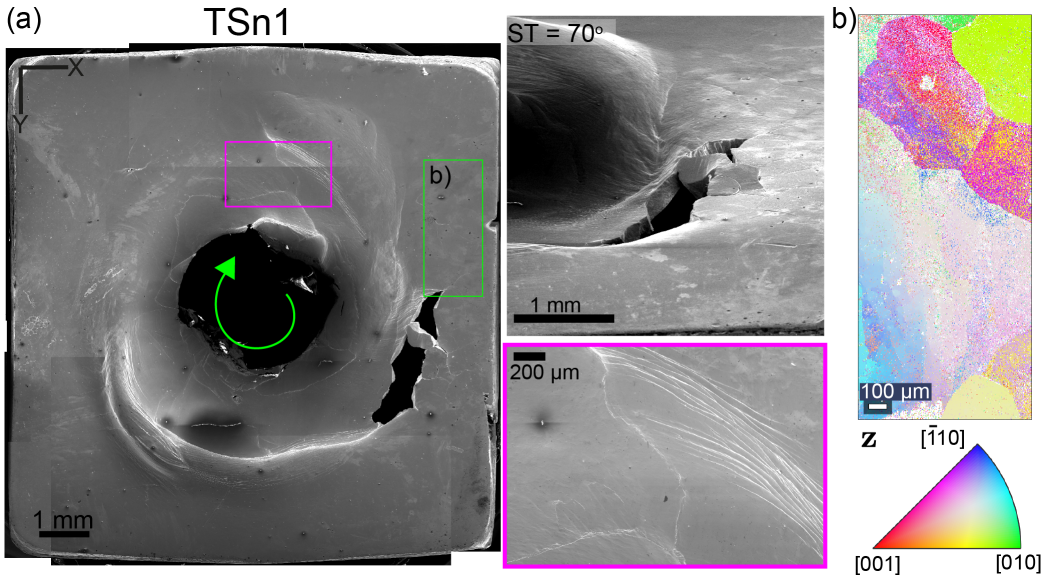


Figure 5.8: Post-deformation SEM and EBSD characterization of the TSn1 sample. a) Sample overview composed of multiple SEM images. The sample thickness corresponding to the channel area is < 0.5 mm. b) EBSD map of $\beta-$Sn with crystal orientations depicted in the inverse pole figure (IPF) with respect to the direction perpendicular on the viewing plane (Z-axis).

c reveals that the width of the deforming region accommodating the most strain is ~ 300 µm. This width is smaller than the measured width of the channel on the other face of the sample by a factor of 6 (Table 5.1), indicated that the stress has been accommodated in the immediate vicinity of the inner ring of the channel, which has larger resolved shear stresses (Figure 5.3). The length of the inner ring of the channel is 18.57 mm. For an imposed shear by 45°, the fiducial marks are separated by $\sim$ 3.5 mm of tangential displacement localised in a region ~ 0.8 mm wide in Figure 5.9. Thus, the fiducial marks indicate $\sim 400\%$ strain. The DIC measurements presented in Figure 5.9 reveal that the imposed shear stress of 150 MPa generated a deformation area superimposed to the channel cut out, with corresponding in-plane shear strains of magnitudes of $2 \cdot 1.6$, in line with expectations based on the indications from the fiducial mark and sample geometry. Maximum in-plane shear strains with values up to $\sim 270\%$ are presented in Figure 5.10 and further demonstrate strain localization within the channel.

In-situ measurements

Figure 5.12a displays two *in-situ* frames acquired with ARGUS^{TM}. The images highlight the change in surface topography with increased imposed deformation and

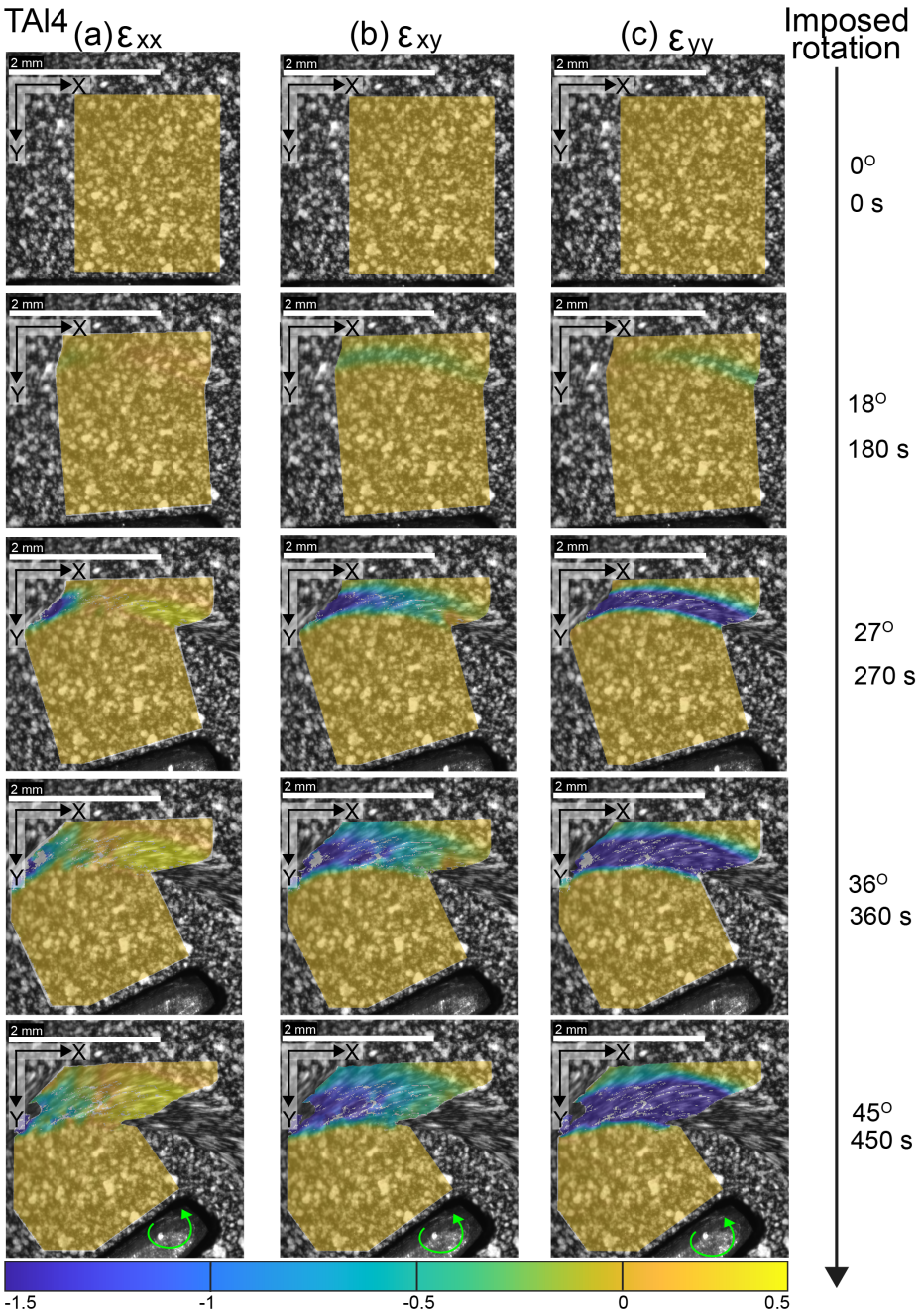


Figure 5.9: Full strain DIC results for the Euler-Almanasi strain in the high-purity Al sample, for the a) ε_{xx} component, the b) ε_{xy} component, and the ε_{yy} component, presented without subtracting the rigid body rotation of the sample. Due to the DIC set-up (Xiong et al., 2021), the images appear mirrored, and consequently the driving shaft at the bottom appears to be moving anticlockwise.

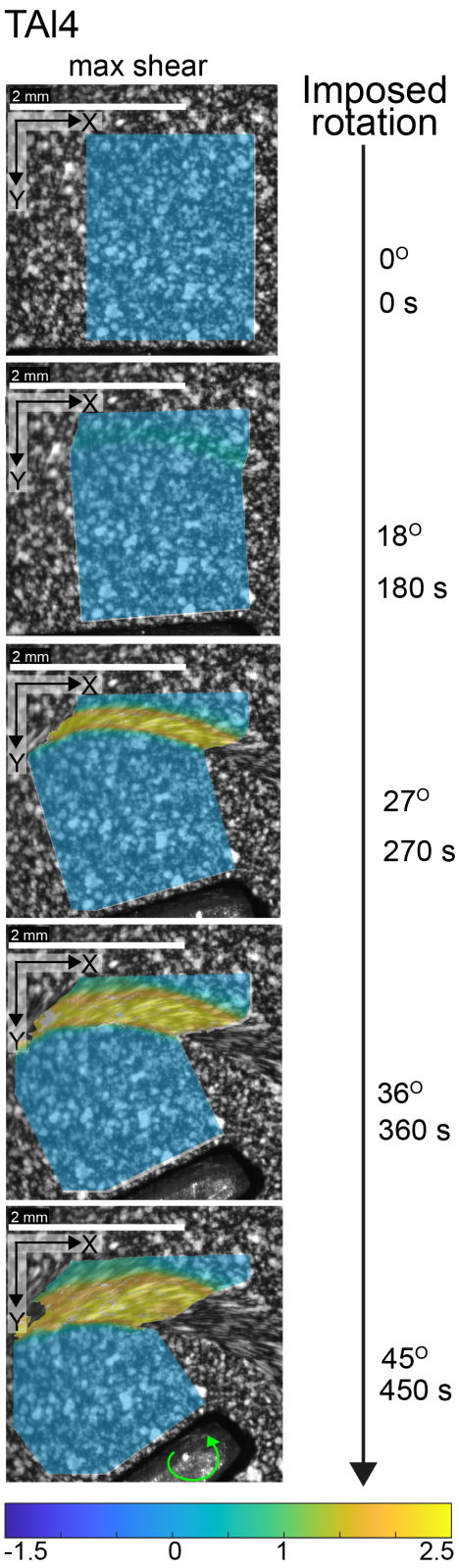


Figure 5.10: The distribution of maximum, in-plane shear strains in the high-purity Al sample. The calculation uses the values of strain presented in Figure 5.9. Note the different values of the colour map compared to Figure 5.9.

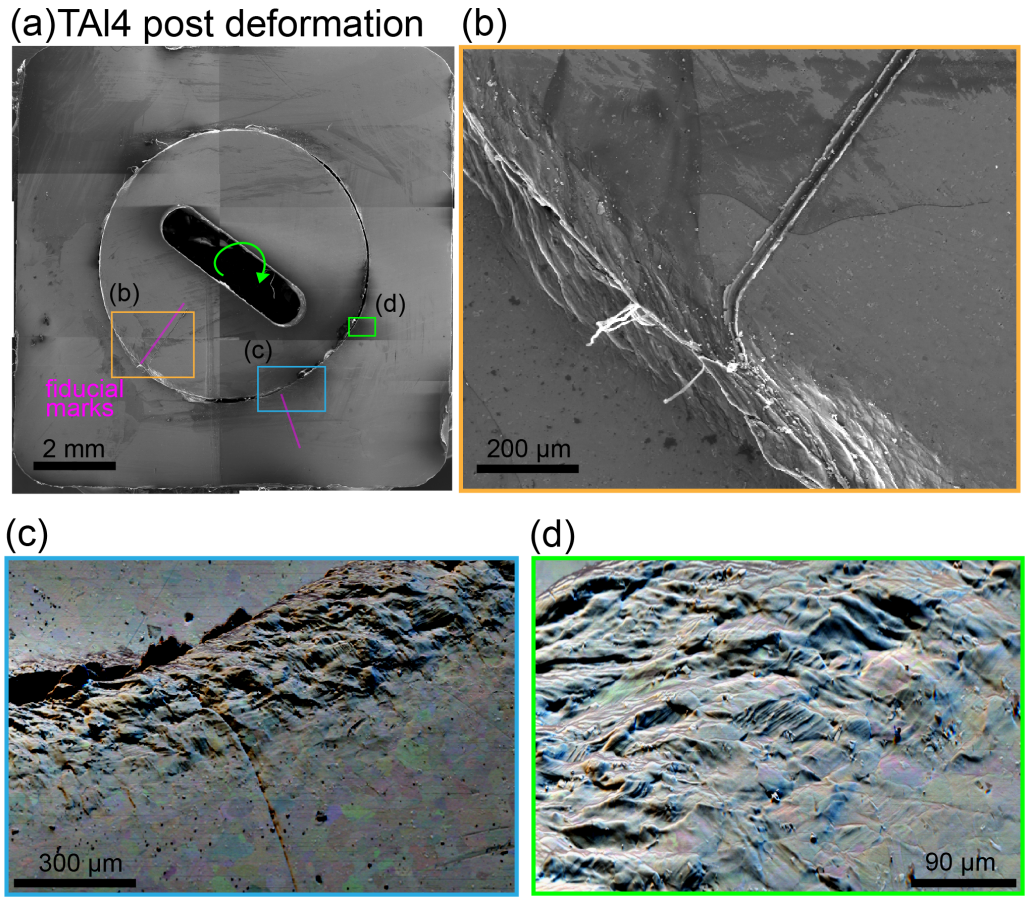


Figure 5.11: a, b) SEM characterization of the TAl4 sample after deformation and paint removal. The surface is presented after deformation, without any further polishing or preparation. c,d) ARGUS^{TM}images of the fiducial mark and the area of localised strain. The images were captured with the stage tilted at 70° and have an tilt correction applied via the SmartSEM interface. For the acquisition of these images the EBSD camera was positioned at 35 mm from the sample, and had a tilt of 4°.

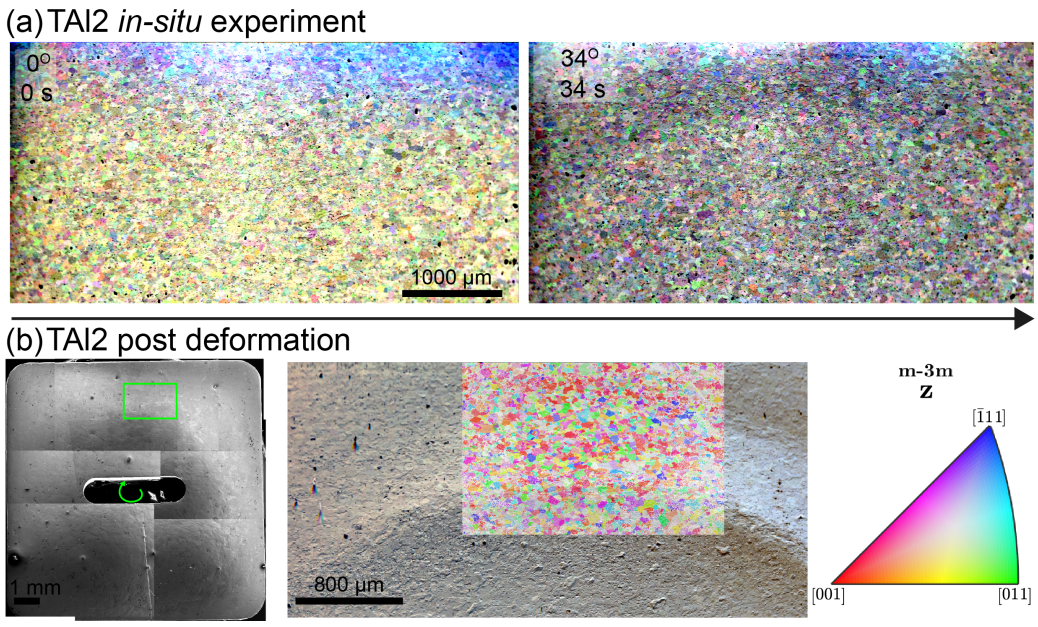


Figure 5.12: a) *In-situ* images captured with ARGUS^{TM}of the TAl2 sample. b) Post-deformation SEM and EBSD characterization of the sample displayed alongside an inverse pole figure (IPF) depicting crystallographic orientations with respect to the direction perpendicular on the viewing plane (Z-axis).

strain localization overlaying the channel. Some grains in the deformation ring display grain elongation. Figure 5.12b displays post-deformation characterization of the TAl2 sample. We collected SEM images of the surface alongside an EBSD map to highlight any microstructural changes present at small strains.

5.5 Discussion

5.5.1 Implications and limitations

In this study, we have demonstrated the capabilities of our apparatus and sample geometry to impose shearing on a thin sheet (< 0.5 mm) with a width of 2 mm via an applied torque. We used DIC measurements to illustrate that in a PbSn alloy and high-purity Al the strain localised according to the expectations based on the sample geometry. We have also tested the range of materials that could be investigated by this technique. The TPbSn4 sample presents a small amount of plastic deformation near the driving shaft, while the TAl4 presents no plastic deformation near the driving shaft. Therefore Al alloys are particularly suitable target for deformation with this apparatus because of the good coupling between sample and motor. In contrast, our results for β-Sn indicate that this material is too soft for this application, and intense

deformation near the driving shaft results in decoupling such that a torque is no longer maintained on the sample. In ductile samples, the ratio between the bulk sample thickness the thickness within the channel has to be as large as physically possible such that the stresses in the channel are sufficiently large to focus deformation away from the driving shaft (Figure 5.3).

The *in-situ* compatibility of our apparatus represents the key technological advancement in our study and facilitates the fundamental investigation of a number of mesocale material deformation processes. We demonstrate that this experimental set-up can be implemented in studies of slip band formation and interactions between slip bands and grain boundaries (Figure 5.7). Our apparatus can also be used in samples with finer grain sizes and to investigate grain-size evolution and texture evolution with increasing strain (Figure 5.12). We chose to collect microstructural data using the ARGUS^{TM}capabilities of our EBSD set-up due to its fast acquisition rate compared to EBSD. However, our proposed experimental set-up is fully compatible with acquisition of EBSD data between deformation steps. The caveats of our proposed technique are similar to the common challenges of *in-situ* testing such as buckling, rigid-body rotation, and potential differences between surface and subsurface processes.

5.5.2 Comparison with existing strategies for simple shear testing

The key advantage of this innovation is that simple shear can be imposed on samples with a wide variety of starting microstructures while recording the microstructural evolution. We demonstrate this with tests on a coarse-grained β-Sn sample and a finer grained, high-purity Al sample. Additionally, our sample geometry ensures repeatability, and the presence of a flat initial surface for imaging. These advantages mitigate caveats of other *in-situ* techniques, which require small volume samples and do are not suitable for investigating polycrystalline materials with grain sizes > 3 μm (e.g., Figures 5.1a and b). Other *in-situ* techniques with capabilities of testing polycrystalline samples, such as tensile stages (e.g., Figure 5.1c) are limited in the amount of strain that can be achieved. In our specimen geometry (Figure 5.1e), the sample preparation is less expensive and time consuming compared to techniques requiring FIB milling such as *in-situ* micro-double shear testing (Figure 5.1a). Compared to mascroscale deformation specimens, which can be analysed via DIC (e.g., CFSS in Figure 5.1f), our experimental set-up can achieve higher strains and can provide information on both the strain field and microstructure. Furthermore,

the channel width and the thickness of the resulting thin sheet can be easily varied to achieve optimal conditions for strain localisation in materials with varying ductility.

5.5.3 Future applications and developments

In this contribution, we describe a new apparatus and sample geometry for testing materials under simple shear. We have demonstrated that our apparatus is compatible with both the more commonly used optical DIC set-up and analysis, as well as *in-situ* SEM analysis. According to the features of the EBSD detector associated with the SEM, our proposed apparatus expands the existing *in-situ* investigation capabilities to EBSD and high-angular resolution EBSD analyses (e.g., Ast et al., 2017; Zoller et al., 2020) and *in-situ* high-spatial resolution DIC (e.g., Zhang et al., 2014; Edwards et al., 2017; Guan et al., 2017; Doquet and Barkia, 2016) of materials deformed in simple shear.

Our proposed apparatus and sample geometry, alongside established techniques for characterization of microstructural evolution, could provide new insights into material deformation across a wide range of strain rates and varied strain paths. One area of particular interest that is studied at large strains is superplastic deformation (i.e., elongations $> 400\%$ prior to failure). This apparatus is particularly well suited for the experimental study of grain-boundary sliding, which is the underlying deformation mechanism enabling superplasticity (for review, see Langdon, 2009; Mohamed, 2020). Our proposed apparatus and sample geometry could be implemented in the study of grain-boundary sliding in various materials (e.g., Ti-6Al4-V in Alabort et al., 2016; Salishchev et al., 2001), room-temperature superplasticity in ultrafine-grained alloys (grain size < 1 μm) deformed at high-strain rates ($> 10^{-1}$ s^{-1}) (e.g., Mohamed, 2020; Masuda and Sato, 2020; Sabirov et al., 2008), and strain localisation in plastically anisotropic materials (e.g., Nizolek et al., 2021; Dunne et al., 2012; Bouvier et al., 2006; Pedersen et al., 2008). Moreover, our proposed apparatus is also suitable for the investigation of room-temperature superplasticity induced by precipitates at grain boundaries (e.g., Mostaed et al., 2019) and impurities (Uesugi et al., 2015), and by deforming nanocrystalline materials (e.g., Edalati et al., 2018; Lu et al., 2000). Our apparatus can couple EBSD observations with strain field measurements in materials with different starting grain sizes during high-strain rate deformation (e.g., Meyers et al., 1995) at a spatial scale complementary to high-strain *in-situ* TEM testing (e.g., Voisin et al., 2020).

This apparatus can also be implemented in the study of Earth materials. Some studies into the deformation of olivine, a mineral dominant in Earth's upper mantle, use

an analogous organic material, borneol $C_{10}H_{18}O$ (e.g., Sasaki et al., 2019; McCarthy and Takei, 2011). Borneol has a much lower melting temperature compared to olivine (200°C in borneol vs 1200–1900°C in olivine) and similar plastic deformation mechanisms (e.g., Takei, 2005, 2019). Thus, room-temperature experiments on borneol provide an analogous for high-temperature deformation of olivine (e.g., melting at grain boundaries Takei, 2005). This apparatus could also operate at low temperatures in which water ice is stable, and enable observations of ice deformation in simple using optical microscopy and DIC methods. Our proposed apparatus and sample geometry could expand the ranges of shear strain imposed on deforming ice in previous studies (e.g., Qi et al., 2019) and provide direct microstructural evidence for comparison with naturally-deformed ice in glacier setting (e.g., Monz et al., 2021) or simulations of microstructure evolution (e.g., Journaux et al., 2019; Llorens et al., 2016).

Experiments performed with this apparatus could also inform numerical models investigating dislocation-based hardening (e.g., Zecevic and Knezevic, 2018; Eghtesad and Knezevic, 2020), the evolution of intracrystalline misorientation and geometrically necessary dislocations (e.g., Zecevic et al., 2018; Dunne et al., 2012), twin formation and evolution (e.g., Knezevic et al., 2013; Zecevic et al., 2016), particle hardening (e.g., Ghorbanpour et al., 2017), grain boundary sliding (e.g., Doquet and Barkia, 2016), and the stress state at grain boundaries during plastic deformation (e.g., Gonzalez et al., 2014). Moreover, our proposed experimental set-up facilitates comparison with numerical studies simulating reversal of strain paths and fatigue (e.g., Jeong and Tomé, 2020; Seiler et al., 2020).

Further developments include expanding the temperature range and quantifying the applied torque. Higher temperatures would expand the range of materials in which superplasticity could be observed (e.g., 150–200° C for Mg alloys, Lin et al., 2005; Watanabe et al., 2013, 2012).

5.6 Conclusion

In this study, we propose a novel apparatus and sample geometry for the characterization of microstructural evolution in ductile materials. We demonstrate that our proposed apparatus is compatible with established *in-situ* techniques for microstructural characterization, such as EBSD. Our proposed apparatus and sample geometry is also compatible with optical DIC instruments and analysis, and could provide detailed strain analysis using *in-situ* DIC. We propose a series of applications, in which our proposed experimental set-up complements existing techniques resulting

in load-displacement data. Ultimately, our study provides a proof-of-concept for our proposed apparatus, and opens multiple lines of enquiry for future research.

Chapter 6

Conclusion

"There is a need to develop materials science-specific machine learning models by including physics dictated constraints into property predictions."

(Raabe et al., 2020)

6.1 Summary of Results

This thesis presents novel results on the mechanics of deformation of forsterite grain boundaries. Chapter 3 presents room-temperature nanoindentation with sharp and spherical tips on forsterite bicrystals with low- and high-angle grain boundaries. The indents were placed at varying distances from the vertical interface and probe the impact of the grain boundary on dislocation generation and slip transmission. The symmetry of the two crystals on each side of the interface results in a consistent nanoindentation direction across the grain boundary. Thus, although the stress field in indentation is heterogeneous, this consistent indentation direction means that the distance to the grain boundary is the only free variable in these experiments. Two key observations are presented in this chapter: 1) the high-angle grain boundary is a potent source of dislocations, in contrast to the low-angle grain boundary, which does not facilitate dislocation nucleation compared to the crystal interior; and 2) the high-angle grain boundary acts as a strong barrier to slip transmission, while the low-angle grain boundary does not exhibit a detectable impact on slip transmission.

High-temperature investigations of forsterite bicrystals are presented in Chapter 4. In this study, forsterite grain boundaries are investigated via *in-situ* micropillar testing at 700°C. Microstructural characterization of the deformed pillars confirm that the deformation is accommodated at the top of the pillars, and that the grain boundary remains intact. The key observations from this study are that 1) the pillars with the grain boundary display a higher yield stress, 2) the pillars without the grain boundary display higher plastic strain, and 3) the grain boundary does not accommodate any of the plastic strain.

The interaction of grain boundaries and dislocations can be studied via small-scale mechanical testing and directly observed during *in-situ* experiments. Each method of investigation has its associated advantages and caveats. Chapter 2 presents tests and adaptations of published strategies for calibration of spherical tip shape and machine stiffness in spherical nanoindentation. The results of this section are synthesised in an improved work flow to extract stress-strain curves from materials using spherical nanoindentation. Importantly, this section highlights the impact of different instrument calibrations on data collected with spherical tips.

Adapting experimental capabilities to *in-situ* testing has been an area of intense development, due to its potential to provide direct observations of material deformation. Chapter 5 proposes a new apparatus and sample geometry developed to circumvent current challenges in existing techniques for the *in-situ* testing of materials under simple

shear. This section demonstrates the capabilities of the apparatus, and compares the proposed testing routine with established techniques to characterize microstructure and quantify strain.

6.2 Future Directions

The implications of the results presented in this thesis outline potential areas of future research. First, the impact of grain boundaries in the deformation of forsterite at temperatures below 700°C has implications for the deformation of olivine-rich materials in different tectonics settings. In the experiments presented here, high-angle grain boundaries act as dislocation sources and barriers to slip transmission, while low-angle grain boundaries do not have a detectable impact on deformation. Furthermore, the same high-angle grain boundary tested in Chapter 3 is harder to deform than the crystal interior when subjected to a shear stress in the experiments in Chapter 4. Thus, in the context of mascroscale deformation at geological strain rates, the distribution and orientation of grain boundary planes with different abilities to transmit strain and generate dislocations potentially adds another layer of local plastic anisotropy. The differences of the response of the grain-boundary network to an applied stress could impact strain hardening and strain localisation in the deforming lithosphere, with a particular emphasis on deformation at small strains.

More general investigations of grain-boundary networks in polycrystalline forsterite could be undertaken by implementing the latest development of high-throughput nanoindentation mapping (e.g., Besharatloo and Wheeler, 2021). These experiments could reveal the correlations between microstructure and local variation in hardness around grain boundaries with different character. Importantly, alongside the results presented in this thesis, data from nanoindentation mapping could underpin the next generation of numerical models of microstructural evolution of polycrystalline olivine (e.g., Gardner et al., 2017; Piazolo et al., 2019), in which the relative abundance and distribution of grain boundaries represents a free variable. Our experiments could inform the starting conditions of such models, in which certain grain boundaries act as barriers to slip transmission, and others are completely transparent. With increasing plastic strain, the distribution of mechanical interactions in the grain boundary network could provide mechanisms for strain localization in settings similar to the oceanic lithosphere deforming at low temperatures.

This thesis demonstrates the applicability of small-scale, *in-situ* testing to geological materials. Following from the micropillar experiments presented in Chapter 4, further

avenues of research include testing geological materials and forsterite with different micropillar geometries. For example, orienting the grain boundary parallel to the loading direction could provide *in-situ* evidence of slip transmission and dislocation generation at grain boundaries (e.g., Dehm et al., 2018). A pillar geometry with a square, flat, side surface permits further *in-situ* microstructural investigations of the lattice orientations around the formed slip bands, or serial slicing parallel to a chosen orientation (e.g., Kalácska et al., 2020). In undeformed forsterite, implementing micropillar testing in oriented single crystals at varying temperatures would provide an avenue for quantifying the temperature dependence of the critical resolved shear stresses for activating the same slip system (e.g., Soler et al., 2014). Moreover, varying pillar diameter at constant temperature of testing, would provide constraints on the size dependence of the critical resolved shear stresses for a slip system (e.g., Soler et al., 2014). Micropillar testing of forsterite at the high end of temperature capabilities of existing techniques (1000°C, Korte-Kerzel (2017)) could quantify the transition between [001]-dominated slip at lower temperatures, to the activation of [100]-dominated slip at higher temperatures, as well as quantifying the relative strengths of different slip systems.

Further development and improvements of characterization techniques of deformation of materials provide reliable, direct observations of microstructure evolution and the interaction of slip bands and grain boundaries. The apparatus described in Chapter 5 presents wide ranging opportunities for future investigations of grain-boundary sliding and superplasticity in various metals (e.g., Ti-6Al4-V Alabort et al. (2016); Salishchev et al. (2001), Al Mohamed (2020); Masuda and Sato (2020); Sabirov et al. (2008)), investigations on the impact of precipitates and impurities on the evolution of microtexture (e.g., Mostaed et al., 2019; Uesugi et al., 2015), as well as investigations of shear deformation of Earth materials (e.g., borneol, ice Takei, 2005; Qi et al., 2019). Importantly, experiments performed with this apparatus could also inform numerical models investigating dislocation-based hardening (e.g., Zecevic and Knezevic, 2018; Eghtesad and Knezevic, 2020), the evolution of intracrystalline misorientation and geometrically necessary dislocations (e.g., Zecevic et al., 2018; Dunne et al., 2012), twin formation and evolution (e.g., Knezevic et al., 2013; Zecevic et al., 2016), particle hardening (e.g., Ghorbanpour et al., 2017), grain boundary sliding (e.g., Doquet and Barkia, 2016), and the stress state at grain boundaries during plastic deformation (e.g., Gonzalez et al., 2014). Further developments of this apparatus include expanding the ranges of temperatures of testing, and quantifying the applied torque.

Appendix A

Supplementary Materials for Chapter 2

Table A.1: Summary of results presented in Figure 2.2. For each nominal radius R_n the Table presents R_{eff} calculated similar to Li et al. (2013) using data collected in fused silica (FS), glassy carbon (GC), and sapphire (SPH) and R_{eff} calculated as a function of load as outlined in Section 2.3.2.1.

R_n µm	R_{eff} µm after Li et al. (2013)			$R_{eff}(P)$	
	FS - SPH	GC - FS	GC-SPH	R_{eff} µm	P (N)
2	0.3	0.25	0.41	0.76 ± 0.63	$2.5 * 10^{-3}$
5	6.97	6.97	8.4	3.43 ± 0.63	0.07
10	10.36	9.04	10.45	6.6 ± 0.8	0.08
20	23.5	32.3	28.75	18.2 ± 5.8	0.2
50	31.4	46	40	32 ± 4.7	0.25

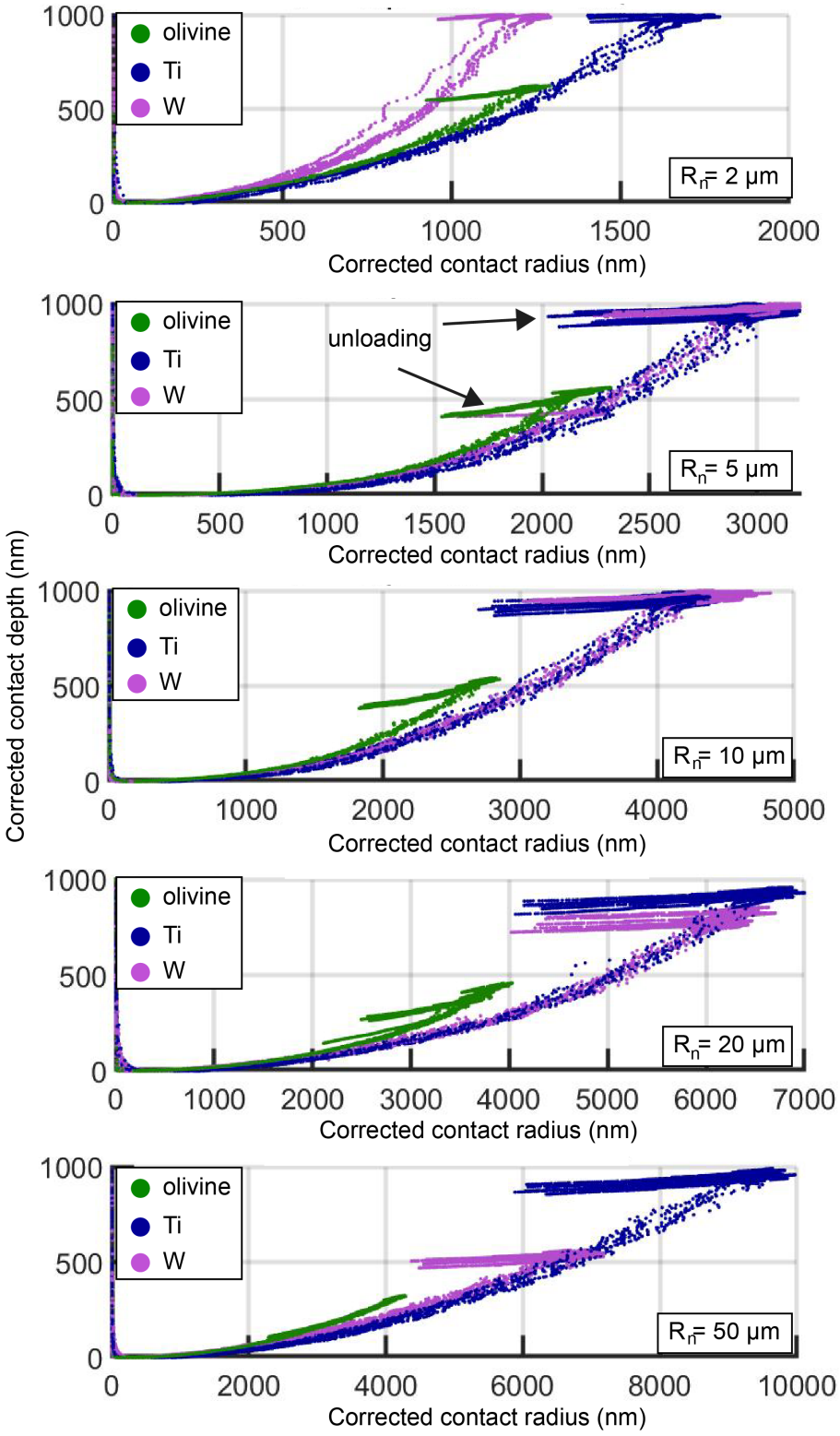


Figure A.1: Effective tip shape calculated with corrected data in olivine, tungsten, and titanium, with tips with varying radii. Note the differences in the horizontal axis. For largest tip radii, the indent experiments in olivine are purely elastic, whereas the residual imprint increases with decreasing radius, as displayed by the segment corresponding to the unloading.

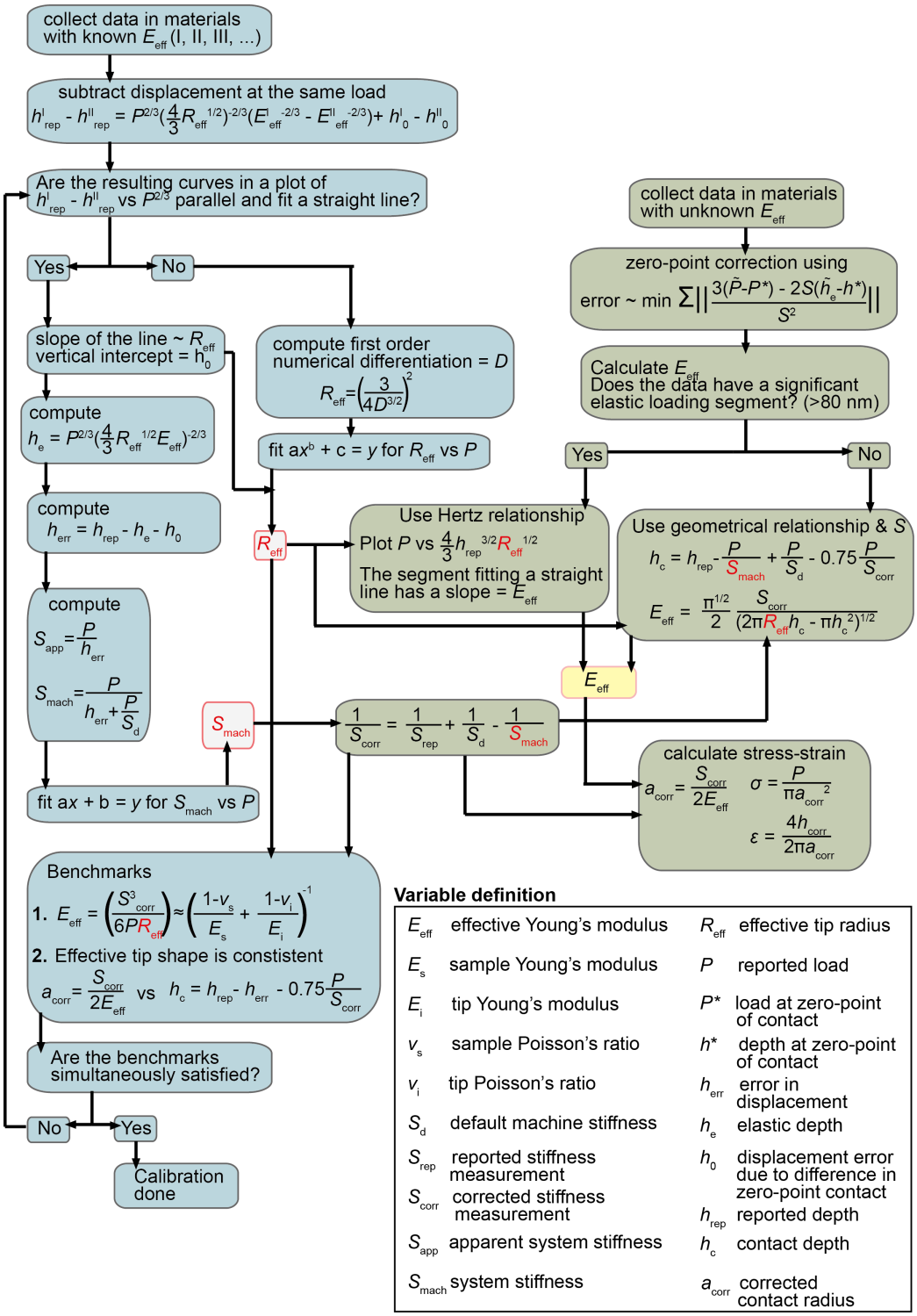


Figure A.2: Schematic flow-chart diagram summarising Section 2.3.2 in blue and Section 2.3.3 in green.

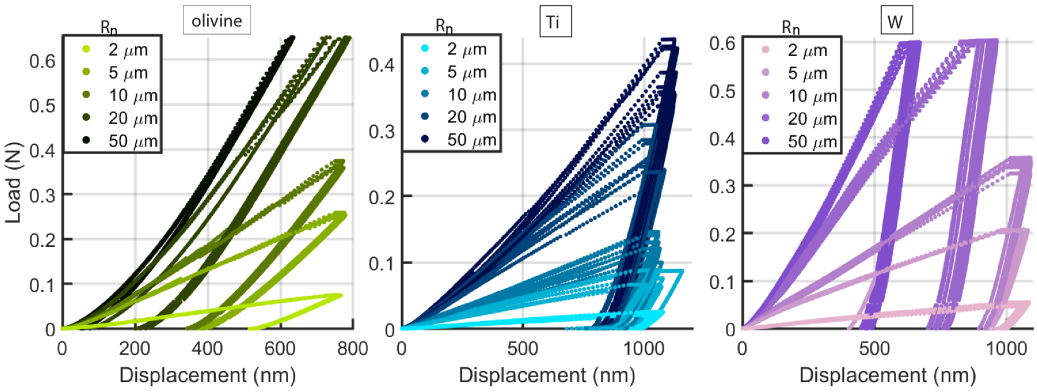


Figure A.3: Load-displacement curves in olivine, titanium, and tungsten collected during displacement-controlled experiments with spherical tips with nominal radii ranging $2 - 50$ μm .

Appendix B

Supplementary Materials for Chapter 3

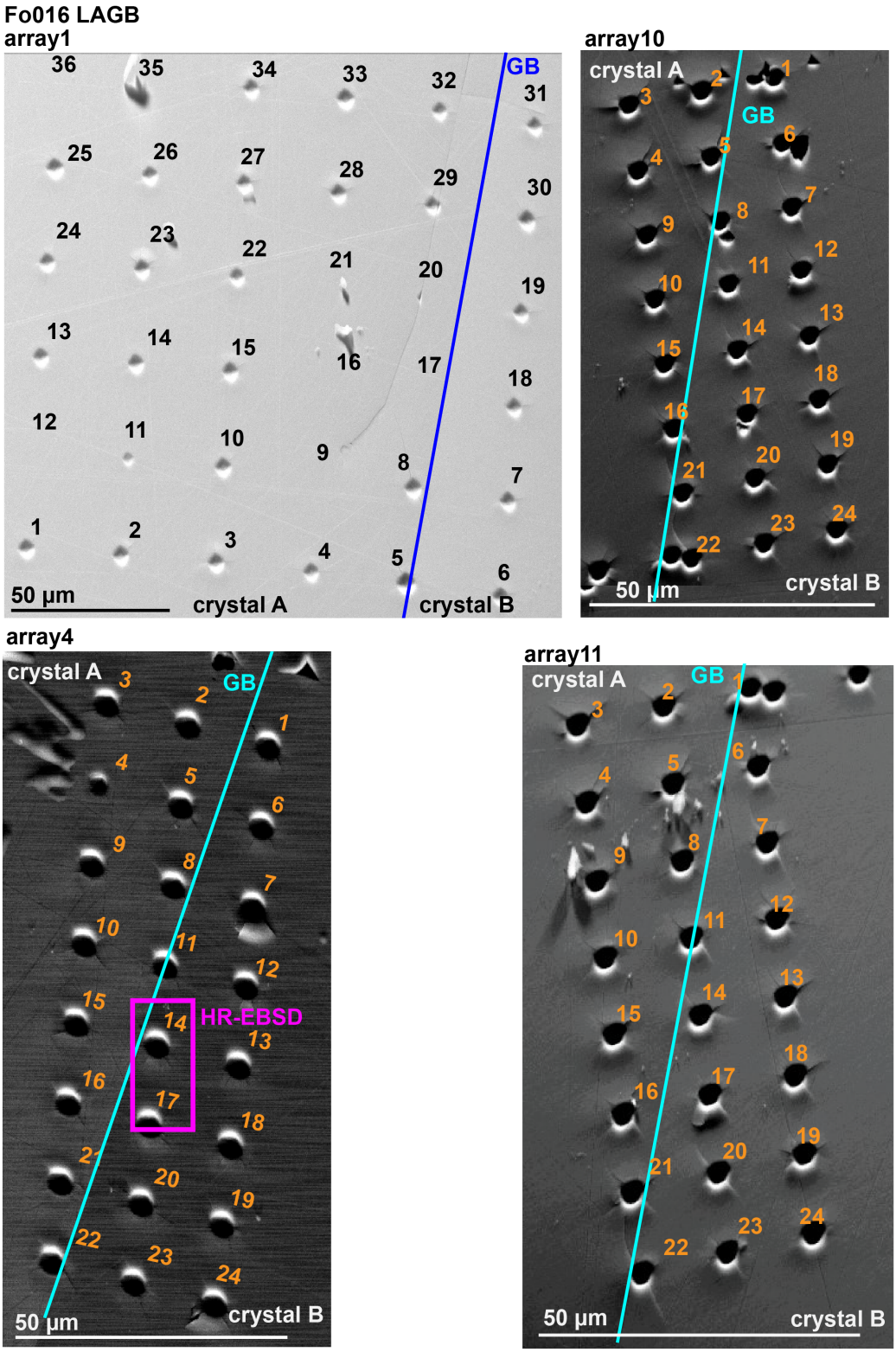


Figure B.1: Backscatter images depicting the arrays placed in the LAGB sample with a spherical indenter as detailed in Table 3.1. The position of the further microstructural investigations with respect to the other indents and the GB is marked by the magenta square. The numbers hear each indent mark corresponds to the order in which the indents have been places.

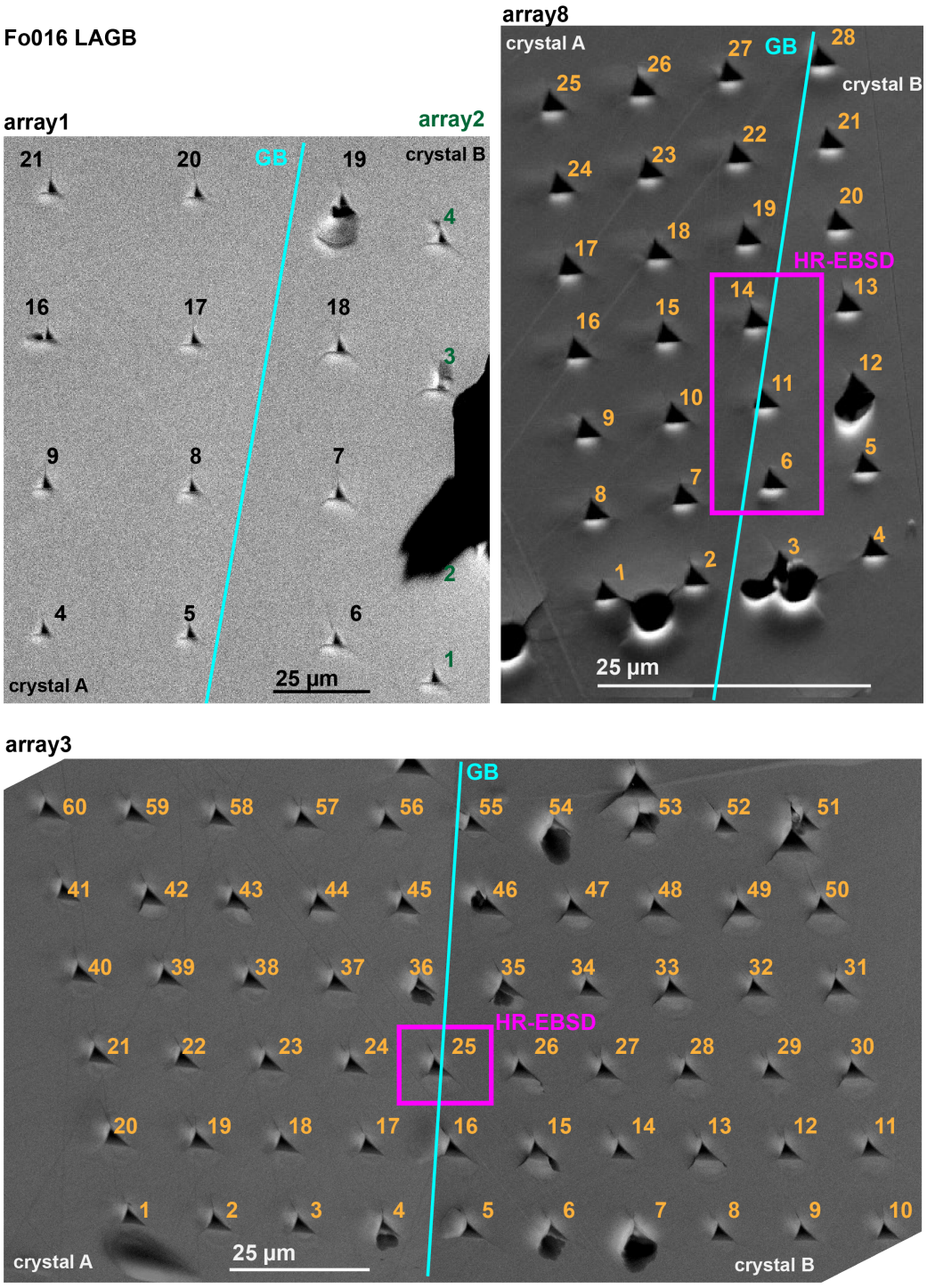


Figure B.2: Backscatter images depicting the arrays placed in the LAGB sample with a sharp indenter. The position of the further microstructural investigations with respect to the other indents and the GB is marked by the magenta square. The numbers hear each indent mark corresponds to the order in which the indents have been places.

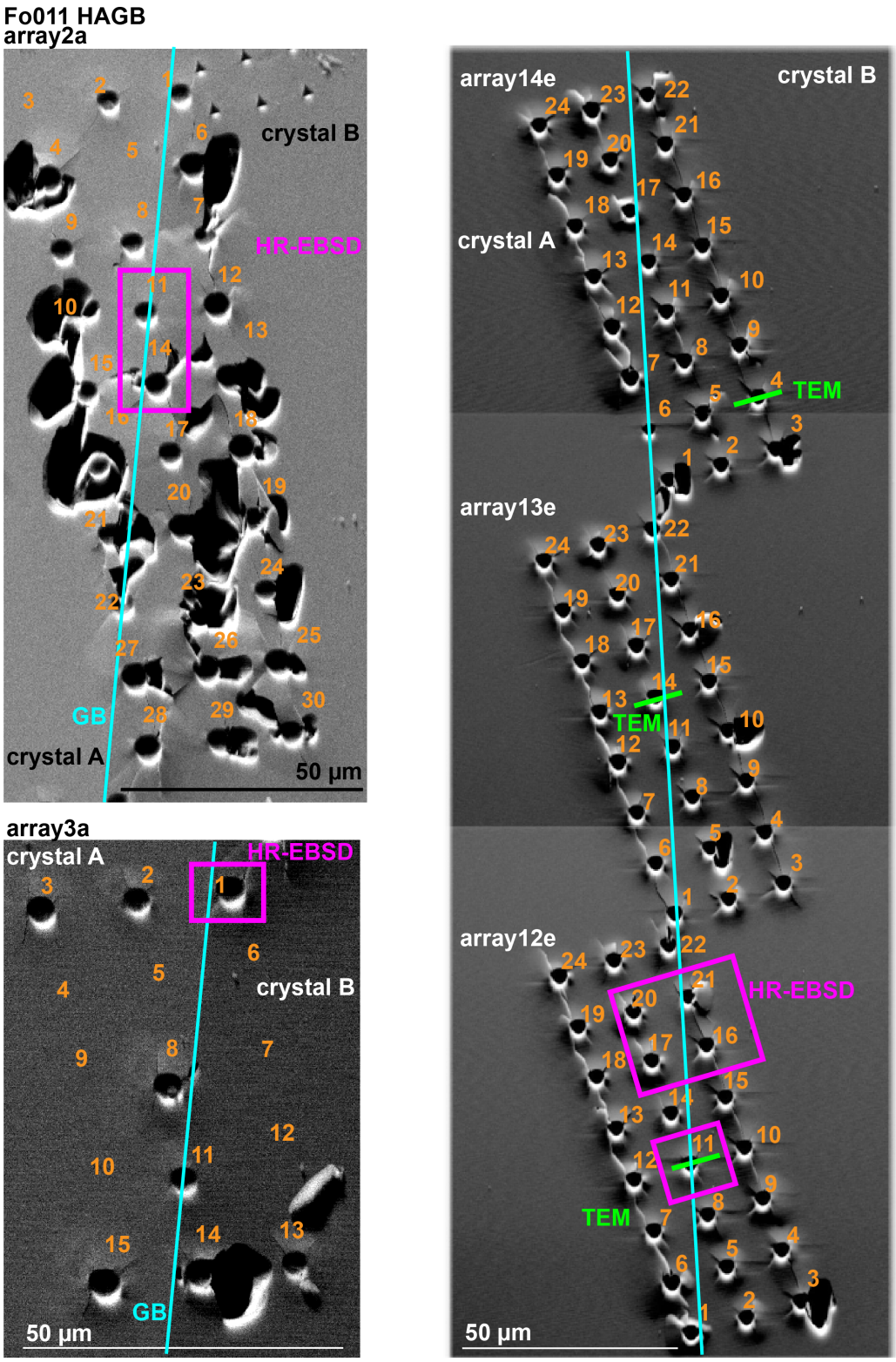


Figure B.3: Backscatter images depicting the arrays placed in the HAGB sample with a spherical indenter as detailed in Table 3.1. The position of the further microstructural investigations with respect to the other indents and the GB is marked by the magenta square. The numbers hear each indent mark corresponds to the order in which the indents have been places.

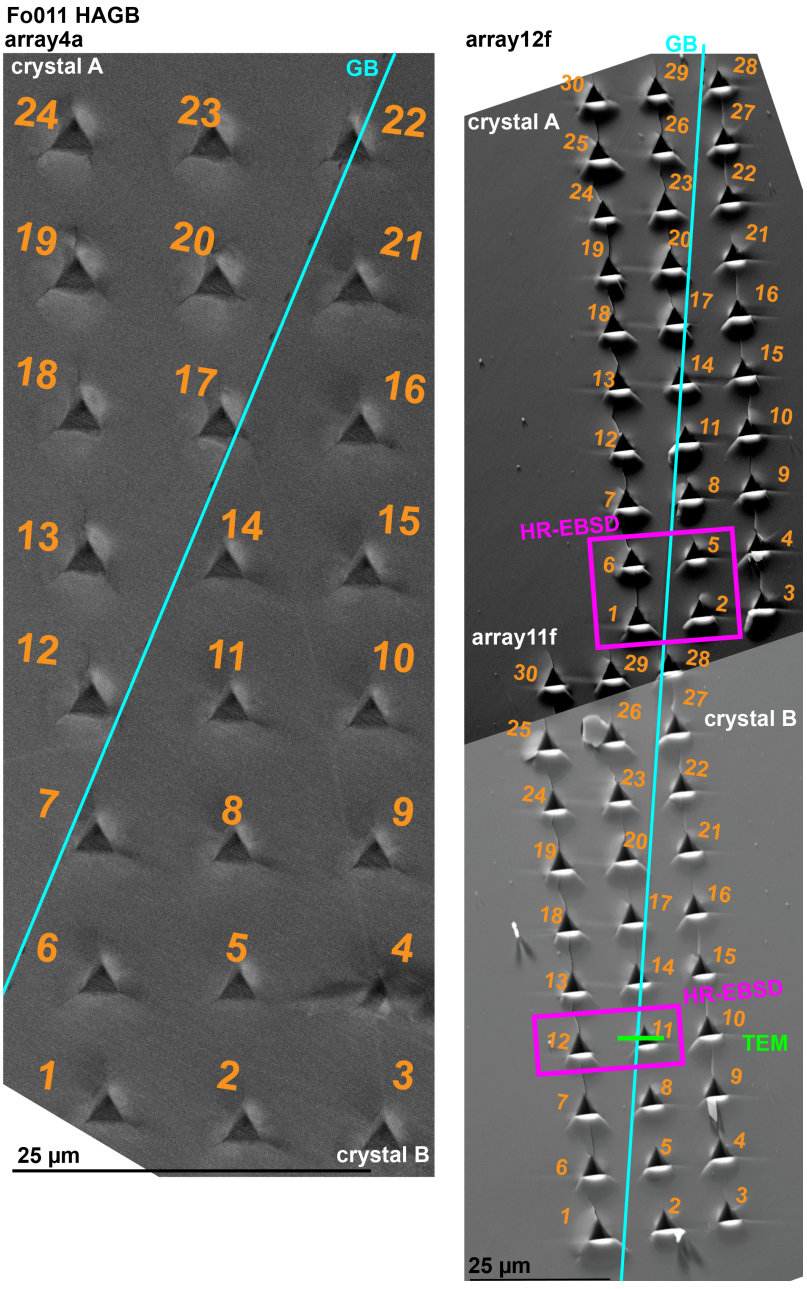


Figure B.4: Backscatter images depicting the arrays placed in the HAGB sample with a sharp indenter. The position of the further microstructural investigations with respect to the other indents and the GB is marked by the magenta square. The numbers hear each indent mark corresponds to the order in which the indents have been places.

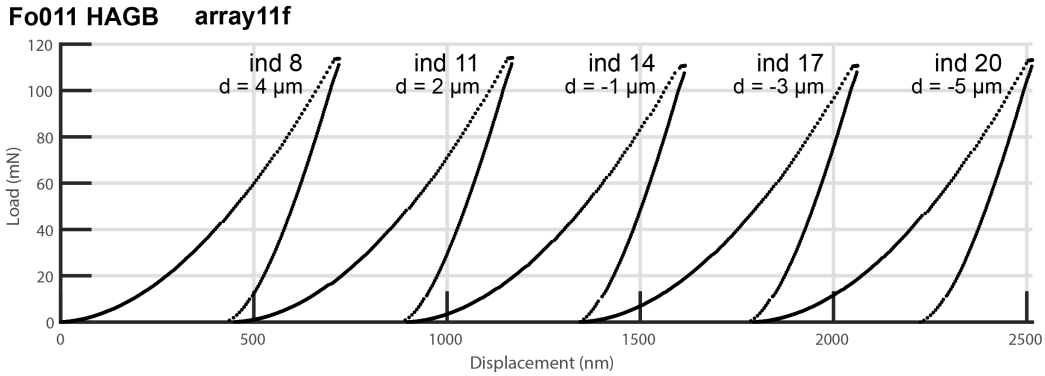


Figure B.5: Examples of load-displacement curves collected with a Berkovich tip, arranges according to distance d from the grain boundary. The indents are part of array11f in Figure B.4. Microstructural TEM investigations corresponding to indent 11 are presented in Figure 3.12 and HR-EBSD investigations are presented in Figure 3.7.

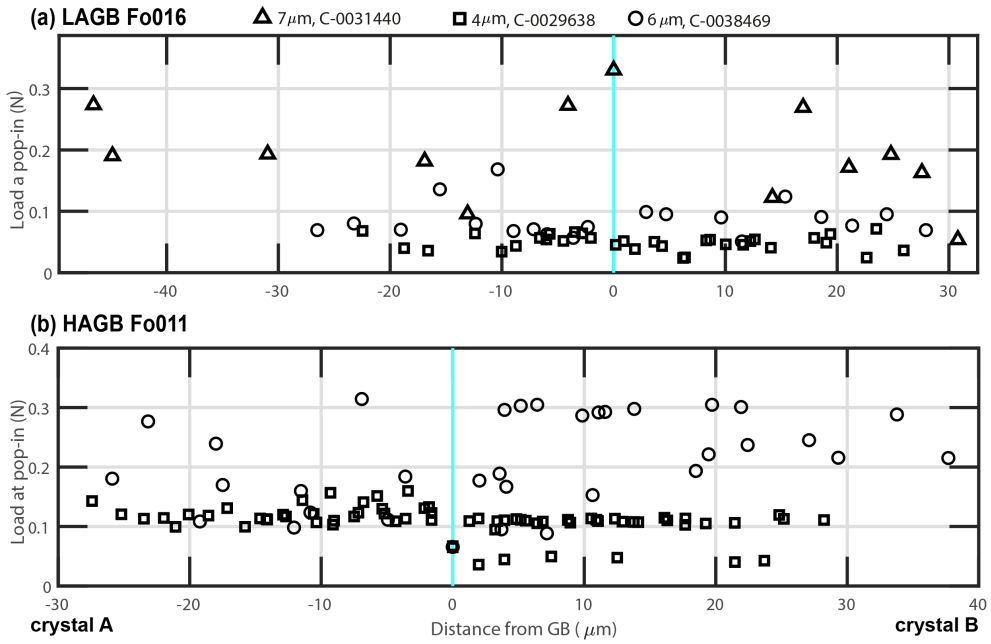


Figure B.6: Load at pop-in in spherical indents placed in the a) LAGB sample and b) in the HAGB sample displayed with respect to distance from the grain boundary. The indents without a pop-in are not displayed.

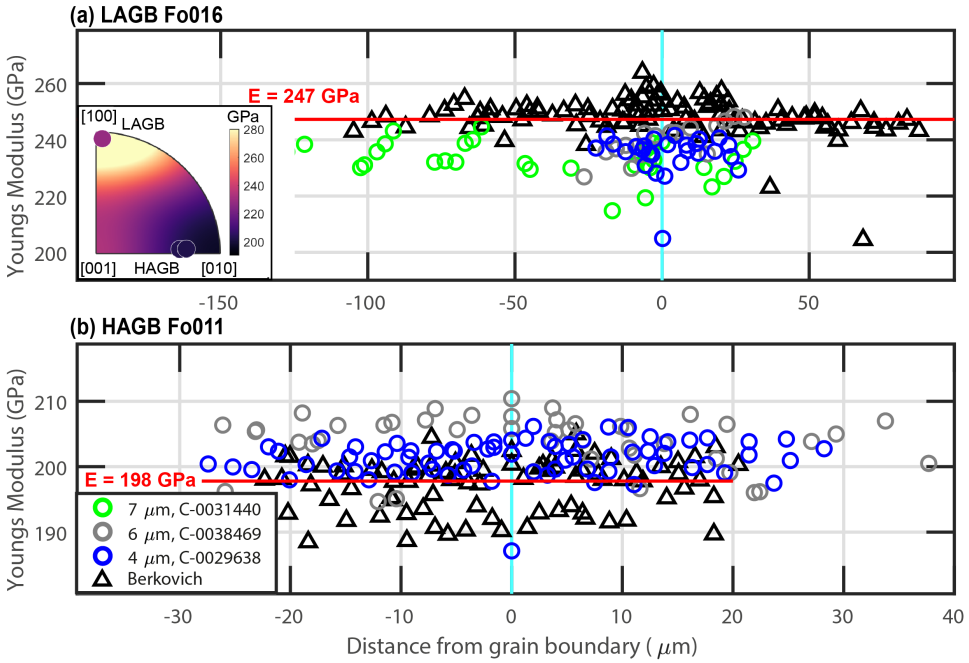


Figure B.7: Results of Young's modulus calculations using Berkovich (open triangles) and spherical (open circles) nanoindentation in the a) low-angle GB sample and b) high-angle GB sample. The red line corresponds to the average value across all the data points. The Young's modulus is calculated fitting Equation 3.6 over the elastic loading segment for spherical nanoindentation data and using Equation 3.8 to average the value of Young's modulus over indentation depths greater than 200 nm for the Berkovich data. The insert in a) represents an inverse pole figure displaying the average values in both samples against a background coloured according to the theoretical Young's modulus from Abramson et al. (1997) for San Carlos olivine.

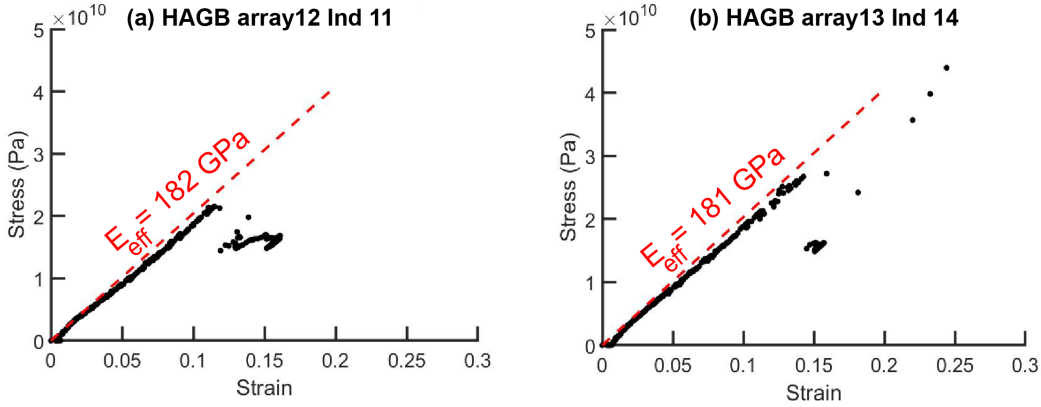


Figure B.8: Stress-strain curves corresponding to the indents displayed in a) Figure 3.9 and Figure b) 3.10.

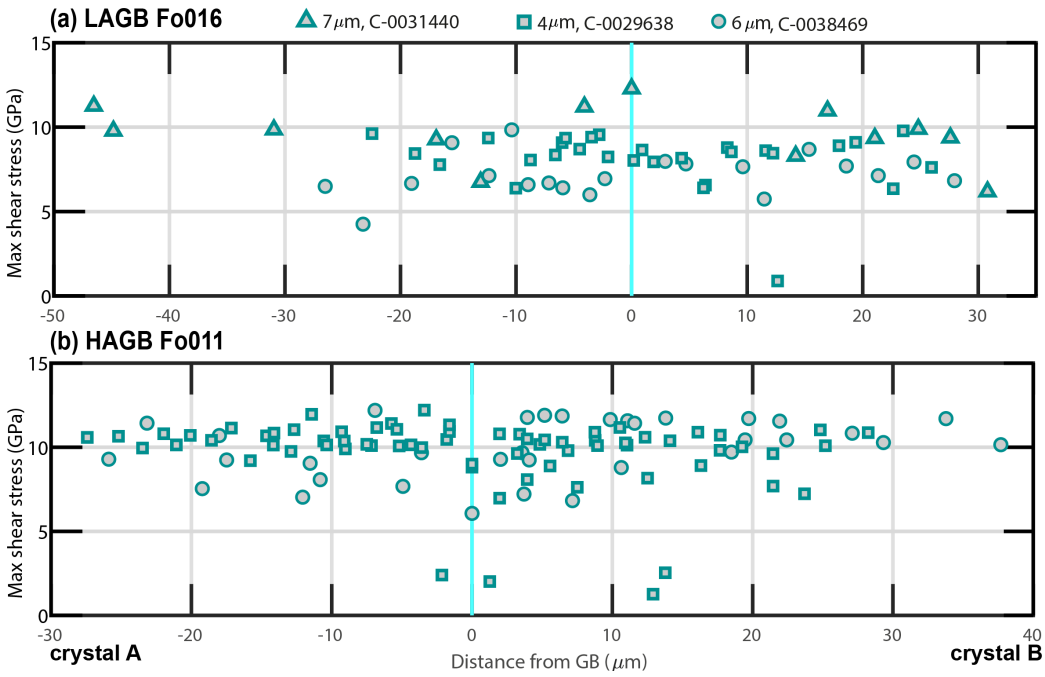


Figure B.9: Shear stress calculated using the load at pop-in displayed in Figure B.6 and Equation 3.7. For a general isotropic case, we can approximate the theoretical shear strength of a crystal with a Poisson's ratio of 0.24 as $E/15.57$ (e.g., Fang et al., 2021). Using the mean Young's modulus values in Figure B.7 we can calculate the theoretical shear strength for the a) LAGB sample as 15.86 GPa and for the b) HAGB sample as 12.71 GPa. Note that in the single crystal, the shear stress value for dislocation nucleation is closer to the theoretical limit.

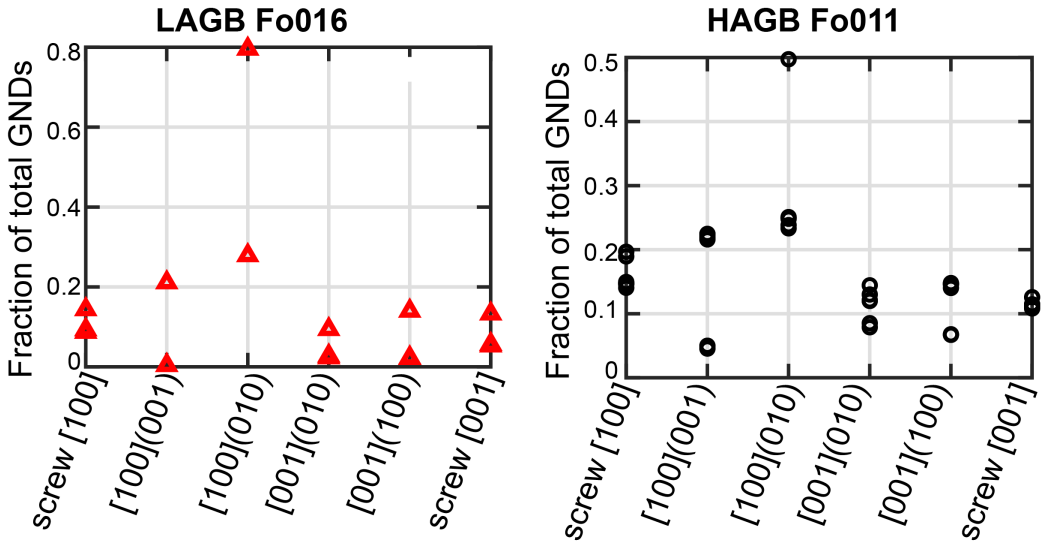


Figure B.10: Fraction of total GNDs corresponding to each slip system accounted into the HR-EBSD calculation for olivine (Wallis et al., 2016).

Appendix C

Supplementary Materials for Chapter 4

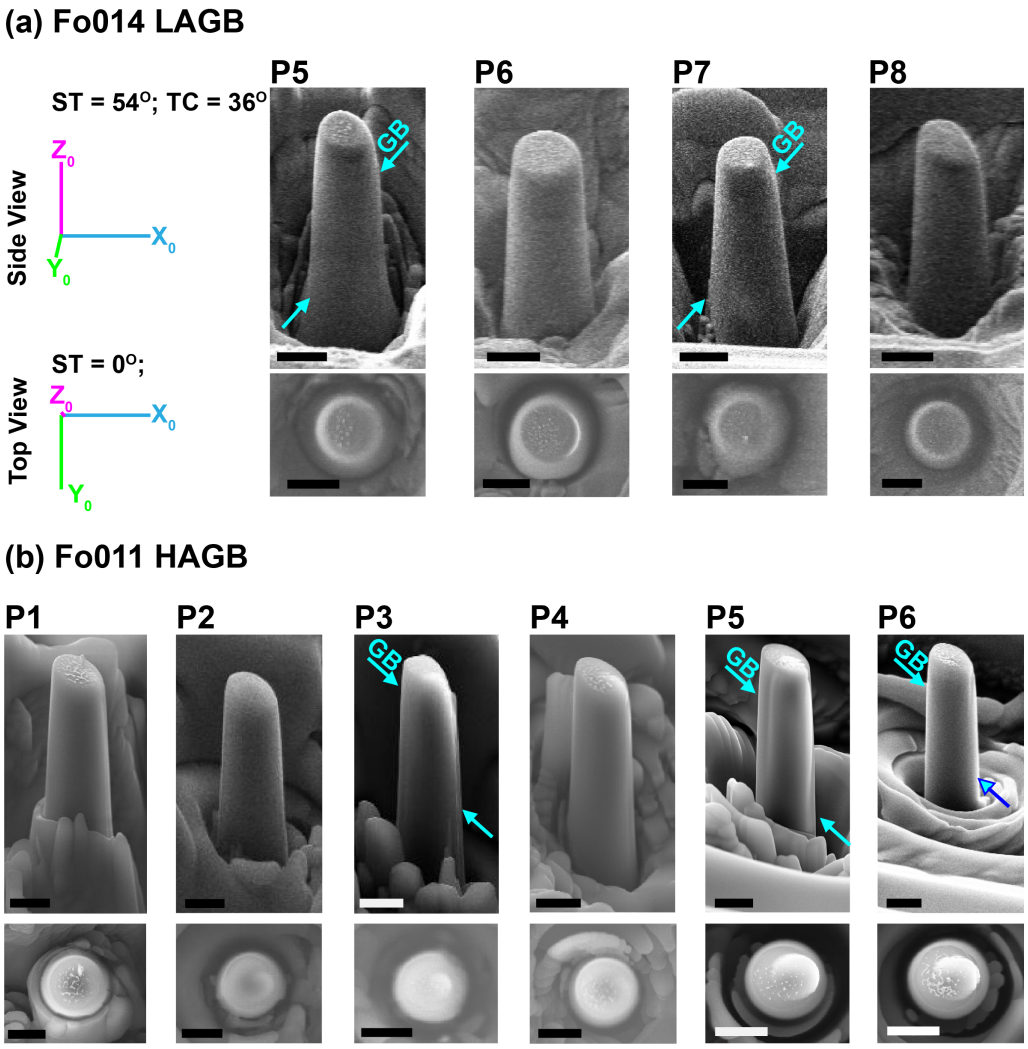


Figure C.1: SEM images of the micropillars in this study before deformation. The first row represent the side view imaged at stage stilt (ST) of 54°, with a tilt correction (TC) of 36°. The second row in each subfigure represents the top view of the micropillars. The axis represent the coordinate system in the reference plane of the sample surface and remain consistent within each row. The blue arrows mark the trace of the grain boundary. a) Micropillars containing a low-angle grain boundary. b) Micropillars containing the high-angle grain boundary. All scalebars are 2 μm.

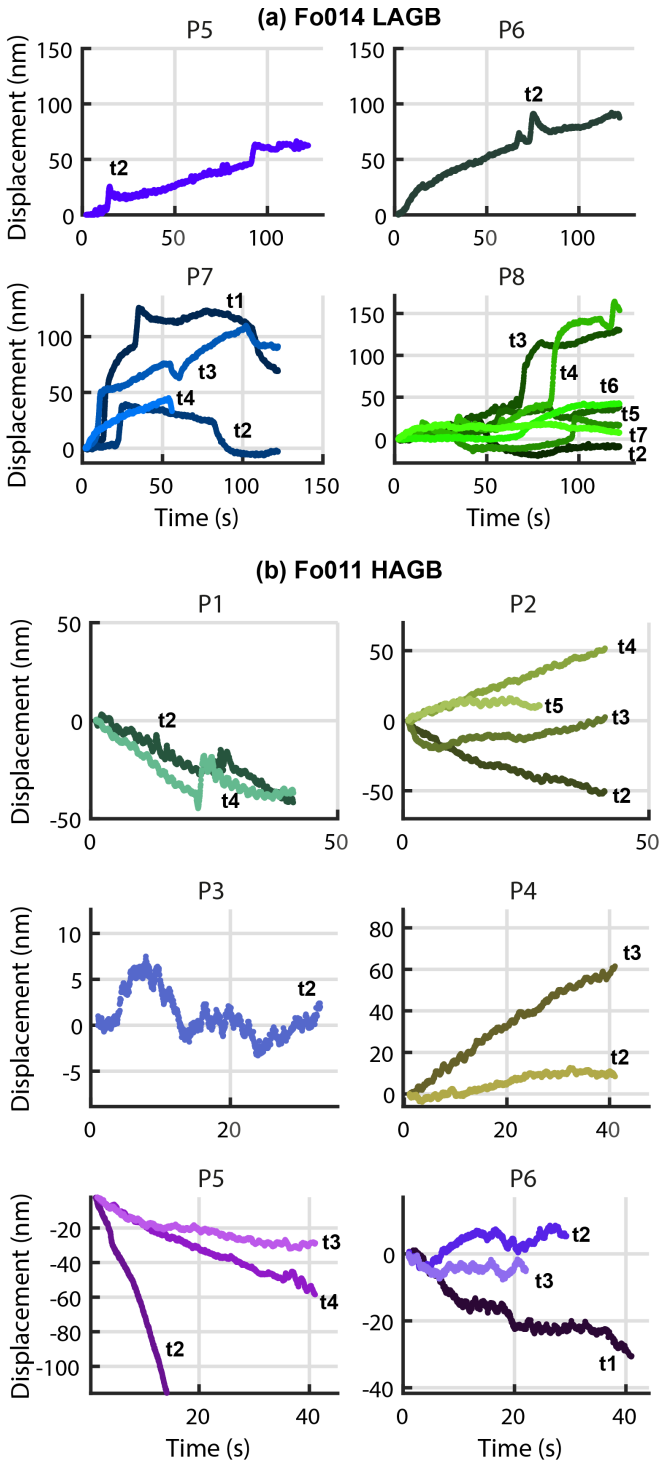


Figure C.2: Thermal drift of displacements during tests in the a) low-angle grain boundary sample and b) high-angle grain boundary sample. These drifts have been automatically accounted for by the acquisition software.

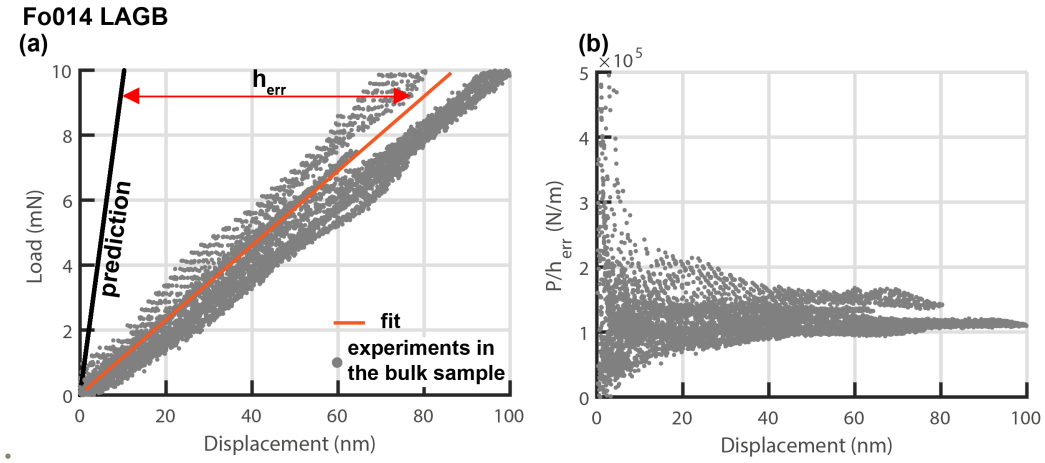


Figure C.3: Example of experiments used for correcting the impact of the compliance of the machine and the sample assembly. a) The prediction is calculated using Equation 4.2 and compared with experiments in the bulk crystal at 700°C (grey) to calculate the error. b) The reported load divided by the computed error is proportional to the compliance of the system.

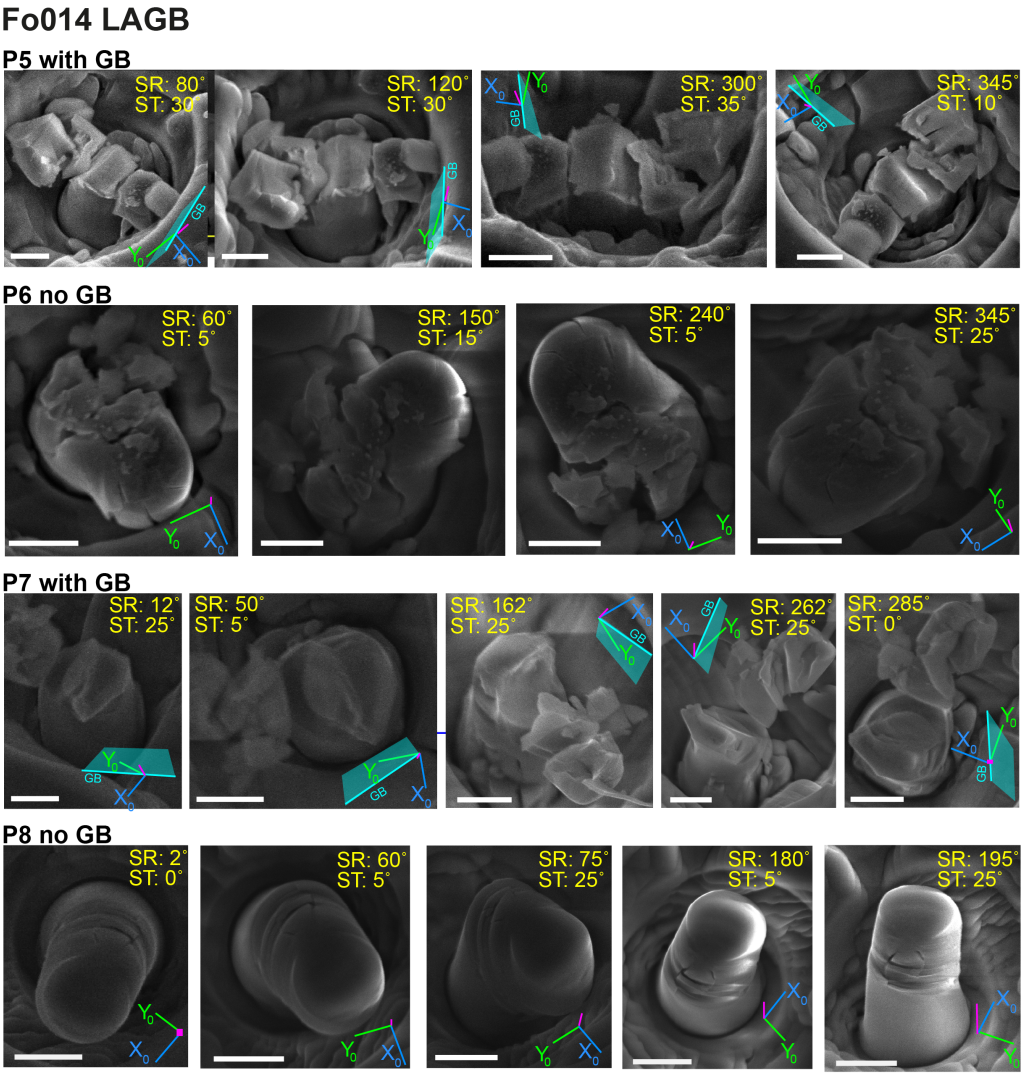


Figure C.4: Post-deformation SEM characterization of micropillars in the SB sample Fo014. The colour-coded axis track the rotation of the surface rotation with respect to Figure 4.1 a). Stage rotation (SR) and stage tilt (ST) denote the stage position during image acquisition. The tilt correction is 0 in all images. The scalebars are 2 µm. The fracture in P7 is consistent with cleavage on the (010) plane.

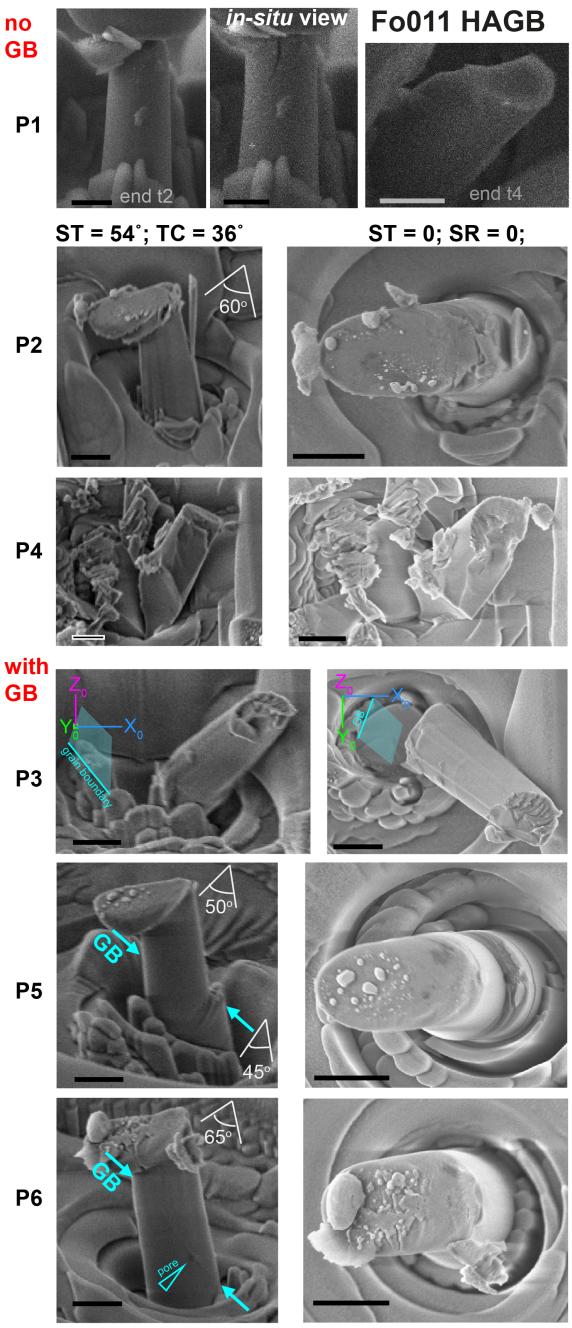


Figure C.5: Post-deformation SEM characterization of micropillars in the HAGB sample Fo011. The colour-coded axis track the rotation of the surface rotation with respect to Figure 4.1 b). The top row displays images during the deformation experiments for P1, which has been decoupled from the base and lost during the indenter lift. Vertical fracture in P4, P3, and possibly P1 correspond to fracture along the (010) plane, which is the cleavage plane of forsterite (Durham et al., 1979; Darot et al., 1985). For the remaining pillars, the first column is the side view, and the second column is the top view. Stage tilt (ST) and tilt correction (TC) denote image acquisition settings. The scalebars are 2 μm.

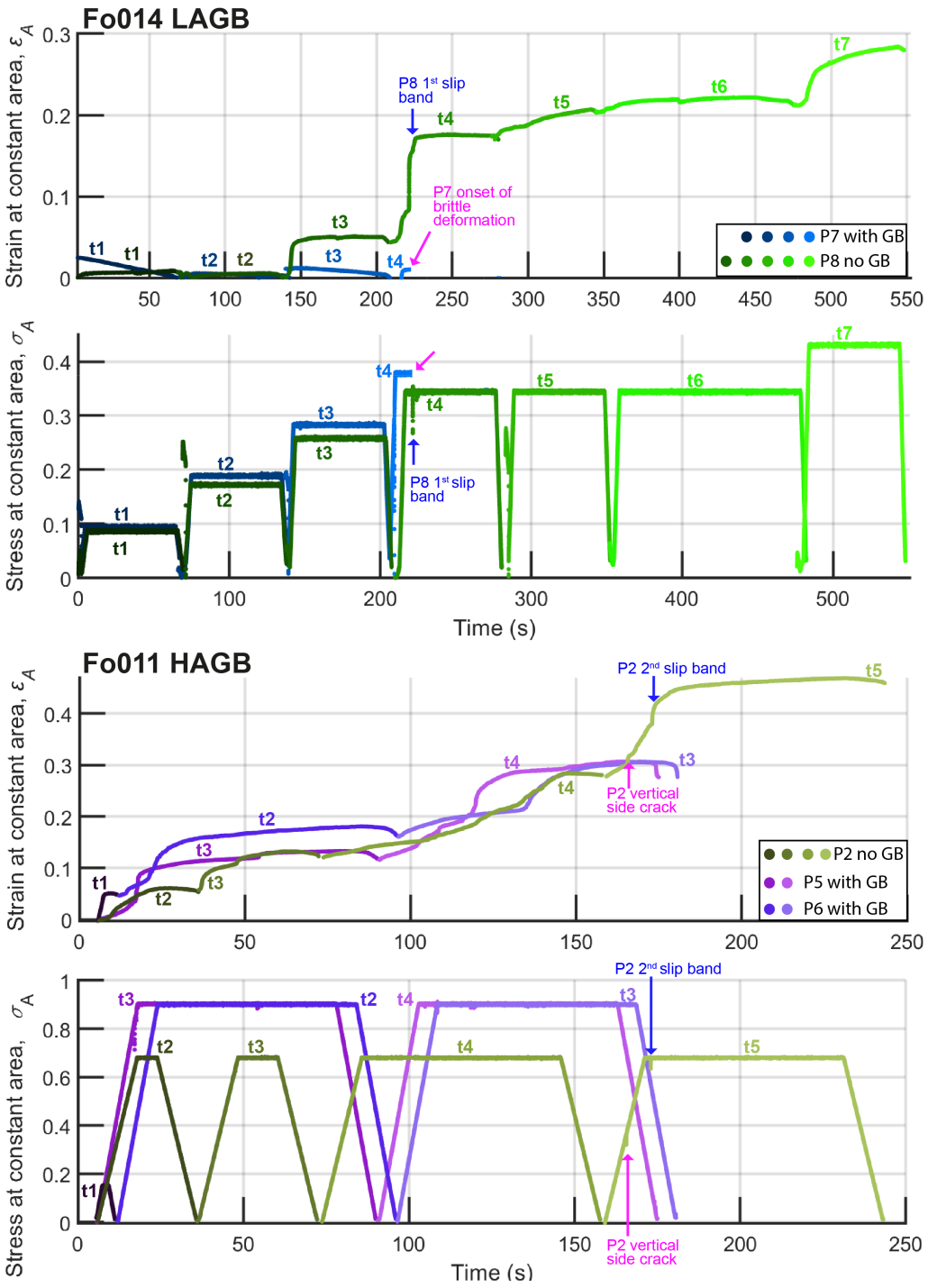


Figure C.6: Strain versus time in the creep tests detailed in Table 4.2.

Appendix D

Supplementary Materials for Chapter 5

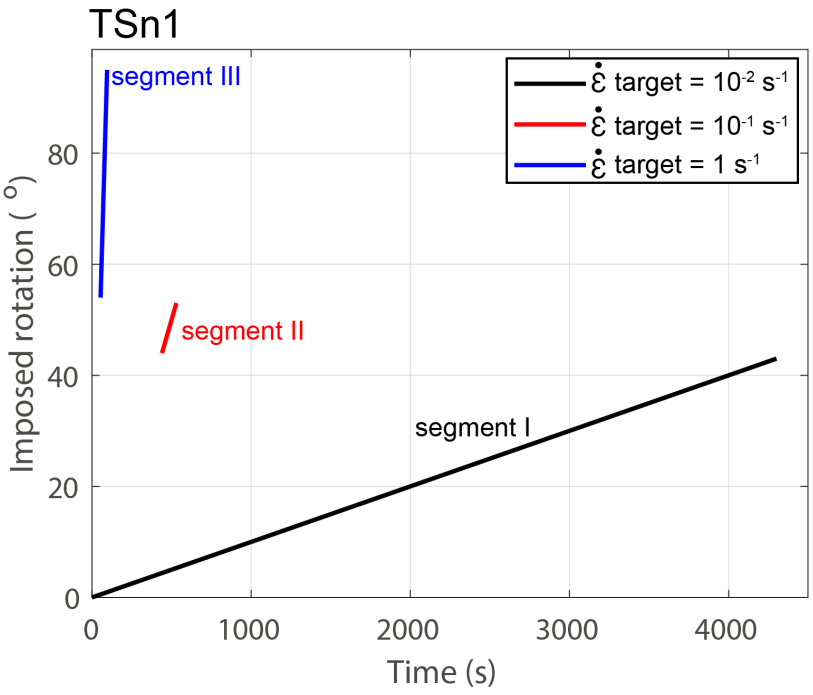


Figure D.1: Imposed strain path for the *in-situ* experiment on the sample TSn1.

Bibliography

EH Abramson, JM Brown, LJ Slutsky, and J Zaug. The elastic constants of san carlos olivine to 17 gpa. *Journal of Geophysical Research: Solid Earth*, 102(B6): 12253–12263, 1997.

Omar Adjaoud, Katharina Marquardt, and Sandro Jahn. Atomic structures and energies of grain boundaries in mg2sio4 forsterite from atomistic modeling. *Physics and Chemistry of Minerals*, 39(9):749–760, 2012.

KE Aifantis, WA Soer, J Th M De Hosson, and JR Willis. Interfaces within strain gradient plasticity: theory and experiments. *Acta Materialia*, 54(19):5077–5085, 2006.

E Alabort, P Kontis, D Barba, K Dragnevski, and RC Reed. On the mechanisms of superplasticity in ti–6al–4v. *Acta Materialia*, 105:449–463, 2016.

Mohsen Taheri Andani, Aaditya Lakshmanan, Mohammadreza Karamooz-Ravari, Veera Sundararaghavan, John Allison, and Amit Misra. A quantitative study of stress fields ahead of a slip band blocked by a grain boundary in unalloyed magnesium. *Scientific reports*, 10(1):1–8, 2020.

D Andrault, MA Bouhifd, JP Itie, and P Richet. Compression and amorphization of (mg, fe) 2sio4 olivines: An x-ray diffraction study up to 70 gpa. *Physics and Chemistry of Minerals*, 22(2):99–107, 1995.

A.P.Sutton and R.W.Balluffi. *Interfaces in Crystalline Materials*. Oxford University Press, 1995.

DEJ Armstrong, CD Hardie, JSKL Gibson, AJ Bushby, PD Edmondson, and SG Roberts. Small-scale characterisation of irradiated nuclear materials: Part ii nanoindentation and micro-cantilever testing of ion irradiated nuclear materials. *Journal of Nuclear Materials*, 462:374–381, 2015. URL `https://doi.org/10.1016/j.jnucmat.2015.01.053`.

MF Ashby. Boundary defects, and atomistic aspects of boundary sliding and diffusional creep. *Surface Science*, 31:498–542, 1972.

Johannes Ast, Gaurav Mohanty, Yi Guo, Johann Michler, and Xavier Maeder. In situ micromechanical testing of tungsten micro-cantilevers using hr-ebsd for the assessment of deformation evolution. *Materials & Design*, 117:265–266, 2017.

DH Bae and AK Ghosh. A planar simple shear test and flow behavior in a superplastic al-mg alloy. *Metallurgical and Materials Transactions A*, 34(11):2465–2471, 2003.

Quan Bai and DL Kohlstedt. High-temperature creep of olivine single crystals, 2. dislocation structures. *Tectonophysics*, 206(1-2):1–29, 1992.

Paul Baral, Andrey Orekhov, Ralf Dohmen, Michaël Coulombier, Jean Pierre Raskin, Patrick Cordier, Hosni Idrissi, and Thomas Pardoen. Rheology of amorphous olivine thin films characterized by nanoindentation. *Acta Materialia*, 219:117257, 2021.

Sandip Basu, Alexander Moseson, and Michel W Barsoum. On the determination of spherical nanoindentation stress–strain curves. *Journal of materials research*, 21 (10):2628–2637, 2006.

Vladimir Bata and Elena V Pereloma. An alternative physical explanation of the hall–petch relation. *Acta materialia*, 52(3):657–665, 2004.

E Bayerschen, AT McBride, BD Reddy, and T Böhlke. Review on slip transmission criteria in experiments and crystal plasticity models. *Journal of materials science*, 51(5):2243–2258, 2016.

Wiktor Bednarczyk, Jakub Kawalko, Maria Wkatroba, and Piotr Bala. Achieving room temperature superplasticity in the zn-0.5 cu alloy processed via equal channel angular pressing. *Materials Science and Engineering: A*, 723:126–133, 2018.

H Bei, ZP Lu, and EP George. Theoretical strength and the onset of plasticity in bulk metallic glasses investigated by nanoindentation with a spherical indenter. *Physical Review Letters*, 93(12):125504, 2004.

Hongbin Bei, YZ Xia, Rozaliya I Barabash, and YF Gao. A tale of two mechanisms: Strain-softening versus strain-hardening in single crystals under small stressed volumes. *Scripta Materialia*, 110:48–52, 2016.

Hossein Besharatloo and Jeffrey M Wheeler. Influence of indentation size and spacing on statistical phase analysis via high-speed nanoindentation mapping of metal alloys. *Journal of Materials Research*, 36(11):2198–2212, 2021.

Magali I Billen and Greg Hirth. Rheologic controls on slab dynamics. *Geochemistry, Geophysics, Geosystems*, 8(8), 2007.

J Blaber, B Adair, and A Antoniou. Ncorr: open-source 2d digital image correlation matlab software. *Experimental Mechanics*, 55(6):1105–1122, 2015.

Caroline Bollinger, Katharina Marquardt, and Filippe Ferreira. Intragranular plasticity vs. grain boundary sliding (gbs) in forsterite: Microstructural evidence at high pressures (3.5–5.0 gpa). *American Mineralogist: Journal of Earth and Planetary Materials*, 104(2):220–231, 2019.

L Borkowski, JA Sharon, and A Staroselsky. In situ micromechanical testing for single crystal property characterization. *Metallurgical and Materials Transactions A*, 49 (12):6022–6033, 2018.

S Bouvier, H Haddadi, P Levée, and C Teodosiu. Simple shear tests: Experimental techniques and characterization of the plastic anisotropy of rolled sheets at large strains. *Journal of Materials Processing Technology*, 172(1):96–103, 2006.

TP. Breithaupt, LN. Hansen, DW. Wallis, and DEJ. Armstrong. Low-temperature plasticity of plagioclase from indentation. Master's thesis, University of Oxford, 2017.

TB Britton and AJ Wilkinson. Measurement of residual elastic strain and lattice rotations with high resolution electron backscatter diffraction. *Ultramicroscopy*, 111 (8):1395–1404, 2011.

TB Britton and Angus J Wilkinson. High resolution electron backscatter diffraction measurements of elastic strain variations in the presence of larger lattice rotations. *Ultramicroscopy*, 114:82–95, 2012.

TB Britton, D Randman, and AJ Wilkinson. Nanoindentation study of slip transfer phenomenon at grain boundaries. *Journal of Materials Research*, 24(3):607–615, 2009.

TB Britton, H Liang, FPE Dunne, and AJ Wilkinson. The effect of crystal orientation on the indentation response of commercially pure titanium: experiments and simulations. *Proceedings of the Royal Society A: Mathematical, Physical and Engineering Sciences*, 466(2115):695–719, 2010.

Emily E Brodsky, James D Kirkpatrick, and Thibault Candela. Constraints from fault roughness on the scale-dependent strength of rocks. *Geology*, 44(1):19–22, 2016.

CA Bronkhorst, EK Cerreta, Q Xue, PJ Maudlin, TA Mason, and GT Gray Iii. An experimental and numerical study of the localization behavior of tantalum and stainless steel. *International Journal of Plasticity*, 22(7):1304–1335, 2006.

Andrew J Bushby and Nigel M Jennett. Determining the area function of spherical indenters for nanoindentation. *MRS Online Proceedings Library*, 649(1):7171–7176, 2000. URL `https://doi.org/10.1557/PROC-649-Q7.17`.

Andrew J Bushby, Steve G Roberts, and Christopher D Hardie. Nanoindentation investigation of ion-irradiated fe–cr alloys using spherical indenters. *Journal of Materials Research*, 27(1):85–90, 2012. URL `https://doi.org/10.1557/jmr.2011.304`.

M Cabibbo, P Ricci, R Cecchini, Z Rymuza, J Sullivan, S Dub, and S Cohen. An international round-robin calibration protocol for nanoindentation measurements. *Micron*, 43(2-3):215–222, 2012. URL `https://doi.org/10.1016/j.micron.2011.07.016`.

N Chandra and H Ghonem. Interfacial mechanics of push-out tests: theory and experiments. *Composites part A: applied science and manufacturing*, 32(3-4):575–584, 2001.

Siwei Chen, Yuichi Miyahara, and Akiyoshi Nomoto. Crystallographic orientation dependence of nanoindentation hardness in austenitic phase of stainless steel. *Philosophical Magazine Letters*, 98(11):473–485, 2018.

In-Chul Choi, Yakai Zhao, Byung-Gil Yoo, Yong-Jae Kim, Jin-Yoo Suh, Upadrasta Ramamurty, and Jae-il Jang. Estimation of the shear transformation zone size in a bulk metallic glass through statistical analysis of the first pop-in stresses during spherical nanoindentation. *Scripta Materialia*, 66(11):923–926, 2012.

Zachary C Cordero, Braden E Knight, and Christopher A Schuh. Six decades of the hall–petch effect–a survey of grain-size strengthening studies on pure metals. *International Materials Reviews*, 61(8):495–512, 2016.

Patrick Cordier, Sylvie Demouchy, Benoit Beausir, Vincent Taupin, Fabrice Barou, and Claude Fressengeas. Disclinations provide the missing mechanism for deforming olivine-rich rocks in the mantle. *Nature*, 507(7490):51–56, 2014.

F Cosandey, S Ui, B Cao, R Schaller, and W Benoit. Grain boundary sliding kinetics and stress relaxation phenomena in ni alloys. *MRS Online Proceedings Library (OPL)*, 229, 1991.

Ao H Cottrell and B Ao Bilby. Dislocation theory of yielding and strain ageing of iron. *Proceedings of the Physical Society. Section A*, 62(1):49, 1949.

Zachary S Courtright, Nicolas P Leclerc, Hyung Nun Kim, and Surya R Kalidindi. Critical comparison of spherical microindentation, small punch test, and uniaxial tensile testing for selective laser melted inconel 718. *Applied Sciences*, 11(3):1061, 2021.

FW Crossman and MF Ashby. The non-uniform flow of polycrystals by grain-boundary sliding accommodated by power-law creep. *Acta Metallurgica*, 23(4):425–440, 1975.

M Darot, Y Gueguen, Z Benchemam, and R Gaboriaud. Ductile-brittle transition investigated by micro-indentation: results for quartz and olivine. *Physics of the Earth and Planetary Interiors*, 40(3):180–186, 1985.

Michel Darot and Yves Gueguen. High-temperature creep of forsterite single crystals. *Journal of Geophysical Research: Solid Earth*, 86(B7):6219–6234, 1981.

Gerhard Dehm, Balila Nagamani Jaya, Rejin Raghavan, and Christoph Kirchlechner. Overview on micro-and nanomechanical testing: New insights in interface plasticity and fracture at small length scales. *Acta Materialia*, 142:248–282, 2018.

Sylvie Demouchy. Defects in olivine. *European Journal of Mineralogy*, 33(3):249–282, 2021.

Sylvie Demouchy, Andréa Tommasi, Fabrice Barou, David Mainprice, and Patrick Cordier. Deformation of olivine in torsion under hydrous conditions. *Physics of the Earth and Planetary Interiors*, 202:56–70, 2012.

Sylvie Demouchy, Andréa Tommasi, Tiziana Boffa Ballaran, and Patrick Cordier. Low strength of earths uppermost mantle inferred from tri-axial deformation experiments on dry olivine crystals. *Physics of the Earth and Planetary Interiors*, 220:37–49, 2013.

Sylvie Demouchy, Alexandre Mussi, Fabrice Barou, Andrea Tommasi, and Patrick Cordier. Viscoplasticity of polycrystalline olivine experimentally deformed at high pressure and 900 c. *Tectonophysics*, 623:123–135, 2014.

M Dewald and WA Curtin. Multiscale modeling of dislocation/grain-boundary interactions: Iii. 60 dislocations impinging on $\sigma 3$, $\sigma 9$ and $\sigma 11$ tilt boundaries in al. *Modelling and Simulation in Materials Science and Engineering*, 19(5):055002, 2011.

MP Dewald and WA Curtin. Multiscale modelling of dislocation/grain boundary interactions. ii. screw dislocations impinging on tilt boundaries in al. *Philosophical Magazine*, 87(30):4615–4641, 2007.

Robert S Dietz. Continent and ocean basin evolution by spreading of the sea floor. *Nature*, 190(4779):854–857, 1961.

Véronique Doquet and B Barkia. Combined afm, sem and crystal plasticity analysis of grain boundary sliding in titanium at room temperature. *Mechanics of Materials*, 103:18–27, 2016.

Anthony Druiventak, Claudia A Trepmann, Jörg Renner, and Karin Hanke. Low-temperature plasticity of olivine during high stress deformation of peridotite at lithospheric conditionsan experimental study. *Earth and Planetary Science Letters*, 311(3-4):199–211, 2011.

Martyn R Drury, Reinoud LM Vissers, Dirk Van der Wal, and Eilard H Hoogerduijn Strating. Shear localisation in upper mantle peridotites. *Pure and Applied Geophysics*, 137(4):439–460, 1991.

FPE Dunne, R Kiwanuka, and AJ Wilkinson. Crystal plasticity analysis of microdeformation, lattice rotation and geometrically necessary dislocation density. *Proceedings of the Royal Society A: Mathematical, Physical and Engineering Sciences*, 468(2145):2509–2531, 2012.

WB Durham and C Goetze. Plastic flow of oriented single crystals of olivine: 1. mechanical data. *Journal of geophysical Research*, 82(36):5737–5753, 1977.

WB Durham, C Froidevaux, and O Jaoul. Transient and steady-state creep of pure forsterite at low stress. *Physics of the Earth and Planetary Interiors*, 19(3):263–274, 1979.

Julien Durinck, Alexandre Legris, and Patrick Cordier. Influence of crystal chemistry on ideal plastic shear anisotropy in forsterite: First principle calculations. *American Mineralogist*, 90(7):1072–1077, 2005.

Julien Durinck, Benoit Devincre, Ladislas Kubin, and Patrick Cordier. Modeling the plastic deformation of olivine by dislocation dynamics simulations. *American Mineralogist*, 92(8-9):1346–1357, 2007.

Kaveh Edalati, Zenji Horita, and Ruslan Z Valiev. Transition from poor ductility to room-temperature superplasticity in a nanostructured aluminum alloy. *Scientific reports*, 8(1):1–8, 2018.

TEJ Edwards, Fabio Di Gioacchino, HP Springbett, RA Oliver, and WJ Clegg. Stable speckle patterns for nano-scale strain mapping up to 700 c. *Experimental mechanics*, 57(9):1469–1482, 2017.

Adnan Eghtesad and Marko Knezevic. High-performance full-field crystal plasticity with dislocation-based hardening and slip system back-stress laws: application to modeling deformation of dual-phase steels. *Journal of the Mechanics and Physics of Solids*, 134:103750, 2020.

Philip England and Peter Molnar. Rheology of the lithosphere beneath the central and western tien shan. *Journal of Geophysical Research: Solid Earth*, 120(5):3803–3823, 2015.

Brian Evans and Christopher Goetze. The temperature variation of hardness of olivine and its implication for polycrystalline yield stress. *Journal of Geophysical Research: Solid Earth*, 84(B10):5505–5524, 1979.

Xufei Fang, Hanna Bishara, Kuan Ding, Hanna Tsybenko, Lukas Porz, Marion Höfling, Enrico Bruder, Yingwei Li, Gerhard Dehm, and Karsten Durst. Nanoindentation pop-in in oxides at room temperature: dislocation activation or crack formation? *Journal of the American ceramic society*, 104(9):4728–4741, 2021.

Ulrich Faul and Ian Jackson. Transient creep and strain energy dissipation: An experimental perspective. *Annual Review of Earth and Planetary Sciences*, 43: 541–569, 2015.

Ulrich H Faul, JD Fitz Gerald, RJM Farla, Rose Ahlefeldt, and Ian Jackson. Dislocation creep of fine-grained olivine. *Journal of Geophysical Research: Solid Earth*, 116(B1), 2011.

Hongzhan Fei, Sanae Koizumi, Naoya Sakamoto, Minako Hashiguchi, Hisayoshi Yurimoto, Katharina Marquardt, Nobuyoshi Miyajima, Daisuke Yamazaki, and Tomoo Katsura. New constraints on upper mantle creep mechanism inferred from silicon grain-boundary diffusion rates. *Earth and Planetary Science Letters*, 433: 350–359, 2016.

Huiyang Fei, Amit Abraham, Nikhilesh Chawla, and Hanqing Jiang. Evaluation of micro-pillar compression tests for accurate determination of elastic-plastic constitutive relations. *Journal of Applied Mechanics*, 79(6), 2012.

Filippe Ferreira, Lars N Hansen, and Katharina Marquardt. The effect of grain boundaries on plastic deformation of olivine. *Journal of Geophysical Research: Solid Earth*, 126(7):e2020JB020273, 2021.

Richard P Feynman. There's plenty of room at the bottom [data storage]. *Journal of microelectromechanical systems*, 1(1):60–66, 1992.

JS Field and MV Swain. A simple predictive model for spherical indentation. *Journal of Materials Research*, 8(2):297–306, 1993. doi:https://doi.org/10.1557/JMR.1993.0297.

Anthony C Fischer-Cripps. Analysis of nanoindentation test data. In *Nanoindentation*, pages 39–75. Springer, 2011.

Anthony C Fischer-Cripps and DW Nicholson. Nanoindentation. mechanical engineering series. *Appl. Mech. Rev.*, 57(2):B12–B12, 2004.

Harold J Frost and Michael F Ashby. *Deformation mechanism maps: the plasticity and creep of metals and ceramics*. Pergamon press, 1982.

M Furukawa, Zenji Horita, M Nemoto, and TG Langdon. Processing of metals by equal-channel angular pressing. *Journal of materials science*, 36(12):2835–2843, 2001.

RJ Gaboriaud, M Darot, Y Gueguen, and J Woirgard. Dislocations in olivine indented at low temperatures. *Physics and Chemistry of Minerals*, 7(2):100–104, 1981.

Yanfei Gao and Hongbin Bei. Strength statistics of single crystals and metallic glasses under small stressed volumes. *Progress in Materials Science*, 82:118–150, 2016.

Emmanuel Gardés, David Gibouin, Bertrand Radiguet, Adrian David, Wilfrid Prellier, and Katharina Marquardt. Magnesium transport in olivine mantle: new insights from miniaturized study of volume and grain boundary diffusion in mg2sio4 bicrystals. *Contributions to Mineralogy and Petrology*, 176(12):1–16, 2021.

Robyn Gardner, Sandra Piazolo, Lynn Evans, and Nathan Daczko. Patterns of strain localization in heterogeneous, polycrystalline rocks–a numerical perspective. *Earth and Planetary Science Letters*, 463:253–265, 2017.

Julien Gasc, Sylvie Demouchy, Fabrice Barou, Sanae Koizumi, and Patrick Cordier. Creep mechanisms in the lithospheric mantle inferred from deformation of iron-free forsterite aggregates at 900–1200 c. *Tectonophysics*, 761:16–30, 2019.

Saeede Ghorbanpour, Milovan Zecevic, Anil Kumar, Mohammad Jahedi, Jonathan Bicknell, Luke Jorgensen, Irene J Beyerlein, and Marko Knezevic. A crystal plasticity model incorporating the effects of precipitates in superalloys: application to tensile, compressive, and cyclic deformation of inconel 718. *International Journal of Plasticity*, 99:162–185, 2017.

Jonathan G Gigax, Jon K Baldwin, Chris J Sheehan, Stuart A Maloy, and Nan Li. Microscale shear specimens for evaluating the shear deformation in single-crystal and nanocrystalline cu and at cu–si interfaces. *Journal of Materials Research*, 34 (9):1574–1583, 2019.

H Gleiter. The nature of dislocations in high-angle grain boundaries. *Philosophical Magazine*, 36(5):1109–1120, 1977.

Christopher Goetze and Brian Evans. Stress and temperature in the bending lithosphere as constrained by experimental rock mechanics. *Geophysical Journal International*, 59(3):463–478, 1979.

Jicheng Gong and Angus J Wilkinson. Sample size effects on grain boundary sliding. *Scripta Materialia*, 114:17–20, 2016.

David Gonzalez, Igor Simonovski, Philip J Withers, and J Quinta da Fonseca. Modelling the effect of elastic and plastic anisotropies on stresses at grain boundaries. *International Journal of Plasticity*, 61:49–63, 2014.

George Thompson Gray III, KS Vecchio, and Veronica Livescu. Compact forced simple-shear sample for studying shear localization in materials. *Acta Materialia*, 103:12–22, 2016.

David Griggs. Hydrolytic weakening of quartz and other silicates. *Geophysical Journal International*, 14(1-4):19–31, 1967.

David T Griggs. Deformation of rocks under high confining pressures: I. experiments at room temperature. *The Journal of Geology*, 44(5):541–577, 1936.

Yongjun Guan, Bo Chen, Jinwen Zou, T Ben Britton, Jun Jiang, and Fionn PE Dunne. Crystal plasticity modelling and hr-dic measurement of slip activation and strain localization in single and oligo-crystal ni alloys under fatigue. *International Journal of Plasticity*, 88:70–88, 2017.

Y Guo, TB Britton, and AJ Wilkinson. Slip band–grain boundary interactions in commercial-purity titanium. *Acta Materialia*, 76:1–12, 2014.

Yi Guo, David M Collins, Edmund Tarleton, Felix Hofmann, Angus J Wilkinson, and T Ben Britton. Dislocation density distribution at slip band-grain boundary intersections. *Acta Materialia*, 182:172–183, 2020.

BL Hackett, Andrew A Wereszczak, and GM Pharr. Evaluation of new technique to estimate yield stress in brittle materials via spherical indentation testing. In *Proceeding of the 42nd International Conference on Advanced Ceramics and Composites: Ceramic Engineering and Science Proceedings Volume 39, Issue 2*, volume 39, pages 61–71. John Wiley & Sons, Inc. Hoboken, NJ, USA, 2019.

EO Hall. The deformation and ageing of mild steel: Iii discussion of results. *Proceedings of the Physical Society. Section B*, 64(9):747, 1951.

Jian Han, Spencer L Thomas, and David J Srolovitz. Grain-boundary kinetics: A unified approach. *Progress in Materials Science*, 98:386–476, 2018.

Lars N Hansen, Mark E Zimmerman, Amanda M Dillman, and David L Kohlstedt. Strain localization in olivine aggregates at high temperature: A laboratory comparison of constant-strain-rate and constant-stress boundary conditions. *Earth and Planetary Science Letters*, 333:134–145, 2012a.

Lars N Hansen, Kathryn M Kumamoto, Christopher A Thom, David Wallis, William B Durham, David L Goldsby, Thomas Breithaupt, Cameron D Meyers, and David L Kohlstedt. Low-temperature plasticity in olivine: Grain size, strain hardening, and the strength of the lithosphere. *Journal of Geophysical Research: Solid Earth*, 124 (6):5427–5449, 2019.

Lars N Hansen, Emmanuel C David, Nicolas Brantut, and David Wallis. Insight into the microphysics of antigorite deformation from spherical nanoindentation. *Philosophical Transactions of the Royal Society A*, 378(2165):20190197, 2020. URL `https://doi.org/10.1098/rsta.2019.0197`.

Lars N Hansen, Manuele Faccenda, and Jessica M Warren. A review of mechanisms generating seismic anisotropy in the upper mantle. *Physics of the Earth and Planetary Interiors*, 313:106662, 2021.

LN Hansen and David L Kohlstedt. 2.18 constitutive equations, rheological behavior, and viscosity of rocks. *Treatise on Geophysics, second edition*, 2:441–472, 2015.

LN Hansen, ME Zimmerman, and David L Kohlstedt. Grain boundary sliding in san carlos olivine: Flow law parameters and crystallographic-preferred orientation. *Journal of Geophysical Research: Solid Earth*, 116(B8), 2011.

LN Hansen, ME Zimmerman, and DL Kohlstedt. The influence of microstructure on deformation of olivine in the grain-boundary sliding regime. *Journal of Geophysical Research: Solid Earth*, 117(B9), 2012b.

R Harilal et al. Adaptation of open source 2d dic software ncorr for solid mechanics applications. 2014.

Katharina Hartmann, Richard Wirth, and Wilhelm Heinrich. Synthetic near $\sigma 5$ (210)/[100] grain boundary in yag fabricated by direct bonding: structure and stability. *Physics and Chemistry of Minerals*, 37(5):291–300, 2010.

Li Hong He, Naoki Fujisawa, and Michael V Swain. Elastic modulus and stress–strain response of human enamel by nano-indentation. *Biomaterials*, 27(24):4388–4398, 2006. URL `https://doi.org/10.1016/j.biomaterials.2006.03.045`.

S Heinemann, Richard Wirth, and Georg Dresen. Synthesis of feldspar bicrystals by direct bonding. *Physics and Chemistry of Minerals*, 28(10):685–692, 2001.

S Heinemann, Richard Wirth, Matthias Gottschalk, and Georg Dresen. Synthetic [100] tilt grain boundaries in forsterite: 9.9 to 21.5. *Physics and chemistry of minerals*, 32(4):229–240, 2005.

EG Herbert, GM Pharr, WC Oliver, BN Lucas, and JL Hay. On the measurement of stress–strain curves by spherical indentation. *Thin solid films*, 398:331–335, 2001.

HH Hess, AEJ Engel, HL James, and BF Leonard. History of ocean basins. 1962.

J-K Heyer, Steffen Brinckmann, Janine Pfetzing-Micklich, and G Eggeler. Microshear deformation of gold single crystals. *Acta materialia*, 62:225–238, 2014.

Eric D Hintsala, Ude Hangen, and Douglas D Stauffer. High-throughput nanoindentation for statistical and spatial property determination. *Jom*, 70(4):494–503, 2018.

Greg Hirth and D Kohlstedt. Rheology of the upper mantle and the mantle wedge: A view from the experimentalists. *Geophysical monograph-american geophysical union*, 138:83–106, 2003.

Greg Hirth and David L Kohlstedt. Experimental constraints on the dynamics of the partially molten upper mantle: 2. deformation in the dislocation creep regime. *Journal of Geophysical Research: Solid Earth*, 100(B8):15441–15449, 1995.

John P Hirth. The influence of grain boundaries on mechanical properties, 1972.

RoEo Hook and JP Hirth. The deformation behavior of isoaxial bicrystals of fe-3% si. *Acta Metallurgica*, 15(3):535–551, 1967.

XD Hou, AJ Bushby, and NM Jennett. Study of the interaction between the indentation size effect and hall–petch effect with spherical indenters on annealed polycrystalline copper. *Journal of Physics D: Applied Physics*, 41(7):074006, 2008.

J Hunter and AB Watts. Gravity anomalies, flexure and mantle rheology seaward of circum-pacific trenches. *Geophysical Journal International*, 207(1):288–316, 2016.

Hosni Idrissi, Caroline Bollinger, Francesca Boioli, Dominique Schryvers, and Patrick Cordier. Low-temperature plasticity of olivine revisited with in situ tem nanomechanical testing. *Science advances*, 2(3):e1501671, 2016.

Peter J Imrich, Christoph Kirchlechner, Christian Motz, and Gerhard Dehm. Differences in deformation behavior of bicrystalline cu micropillars containing a twin boundary or a large-angle grain boundary. *Acta materialia*, 73:240–250, 2014.

Y Ishida and M Henderson Brown. Dislocations in grain boundaries and grain boundary sliding. *Acta metallurgica*, 15(5):857–860, 1967.

Almambet Iskakov and Surya R Kalidindi. Multiresolution investigations of thermally aged steels using spherical indentation stress-strain protocols and image analysis. *Mechanics of Materials*, 167:104265, 2022.

Ian Jackson, Ulrich H Faul, and Richard Skelton. Elastically accommodated grain-boundary sliding: New insights from experiment and modeling. *Physics of the Earth and Planetary Interiors*, 228:203–210, 2014.

Farhan Javaid, Yukun Xu, Enrico Bruder, and Karsten Durst. Indentation size effect in tungsten: quantification of geometrically necessary dislocations underneath the indentations using hr-ebsd. *Materials Characterization*, 142:39–42, 2018.

Farhan Javaid, Habib Pouriayevali, and Karsten Durst. Dislocation–grain boundary interactions: Recent advances on the underlying mechanisms studied via nanoindentation testing. *Journal of Materials Research*, 36(12):2545–2557, 2021.

Raymond Jeanloz, Thomas J Ahrens, JS Lally, GL Nord Jr, JM Christie, and AH Heuer. Shock-produced olivine glass: First observation. *Science*, 197(4302):457–459, 1977.

Youngung Jeong and Carlos N Tomé. An efficient elasto-visco-plastic self-consistent formulation: Application to steel subjected to loading path changes. *International Journal of Plasticity*, 135:102812, 2020.

Katharine E Johanesen and John P Platt. Rheology, microstructure, and fabric in a large scale mantle shear zone, ronda peridotite, southern spain. *Journal of Structural Geology*, 73:1–17, 2015.

KL Johnson. The correlation of indentation experiments. *Journal of the Mechanics and Physics of Solids*, 18(2):115–126, 1970.

Baptiste Journaux, Thomas Chauve, Maurine Montagnat, Andrea Tommasi, Fabrice Barou, David Mainprice, and Léa Gest. Recrystallization processes, microstructure and crystallographic preferred orientation evolution in polycrystalline ice during high-temperature simple shear. *The Cryosphere*, 13(5):1495–1511, 2019.

J Kacher, C Kirchlechner, J Michler, E Polatidis, R Schwaiger, H Van Swygenhoven, M Taheri, and Marc Legros. Impact of in situ nanomechanics on physical metallurgy. *Mrs Bulletin*, 44(6):465–470, 2019.

Josh Kacher, BP Eftink, B Cui, and IM Robertson. Dislocation interactions with grain boundaries. *Current Opinion in Solid State and Materials Science*, 18(4): 227–243, 2014.

Szilvia Kalácska, Zoltán Dankházi, Gyula Zilahi, Xavier Maeder, Johann Michler, Péter Dusán Ispánovity, and István Groma. Investigation of geometrically necessary dislocation structures in compressed cu micropillars by 3-dimensional hr-ebsd. *Materials Science and Engineering: A*, 770:138499, 2020.

Surya R Kalidindi and Siddhartha Pathak. Determination of the effective zero-point and the extraction of spherical nanoindentation stress–strain curves. *Acta Materialia*, 56(14):3523–3532, 2008a. URL `https://doi.org/10.1016/j.actamat.2008.03.036`.

Surya R Kalidindi and Siddhartha Pathak. Determination of the effective zero-point and the extraction of spherical nanoindentation stress–strain curves. *Acta Materialia*, 56(14):3523–3532, 2008b.

Surya R Kalidindi and Shraddha J Vachhani. Mechanical characterization of grain boundaries using nanoindentation. *Current Opinion in Solid State and Materials Science*, 18(4):196–204, 2014.

Y Kamimura, K Edagawa, and S Takeuchi. Experimental evaluation of the peierls stresses in a variety of crystals and their relation to the crystal structure. *Acta materialia*, 61(1):294–309, 2013.

Seung-Kyun Kang, Young-Cheon Kim, Yun-Hee Lee, Ju-Young Kim, and Dongil Kwon. Determining effective radius and frame compliance in spherical nanoindentation. *Materials Science and Engineering: A*, 538:58–62, 2012. URL `https://doi.org/10.1016/j.msea.2012.01.013`.

M Karami and R Mahmudi. Shear punch superplasticity in equal-channel angularly pressed mg–12li–1zn alloy. *Materials Science and Engineering: A*, 576:156–159, 2013.

Shun-ichiro Karato. *Deformation of earth materials*, volume 463. Cambridge Press Cambridge, 2008.

Shun-ichiro Karato. Rheology of the earth's mantle: A historical review. *Gondwana Research*, 18(1):17–45, 2010.

Ikuo Katayama and Shun-ichiro Karato. Low-temperature, high-stress deformation of olivine under water-saturated conditions. *Physics of the Earth and Planetary Interiors*, 168(3-4):125–133, 2008.

Philip Kearey, Keith A Klepeis, and Frederick J Vine. *Global tectonics*. John Wiley & Sons, 2009.

Lukas M Keller, Jakob J Schwiedrzik, Philippe Gasser, and Johann Michler. Understanding anisotropic mechanical properties of shales at different length scales: In situ micropillar compression combined with finite element calculations. *Journal of Geophysical Research: Solid Earth*, 122(8):5945–5955, 2017.

Nousha Kheradmand, Alain Franz Knorr, Michael Marx, and Yun Deng. Microscopic incompatibility controlling plastic deformation of bicrystals. *Acta Materialia*, 106: 219–228, 2016.

Ali Khosravani, Lutz Morsdorf, Cemal Cem Tasan, and Surya R Kalidindi. Multiresolution mechanical characterization of hierarchical materials: Spherical nanoindentation on martensitic fe-ni-c steels. *Acta Materialia*, 153:257–269, 2018.

Marko Knezevic, Rodney J McCabe, Carlos N Tomé, Ricardo A Lebensohn, Shuh Rong Chen, Carl M Cady, George T Gray III, and Bogdan Mihaila. Modeling mechanical response and texture evolution of α-uranium as a function of strain rate and temperature using polycrystal plasticity. *International Journal of Plasticity*, 43: 70–84, 2013.

Sanae Koizumi, Takehiko Hiraga, and Tohru S Suzuki. Vickers indentation tests on olivine: size effects. *Physics and Chemistry of Minerals*, 47(2):1–14, 2020.

Jun Korenaga. Plate tectonics and surface environment: Role of the oceanic upper mantle. *Earth-Science Reviews*, 205:103185, 2020.

S Korte and WJ Clegg. Micropillar compression of ceramics at elevated temperatures. *Scripta Materialia*, 60(9):807–810, 2009.

Sandra Korte-Kerzel. Microcompression of brittle and anisotropic crystals: recent advances and current challenges in studying plasticity in hard materials. *Mrs Communications*, 7(2):109–120, 2017.

Kelly Kranjc, Zachary Rouse, Katharine M Flores, and Philip Skemer. Low-temperature plastic rheology of olivine determined by nanoindentation. *Geophysical Research Letters*, 43(1):176–184, 2016.

Kelly Kranjc, Arashdeep S Thind, Albina Y Borisevich, Rohan Mishra, Katharine M Flores, and Philip Skemer. Amorphization and plasticity of olivine during low-temperature micropillar deformation experiments. *Journal of Geophysical Research: Solid Earth*, 125(5):e2019JB019242, 2020.

Ekkehart Kröner et al. Continuum theory of defects. *Physics of defects*, 35:217–315, 1981.

Kathryn M Kumamoto, Christopher A Thom, David Wallis, Lars N Hansen, David EJ Armstrong, Jessica M Warren, David L Goldsby, and Angus J Wilkinson. Size effects resolve discrepancies in 40 years of work on low-temperature plasticity in olivine. *Science advances*, 3(9):e1701338, 2017. doi:10.1126/sciadv.1701338.

Mineo Kumazawa and Orson L Anderson. Elastic moduli, pressure derivatives, and temperature derivatives of single-crystal olivine and single-crystal forsterite. *Journal of Geophysical Research*, 74(25):5961–5972, 1969.

Allison Kunz, Siddhartha Pathak, and Julia R Greer. Size effects in al nanopillars: Single crystalline vs. bicrystalline. *Acta Materialia*, 59(11):4416–4424, 2011.

A Lacam, M Madon, and JP Poirier. Olivine glass and spinel formed in a laser heated, diamond-anvil high pressure cell. *Nature*, 288(5787):155–157, 1980.

HG Ave Lallemant, JC C Mercier, NL Carter, and JV Ross. Rheology of the upper mantle: inferences from peridotite xenoliths. *Tectonophysics*, 70(1-2):85–113, 1980.

Robert J Lancaster, SP Jeffs, BJ Haigh, and NC Barnard. Derivation of material properties using small punch and shear punch test methods. *Materials & Design*, 215:110473, 2022.

Terence G Langdon. Seventy-five years of superplasticity: historic developments and new opportunities. *Journal of materials science*, 44(22):5998–6010, 2009.

G Laplanche, N Wieczorek, F Fox, S Berglund, J Pfetzing-Micklich, K Kishida, H Inui, and G Eggeler. On the influence of crystallography and dendritic microstructure on micro shear behavior of single crystal ni-based superalloys. *Acta Materialia*, 160: 173–184, 2018.

TC Lee, IM Robertson, and HK Birnbaum. Prediction of slip transfer mechanisms across grain boundaries. *Scripta metallurgica*, 23(5):799–803, 1989.

TC Lee, IM Robertson, and HK Birnbaum. Anin situ transmission electron microscope deformation study of the slip transfer mechanisms in metals. *Metallurgical Transactions A*, 21(9):2437–2447, 1990.

A Leitner, V Maier-Kiener, and D Kiener. Essential refinements of spherical nanoindentation protocols for the reliable determination of mechanical flow curves. *Materials & Design*, 146:69–80, 2018. URL `https://doi.org/10.1016/j.matdes.2018.03.003`.

James CM Li. Petch relation and grain boundary sources. *Transactions of the Metallurgical Society of AIME*, 227(1):239, 1963.

Juan Li, George M Pharr, and Christoph Kirchlechner. Quantitative insights into the dislocation source behavior of twin boundaries suggest a new dislocation source mechanism. *Journal of Materials Research*, 36(10):2037–2046, 2021a.

Juan Li, GM Pharr, and C Kirchlechner. Quantitative insights into the dislocation source behavior of twin boundaries suggest a new dislocation source mechanism. *Journal of Materials Research*, pages 1–10, 2021b. doi:https://doi.org/10.1557/s43578-021-00253-y.

TL Li, YF Gao, Hongbin Bei, and Easo P George. Indentation schmid factor and orientation dependence of nanoindentation pop-in behavior of nial single crystals. *Journal of the Mechanics and Physics of Solids*, 59(6):1147–1162, 2011.

Weidong Li, Hongbin Bei, Jun Qu, and Yanfei Gao. Effects of machine stiffness on the loading-displacement curve during spherical nano-indentation. *Journal of Materials Research*, 28(14):1903, 2013. doi:DOI:10.1557/jmr.2013.164.

Xiaodong Li and Bharat Bhushan. A review of nanoindentation continuous stiffness measurement technique and its applications. *Materials characterization*, 48(1): 11–36, 2002. URL `https://doi.org/10.1016/S1044-5803(02)00192-4`.

Yuan Li, Andy J Bushby, and David J Dunstan. The hall–petch effect as a manifestation of the general size effect. *Proceedings of the Royal Society A: Mathematical, Physical and Engineering Sciences*, 472(2190):20150890, 2016.

HK Lin, JC Huang, and TG Langdon. Relationship between texture and low temperature superplasticity in an extruded az31 mg alloy processed by ecap. *Materials Science and Engineering: A*, 402(1-2):250–257, 2005.

Yang Liu, Helen E King, Marijn A Van Huis, Martyn R Drury, and Oliver Plümper. Nano-tomography of porous geological materials using focused ion beam-scanning electron microscopy. *Minerals*, 6(4):104, 2016.

Maria-Gema Llorens, Albert Griera, Paul D Bons, Ricardo A Lebensohn, Lynn A Evans, Daniela Jansen, and Ilka Weikusat. Full-field predictions of ice dynamic recrystallisation under simple shear conditions. *Earth and Planetary science letters*, 450:233–242, 2016.

AB Lopes, F Barlat, JJ Gracio, JF Ferreira Duarte, and EF Rauch. Effect of texture and microstructure on strain hardening anisotropy for aluminum deformed in uniaxial tension and simple shear. *International Journal of Plasticity*, 19(1):1–22, 2003.

Lian Lu, ML Sui, and Ke Lu. Superplastic extensibility of nanocrystalline copper at room temperature. *Science*, 287(5457):1463–1466, 2000.

D Lunt, R Thomas, M Roy, J Duff, M Atkinson, P Frankel, M Preuss, and J Quinta Da Fonseca. Comparison of sub-grain scale digital image correlation calculated using commercial and open-source software packages. *Materials Characterization*, 163:110271, 2020.

Jörg Luster and MA Morris. Compatibility of deformation in two-phase ti-al alloys: Dependence on microstructure and orientation relationships. *Metallurgical and Materials Transactions A*, 26(7):1745–1756, 1995.

R Maaß and PM Derlet. Micro-plasticity and recent insights from intermittent and small-scale plasticity. *Acta Materialia*, 143:338–363, 2018.

Verena Maier, Christopher Schunk, Mathias Göken, and Karsten Durst. Microstructure-dependent deformation behaviour of bcc-metals–indentation size effect and strain rate sensitivity. *Philosophical Magazine*, 95(16-18):1766–1779, 2015.

Katharina Marquardt and Ulrich H Faul. The structure and composition of olivine grain boundaries: 40 years of studies, status and current developments. *Physics and Chemistry of Minerals*, 45(2):139–172, 2018.

Katharina Marquardt, Quentin M Ramasse, Christian Kisielowski, and Richard Wirth. Diffusion in yttrium aluminium garnet at the nanometer-scale: Insight into the effective grain boundary width. *American Mineralogist*, 96(10):1521–1529, 2011.

Katharina Marquardt, Gregory S Rohrer, Luiz Morales, Erik Rybacki, Hauke Marquardt, and Brian Lin. The most frequent interfaces in olivine aggregates: the gbcd and its importance for grain boundary related processes. *Contributions to Mineralogy and Petrology*, 170(4):1–17, 2015.

G Maruyama and T Hiraga. Grain-to multiple-grain-scale deformation processes during diffusion creep of forsterite+ diopside aggregate: 1. direct observations. *Journal of Geophysical Research: Solid Earth*, 122(8):5890–5915, 2017.

Hiroshi Masuda and Eiichi Sato. Diffusional and dislocation accommodation mechanisms in superplastic materials. *Acta Materialia*, 197:235–252, 2020.

Hiroshi Masuda, Hirobumi Tobe, Eiichi Sato, Yoshito Sugino, and Shigeharu Ukai. Two-dimensional grain boundary sliding and mantle dislocation accommodation in ods ferritic steel. *Acta Materialia*, 120:205–215, 2016.

Carl Mayer, Nan Li, N Mara, and Nikhilesh Chawla. Micromechanical and in situ shear testing of al–sic nanolaminate composites in a transmission electron microscope (tem). *Materials Science and Engineering: A*, 621:229–235, 2015.

Christine McCarthy and Yasuko Takei. Anelasticity and viscosity of partially molten rock analogue: Toward seismic detection of small quantities of melt. *Geophysical Research Letters*, 38(18), 2011.

S Mei, AM Suzuki, DL Kohlstedt, NA Dixon, and WB Durham. Experimental constraints on the strength of the lithospheric mantle. *Journal of Geophysical Research: Solid Earth*, 115(B8), 2010.

David Mercier, Vincent Mandrillon, Guillaume Parry, Marc Verdier, Rafael Estevez, Yves Bréchet, and Tony Maindron. Investigation of the fracture of very thin amorphous alumina film during spherical nanoindentation. *Thin Solid Films*, 638: 34–47, 2017. URL `https://doi.org/10.1016/j.tsf.2017.07.040`.

Benoit Merle, Verena Maier, Mathias Göken, and Karsten Durst. Experimental determination of the effective indenter shape and ε-factor for nanoindentation by continuously measuring the unloading stiffness. *Journal of Materials Research*, 27 (1):214–221, 2012.

LW Meyer and S Manwaring. Critical adiabatic shear strength of low alloyed steel under compressive loading. In *International Conference on Metallurgical Applications of Shock-Wave and High-Strain-Rate Phenomena(EXPLOMET85)*, pages 657–674, 1985.

Marc A Meyers, Umberto R Andrade, and Atul H Chokshi. The effect of grain size on the high-strain, high-strain-rate behavior of copper. *Metallurgical and materials transactions A*, 26(11):2881–2893, 1995.

Marc A Meyersm and E Ashworth. A model for the effect of grain size on the yield stress of metals. *Philosophical Magazine A*, 46(5):737–759, 1982.

TE Mitchell. Application of transmission electron microscopy to the study of deformation in ceramic oxides. *Journal of the American Ceramic Society*, 62(5-6):254–267, 1979.

Farghalli A Mohamed. Creep and superplasticity: evolution and rationalization. *Advanced Engineering Materials*, 22(1):1900532, 2020.

Alex Montagne, Siddhartha Pathak, Xavier Maeder, and Johann Michler. Plasticity and fracture of sapphire at room temperature: Load-controlled microcompression of four different orientations. *Ceramics International*, 40(1):2083–2090, 2014.

Morgan E Monz, Peter J Hudleston, David J Prior, Zachary Michels, Sheng Fan, Marianne Negrini, Pat J Langhorne, and Chao Qi. Full crystallographic orientation (c and a axes) of warm, coarse-grained ice in a shear-dominated setting: a case study, storglaciären, sweden. *The Cryosphere*, 15(1):303–324, 2021.

James R Morris, Hongbin Bei, George M Pharr, and Easo P George. Size effects and stochastic behavior of nanoindentation pop in. *Physical review letters*, 106(16): 165502, 2011a. doi:https://doi.org/10.1103/PhysRevLett.106.165502.

James R Morris, Hongbin Bei, George M Pharr, and Easo P George. Size effects and stochastic behavior of nanoindentation pop in. *Physical review letters*, 106(16): 165502, 2011b.

Alexander J Moseson, Sandip Basu, and Michel W Barsoum. Determination of the effective zero point of contact for spherical nanoindentation. *Journal of Materials Research*, 23(1):204–209, 2008.

DR Mosher and R Raj. Use of the internal friction technique to measure rates of grain boundary sliding. *Acta Metallurgica*, 22(12):1469–1474, 1974.

Ehsan Mostaed, Morteza Shaker Ardakani, Malgorzata Sikora-Jasinska, and Jaroslaw W Drelich. Precipitation induced room temperature superplasticity in zn-cu alloys. *Materials letters*, 244:203–206, 2019.

LE Murr. Some observations of grain boundary ledges and ledges as dislocation sources in metals and alloys. *Metallurgical Transactions A*, 6(3):505–513, 1975.

LE Murr. Strain-induced dislocation emission from grain boundaries in stainless steel. *Materials Science and Engineering*, 51(1):71–79, 1981.

Alexandre Mussi, Patrick Cordier, Sylvie Demouchy, and Claude Vanmansart. Characterization of the glide planes of the [001] screw dislocations in olivine using electron tomography. *Physics and Chemistry of Minerals*, 41(7):537–545, 2014.

Alexandre Mussi, Patrick Cordier, and Sylvie Demouchy. Characterization of dislocation interactions in olivine using electron tomography. *Philosophical Magazine*, 95 (4):335–345, 2015a.

Alexandre Mussi, Maula Nafi, Sylvie Demouchy, and Patrick Cordier. On the deformation mechanism of olivine single crystals at lithospheric temperatures: an electron tomography study. *European Journal of Mineralogy*, 27(6):707–715, 2015b.

Sia Nemat-Nasser, Jon B Isaacs, and Mingqi Liu. Microstructure of high-strain, high-strain-rate deformed tantalum. *Acta Materialia*, 46(4):1307–1325, 1998.

Julie Newman and Martyn R Drury. Control of shear zone location and thickness by initial grain size variations in upper mantle peridotites. *Journal of Structural Geology*, 32(6):832–842, 2010.

RM-3 Motorized Rotary Stage. Newmark Systems.inc. URL `http://www.newmarksystems.com/rotary-positioners/rm-3-motorized-rotary-stage/#prettyPhoto`.

KS Ng and AHW Ngan. Deformation of micron-sized aluminium bi-crystal pillars. *Philosophical Magazine*, 89(33):3013–3026, 2009.

TJ Nizolek, HM Mourad, C Liu, JA Valdez, MA Torrez, and GT Gray III. Compact forced simple shear specimen: Design improvement based on quasi-static experiments and finite element simulations. *International Journal of Solids and Structures*, 233: 111195, 2021.

Gert Nolze, Ralf Hielscher, and Aimo Winkelmann. Electron backscatter diffraction beyond the mainstream. *Crystal Research and Technology*, 52(1):1600252, 2017.

John F Nye. Some geometrical relations in dislocated crystals. *Acta metallurgica*, 1 (2):153–162, 1953.

Markus Ohl, Oliver Plümper, Vasileios Chatzaras, David Wallis, Christian Vollmer, and Martyn Drury. Mechanisms of fault mirror formation and fault healing in carbonate rocks. *Earth and Planetary Science Letters*, 530:115886, 2020.

Takahito Ohmura and Kaneaki Tsuzaki. Plasticity initiation and subsequent deformation behavior in the vicinity of single grain boundary investigated through nanoindentation technique. *Journal of materials science*, 42(5):1728–1732, 2007.

Tomohiro Ohuchi, Takaaki Kawazoe, Yuji Higo, Ken-ichi Funakoshi, Akio Suzuki, Takumi Kikegawa, and Tetsuo Irifune. Dislocation-accommodated grain boundary sliding as the major deformation mechanism of olivine in the earths upper mantle. *Science advances*, 1(9):e1500360, 2015.

Warren Carl Oliver and George Mathews Pharr. An improved technique for determining hardness and elastic modulus using load and displacement sensing indentation experiments. *Journal of materials research*, 7(6):1564–1583, 1992a.

Warren Carl Oliver and George Mathews Pharr. An improved technique for determining hardness and elastic modulus using load and displacement sensing indentation experiments. *Journal of materials research*, 7(6):1564–1583, 1992b. doi:https://doi.org/10.1557/JMR.1992.1564.

Dipen K Patel and Surya R Kalidindi. Correlation of spherical nanoindentation stress-strain curves to simple compression stress-strain curves for elastic-plastic isotropic materials using finite element models. *Acta Materialia*, 112:295–302, 2016.

Hetal D Patel and Seok-Woo Lee. Spherical nanoindentation on tungsten single crystal: The transition from source-controlled plasticity to bulk plasticity. *Scripta Materialia*, 175:16–19, 2020.

MS Paterson. A high-pressure, high-temperature apparatus for rock deformation. In *International Journal of Rock Mechanics and Mining Sciences & Geomechanics Abstracts*, volume 7, pages 517–526. Elsevier, 1970.

Siddhartha Pathak and Surya R Kalidindi. Spherical nanoindentation stress–strain curves. *Materials science and engineering: R: Reports*, 91:1–36, 2015a.

Siddhartha Pathak and Surya R Kalidindi. Spherical nanoindentation stress–strain curves. *Materials science and engineering: R: Reports*, 91:1–36, 2015b. URL `https://doi.org/10.1016/j.mser.2015.02.001`.

Siddhartha Pathak, Shraddha J Vachhani, Karl J Jepsen, Haviva M Goldman, and Surya R Kalidindi. Assessment of lamellar level properties in mouse bone utilizing a novel spherical nanoindentation data analysis method. *Journal of the mechanical behavior of biomedical materials*, 13:102–117, 2012. URL `https://doi.org/10.1016/j.jmbbm.2012.03.018`.

Siddhartha Pathak, Surya R Kalidindi, Jordan S Weaver, Yongqiang Wang, Russell P Doerner, and Nathan A Mara. Probing nanoscale damage gradients in ion-irradiated metals using spherical nanoindentation. *Scientific reports*, 7(1):1–12, 2017. URL `https://doi.org/10.1038/s41598-017-12071-6`.

KO Pedersen, O-G Lademo, T Berstad, T Furu, and OS Hopperstad. Influence of texture and grain structure on strain localisation and formability for almgsi alloys. *Journal of materials processing technology*, 200(1-3):77–93, 2008.

NJ Petch. The cleavage strength of polycrystals. *Journal of the iron and steel institute*, 174:25–28, 1953.

J Pfetzing-Micklich, S Brinckmann, Suhash Ranjan Dey, F Otto, A Hartmaier, and G Eggeler. Micro-shear deformation of pure copper. *Materialwissenschaft und Werkstofftechnik*, 42(3):219–223, 2011.

Prem Phakey, Gerald Dollinger, and John Christie. Transmission electron microscopy of experimentally deformed olivine crystals. *Washington DC American Geophysical Union Geophysical Monograph Series*, 16:117–138, 1972.

George M Pharr, Erik G Herbert, and Yanfei Gao. The indentation size effect: a critical examination of experimental observations and mechanistic interpretations. *Annual Review of Materials Research*, 40:271–292, 2010.

Sandra Piazolo, Paul D Bons, Albert Griera, M-G Llorens, Enrique Gomez-Rivas, Daniel Koehn, John Wheeler, Robyn Gardner, Jose RA Godinho, L Evans, et al. A review of numerical modelling of the dynamics of microstructural development in rocks and ice: Past, present and future. *Journal of Structural Geology*, 125:111–123, 2019.

Alexandra Pleus, Garrett Ito, Paul Wessel, and L Neil Frazer. Rheology and thermal structure of the lithosphere beneath the hawaiian ridge inferred from gravity data and models of plate flexure. *Geophysical Journal International*, 222(1):207–224, 2020.

Joana Polednia, Ralf Dohmen, and Katharina Marquardt. Grain boundary diffusion and its relation to segregation of multiple elements in yttrium aluminum garnet. *European Journal of Mineralogy*, 32(6):675–696, 2020.

RC Pond and DS Vlachavas. Bicrystallography. *Proceedings of the royal society of London. A. mathematical and physical sciences*, 386(1790):95–143, 1983.

CW Price and JP Hirth. A mechanism for the generation of screw dislocations from grain-boundary ledges. *Materials science and engineering*, 9:15–18, 1972.

Chao Qi, David J Prior, Lisa Craw, Sheng Fan, Maria-Gema Llorens, Albert Griera, Marianne Negrini, Paul D Bons, and David L Goldsby. Crystallographic preferred orientations of ice deformed in direct-shear experiments at low temperatures. *The Cryosphere*, 13(1):351–371, 2019.

Dierk Raabe, Binhan Sun, Alisson Kwiatkowski Da Silva, Baptiste Gault, Hung-Wei Yen, Karo Sedighiani, Prithiv Thoudden Sukumar, Isnaldi R Souza Filho, Shyam Katnagallu, Eric Jägle, et al. Current challenges and opportunities in microstructure-related properties of advanced high-strength steels. *Metallurgical and Materials Transactions A*, 51(11):5517–5586, 2020.

R Raj and MF Ashby. Grain boundary sliding, and the effects of particles on its rate. *Metallurgical and Materials Transactions B*, 3(7):1937–1942, 1972.

Rishi Raj and MF Ashby. On grain boundary sliding and diffusional creep. *Metallurgical transactions*, 2(4):1113–1127, 1971.

CB Raleigh. Mechanisms of plastic deformation of olivine. *Journal of Geophysical Research*, 73(16):5391–5406, 1968.

Paul Raterron, Yujun Wu, Donald J Weidner, and Jiuhua Chen. Low-temperature olivine rheology at high pressure. *Physics of the Earth and Planetary Interiors*, 145 (1-4):149–159, 2004.

Paul Raterron, Jiuhua Chen, Li Li, Donald Weidner, and Patrick Cordier. Pressure-induced slip-system transition in forsterite: Single-crystal rheological properties at mantle pressure and temperature. *American Mineralogist*, 92(8-9):1436–1445, 2007.

William T Read and WJPR Shockley. Dislocation models of crystal grain boundaries. *Physical review*, 78(3):275, 1950.

Darren Rowland. *diffxy*. URL `https://www.mathworks.com/matlabcentral/fileexchange/29312-diffxy`.

MA Rust and RI Todd. Surface studies of region ii superplasticity of aa5083 in shear: Confirmation of diffusion creep, grain neighbour switching and absence of dislocation activity. *Acta materialia*, 59(13):5159–5170, 2011.

Ilchat Sabirov, Yuri Estrin, Matthew R Barnett, Ilana Timokhina, and Peter Damian Hodgson. Tensile deformation of an ultrafine-grained aluminium alloy: Micro shear banding and grain boundary sliding. *Acta Materialia*, 56(10):2223–2230, 2008.

GA Salishchev, RM Galeyev, OR Valiakhmetov, RV Safiullin, R Ya Lutfullin, O_N Senkov, FH Froes, and OA Kaibyshev. Development of ti–6al–4v sheet with low temperature superplastic properties. *Journal of Materials Processing Technology*, 116(2-3):265–268, 2001.

Vahid Samae, Patrick Cordier, Sylvie Demouchy, Caroline Bollinger, Julien Gasc, Sanae Koizumi, Alexandre Mussi, Dominique Schryvers, and Hosni Idrissi. Stress-induced amorphization triggers deformation in the lithospheric mantle. *Nature*, 591 (7848):82–86, 2021.

S Sangal, KJ Kurzydlowski, and K Tangri. The effect of extrinsic grain boundary dislocations on the grain size strengthening in polycrystals. *Acta metallurgica et materialia*, 39(6):1281–1288, 1991.

Michael D Sangid, Tawhid Ezaz, Huseyin Sehitoglu, and Ian M Robertson. Energy of slip transmission and nucleation at grain boundaries. *Acta materialia*, 59(1): 283–296, 2011.

Yuto Sasaki, Yasuko Takei, Christine McCarthy, and John F Rudge. Experimental study of dislocation damping using a rock analogue. *Journal of Geophysical Research: Solid Earth*, 124(7):6523–6541, 2019.

Erich Schmid and Walter Boas. Plasticity of crystals. 1950.

JM Scott, TE Waight, QHA Van der Meer, JM Palin, AF Cooper, and C Münker. Metasomatized ancient lithospheric mantle beneath the young z ealandia microcontinent and its role in himu-like intraplate magmatism. *Geochemistry, Geophysics, Geosystems*, 15(9):3477–3501, 2014.

Martha Seiler, Thomas Linse, Peter Hantschke, and Markus Kästner. An efficient phase-field model for fatigue fracture in ductile materials. *Engineering Fracture Mechanics*, 224:106807, 2020.

Z Shen, RH Wagoner, and WAT Clark. Dislocation pile-up and grain boundary interactions in 304 stainless steel. *Scripta metallurgica*, 20(6):921–926, 1986.

Oleg D Sherby and Jeffrey Wadsworth. Observations on historical and contemporary developments in superplasticity. *MRS Online Proceedings Library (OPL)*, 196, 1990.

S Shim, Hongbin Bei, Easo P George, and George Mathews Pharr. A different type of indentation size effect. *Scripta Materialia*, 59(10):1095–1098, 2008.

Michael K Sly, Arashdeep S Thind, Rohan Mishra, Katharine M Flores, and Philip Skemer. Low-temperature rheology of calcite. *Geophysical Journal International*, 221(1):129–141, 2020.

Ian N Sneddon. The relation between load and penetration in the axisymmetric boussinesq problem for a punch of arbitrary profile. *International journal of engineering science*, 3(1):47–57, 1965a. doi:https://doi.org/10.1016/0020-7225(65)90019-4.

Ian N Sneddon. The relation between load and penetration in the axisymmetric boussinesq problem for a punch of arbitrary profile. *International journal of engineering science*, 3(1):47–57, 1965b.

Rafael Soler, Jeffrey M Wheeler, Hyung-Jun Chang, Javier Segurado, Johann Michler, Javier Llorca, and Jon M Molina-Aldareguia. Understanding size effects on the strength of single crystals through high-temperature micropillar compression. *Acta Materialia*, 81:50–57, 2014.

IJ Spary, AJ Bushby, and Nigel M Jennett. On the indentation size effect in spherical indentation. *Philosophical magazine*, 86(33-35):5581–5593, 2006. URL `https://doi.org/10.1080/14786430600854988`.

Stephan Stich, Kuan Ding, Qaisar Khushi Muhammad, Lukas Porz, Christian Minnert, Wolfgang Rheinheimer, Karsten Durst, Jürgen Rödel, Till Frömling, and Xufei Fang. Room-temperature dislocation plasticity in srtio3 tuned by defect chemistry. *Journal of the American Ceramic Society*, 105(2):1318–1329, 2022.

Xiao-Yu Sun, Patrick Cordier, Vincent Taupin, Claude Fressengeas, and Sandro Jahn. Continuous description of a grain boundary in forsterite from atomic scale simulations: the role of disclinations. *Philosophical Magazine*, 96(17):1757–1772, 2016.

Marshall Sundberg and Reid F Cooper. Crystallographic preferred orientation produced by diffusional creep of harzburgite: Effects of chemical interactions among phases during plastic flow. *Journal of Geophysical Research: Solid Earth*, 113(B12), 2008.

J Gregory Swadener and George M Pharr. A methodology for the calibration of spherical indenters. *MRS Online Proceedings Library (OPL)*, 594, 1999.

JG Swadener, EP George, and GM Pharr. The correlation of the indentation size effect measured with indenters of various shapes. *Journal of the Mechanics and Physics of Solids*, 50(4):681–694, 2002. doi:https://doi.org/10.1016/S0022-5096(01)00103-X.

Yasuko Takei. Deformation-induced grain boundary wetting and its effects on the acoustic and rheological properties of partially molten rock analogue. *Journal of Geophysical Research: Solid Earth*, 110(B12), 2005.

Yasuko Takei. Phase-field modeling of grain boundary premelting. *Journal of Geophysical Research: Solid Earth*, 124(8):8057–8076, 2019.

Manuel Thieme, Sylvie Demouchy, David Mainprice, Fabrice Barou, and Patrick Cordier. Stress evolution and associated microstructure during transient creep of olivine at 1000–1200 c. *Physics of the Earth and Planetary Interiors*, 278:34–46, 2018.

CA Thom, EE Brodsky, RW Carpick, GM Pharr, WC Oliver, and DL Goldsby. Nanoscale roughness of natural fault surfaces controlled by scale-dependent yield strength. *Geophysical Research Letters*, 44(18):9299–9307, 2017.

Christopher Thom, Lars Hansen, David Goldsby, and Emily Brodsky. A microphysical model of rock friction and the brittle-ductile transition controlled by dislocation glide and backstress evolution. 2022.

Jacob A Tielke, Lars N Hansen, Miki Tasaka, Cameron Meyers, Mark E Zimmerman, and David L Kohlstedt. Observations of grain size sensitive power law creep of olivine aggregates over a large range of lattice-preferred orientation strength. *Journal of Geophysical Research: Solid Earth*, 121(2):506–516, 2016a.

Jacob A Tielke, Mark E Zimmerman, and David L Kohlstedt. Direct shear of olivine single crystals. *Earth and Planetary Science Letters*, 455:140–148, 2016b.

Andréa Tommasi, David Mainprice, Gilles Canova, and Yvan Chastel. Viscoplastic self-consistent and equilibrium-based modeling of olivine lattice preferred orientations: Implications for the upper mantle seismic anisotropy. *Journal of Geophysical Research: Solid Earth*, 105(B4):7893–7908, 2000.

Michael D Uchic, Dennis M Dimiduk, Jeffrey N Florando, and William D Nix. Sample dimensions influence strength and crystal plasticity. *Science*, 305(5686):986–989, 2004.

Tokuteru Uesugi, Megumi Kawasaki, Masaki Ninomiya, Yuhei Kamiya, Yorinobu Takigawa, and Kenji Higashi. Significance of si impurities on exceptional room-temperature superplasticity in a high-purity zn-22% al alloy. *Materials Science and Engineering: A*, 645:47–56, 2015.

Shraddha J Vachhani, Roger D Doherty, and Surya R Kalidindi. Studies of grain boundary regions in deformed polycrystalline aluminum using spherical nanoindentation. *International Journal of Plasticity*, 81:87–101, 2016a. URL `https://doi.org/10.1016/j.ijplas.2016.01.001`.

Shraddha J Vachhani, Roger D Doherty, and Surya R Kalidindi. Studies of grain boundary regions in deformed polycrystalline aluminum using spherical nanoindentation. *International Journal of Plasticity*, 81:87–101, 2016b.

Ruslan Z Valiev and Terence G Langdon. Principles of equal-channel angular pressing as a processing tool for grain refinement. *Progress in materials science*, 51(7): 881–981, 2006.

RA Varin, KJ Kurzydlowski, and K Tangri. Analytical treatment of grain boundary sources for dislocations. *Materials Science and Engineering*, 85:115–126, 1987.

H Vehoff, P Ochmann, M Göken, and M Große Gehling. Deformation processes at crack tips in nial single-and bicrystals. *Materials Science and Engineering: A*, 239: 378–385, 1997.

FJ Vine and DH Matthews. Magnetic anomalies over oceanic ridges. *A century*, 1963.

T Voisin, MD Grapes, TT Li, MK Santala, Y Zhang, JP Ligda, NJ Lorenzo, BE Schuster, GH Campbell, and TP Weihs. In situ tem observations of high-strain-rate deformation and fracture in pure copper. *Materials Today*, 33:10–16, 2020.

George Z Voyiadjis and Cheng Zhang. The mechanical behavior during nanoindentation near the grain boundary in a bicrystal fcc metal. *Materials Science and Engineering: A*, 621:218–228, 2015.

David Wallis, Lars N Hansen, T Ben Britton, and Angus J Wilkinson. Geometrically necessary dislocation densities in olivine obtained using high-angular resolution electron backscatter diffraction. *Ultramicroscopy*, 168:34–45, 2016.

David Wallis, Lars N Hansen, T Ben Britton, and Angus J Wilkinson. High-angular resolution electron backscatter diffraction as a new tool for mapping lattice distortion in geological minerals. *Journal of Geophysical Research: Solid Earth*, 124(7):6337–6358, 2019.

David Wallis, Lars N Hansen, Kathryn M Kumamoto, Christopher A Thom, Oliver Plümper, Markus Ohl, William B Durham, David L Goldsby, David EJ Armstrong, Cameron D Meyers, et al. Dislocation interactions during low-temperature plasticity of olivine and their impact on the evolution of lithospheric strength. *Earth and Planetary Science Letters*, 543:116349, 2020.

MG Wang and AHW Ngan. Indentation strain burst phenomenon induced by grain boundaries in niobium. *Journal of materials research*, 19(8):2478–2486, 2004.

Jessica M Warren and Greg Hirth. Grain size sensitive deformation mechanisms in naturally deformed peridotites. *Earth and Planetary Science Letters*, 248(1-2): 438–450, 2006.

H Watanabe, K Kurimoto, T Uesugi, Y Takigawa, and K Higashi. Isotropic superplastic flow in textured magnesium alloy. *Materials Science and Engineering: A*, 558:656–662, 2012.

Hiroyuki Watanabe, Kouhei Kurimoto, Tokuteru Uesugi, Yorinobu Takigawa, and Kenji Higashi. Accommodation mechanisms for grain boundary sliding as inferred from texture evolution during superplastic deformation. *Philosophical Magazine*, 93 (22):2913–2931, 2013.

Brock Watson, Yogesh Nandwani, Michael J Worswick, and Duane S Cronin. Metallic multi-material adhesive joint testing and modeling for vehicle lightweighting. *International Journal of Adhesion and Adhesives*, 95:102421, 2019.

AB Watts and S Zhong. Observations of flexure and the rheology of oceanic lithosphere. *Geophysical Journal International*, 142(3):855–875, 2000.

Jordan S Weaver and Surya R Kalidindi. Mechanical characterization of ti-6al-4v titanium alloy at multiple length scales using spherical indentation stress-strain measurements. *Materials & Design*, 111:463–472, 2016.

Jordan S Weaver, Matthew W Priddy, David L McDowell, and Surya R Kalidindi. On capturing the grain-scale elastic and plastic anisotropy of alpha-ti with spherical nanoindentation and electron back-scattered diffraction. *Acta Materialia*, 117:23–34, 2016.

Jordan S Weaver, David R Jones, Nan Li, Nathan Mara, Saryu Fensin, and George T Gray III. Quantifying heterogeneous deformation in grain boundary regions on shock loaded tantalum using spherical and sharp tip nanoindentation. *Materials Science and Engineering: A*, 737:373–382, 2018. URL `https://doi.org/10.1016/j.msea.2018.09.075`.

Jeffrey M Wheeler. Mechanical phase mapping of the taza meteorite using correlated high-speed nanoindentation and edx. *Journal of Materials Research*, 36(1):94–104, 2021.

JM Wheeler, DEJ Armstrong, W Heinz, and R Schwaiger. High temperature nanoindentation: The state of the art and future challenges. *Current Opinion in Solid State and Materials Science*, 19(6):354–366, 2015.

N Wieczorek, G Laplanche, J-K Heyer, AB Parsa, J Pfetzing-Micklich, and G Eggeler. Assessment of strain hardening in copper single crystals using in situ sem microshear experiments. *Acta Materialia*, 113:320–334, 2016.

Angus J Wilkinson. High resolution measurements of strain and tilt distributions in sige mesas using electron backscatter diffraction. *Applied physics letters*, 89(24): 241910, 2006.

Angus J Wilkinson and David Randman. Determination of elastic strain fields and geometrically necessary dislocation distributions near nanoindents using electron back scatter diffraction. *Philosophical magazine*, 90(9):1159–1177, 2010.

Angus J Wilkinson, Graham Meaden, and David J Dingley. High-resolution elastic strain measurement from electron backscatter diffraction patterns: new levels of sensitivity. *Ultramicroscopy*, 106(4-5):307–313, 2006.

Q Williams, E Knittle, R Reichlin, S Martin, and R Jeanloz. Structural and electronic properties of fe2sio4-fayalite at ultrahigh pressures: Amorphization and gap closure. *Journal of Geophysical Research: Solid Earth*, 95(B13):21549–21563, 1990.

Yi Xiong, Nicolo Grilli, Phani S Karamched, Bo-Shiuan Li, Edmund Tarleton, and Angus J Wilkinson. Cold dwell behaviour of ti _6 al alloy: Understanding load shedding using digital image correlation and crystal plasticity simulations. *arXiv preprint arXiv:2106.12227*, 2021.

Miroslav Zecevic and Marko Knezevic. A new visco-plastic self-consistent formulation implicit in dislocation-based hardening within implicit finite elements: Application to high strain rate and impact deformation of tantalum. *Computer Methods in Applied Mechanics and Engineering*, 341:888–916, 2018.

Miroslav Zecevic, Marko Knezevic, Irene J Beyerlein, and Rodney J McCabe. Texture formation in orthorhombic alpha-uranium under simple compression and rolling to high strains. *Journal of Nuclear Materials*, 473:143–156, 2016.

Miroslav Zecevic, Ricardo A Lebensohn, Rodney J McCabe, and Marko Knezevic. Modeling of intragranular misorientation and grain fragmentation in polycrystalline

materials using the viscoplastic self-consistent formulation. *International Journal of Plasticity*, 109:193–211, 2018.

Carolin Zenk, James SKL Gibson, Verena Maier-Kiener, Steffen Neumeier, Mathias Göken, and Sandra Korte-Kerzel. Low temperature deformation of mosi2 and the effect of ta, nb and al as alloying elements. *Acta Materialia*, 181:385–398, 2019.

TH Zhang, JH Ye, YH Feng, and Y Ma. On the spherical nanoindentation creep of metallic glassy thin films at room temperature. *Materials Science and Engineering: A*, 685:294–299, 2017. URL `https://doi.org/10.1016/j.msea.2017.01.018`.

Yuzheng Zhang, Troy D Topping, Enrique J Lavernia, and Steven R Nutt. Dynamic micro-strain analysis of ultrafine-grained aluminum magnesium alloy using digital image correlation. *Metallurgical and Materials Transactions A*, 45(1):47–54, 2014.

Shijie Zhong and AB Watts. Lithospheric deformation induced by loading of the hawaiian islands and its implications for mantle rheology. *Journal of Geophysical Research: Solid Earth*, 118(11):6025–6048, 2013.

Chaoyi Zhu, Tyler Harrington, Veronica Livescu, George T Gray III, and Kenneth S Vecchio. Determination of geometrically necessary dislocations in large shear strain localization in aluminum. *Acta Materialia*, 118:383–394, 2016.

Chaoyi Zhu, Veronica Livescu, Tyler Harrington, Olivia Dippo, George T Gray III, and Kenneth S Vecchio. Investigation of the shear response and geometrically necessary dislocation densities in shear localization in high-purity titanium. *International Journal of Plasticity*, 92:148–163, 2017.

TT Zhu, AJ Bushby, and DJ Dunstan. Size effect in the initiation of plasticity for ceramics in nanoindentation. *Journal of the Mechanics and Physics of Solids*, 56(4): 1170–1185, 2008. URL `https://doi.org/10.1016/j.jmps.2007.10.003`.

Kolja Zoller, Szilvia Kalácska, Péter Dusán Ispánovity, and Katrin Schulz. Microstructure evolution of compressed micropillars investigated by in situ hr-ebsd analysis and dislocation density simulations. *arXiv preprint arXiv:2011.08587*, 2020.